

UNIVERSITY OF OKLAHOMA

GRADUATE COLLEGE

FRACTURE CHARACTERIZATION, STRUCTURAL CONTROLS AND
SIMULATION

A DISSERTATION

SUBMITTED TO THE GRADUATE FACULTY

in partial fulfillment of the requirements for the

Degree of

DOCTOR OF PHILOSOPHY

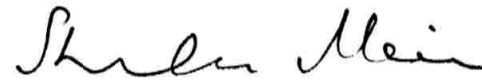
By

KAJARI GHOSH
Norman, Oklahoma
2009

FRACTURE CHARACTERIZATION, STRUCTURAL CONTROLS AND
SIMULATION

A DISSERTATION APPROVED FOR THE
CONOCOPHILIPS SCHOOL OF GEOLOGY AND GEOPHYSICS

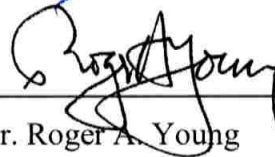
BY



Dr. Shankar Mitra (Chair)



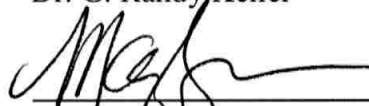
Dr. Ze'ev Reches



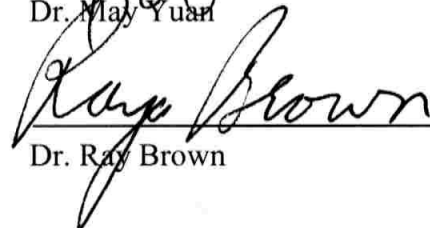
Dr. Roger A. Young



Dr. G. Randy Keller



Dr. May Yuan



Dr. Ray Brown

©Copyright by KAJARI GHOSH 2009
ALL RIGHTS RESERVED.

ACKNOWLEDGMENTS

I am greatly indebted to my mentor and advisor, Dr. Shankar Mitra for providing invaluable professional, academic, and personal counsel. I wish to thank Dr. Roger Young, Dr. Ze'ev Reches, Dr. G. Randy Keller, Dr. May Yuan, and Dr. Ray Brown for their time, suggestions and for being part of my committee. I would like to express my sincere gratitude to the personnel at the SCIF lab at OU and OU IT. I am also sincerely grateful to Dr. Dave Stearns for several technical discussions we had and the time he shared while showing his vast collection of slides he accumulated over years of field work in the Sawtooth Range, MT. I would also like to express my thanks to all the graduate students and staff at the University of Oklahoma, School of Geology and Geophysics for being an essential source of friendship and support. My co-workers Shamik Bose and Jim Miller were involved in many technical discussions and I am thankful to them. My friends Sankar Muhuri and Satavisa Sarkar always acted as a guide and helped me with numerous technical discussions on structural geology. I wish to thank my parents and my brother Kaushik Ghosh for their emotional and moral support. Finally, I would like to thank my co-worker and husband Subho Banerjee, whose professional and emotional support during the course of my PhD made it possible.

TABLE OF CONTENTS

	<u>Page</u>
ACKNOWLEDGMENTS	iv
LIST OF TABLES	vii
LIST OF FIGURES	viii
ABSTRACT	xxvi
CHAPTER 1: INTRODUCTION	1
1.1 Introduction.....	2
1.2 Objective	3
1.3 Significance of the study.....	5
CHAPTER 2: FRACTURE DISTRIBUTION IN TETON ANTICLINE.....	7
2.1 Introduction.....	8
2.2 Objectives	9
2.3 Structural background on Teton Anticline.....	10
2.4 Previous work	11
2.5 Approach.....	13
2.6 Fracture characterization.....	16
2.7 Controls of structural position	18
2.8 Relationship of fracture densities to macroscopic structural evolution	18
2.9 Fracture connectivity and cluster analysis	20
2.10 Discussion and conclusions	23
CHAPTER 3: FRACTURE SIMULATION	38
3.1 Introduction.....	39
3.2 Previous work in fracture simulation.....	40
3.3 Local fracture simulation method	41
3.4 Structurally controlled simulation method.....	49
3.5 Review of results of fracture simulation.....	54
3.6 Conclusions.....	62

CHAPTER 4: FRACTURE DISTRIBUTIONS OF CANYONLANDS	83
4.1 Introduction.....	84
4.2 Structural background of Canyonlands.....	85
4.3 Fracture characteristics in the Canyonlands	86
4.4 Structural controls of fractures in the Canyonlands.....	89
4.5 Fracture connectivity in the Canyonlands.....	91
4.6 Conclusions.....	92
CHAPTER 5: FRACTURE CONNECTIVITY.....	110
5.1 Introduction.....	111
5.2 Approach.....	112
5.3 Methodology	113
5.4 Single fracture set	114
5.5 Two fracture set, one set dominant.....	116
5.6 Two fracture sets, both set varying.....	119
5.7 Connectivity pattern from outcrop examples.....	120
5.8 Conclusions.....	127
REFERENCES	147
APPENDIX A.....	162
APPENDIX B.....	167

LIST OF TABLES

		<u>Page</u>
Table 3.1	Comparison chart of longitudinal fracture parameters	57
Table 3.2	Comparison chart of transverse fracture parameters	58
Table 3.3	Comparison chart of oblique fracture parameters	59
Table 3.4	Comparison chart of connectivity	62
Table 5.1	Summary table of acute angle between systematic and cross fracture orientation (θ) (in degree) and the critical length (L_x) (in meter) of cross fracture. The spacing between systematic fractures is constant at 1 meter.	118
Table A1	Fracture simulation models, (Dershowtiz et al. 1999)	163

LIST OF FIGURES

		<u>Page</u>
Figure 2.1	(a) Map of northwestern Montana showing the location the study area. (b) Location of fracture measurements on 1meter resolution digital color orthophoto. (c) Generalized geologic map of study area after Mudge (1972).	26
Figure 2.2	Map showing locations of fracture measurements. Large fracture maps locations (1 to 13) are marked by triangles and small fracture map locations (a to o)) are marked by circles. The locations of subtle hinge zones are shown by stippled pattern. The dip is contoured at 1 degree interval.	27
Figure 2.3	(a) Map showing locations of fracture measurements. The locations of the hinge zones are shown by stippled. Large fracture map locations (1 to 13) are marked by triangles and small fracture locations (a to o) are marked by circles. (b) Photograph of Teton anticline looking NNW, the dotted line showing the approximate location of the area studied.	28
Figure 2.4	Example of fracture map of two different scales. (a) fracture maps of ~90 sq.m., overalin by a 1m grid. (b) photograph of location of fracture map where fractures are mapped out of georectified photographs. (c) fracture traces digitized out of (b).	29
Figure 2.5	a-c. Rose diagrams showing the strikes of (a) Longitudinal (b) Transverse and (c) Oblique fractures. d-f. Equal area stereographic plots showing poles to planes of fractures and bedding. (d) Longitudinal fractures. (e) Transverse and (f) Oblique fractures. F.A.= the local orientation of fold axis, plunging 2 degree towards 352 degree. g-i. Rose diagrams and stereographic plots of the orientation of Longitudinal, Transverse and Oblique fractures, with bedding rotated.	30
Figure 2.6	(a) Schematic diagram showing the method of calculating the fracture density for a single fracture set. (b) Mapped longitudinal fractures for location 6 (hinge location) in figure 2. (c) Fracture density map of longitudinal fractures for location 6. (c) Mapped longitudinal fractures for location 3 (limb location) in figure 2. (e) Fracture density map of longitudinal fractures for location 3.	31

Figure 2.7	Histogram showing density distribution of (a) Longitudinal fractures (b) Transverse fractures (c) NNE oblique fractures and (d) WNW oblique fractures. Histogram showing length distribution of (e) Longitudinal fractures (f) Transverse fractures (g) NNE oblique fractures (h) WNW oblique fractures.	32
Figure 2.8	Length distribution of (a) longitudinal fractures of hinge locations; (b) longitudinal fractures of limb locations. (c) Density distribution of longitudinal fractures of hinge locations. (d) Density distribution of longitudinal fractures of limb locations.	33
Figure 2.9	(a) Map showing the density of longitudinal fractures for all locations. The gray areas mark the locations of subtle hinge zones. The oriented line indicates the average strike of longitudinal fractures at each location and the number indicates the fracture density of Longitudinal fractures. (b) Plot showing the variation of Longitudinal Fracture Density with Distance from the nearest hinge zone.	34
Figure 2.10	(a-b) Schematic fracture maps showing two areas with same fractional connected area. Gray polygons show the individual clusters for each case. (c) Histogram of distribution of cluster area for case 1 (d) Histogram of distribution of cluster area for case 2.	35
Figure 2.11	(a) Cluster areas (represented by gray polygons) for location 3 in figure 4.1 (limb location). (b) Cluster areas for location 6 in figure 4.1 (hinge location). (c) Histogram showing distribution of cluster areas for location 3. (d) Histogram showing distribution of cluster areas for location 6.	36
Figure 2.12	Figure 2.11. (a) Cluster areas (represented by gray polygons) for location 3 in figure 4.1 (limb location). (b) Cluster areas for location 6 in figure 4.1 (hinge location). (c) Histogram showing distribution of cluster areas for location 3. (d) Histogram showing distribution of cluster areas for location 6.	37
Figure 3.1	Illustration of simulation of fracture length from a small sample area to a larger simulation area. (a) Sample and simulation area. (b) Sample map used for simulation. (c) Cumulative frequency distribution of fracture length for sample map (d) Cumulative frequency distribution of fracture length for the simulation are derived from the	64

sample fracture map.

Figure 3.2	(a) Length grid of sample fractures (b) Length grid derived from random points with length values assigned using the data from sample fractures. (c) Semivariogram to compare the sample area length grid and that derived, using the length distribution pattern.	65
Figure 3.3	(a) Density grid of sample map calculated as the summation of length within a search radius divided by the circular search area. (b) Density grid of simulated fractures. (c) Semivariogram derived from the sample fracture density grid and simulated fracture density grid to compare the closeness of result.	66
Figure 3.4	Illustration of simulation of fracture density (= number of fractures/sq. area). (a) Fracture density of sample area. (b) semivariogram derived from sample map fracture density (c) simulation of fracture density over larger area using the semivariogram (d) fracture density of the sample area extracted from the simulated area.	67
Figure 3.5	Illustration of fracture center generation: (a) value of each cell in the grid represents the number the fractures within a specified search area, (b) a zoomed in view of 1(a), (c) Grid resampled such that the cell size is equal to the search area. Each cell has a value that represents the number of fracture centers within the cell. (d) Fractures generated from fracture centers generated within each cell.	68
Figure 3.6	(a) Sample fracture map used for simulation. (b) Simulated fracture map.(c) Simulated fracture map zoomed in to the area of sample map. (d) Mean orientation of sample fractures.(e) Mean orientation of simulated fractures. (f) Mean orientation of simulated fractures extracted from the sample area.	69
Figure 3.7	Plots showing variation of density of (a) longitudinal fractures with respect to subtle hinges of Teton anticline and (b) transverse fractures with respect to the regional fractures of the area.	70
Figure 3.8	(a) Top view of Teton anticline, color coded by distance from hinge. (b) Profile of Teton anticline, yellow dots marking the location of subtle hinges. (c) Theoretical curve fitted through longitudinal fracture density.	71
Figure 3.9	Longitudinal fracture density draped on the fold surface. (a) Oblique view (b) Top view.	72

Figure 3.10	Length distribution of longitudinal fractures. (a) Mean length of sample locations plotted against distance from hinge of each location. (b) Length distribution of longitudinal fractures on hinges. (c) Length distribution of longitudinal fractures on limbs	73
Figure 3.11	Simulated length grids. (a) Length grid for the area within 25m from the hinges. (b) Length grid for area at least 25m away from hinge. (c) Integrated length grid for the entire structure.	74
Figure 3.12	(a)Index map showing the location of hinges and longitudinal fracture density (in m/sq.m) for simulated and sample maps. Fracture map and respective simulation of longitudinal set of locations marked in red are displayed in figures b through g. Location 1 and 3 area hinge locations while location 2 is a limb location. (b) Longitudinal fracture map of location 1. (c) Simulated longitudinal fracture map of location 1.(d) Longitudinal fracture map of location 2. (e) Simulated longitudinal fracture map of location 2. (f) Longitudinal fracture map of location 3. (g) Simulated longitudinal fracture map of location 3.	75
Figure 3.13	(a) Plot of density of sample versus simulated fractures for all the locations. Red line in the plot is a line of 45 degree slope, black line is the trend line fitted to data points. (b) Plot of length of sample versus simulated fractures for all the locations. Red line in the plot is a line of 45 degree slope, black line is the trend line fitted to data points. (c) Frequency distribution of length for longitudinal fractures of sample maps. (d) Frequency distribution of length for longitudinal fractures of simulated maps.	76
Figure 3.14	(a)Index map showing the location of hinges and transverse fracture density (in m/sq.m) for simulated and sample maps. Fracture map and respective simulation of transverse set of locations marked in red are displayed in figures b through g. Location 1 and 3 are hinge locations while location 2 is a limb location. (b) Transverse fracture map of location 1. (c) Simulated transverse fracture map of location 1.(d) Transverse fracture map of location 2. (e) Simulated transverse fracture map of location 2. (f) Transverse fracture map of location 3. (g) Simulated transverse fracture map of location 3.	77
Figure 3.15	(a) Plot of density of sample versus simulated fractures for	78

	all the locations. Red line in the plot is a line of 45 degree slope, black line is the trend line fitted to data points. (b) Plot of length of sample versus simulated fractures for all the locations. Red line in the plot is a line of 45 degree slope, black line is the trend line fitted to data points. (c) Frequency distribution of length for transverse fractures of sample maps. (d) Frequency distribution of length for transverse fractures of simulated maps.	
Figure 3.16	(a)Index map showing the location of hinges and oblique fracture density (in m/sq.m) for simulated and sample maps. Fracture map and respective simulation of oblique set of locations marked in red are displayed in figures b through g. Location 1 and 3 area hinge locations while location 2 is a limb location. (b) Oblique fracture map of location 1. (c) Simulated oblique fracture map of location 1.(d) Oblique fracture map of location 2. (e) Simulated oblique fracture map of location 2. (f) Oblique fracture map of location 3. (g) Simulated oblique fracture map of location 3.	79
Figure 3.17	(a) Frequency distribution of length for NNE oblique fractures of sample maps. (b) Frequency distribution of length for NNE oblique fractures of simulated maps. (c) Frequency distribution of length for NNW oblique fractures of sample maps. (d) Frequency distribution of length for NNW oblique fractures of simulated maps.	80
Figure 3.18	(a)Index map showing the location of hinges and Fractional Connected Area for simulated and sample maps. Fracture map and respective simulation of all sets of locations marked in red are displayed in figures b through g. Location 1 and 3 are hinge locations while location 2 is a limb location. (b) Connectivity map of location 1. (c) Simulated connectivity map of location 1.(d) Connectivity map of location 2. (e) Simulated connectivity map of location 2. (f) Connectivity map of location 3. (g) Simulated connectivity map of location 3.	81
Figure 3.19	Histogram of fractional connected area from all the sample maps and the simulated fractures extracted using the sample map area. The statistics for the same is recorded in the adjacent table.	82
Figure 4.1	(a) Location of study area marked by a red dot on state map of Utah. (b) Generalized structure map of	94

	Canyonlands area ((Hintze, 2000) (c) Generalized geologic map of study area (Hintze, 2000).	
Figure 4.2	(a) Location of Canyonlands needles district in Utah. (b) General geologic map of the study area, red boundary showing the extent of the study area. (c) Location of fracture data measurement on 60cm resolution Quickbird image. The yellow lines on the image indicate traces of normal faults in the area, acquired from Utah geological survey, (Hintze et al., 2000).	95
Figure 4.3	Fractures mapped on 60cm resolution Quickbird image. The yellow lines on the image indicate traces of normal faults in the area, acquired from Utah geological survey, (Hintze et al., 2000).	96
Figure 4.4	Fractures mapped on 60cm resolution Quickbird image. The yellow lines on the image indicate traces of normal faults in the area, acquired from Utah geological survey, (Hintze et al., 2000). Red lines indicating fractures striking 14° and green lines indicating fractures striking 30°. (b) Rose diagram showing strikes of 30° set. (c) Equal area stereographic plots showing poles to planes of 30° set. (d) Rose diagram showing strikes of 14° set. (c) Equal area stereographic plots showing poles to planes of 14° set.	97
Figure 4.5	Fractures mapped on 60cm resolution Quickbird image. The yellow lines on the image indicate traces of normal faults in the area, acquired from Utah geological survey, (Hintze et al., 2000). Red lines indicating fractures striking 121° and green lines indicating fractures striking 137°. (b) Rose diagram showing strikes of 137° set. (c) Equal area stereographic plots showing poles to planes of 137° set. (d) Rose diagram showing strikes of 121° set. (c) Equal area stereographic plots showing poles to planes of 121° set. N: Number of fractures	98
Figure 4.6	Orientation of oblique sets. a-b. Rose diagrams showing the strikes of (a) 44° and (b) 76° fracture set. c-d. Equal area stereographic plots showing poles to planes of fractures and great circle bedding. (c) 44° (d) 76° fracture. e-f. Rose diagrams showing the strikes of (e) 102 and (f) 166° fracture set. g-h. Equal area stereographic plots showing poles to planes of fractures and great circle of bedding. (g) 102 (h) 166 fracture set.	99

Figure 4.7	Fractures mapped on 60cm resolution Quickbird image. The yellow lines on the image indicate traces of normal faults in the area, acquired from Utah geological survey, (Hintze et al., 2000). Red lines indicating fault parallel fractures striking 14° degree set and green lines indicating fault parallel fractures striking 30° degree set. (b) Length histogram of 14° degree set. (c) Length histogram of 30° degree set.	100
Figure 4.8	Fractures mapped on 60cm resolution Quickbird image. The yellow lines on the image indicate traces of normal faults in the area, acquired from Utah geological survey, (Hintze et al., 2000). Red lines indicating fault parallel fractures striking 14° set and green lines indicating fault parallel fractures striking 30° set. (b) Density histogram of 14° set. (c) Density histogram of 30° set.	101
Figure 4.9	Fractures mapped on 60cm resolution Quickbird image. The yellow lines on the image indicate traces of normal faults in the area, acquired from Utah geological survey, (Hintze et al., 2000). Red lines indicating fault normal fractures striking 121° and green lines indicating fault normal fractures striking 137°. (b) Length distribution of 137° set. (c) Length distribution of 121° set. N: Number of fractures.	102
Figure 4.10	Fractures mapped on 60cm resolution Quickbird image. The yellow lines on the image indicate traces of normal faults in the area, acquired from Utah geological survey, (Hintze et al., 2000). Red lines indicating fault normal fractures striking 121 and green lines indicating fault normal fractures striking 137. (b) Density distribution of 137° set. (c) Density distribution of 121° set. N: Number of fractures	103
Figure 4.11	Fault parallel and fault normal fracture exposed on the surface of an interlayer within Cedar Mesa sandstone. Pen (15cm) in photograph for scale. Point to note is that the termination of fault normal fracture against fault parallel set. (b) Same relation of termination is observed in remotely sensed image.	104
Figure 4.12	Map showing density distribution of fault parallel and fault normal fracture set. (a) Fault parallel (14°) fracture set (b) Fault parallel (30°) fracture set (c) Fault normal (121°) fracture set and (d) Fault normal (137°) fracture set.	105

Figure 4.13	Map showing density distribution (a) 44° fracture set (b) 76° fracture set (c) 102° fracture set and (d) 166° fracture set.	106
Figure 4.14	(a) Schematic diagram showing distance calculation from fault traces. (b) Plot of fault parallel fracture Density against Distance from nearest fault. (c) Plot of fault normal fracture Density against Distance from nearest fault. (d) Schematic diagram showing distance calculation from fault intersection and/or tip. (e) Plot of fault parallel fracture Density against Distance from nearest fault tip; gray area marks the no-data region. (f) Plot of fault normal fracture Density against Distance from nearest fault tip; gray area marks the no-data region.	107
Figure 4.15	Fracture connectivity patterns in Canyonlands area. The yellow polygons represent the connected area, the red lines are traces of normal faults, and the black lines are the traces of connected group of fractures.	108
Figure 4.16	(a) Map showing density distribution of connected fractures (b) Plot showing Fractional connected length (connected fracture density) against Distance from normal fault	109
Figure 5.1	(a) Single set of fracture with an angular dispersion of 15 degree. (b) Two sets of fractures with one dominant set extending across the study area and a second set of cross fractures developed in between the dominant set. (c) Two orthogonal set of fractures where both sets are dominant.	128
Figure 5.2	Examples from single set of simulated fractures with 10 degree dispersion in strike, varying between 175 to 185 degree. (a-d) Single set of fracture with varying length and spacing. (e) Fracture cluster extracted from 5.2a. (f) Fracture cluster extracted from 5.2b. (g) Fracture cluster extracted from 5.2c. (h) Fracture cluster extracted from 5.2d. L*: Normalized length; S*: Normalized spacing.	129
Figure 5.3	Examples from single set of simulated fractures with 20 degree dispersion in strike, varying between 175 to 185 degree. (a-d) Single set of fracture with varying length and spacing. (e) Fracture cluster extracted from 5.3a. (f) Fracture cluster extracted from 5.3b. (g) Fracture cluster extracted from 5.3c. (h) Fracture cluster extracted from 5.3d. L*: Normalized length; S*: Normalized spacing.	130

Figure 5.4	Examples from single set of simulated fractures with 30 degree dispersion in strike, varying between 165 to 195 degree. (a-d) Single set of fracture with varying length and spacing. (e) Fracture cluster extracted from 5.4a. (f) Fracture cluster extracted from 5.4b. (g) Fracture cluster extracted from 5.4c. (h) Fracture cluster extracted from 5.4d. L*: Normalized length; S*: Normalized spacing.	131
Figure 5.5	Plot of Spacing vs. Fractional Connected Area for varying length and orientation. The curve for varying length in each plot is color coded. L: Normalized length of fracture.	132
Figure 5.6	(a-f) Simulation of two sets of fractures, angle between 2 sets ranges from 15 to 19 degree. (g-l) Angle between 2 sets range from 30 to 34 degree. (m-r) Angle between 2 sets range from 45 to 49 degree. L: Normalized length of cross fractures; A: Angle between two sets in degrees.	133
Figure 5.7	(a-f) Simulation of two sets of fractures, angle between 2 sets ranges from 60 to 64 degree. (g-l) Angle between 2 sets range from 75 to 79 degree. (m-p) Angle between 2 sets range from 86 to 90 degree. L: Normalized length of cross fractures; A: Angle between two sets in degrees.	134
Figure 5.8	(a-f) Plot of fractional connected area and cluster size versus length of cross fractures for different angular difference between two sets. (g) Plot of critical length of cross fracture required for cluster size to be equal to 1 versus the angle between the two sets of fractures.	135
Figure 5.9	Simulation of two orthogonal set of fractures. Normalized length of EW and NS fracture is 0.1. Red lines indicate the connected group of fractures. (a-c) Density of NS set 1m/sq.m and density of EW set vary from 1 to 3m/sq.m. (d-f) Density of NS set 3m/sq.m and density of EW set vary from 1 to 3m/sq.m. FCA: Fractional Connected Area.	136
Figure 5.10	Simulation of two orthogonal set of fractures. Normalized length of EW set is 0.1 and NS set is 0.3. Red lines indicate the connected group of fractures. (a-c) Density of NS set 1m/sq.m and density of EW set vary from 1 to 3m/sq.m. (d-f) Density of NS set 3m/sq.m and density of EW set vary from 1 to 3m/sq.m. FCA: Fractional Connected Area.	137
Figure 5.11	Simulation of two sets at 45 degrees. Length of EW and NS set is 0.1. Red lines indicate the connected group of fractures. (a-c) Density of NS set 1m/sq.m and density of	138

	EW set vary from 1 to 3m/sq.m. (d-f) Density of NS set 3m/sq.m and density of EW set vary from 1 to 3m/sq.m. FCA: Fractional Connected Area.	
Figure 5.12	Simulation of two sets at 45 degrees. Length of EW set is 0.1 and NS set is 0.3. Red lines indicate the connected group of fractures. (a-c) Density of NS set 1m/sq.m and density of EW set vary from 1 to 3m/sq.m. (d-f) Density of NS set 3m/sq.m and density of EW set vary from 1 to 3m/sq.m. FCA: Fractional Connected Area.	139
Figure 5.13	Graphical representation of simulation results for two sets of fractures with changing length and density. Plots of D2 versus Fractional Connected Area. (a) Orthogonal sets with normalized length of of both sets is 0.1 (b) Orthogonal sets with normalized length of L1=0.3 and L2=0.1. (c) 45 degree sets with normalized length of both sets is 0.1. (d) 45 degree sets with normalized length of L1=0.3 and L2=0.1.(e) Orthogonal set and 45 degree set plotted together, curves color coded for varying L1 and D1. L1: Normalized length of NS set; D1: Density of NS set; L2: Normalized length of EW set; D2: Density of EW set.	140
Figure 5.14	(a) Fractures hosted in Tensleep sandstone (Bellahsen et al., 2006). (b) Fracture cluster extracted from photo 5.14a. Red lines indicate fractures contributing to the cluster. (c) Simulated fractures with low strike dispersion. (d) Fractures hosted in Carboniferous sandstone at Telpyn point, Wales, UK, (Rohrbaugh et al.,2002). (e) Anastomosing fracture pattern in Entrada sandstone, Utah, (Lorenz and Cooper, 2000). θ : Dispersion of strike orientation.	141
Figure 5.15	Natural fractures in Lompoc Landing, California. (a) NS trending fractures. (b) Connected group of NNW-SSE and NE-SW trending fractures. (c) EW trending fractures. (d) Connected group of EW trending fractures. (e) Fracture network consisting of all fracture sets. (f) Connected group of fractures constituted of all set of fractures. θ : Dispersion of strike within a singel set.	142
Figure 5.16	(a) Natural fractures hosted in Nashpoint limestone, (Josnin et. al., 2002). (b) Fracture trace of a part of the pavement marked by dotted lines in 5.16a (c) Fractures in Jurassic limestone formation, Llanwit Major, Wales,	143

	(Rohrbaugh et al., 2002). (d) Simulated fractures intersecting at high angle. θ : Dispersion of strike orientation.	
Figure 5.17	(a) Two sets of fractures intersecting at low angle on the flank of Salt Valley Anticline. Some fractures are traced out on the photograph to highlight the angular relation between intersecting fractures. (b) Fracture traces from part of figure 5.17a marked by a dotted line. Two sets of fractures represented by blue and red line. (c) Two sets of simulated fractures intersecting at low angles.	144
Figure 5.18	(a) Two sets of fractures at high angle, hosted in Tensleep sandstone. (b) Fracture traces of the pavement shown in figure 5.18a. Red lines represent fractures that belong to the fracture cluster.(c) Example from simulation of a condition similar to 5.18a.	145
Figure 5.19	Fractures hosted in carbonate unit of western flank of Teton anticline. (a) One dominant set of fracture resulting into continuous connected network. (b) Several set of fractures resulting into connected pattern but not continuous pathway. (c) Low fracture density resulting into low connectivity despite of multiple set of fractures. (d-e) Examples from simulated map.	146
Figure A1	(a) Density map of longitudinal fractures for location M01. (b) Density map of simulated longitudinal fractures for location M01. The fractures for area M01 are extracted from the simulated map generated for the entire Teton anticline. (c) Density map of longitudinal fractures for location M02. (d) Density map of simulated longitudinal fractures for location M02. The fractures for area M02 are extracted from the simulated map generated for the entire Teton anticline. (e) Fracture map of longitudinal set for location M01. (f) Simulated fracture map of longitudinal set for location M01. (g) Fracture map of longitudinal set for location M02. (h) Simulated fracture map of longitudinal set for location M02.	168
Figure A2	(a) Density map of longitudinal fractures for location M03. (b) Density map of simulated longitudinal fractures for location M03. The fractures for area M03 are extracted from the simulated map generated for the entire Teton anticline. (c) Density map of longitudinal fractures for location M04. (d) Density map of simulated longitudinal	169

	fractures for location M04. The fractures for area M04 are extracted from the simulated map generated for the entire Teton anticline. (e) Fracture map of longitudinal set for location M03. (f) Simulated Fracture map of longitudinal set for location M03. (g) Fracture map of longitudinal set for location M04. (h) Simulated fracture map of longitudinal set for location M04.	
Figure A3	(a) Density map of longitudinal fractures for location M05. (b) Density map of simulated longitudinal fractures for location M05. The fractures for area M05 are extracted from the simulated map generated for the entire Teton anticline. (c) Density map of longitudinal fractures for location M06. (d) Density map of simulated longitudinal fractures for location M06. The fractures for area M06 are extracted from the simulated map generated for the entire Teton anticline. (e) Fracture map of longitudinal set for location M05. (f) Simulated Fracture map of longitudinal set for location M05. (g) Fracture map of longitudinal set for location M06. (h) Simulated fracture map of longitudinal set for location M06.	170
Figure A4	(a) Density map of longitudinal fractures for location M07. (b) Density map of simulated longitudinal fractures for location M07. The fractures for area M07 are extracted from the simulated map generated for the entire Teton anticline. (c) Density map of longitudinal fractures for location M08. (d) Density map of simulated longitudinal fractures for location M08. The fractures for area M08 are extracted from the simulated map generated for the entire Teton anticline. (e) Fracture map of longitudinal set for location M07. (f) Simulated fracture map of longitudinal set for location M07. (g) Fracture map of longitudinal set for location M08. (h) Simulated fracture map of longitudinal set for location M08.	171
Figure A5	(a) Density map of longitudinal fractures for location M09. (b) Density map of simulated longitudinal fractures for location M09. The fractures for area M09 are extracted from the simulated map generated for the entire Teton anticline. (c) Density map of longitudinal fractures for location M10. (d) Density map of simulated longitudinal fractures for location M10. The fractures for area M10 are extracted from the simulated map generated for the entire	172

	Teton anticline. (e) Fracture map of longitudinal set for location M09. (f) Simulated fracture map of longitudinal set for location M09. (g) Fracture map of longitudinal set for location M10. (h) Simulated fracture map of longitudinal set for location M10.	
Figure A6	(a) Density map of longitudinal fractures for location M11. (b) Density map of simulated longitudinal fractures for location M11. The fractures for area M11 are extracted from the simulated map generated for the entire Teton anticline. (c) Density map of longitudinal fractures for location M12. (d) Density map of simulated longitudinal fractures for location M12. The fractures for area M12 are extracted from the simulated map generated for the entire Teton anticline. (e) Fracture map of longitudinal set for location M11. (f) Simulated fracture map of longitudinal set for location M11. (g) Fracture map of longitudinal set for location M12. (h) Simulated fracture map of longitudinal set for location M12.	173
Figure A7	(a) Density map of longitudinal fractures for location M13. (b) Density map of simulated longitudinal fractures for location M13. The fractures for area M13 are extracted from the simulated map generated for the entire Teton anticline. (c) Fracture map of longitudinal set for location M13. (d) Simulated fracture map of longitudinal set for location M13.	174
Figure A8	(a) Density map of transverse fractures for location M01. (b) Density map of simulated transverse fractures for location M01. The fractures for area M01 are extracted from the simulated map generated for the entire Teton anticline. (c) Density map of transverse fractures for location M02. (d) Density map of simulated transverse fractures for location M02. The fractures for area M02 are extracted from the simulated map generated for the entire Teton anticline. (e) Fracture map of transverse set for location M01. (f) Simulated fracture map of transverse set for location M01. (g) Fracture map of transverse set for location M02. (h) Simulated fracture map of transverse set for location M02.	175
Figure A9	(a) Density map of transverse fractures for location M03. (b) Density map of simulated transverse fractures for location M03. The fractures for area M03 are extracted	176

	from the simulated map generated for the entire Teton anticline. (c) Density map of transverse fractures for location M04. (d) Density map of simulated transverse fractures for location M04. The fractures for area M04 are extracted from the simulated map generated for the entire Teton anticline. (e) Fracture map of transverse set for location M03. (f) Simulated fracture map of transverse set for location M03. (g) Fracture map of transverse set for location M04. (h) Simulated fracture map of transverse set for location M04.	
Figure A10	(a) Density map of transverse fractures for location M05. (b) Density map of simulated transverse fractures for location M05. The fractures for area M05 are extracted from the simulated map generated for the entire Teton anticline. (c) Density map of transverse fractures for location M06. (d) Density map of simulated transverse fractures for location M06. The fractures for area M06 are extracted from the simulated map generated for the entire Teton anticline. (e) Fracture map of transverse set for location M05. (f) Simulated fracture map of transverse set for location M05. (g) Fracture map of transverse set for location M06. (h) Simulated fracture map of transverse set for location M06.	177
Figure A11	(a) Density map of transverse fractures for location M07. (b) Density map of simulated transverse fractures for location M07. The fractures for area M07 are extracted from the simulated map generated for the entire Teton anticline. (c) Density map of transverse fractures for location M08. (d) Density map of simulated transverse fractures for location M08. The fractures for area M08 are extracted from the simulated map generated for the entire Teton anticline. (e) Fracture map of transverse set for location M07. (f) Simulated fracture map of transverse set for location M07. (g) Fracture map of transverse set for location M08. (h) Simulated fracture map of transverse set for location M08.	178
Figure A12	(a) Density map of transverse fractures for location M09. (b) Density map of simulated transverse fractures for location M09. The fractures for area M09 are extracted from the simulated map generated for the entire Teton anticline. (c) Density map of transverse fractures for	179

	location M10. (d) Density map of simulated transverse fractures for location M10. The fractures for area M10 are extracted from the simulated map generated for the entire Teton anticline. (e) Fracture map of transverse set for location M09. (f) Simulated fracture map of transverse set for location M09. (g) Fracture map of transverse set for location M10. (h) Simulated fracture map of transverse set for location M10.	
Figure A13	(a) Density map of transverse fractures for location M11. (b) Density map of simulated transverse fractures for location M11. The fractures for area M11 are extracted from the simulated map generated for the entire Teton anticline. (c) Density map of transverse fractures for location M12. (d) Density map of simulated transverse fractures for location M12. The fractures for area M12 are extracted from the simulated map generated for the entire Teton anticline. (e) Fracture map of transverse set for location M11. (f) Simulated fracture map of transverse set for location M11. (g) Fracture map of transverse set for location M12. (h) Simulated fracture map of transverse set for location M12.	180
Figure A14	(a) Density map of transverse fractures for location M13. (b) Density map of simulated transverse fractures for location M13. The fractures for area M13 are extracted from the simulated map generated for the entire Teton anticline. (c) Fracture map of transverse set for location M13. (d) Simulated fracture map of transverse set for location M13. (e) Plot of density of sample versus simulated fractures for all the locations. Red line in the plot is a line of 45 degree slope, black line is the trend line fitted to data points. (f) Plot of length of sample versus simulated fractures for all the locations. Red line in the plot is a line of 45 degree slope, black line is the trend line fitted to data points. (g) Frequency distribution of length for transverse fractures of sample maps. (h) Frequency distribution of length for transverse fractures of simulated maps.	181
Figure A15	(a) Density map of oblique fractures for location M01. (b) Density map of simulated oblique fractures for location M01. The fractures for area M01 are extracted from the simulated map generated for the entire Teton anticline. (c)	182

	Density map of oblique fractures for location M02. (d)	
	Density map of simulated oblique fractures for location M02. The fractures for area M02 are extracted from the simulated map generated for the entire Teton anticline. (e)	
	Fracture map of oblique sets for location M01. (f)	
	Simulated fracture map of oblique sets for location M01. (g)	
	Fracture map of oblique sets for location M02. (h)	
	Simulated fracture map of oblique sets for location M02. (a)	
Figure A16	(a) Density map of oblique fractures for location M03. (b)	183
	Density map of simulated oblique fractures for location M03. The fractures for area M03 are extracted from the simulated map generated for the entire Teton anticline. (c)	
	Density map of oblique fractures for location M04. (d)	
	Density map of simulated oblique fractures for location M04. The fractures for area M04 are extracted from the simulated map generated for the entire Teton anticline. (e)	
	Fracture map of oblique sets for location M03. (f)	
	Simulated fracture map of oblique sets for location M03. (g)	
	Fracture map of oblique sets for location M04. (h)	
	Simulated fracture map of oblique sets for location M04. (a)	
Figure A17	(a) Density map of oblique fractures for location M05. (b)	184
	Density map of simulated oblique fractures for location M05. The fractures for area M05 are extracted from the simulated map generated for the entire Teton anticline. (c)	
	Density map of oblique fractures for location M06. (d)	
	Density map of simulated oblique fractures for location M06. The fractures for area M06 are extracted from the simulated map generated for the entire Teton anticline. (e)	
	Fracture map of oblique sets for location M05. (f)	
	Simulated fracture map of oblique sets for location M05. (g)	
	Fracture map of oblique sets for location M06. (h)	
	Simulated fracture map of oblique sets for location M06. (a)	
Figure A18	(a) Density map of oblique fractures for location M07. (b)	185
	Density map of simulated oblique fractures for location M07. The fractures for area M07 are extracted from the simulated map generated for the entire Teton anticline. (c)	
	Density map of oblique fractures for location M08. (d)	
	Density map of simulated oblique fractures for location M08. The fractures for area M08 are extracted from the simulated map generated for the entire Teton anticline. (e)	
	Fracture map of oblique sets for location M07. (f)	

	Simulated fracture map of oblique sets for location M07.	
	(g) Fracture map of oblique sets for location M08. (h)	
Figure A19	Simulated fracture map of oblique sets for location M08. (a) Density map of transverse fractures for location M09. (b) Density map of simulated transverse fractures for location M09. The fractures for area M09 are extracted from the simulated map generated for the entire Teton anticline. (c) Density map of transverse fractures for location M10. (d) Density map of simulated transverse fractures for location M10. The fractures for area M10 are extracted from the simulated map generated for the entire Teton anticline. (e) Fracture map of transverse set for location M09. (f) Simulated fracture map of transverse set for location M09. (g) Fracture map of transverse set for location M10. (h) Simulated fracture map of transverse set for location M10.	186
Figure A20	(a) Density map of oblique fractures for location M11. (b) Density map of simulated oblique fractures for location M11. The fractures for area M11 are extracted from the simulated map generated for the entire Teton anticline. (c) Density map of oblique fractures for location M12. (d) Density map of simulated oblique fractures for location M12. The fractures for area M12 are extracted from the simulated map generated for the entire Teton anticline. (e) Fracture map of oblique sets for location M11. (f) Simulated fracture map of oblique sets for location M11. (g) Fracture map of oblique sets for location M12. (h) Simulated fracture map of oblique sets for location M12.	187
Figure A21	(a) Density map of oblique fractures for location M13. (b) Density map of simulated oblique fractures for location M13. The fractures for area M13 are extracted from the simulated map generated for the entire Teton anticline. (c) Fracture map of oblique sets for location M13. (d) Simulated fracture map of oblique sets for location M13.	188
Figure A22	(a) Fracture cluster map for location M01. (b) Cluster map for fractures of location M01, extracted from the simulated map generated for the entire Teton anticline. (c) Fracture cluster map for location M02. (d) Cluster map for fractures of location M02, extracted from the simulated map generated for the entire Teton anticline.	189

Figure A23	(a) Fracture cluster map for location M03. (b) Cluster map for fractures of location M03, extracted from the simulated map generated for the entire Teton anticline. (c) Fracture cluster map for location M04. (d) Cluster map for fractures of location M04, extracted from the simulated map generated for the entire Teton anticline.	190
Figure A24	(a) Fracture cluster map for location M05. (b) Cluster map for fractures of location M05, extracted from the simulated map generated for the entire Teton anticline. (c) Fracture cluster map for location M06. (d) Cluster map for fractures of location M06, extracted from the simulated map generated for the entire Teton anticline.	191
Figure A25	(a) Fracture cluster map for location M07. (b) Cluster map for fractures of location M07, extracted from the simulated map generated for the entire Teton anticline. (c) Fracture cluster map for location M08. (d) Cluster map for fractures of location M08, extracted from the simulated map generated for the entire Teton anticline.	192
Figure A26	(a) Fracture cluster map for location M09. (b) Cluster map for fractures of location M09, extracted from the simulated map generated for the entire Teton anticline. (c) Fracture cluster map for location M10. (d) Cluster map for fractures of location M10, extracted from the simulated map generated for the entire Teton anticline.	193
Figure A27	(a) Fracture cluster map for location M11. (b) Cluster map for fractures of location M11, extracted from the simulated map generated for the entire Teton anticline. (c) Fracture cluster map for location M12. (d) Cluster map for fractures of location M12, extracted from the simulated map generated for the entire Teton anticline.	194
Figure A28	(a) Fracture cluster map for location M13. (b) Cluster map for fractures of location M13, extracted from the simulated map generated for the entire Teton anticline.	195

Abstract

Fracture network patterns have been studied in two areas with different structural settings: (a) Dolomitic limestones on Teton anticline, in the frontal part of the fold thrust belt in the Sawtooth Range, Montana and (b) Cedar Mesa sandstones within normal faulted structures in the Canyonlands area, Utah. GIS-based techniques were used to study the two-dimensional distribution of fractures on exposed bedding planes in both areas. Individual fracture characteristics, such as fracture length, orientation, and density were analyzed along with the connectivity pattern of fracture networks. The latter parameter is important in determining whether the fractures are isolated or form extensive connected pathways.

Studies on both structures reveal that the fracture patterns vary with structural position. In the Teton anticline, which is a multiple hinge anticline, the longitudinal fractures represent the dominant fracture set, and show the most variation with structural position, with values greater at the hinges than on the limbs. Transverse fractures, on the other hand, show less variation with structural position and show higher densities in the vicinity of regional fractures. A method of fracture simulation which incorporates the structural controls on fracture densities was developed and applied to the Teton anticline. In the Canyonlands area, the higher density of fault-parallel fractures is observed within a narrow zone in the vicinity of normal faults.

Fracture permeability is strongly controlled by the connectivity of fractures. The connectivity of a fracture network depends on the geometry and characteristics of individual fractures and also on how the fracture sets are distributed in space. Increasing fracture propagation leads to the formation of clusters or connected fractures. The connected clusters increase in size as (1) an increasing number of fractures are added to the system, (2) the lengths of the fractures increase to connect individual fractures, (3) the orientations of fractures in a set exhibit a higher degree of dispersion, or (4) fractures of multiple sets are added to the system. A series of fracture simulations were modeled to investigate the influence of the four characteristics on the fracture network, and to identify the relative contribution of each factor towards network connectivity. Fracture clustering was also studied for both the Teton anticline and the Canyonlands area, and found to be strongly controlled by structural position.

CHAPTER 1:

INTRODUCTION

1.1 INTRODUCTION

1.2 OBJECTIVES

1.3 SIGNIFICANCE OF THE STUDY

1.1 Introduction

Natural fractures are increasingly recognized as an important factor in the exploration and production of hydrocarbons and also for many environmental applications. Fracturing increases the porosity, and more importantly, the permeability in otherwise tight rock units, and also enhances the connectivity between different units within an oil field. Fracture distribution is heterogeneous and depends on various geologic factors including lithology, bed thickness, proximity to faults and structural position.

Prediction of the fracture density and orientation in different parts of a subsurface structure is difficult because of limited data availability. Subsurface fracture data is limited to oriented core and/or borehole televiewer or log data. Interpolation of fracture densities between these sparse data points requires good analog models based on field-based fracture analysis. Furthermore, methods for simulating fractures across a structure are necessary to predict the fracture pattern and intensities across the entire structure.

Field analysis of fractures in the past has focused on the following topics: (1) Characterization of fracture parameters, (2) Relationship of Fracture Density or Spacing to structural and lithologic factors, and (3) Simulation of fractures. The focus of this research has been on trying to understand the distribution of fractures around major structures and their mechanics of formation. Significant progress has been made in methods of characterizing fracture patterns and predicting the

controls of lithological parameters on fracture intensities. Although a number of studies have been conducted on the variation of fracture parameters with structural position (McQuillan, 1974, Stearns, 1964, Sinclair, 1980), our understanding of these details are less than complete. Simulation of fractures has been successfully conducted for simple fracture patterns which are homogeneous within the area of observation (Barton, 1995, Josnin et al., 2002). However, no studies of fracture simulation with variable intensities and orientations around a macroscopic structure have been conducted to date.

In order to successfully predict fracture orientations, lengths and densities in the subsurface, it is necessary to have surface analogs of fracture patterns in compressive and extensional setting. The surface model should not only show typical fracture orientations, length distributions, and densities, but the variation of fracture parameters relative to structural position, especially distance from fold hinges or distance from the fault. It is also necessary to develop method of simulating fracture patterns and densities based on variations in structural position. Fractures along Teton anticline in the frontal part of Sawtooth Range, Montana, and in Grabens area of the Canyonlands National Park, Utah, presents excellent example that fulfill these criteria.

1.2 Objectives

The objective of this study is to (1) conduct detailed fracture analyses in different structural settings, to provide good surface analogs for subsurface fracture prediction, and (2) design a method for two dimensional fracture simulation that can incorporate the structural relation inferred from fracture characterization with respect to macroscopic structure. The structures selected for this study are the Teton anticline which exposes Devonian and Mississippian carbonates in the frontal part of Sawtooth fold-thrust belt in Montana and the Canyonlands Graben of Paradox Basin, Utah, which exposes the fractures in Jurassic sandstone within an extensional setting.

More specific targets are (1) to map the fracture pattern in different structural settings and identify the difference in mapped patterns; (2) characterize the fracture orientations, lengths and densities in a number of well-mapped outcrops around the structures; (3) analyze the variation of fracture densities of different fracture sets with structural position; (4) design a method of fracture simulation using the spatial relation of fractures with respect to structural position; and (5) study the interaction of different fracture parameters that control fracture connectivity.

These topics are discussed in chapters 2 through 5. Chapter 2 is dedicated to fracture characterization across a folded carbonate unit. The study is carried out for the Teton anticline, which is an open, asymmetric, multi-hinge fold. Fracture

parameters are related to the structural position on the fold. Also, detailed fracture connectivity analysis is performed to investigate the interaction of different fracture sets and its sensitivity to structural position.

In chapter 3, a two dimensional fracture simulation is designed that is based on the database generated for Teton anticline. The simulation is designed such that it can incorporate the spatial variation of fracture parameters with respect to structural position. The theoretical background for the simulation and the significance of the results are discussed in detail in this chapter.

Chapter 4 is devoted to fracture characterization in an extensional setting. The study is carried out in the Graben Area of the Needles district of Canyonlands National Park, Utah. In this case the variation of fracture parameters is related to normal faults. The spatial variation of fracture density is used as a guide to investigate the evolution of faults and fractures.

In Chapter 5, a series of theoretical fracture simulations is conducted to identify the contribution of different fracture parameters towards fracture connectivity.

1.3 Significance of the Study

Fracture distribution directly affects the hydrologic and mechanical properties of rock. Fractures may serve as conduits for fluid flow or may act as barriers to flow. For example an interconnected network of opening-mode

fractures can transform an otherwise impermeable rock into a viable aquifer or economic hydrocarbon reservoir. Fractures also play a major role in landscape evolution. Thus, a good understanding of fracture geometry, distribution and fracture mechanism is critical for exploring and producing for hydrocarbons, for groundwater modeling and for evaluating rock mass stability.

This study develops techniques to quantify the spatial distribution of fractures. It also explores the geologic factors that control these spatial variations, especially the structural position. The study also provides a means to incorporate the geologic factor in fracture simulation. The permeability of a fractured rock mass is controlled by the extent to which the individual fractures are linked to form a continuous fracture network through the rock. Thus, the connectivity of a fracture system determines the effective permeability of the rock mass, which in turn is dependent on the fracture geometry and distribution. The analytical techniques developed in this study will provide insight on the two dimensional connectivity of fracture networks.

CHAPTER 2:

FRACTURE DISTRIBUTION IN TETON ANTICLINE

2.1 INTRODUCTION

2.2 OBJECTIVES

2.3 STRUCTURAL BACKGROUND OF TETON ANTICLINE

2.4 PREVIOUS WORK

2.5 APPROACH

2.6 FRACTURE CHARACTERIZATION

2.7 CONTROLS OF STRUCTURAL POSITION

2.8 RELATIONSHIP OF FRACTURE DENSITIES TO

MACROSCOPIC STRUCTURAL EVOLUTION

2.9 FRACTURE CONNECTIVITY AND CLUSTER ANALYSIS

2.10 DISCUSSION AND CONCLUSIONS

2.1 Introduction

The Teton anticline is a multiple hinge anticline containing fractured Mississippian-Devonian carbonates in the frontal part of the Sawtooth Range in Montana. The structure serves as a good surface analog for fracture patterns and connectivities within subsurface folded carbonate reservoirs. The primary fracture sets are longitudinal and transverse relative to the axis of the fold, although two additional oblique sets are also present. The length and density of the longitudinal fracture sets are strongly controlled by position relative to multiple hinges. The transverse fractures are related to changes in fold plunge and exhibit less variation in fracture density. Fracture connectivity is dependent on the number of fracture sets, their orientations and dispersions, and the densities of the fracture sets. The connectivity is measured using two parameters: the fractional connected area which represents the fraction of the total sample area that is connected by fractures, and the distribution of clusters of different sizes in any given area. Because the longitudinal fractures represent the dominant fracture set, and also show the most variation with structural position, the fracture connectivity, as measured by both the fractional connected areas and the distribution of cluster sizes, is greater in vicinity of the fold hinges. The results and approaches used in the study have some important implications for subsurface folded fractured carbonate reservoirs. The analysis of sparsely distributed fracture data from wells must be integrated with an understanding of the controls of the macroscopic

structure on fracture parameters, to effectively simulate fracture patterns and connectivities around subsurface structures.

2.2 Objectives

This chapter describes a detailed analysis of fracture parameters on a folded carbonate unit to provide a surface analog for subsurface fracture prediction. The structure selected for this study is the Teton anticline which exposes Devonian and Mississippian carbonates in the frontal part of Sawtooth fold-thrust belt in Montana (Mudge, 1972). The structure serves as a good analogue for many surface fractured reservoirs in the frontal parts of fold and thrust belts.

The detailed objectives are (1) to characterize the fracture orientations, lengths and densities in a number of well-mapped outcrops around the structure; (2) to analyze the variation of fracture densities of different fracture sets with structural position and lithology, and to understand the distribution of different fracture sets with structural position; (3) to use cluster analysis to understand the interaction of different fracture sets to control the fracture connectivity, and the variation of the connectivity with structural position.

2.3 Structural Background of Teton Anticline

The Northern Montana overthrust belt is an arcuate zone of northerly trending and westerly dipping thrust faults and related folds, formed during late Cretaceous to Tertiary times. The thrust belt can be subdivided into two main subprovinces: the Sawtooth Range, which is made up of large thrusts involving Paleozoic carbonates, and the Disturbed belt, which consists of closely-spaced thrusts and related folds in the Cretaceous units (Mudge, 1972). These two subprovinces correspond to the Front Ranges and the Foothills, respectively, of the Canadian Rockies (Bally et al, 1966).

The Teton anticline is an anticline exposing folded Mississippian and Devonian carbonates located in the frontal part of the Sawtooth Range (Figure 2.1). The structure is an asymmetric anticline with a steep, eastern limb and a somewhat more gently-dipping western limb. The crest and western limb of the structure are well exposed, thereby providing adequate outcrops for detailed fracture analysis. The east limb of the structure is forested and contains few well exposed outcrops and was not analyzed. The size, geometry, and structural position of the anticline make it an excellent surface analog for many subsurface fractured anticlines.

2.4 Previous Work

Many techniques have been developed to characterize fractures in rock masses by quantifying fracture attributes such as spacing (and its inverse, fracture density or intensity), length, aperture and fractal dimension (Stearns, 1967; McQuillan, 1974; Priest and Hudson, 1976; LaPointe and Hudson, 1985; Velde et al., 1990; Narr and Suppe, 1991; Dershowitz, and Herda, 1992; Gillespie et al., 1993; Barton, 1995; Wu and Pollard, 1995; Renshaw, 1997; Ehlen, 2000; Mauldon et al., 2001; La Pointe, 2002; Wu and Pollard, 2002; Peacock et al., 2003, Ortega et. al. 2006). Linear fracture spacing (linear) was traditionally measured along scan lines (Piteau, 1970; La Pointe and Hudson, 1985) and results are represented in the form of a statistical parameters (mean/median fracture spacing and its standard deviation) or a parameter derived from the measurements, e.g. Rock Quality Designation, Fracture Spacing Index, Fracture Spacing Ratio (Priest and Hudson, 1976; Narr and Suppe, 1991; Gross, 1993). For outcrop measurements, areal measures of fracture intensity have been developed and these yield more accurate results. Using this approach, the Fracture intensity of a fracture set is measured either by the number of fractures per unit area or the summed lengths of fractures per unit area (Dershowitz and Herda, 1992, Wu and Pollard, 1995, Mauldon and Dershowitz, 2000).

There has been significant research on the stratigraphic controls of fracture intensity, including parameters such gross lithology, grain size, and texture

(Huang and Angelier, 1989; Narr and Suppe, 1991; Gross et al., 1995; Underwood et al., 2003, Bahat, 1988; Becker and Gross, 1996, Price, 1966; Gross, 1993, Gillespie, et. al., 1999; Bai and Pollard, 2001). In addition to bed thickness and lithology, fracture density has also been found to vary with structural position, including proximity to fracture zones or faults (Friedman, 1969, Stearns and Friedman, 1972, Peacock, 2001) and curvature related to fold geometry (Blanchet, 1957; Harris et al., 1960; Stearns and Friedman, 1972; Lisle, 1994; Engelder et al., 1997; Hennings, et al., 2000).

In addition to studying various attributes of fracture population, fracture networks have also been studied by examining their clustering and resulting connectivity (Odling and Webman, 1991; Priest, 1993; Odling, 1997), building on concepts of percolation theory (Chelidze, 1986; Bebbington et al., 1990; Berkowitz and Balberg, 1993; Berkowitz, 1995; and Gueguen, et al., 1997). Fracture connectivity has been analyzed using these concepts of percolation theory by a number of workers (Odling and Webman, 1991; Odling, 1992; Priest, 1993; Jolly and Cosgrove, 2003).

Fracture patterns on the Teton anticline have been analyzed by a number of workers (Stearns and Friedman, 1972; Sinclair, 1980; Spooner, 1984). These studies have focused on the orientations of fracture orientations around the fold, local measures of fracture intensities and the separation of fracture sets into extension and shear fractures on the basis of their orientations. The fracture

measurements in all cases were conducted at isolated locations and no analyses of the interaction of the different sets to form fracture networks were conducted. The results of these studies (Stearns and Friedman, 1972) are commonly used as models for fracture patterns around open folds.

The present study uses and builds upon this existing inventory of techniques and also incorporates some new methods of fracture characterization. The measurement and characterization of fractures is simplified by incorporating all information into a Geographic Information Systems (GIS). This not only enables an efficient analysis of the distribution and orientations of different fracture sets, but the efficient measure of the intensity of different sets in terms of the total length or number per unit area. Some additional parameters for analyzing fracture clustering are used to meaningfully translate the effects of fracture clustering on reservoir drainage.

2.5 Approach

The present study uses and builds upon this existing inventory of techniques and also incorporates some new methods of fracture characterization. The measurement and characterization of fractures is simplified by incorporating all information into a GIS system. This not only enables an efficient analysis of the distribution and orientations of different fracture sets, but the efficient measure of the intensity of different sets in terms of the total length or number per

unit area. Some additional parameters for analyzing fracture clustering are used to meaningfully translate the effects of fracture clustering on reservoir drainage.

Although the Teton anticline appears to be a concentric anticline from aerial photographs, the detailed geometry consists of segments of low curvature separated by multiple hinges. Detailed structural analysis was used to map out the multiple hinges on the west limb and hinge of the Teton anticline. The hinges were mapped by delineating zones of significant dip change in the bedding data (Figure 2.2), and extrapolated along the structural trend where fewer measurements were made. The changes in dip varied from about 3° (hinge E) to about 10° (hinge A). Four main hinges were mapped between the crest and the exposed area on the west limb, and three additional and more closely spaced hinges were mapped on the east limb (Figure 2.2). Some of these hinges were previously identified by Sinclair (1980) and Spooner (1984), and confirmed as part of this study, whereas others were delineated in this study.

Fracture analysis was conducted on the crest and west limb of the Teton anticline, in the best exposed parts of the structure, immediately north of the north fork of the Teton anticline (Figure 2.3). Most measurements were made on dolomitic limestone units of similar thickness. Two types of sample outcrops were studied: (1) larger continuous outcrops with areas ranging between 30 and 100sq.m and (2) smaller outcrops with areas of 1-2.5sq.m. On the larger outcrops, the fractures were mapped out using a 1sq.m grid and later transferred to a digital

data base (Figure 2.4). The smaller outcrops were mapped using field photographs. For both types of sample outcrops, all fractures visible with the naked eye from a distance of a few feet were mapped. To remove distortion on these smaller maps, they were georectified by measuring grids of control points and transferring them to the photographs. The locations of all the measurement stations on the Teton anticline are shown in Figure 2.3a.

The photographs and fracture maps were scanned and uploaded into ArcMap (ESRI, 2006), and the scanned images were rectified by referencing the coordinates of the control points set at the outcrop. These georectified images were then used to generate the digital fracture maps.

All fractures mapped were primarily extensional fractures. The mapping of fractures focused on the following parameters: (1) the lengths of the fractures, (2) the orientations of the different fracture sets, and (3) the densities (or intensities) of each fracture set. The densities of the fractures were determined from the fracture maps, and were defined by two separate parameters: the number of fractures per unit area and the summed lengths of fractures of any set per unit area.

The fracture maps were also used to conduct cluster analysis for the fractures in question to study the connectivities of the networks. The structural controls of these fracture parameters (lengths, orientations, and densities) and fracture aggregate parameters such as cluster distribution and connectivities of the

fracture networks were then analyzed by studying the variations of these parameters with structural position.

2.6 Fracture Characterization

Fracture Orientations

Fracture orientations measured for the outcrops are displayed on rose diagrams and equal angle stereographic net projections for each of the measured locations (Figure 2.5a-f). The fracture data is also shown with bedding rotated to horizontal, to show the orientations of the fractures relative to bedding (Figure 2.5 g-l). The fold axis of Teton anticline trends N8W, and plunges 2° towards 352° in the study area. This orientation was determined from the pole of the great circle through all of the poles to bedding.

Based on the fracture plots and assuming a dispersion of 30° for each fracture set, four main sets of fractures were identified. The two most dominant fracture sets are a longitudinal set with a mean strike of 160° and dip of 76° W, and a transverse set, with a mean strike of 80° , and a dip of 80° S. Two other sets, one with a mean strike of 33° and a dip 82° SE, and another with a strike of 113° and dip of 82° SW, are oblique to the trend of the structure. A number of additional sets are also present, but these are much less abundant than these four main sets. The average strikes of the fracture sets do not change significantly when the corresponding bedding dips are rotated to horizontal (Figures 2.5 g-l).

Fracture Densities and Lengths

For each fracture set, the distributions of lengths and fracture densities were analyzed. In contrast to the use of scan lines to estimate fracture density or spacing, the fracture density of each set was defined as the summed lengths of all fractures of that set per unit area (Figure 2.6). Using this approach a fracture density grid was generated for each fracture set. Figure 2.7 a-d shows the distribution of fracture densities for the longitudinal, transverse, and oblique sets at these locations. The longitudinal fractures were found to have a significantly higher mean density (4.1m/sq.m) than the transverse fractures (2.7m/sq.m). The oblique sets show the lowest mean densities (1.7 and 0.7m/sq.m). The densities of both longitudinal and transverse sets varied for the outcrops in the area, with the longitudinal fractures exhibiting a greater variability. This variation was attributed primarily to structural position, so the control of structural position on fracture density was further analyzed.

The lengths of field scale fractures have been analyzed separately for the longitudinal, transverse and the two oblique sets (Figure 2.7e-h). The longitudinal fractures have a mean length of 0.48m, whereas the transverse fractures have a shorter mean length of 0.3m. The two oblique fracture sets have mean lengths of 0.35m and 0.37m, respectively.

2.7 Controls of Structural Position

Variation of fracture densities and lengths with respect to the hinges was studied on the west limb. Excessive vegetation and lack of continuous outcrops prevented a similar analysis on the east limb. In general the fracture densities are higher on the multiple hinges (mean value of 7.5m/sq.m) than on the limbs (mean value of 2.9 m/sq.m) as shown in Figure 2.8c and 2.8d. This variation is apparent when comparing outcrops located directly on the hinges with those in the centers of the limb (Figure 2.11). Furthermore, the longitudinal fracture sets show significant variation in density with distance from the nearest fold hinge of the multiple hinge fold (Figures 2.9). This pattern is also reflected in the lengths of the fractures which have mean lengths of 0.64m and 0.34m on the hinge and limb, respectively (Figure 2.8a-b). The transverse and oblique fractures, which are unrelated to the hinges, show little variation in fracture intensity or length with respect to distance from hinges.

2.8 Relationship of Fracture Densities to Macroscopic Structural Evolution

The relationship of the fracture densities to the fold evolution can be explained in two possible ways. The first hypothesis is that the Teton and little Teton anticline are fault-bend folds, with all hinges related to active or passive axial surfaces (Suppe, 1983; Medwedeff and Suppe, 1997) formed during the fault-bend folding process. According to this hypothesis, most parts of the hinge

zone would pass through at least one and possibly more than one active axial surface tied to fault bends and would therefore show some degree of fracturing. However, the final locations of the active and passive axial surfaces would show the highest fracture densities, because they represent the zones with the highest finite curvature.

The second hypothesis is that the Teton anticlines originated as detachment folds within the Mississippian-Devonian units cored by weak shales within the Devonian Three Forks-Jefferson Formations. During the early stages of concentric folding, the outer arc was subjected to layer-parallel extension and resulted in the formation of longitudinal fractures. With continuing folding, bending was concentrated along multiple hinges, so that the fracture densities increased along the multiple fixed hinges. The fold was then transported over fault bends to its present stage. The transport of the fold over fault bends resulted in hinge migration and the development of additional fractures. According to this hypothesis, some of the hinge zones with high fracture densities may represent early formed fixed hinges, while others may represent the passive and axial surfaces associated with fault-bend folding.

Because of the limited surface data through the Teton anticlines, it is difficult to determine which of the two hypotheses is supported by the detailed macroscopic geometry of the Teton anticline; however, both hypotheses can be used to satisfactorily explain the distribution of fracture densities of the

longitudinal fractures. The transverse fracture which show little variation in density are probably related to changes in curvature parallel to the fold axis due to variations in fold plunge.

2.9 Fracture Connectivity and Cluster Analysis

The effectiveness of fractures of different orientations and densities in improving the drainage of a reservoir depends not only on the fracture densities of various sets, but on how well the fractures interact to form a continuous network. A method of estimating this effectiveness is by measuring the clustering of fractures.

In a fracture network, a group of linked fractures is known as a *cluster*, a term borrowed from the concepts of percolation theory (Stauffer, 1985, Chelidze, 1986; Bebbington et al., 1990; Berkowitz and Balberg, 1993; Berkowitz, 1995; and Gueguen, et al., 1997). The *cluster size* of any fracture network has been defined as the proportion of the total fracture trace length in the study area belonging to the largest cluster (Odling, 1992, 1995, 1997). Thus,

$$\text{Cluster size} = \frac{\sum \text{Fracture trace length in the largest cluster}}{\sum \text{Fracture trace length in the study area}}$$

A cluster which links opposite sides of the study area is termed a *percolating cluster*. Portions of the fracture patterns that do not lie on the direct pathways through fracture system are termed as *dead-end fractures*. Fractures in

the percolating cluster, which are devoid of any dead-end fracture segments, constitute the *fracture backbone* (Stauffer, 1985, Priest, 1993).

For fractured hydrocarbon reservoirs, our interest is in the mean connectivity of an area and the most likely outcome of connectivity encountered by a drilled well. This can be characterized by defining two parameters, one of which defines the total length or area of connected fracture networks, while the second defines the distribution of cluster sizes (Figure 2.10).

The first parameter can be defined by the *fractional cluster length* or the *fractional connected area*, which represent the proportion of the total length of fractures and total surface area of rock connected by fractures to the total study area.

$$\text{Fractional Cluster Length} = \frac{\text{Total length of Connected Fractures}}{\text{Total Sample Area}}$$

$$\text{Fractional Connected Area} = \frac{\text{Total Surface Area of Rock Connected By Fractures}}{\text{Total Sample Area}}$$

The fractional connected area quantifies the absolute area that can be drained by fracture networks and is perhaps the best measure for estimating the effectiveness of the fracture networks. In Figure 2.10, two networks are shown, both of which have a fractional connected area of 0.31, so that the ratio of summed areas of connected fractures to the total sample area is 0.31. From a practical perspective, this parameter defines the probability of a drilled well encountering a connected fracture network.

The second parameter is a measure of the distribution of cluster sizes for the area in question. For a fixed fractional connected area, this parameter defines the size of the fractured network that will be encountered by a drilled well. In Figure 2.10, the sample area shown in b will have a probability of encountering a larger connected area.

A comparison of these parameters with the densities of different fracture sets enables estimation the importance of different sets in enhancing fracture-controlled drainage. The fractional connected area and the distribution of cluster sizes are dependent on the number of fracture sets, as well as the density of each fracture set. An optimum distribution of fractures of different sizes provides the largest cluster and the highest connectivity.

An assessment of the variation in connectivity with structural position was made for the Teton anticline. The analysis addressed the relative values of connectivity, since absolute values are not measurable for surface outcrops. Since most measured fractures showed no evidence of shear motion, it was assumed that they contributed directly to the connectivity. It was further assumed that all fracture sets had similar apertures so that their relative contribution to the connectivity was dependent only on their lengths and densities.

In the Teton anticline, the density of the longitudinal fractures is strongly controlled by the structural position, namely, the position relative to the hinges. The transverse and oblique fractures present an important component to the

fracture connectivity; however, their density is more uniform and not as dependent on structural position. Therefore, areas close to the hinge zones generally show a high fractional connected area compared to the limbs (Figure 2.11 and 2.12a). Locally high fractional connected areas on the limbs are usually due to a higher density of transverse fractures. Because connectivity is dependent both on the number of fracture sets and the density of each set, the variations in FCA are not as pronounced as those of the densities of longitudinal sets alone (compare figures 2.12a and 2.9a). The distribution of connected areas shows that although both hinge and limb zones show large numbers of small connected clusters, the hinge zone show a significant concentration of larger cluster areas (Figure 2.12b-c).

2.10 Discussion and Conclusions

The Teton anticline presents an excellent opportunity for studying the structural controls of fracture orientations, lengths, and densities in a surface structure. It also serves as a good analog for fracture distribution and connectivities for subsurface folded carbonate reservoirs.

The orientations of fracture patterns in the Teton anticline can be grouped into four primary sets, although additional secondary sets are also present. The primary fracture sets are longitudinal and transverse relative to the axis of the fold, with two additional oblique sets. The length and density of the longitudinal

fracture sets are strongly controlled by position relative to multiple hinges. The transverse fractures are related to changes in fold plunge and exhibit less variation in fracture density.

Fracture connectivity is best represented by two different parameters: the fractional connected area which represents the fraction of the total sample area that is connected by fractures, and the distribution of clusters of different sizes in any given area. The connectivity of fractures is dependent on the number of fracture sets, their orientations and dispersions, and the densities of the fracture sets. Because the longitudinal fractures represent the dominant fracture set, and also show the most variation with structural position, the fracture connectivity, as measured by both the fractional connected areas and the distribution of cluster sizes, is normally greater in vicinity of the fold hinges.

The results and approaches of the study have some important implications for the study of subsurface folded fractured carbonate reservoirs. Fracture analysis in subsurface reservoirs is usually based on sparsely distributed data from production wells. The data usually consists of borehole images and other fracture identification logs, calibrated with core data. The measurements of fracture orientations, lengths and densities and an analysis of their controls are important in obtaining a picture of fracture patterns around the structure. Furthermore, the interaction of different fracture sets and their controls on fracture connectivity are

important in understanding the structural controls of fracture permeabilities in different structural positions.

Curvature analysis is commonly used to obtain a relative measure of fracture density around the curvature. However, as indicated by the results of this study, many structures do not show a smooth variation of curvature around the structure. Instead, fracture densities may increase significantly in narrow hinge zones resulting in discontinuous variations in fracture density. A careful analysis of the geometry and evolution of the macroscopic structure based on surface data, 3-D seismic data, and dipmeter data is essential for conducting predictive fracture analysis. The integration of fracture data, and the controls of the macroscopic structural geometry on fracture parameters, can be used to effectively simulate fracture patterns and connectivities around the structure.

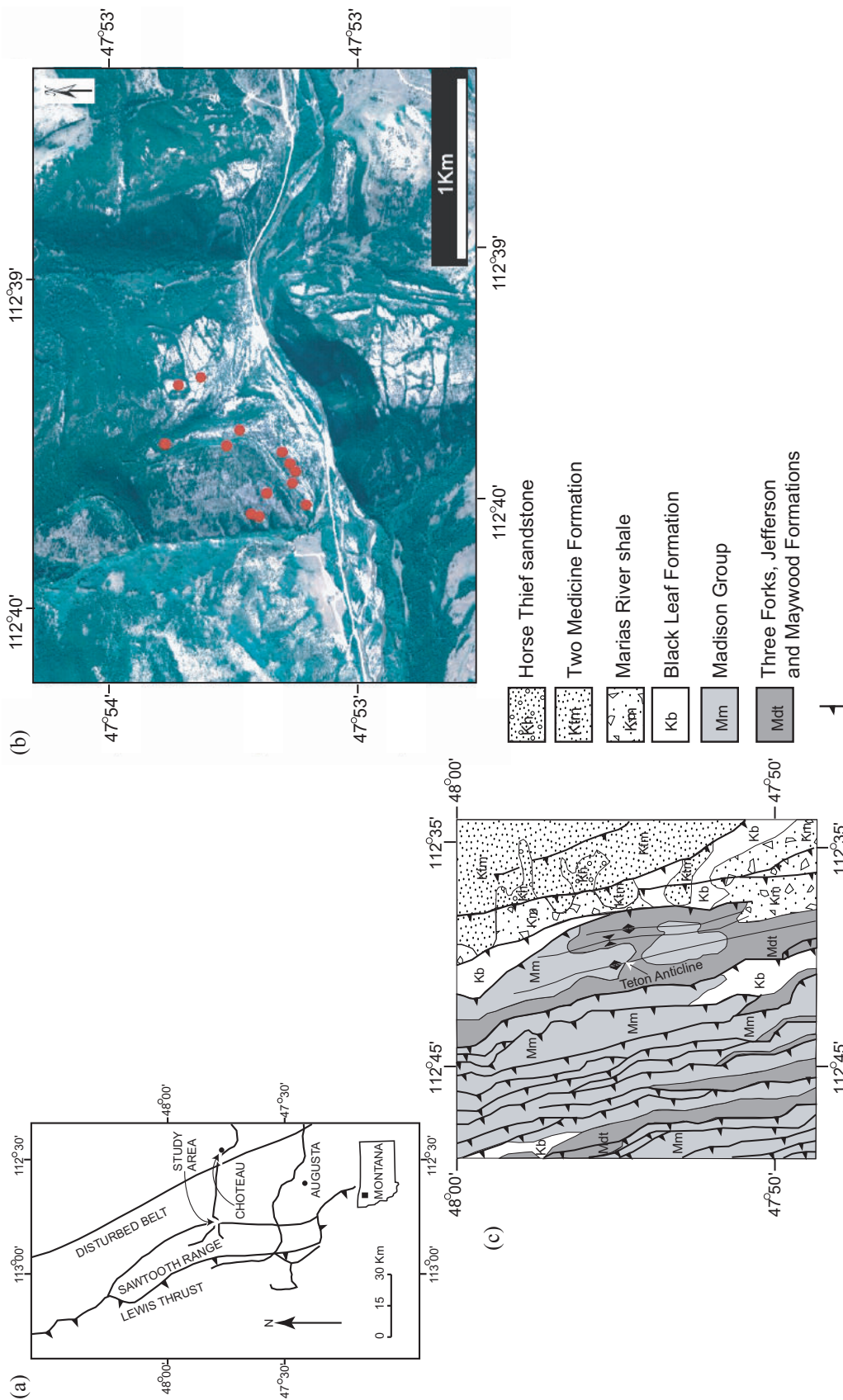


Figure 2.1. (a) Map of northwestern Montana showing the location of the study area. (b) Location of fracture measurements on 1-meter resolution digital color orthophoto. (c) Generalized geologic map of study area after Mudge (1972).

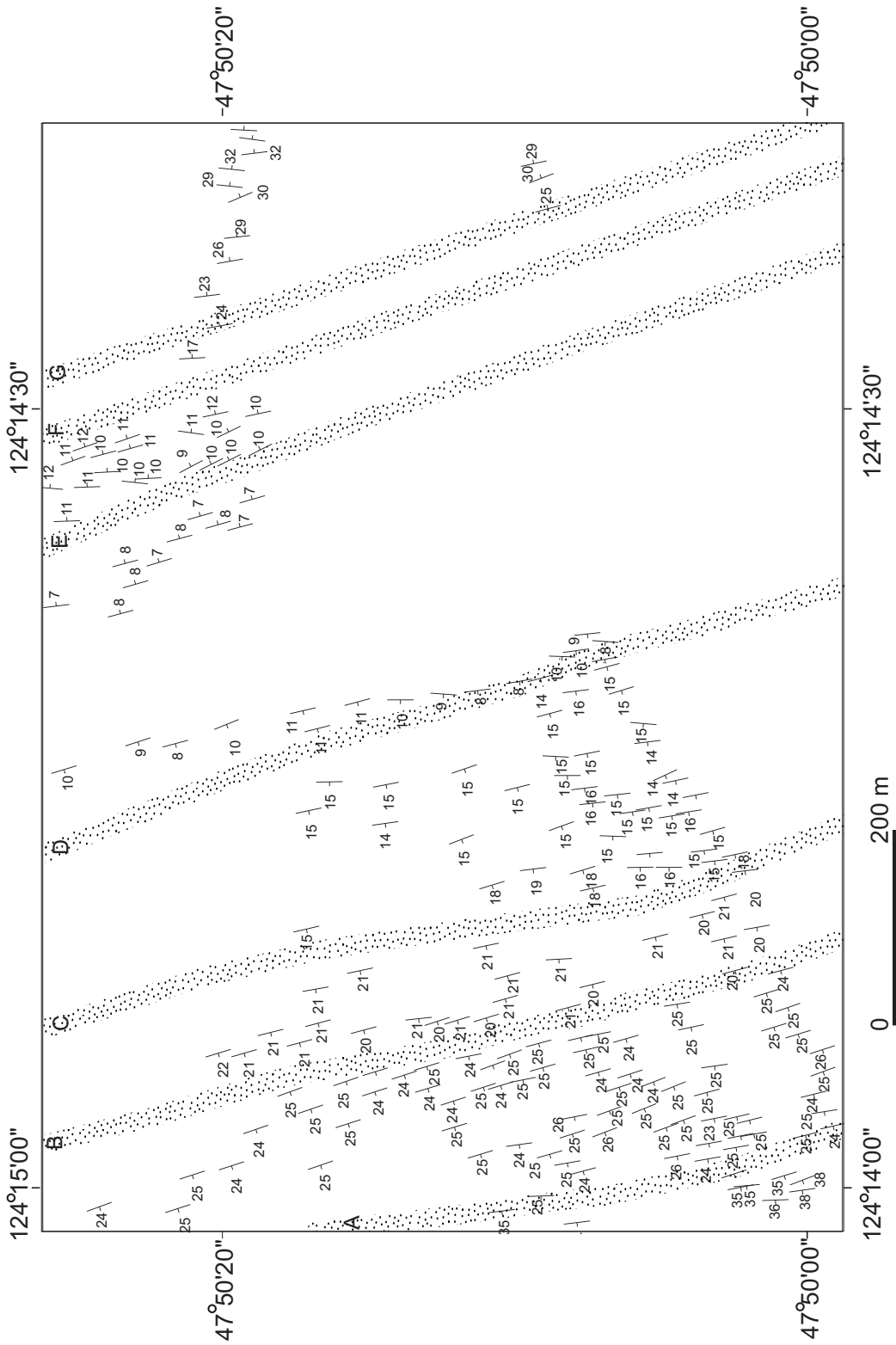


Figure 2.2. Map showing locations of data collection. Locations of hinge zones (A-G) mapped on the basis of dip data. The locations of the hinge zones are shown by stippled. The numbers in the map indicate bedding dip at each location.

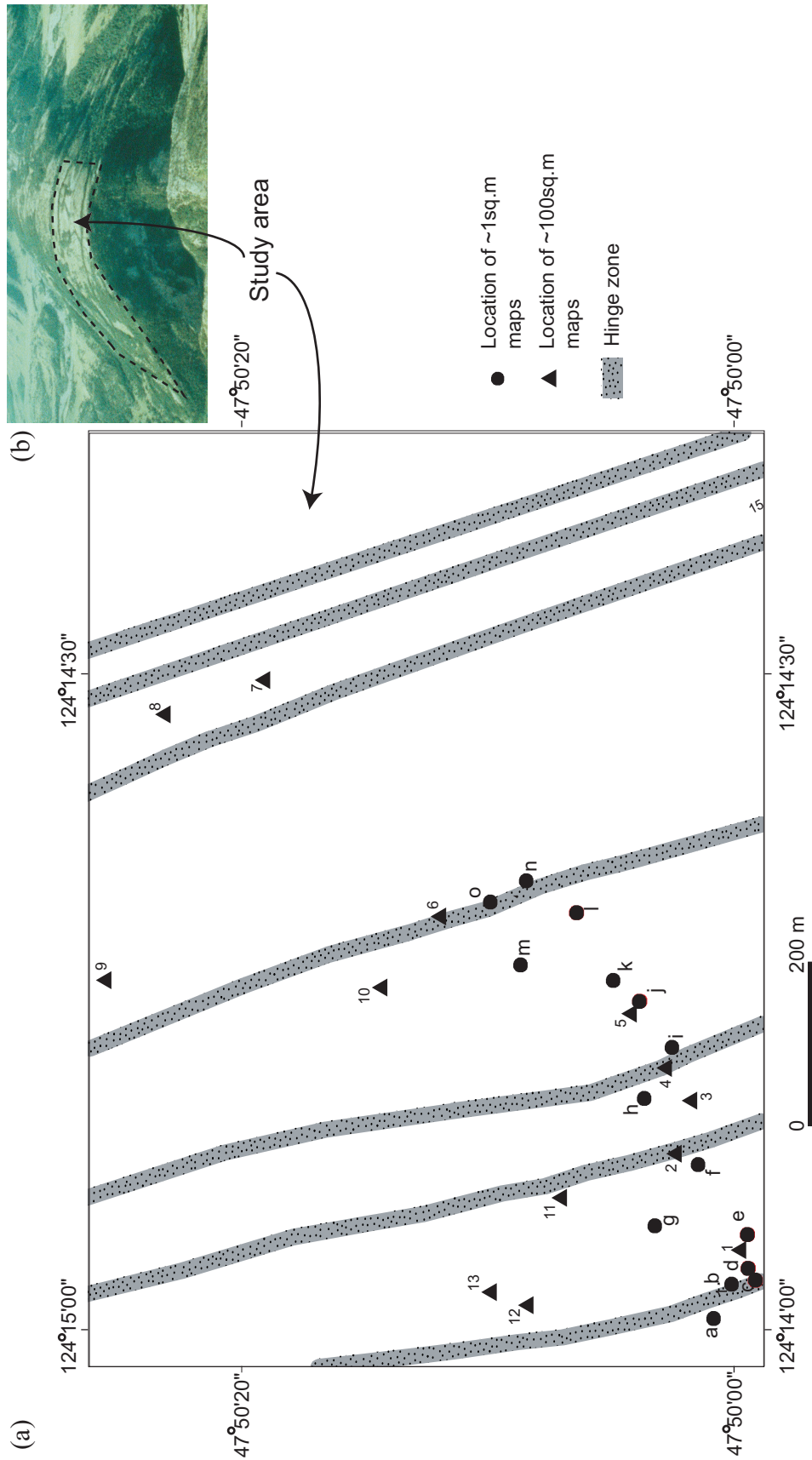


Figure 2.3. (a) Map showing locations of fracture measurements. The locations of the hinge zones are shown by stippled. Large fracture map locations (1 to 13) are marked by triangles and small fracture locations (a to o) are marked by circles. (b) Photograph of Teton anticline looking NNW, the dotted line showing the approximate location of the area studied.

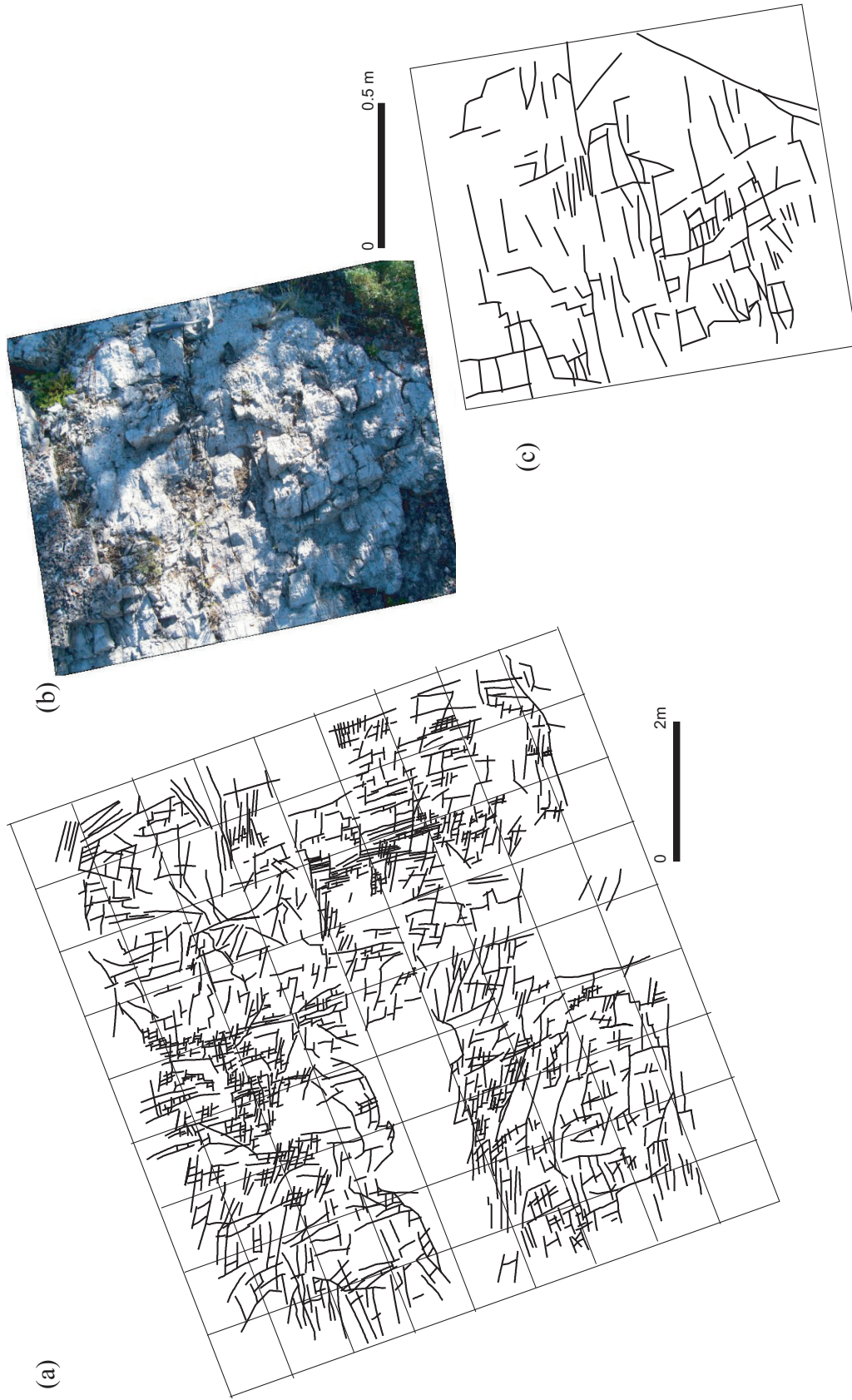


Figure 2.4: Example of fracture map of two different scales. (a) fracture maps of ~ 90 sq.m., overlain by a 1m grid. (b) photograph of location of fracture map where fractures are mapped out of georectified photographs. (c) fracture traces digitized out of (b).

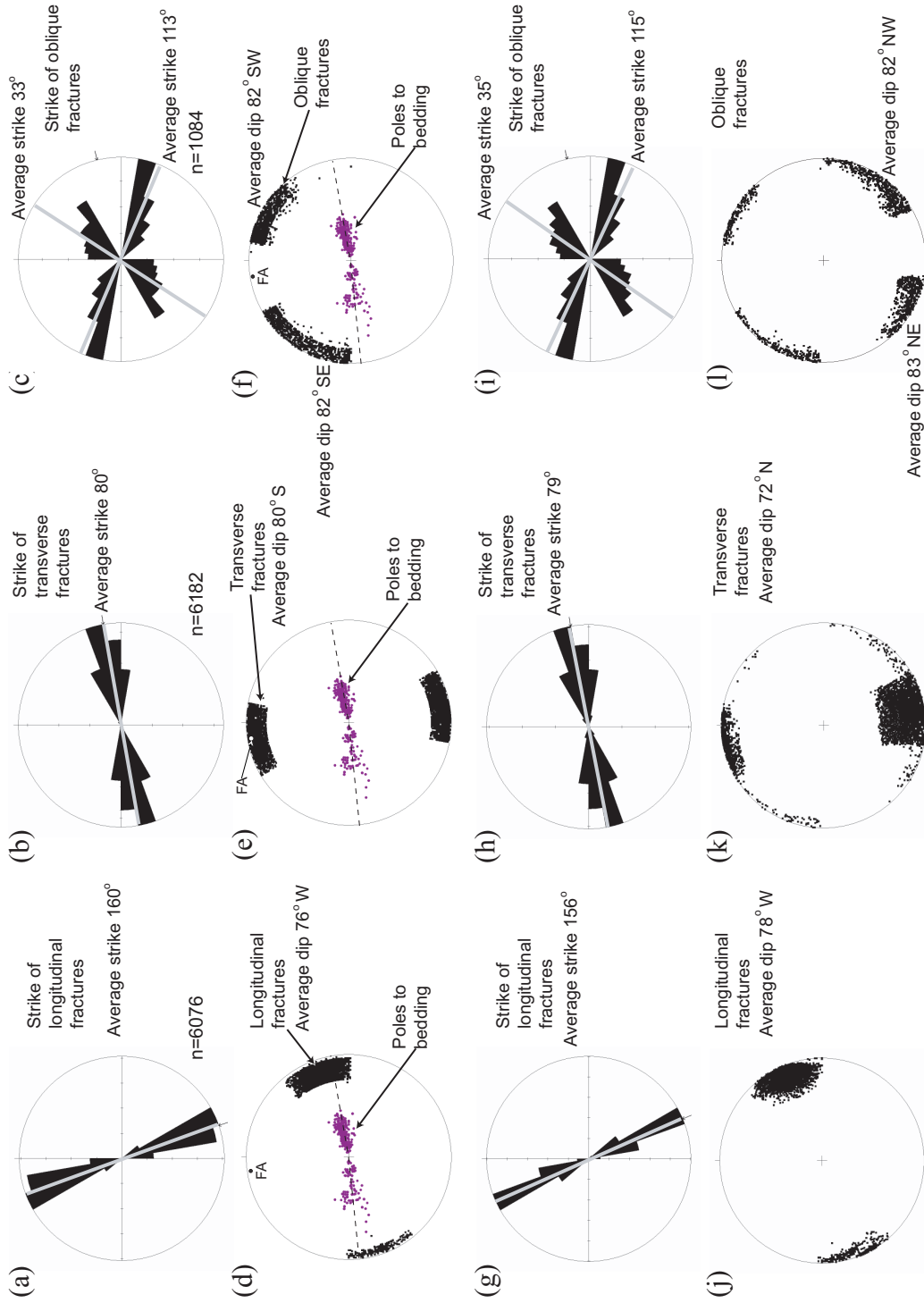


Figure 2.5 a-c. Rose diagrams showing the strikes of (a) Longitudinal (b) Transverse and (c) Oblique fractures. d-f. Equal area stereographic plots showing poles to planes of fractures and bedding. (d) Longitudinal fractures. (e) Transverse and (f) Oblique fractures. F.A.= the local orientation of fold axis, plunging 2 degree towards 352 degree. g-i. Rose diagrams and stereographic plots of the orientation of Longitudinal, Transverse and Oblique fractures, with bedding rotated.

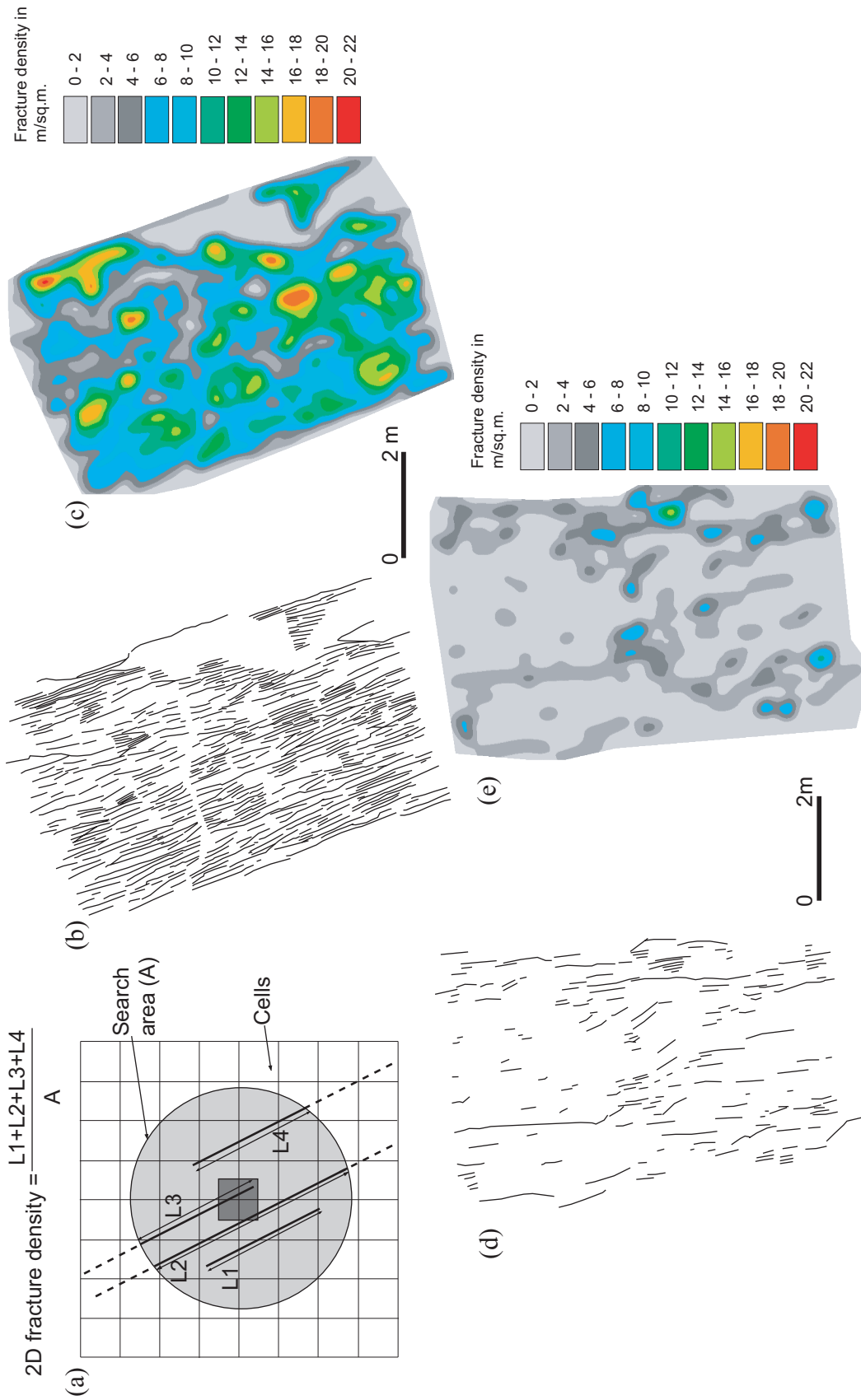


Figure 2.6: (a) Schematic diagram showing the method of calculating the fracture density for a single fracture set. (b) Mapped longitudinal fractures for location 6 (hinge location) in figure 2. (c) Fracture density map of longitudinal fractures for location 6. (d) Mapped longitudinal fractures for location 3 (limb location) in figure 2. (e) Fracture density map of longitudinal fractures for location 3.

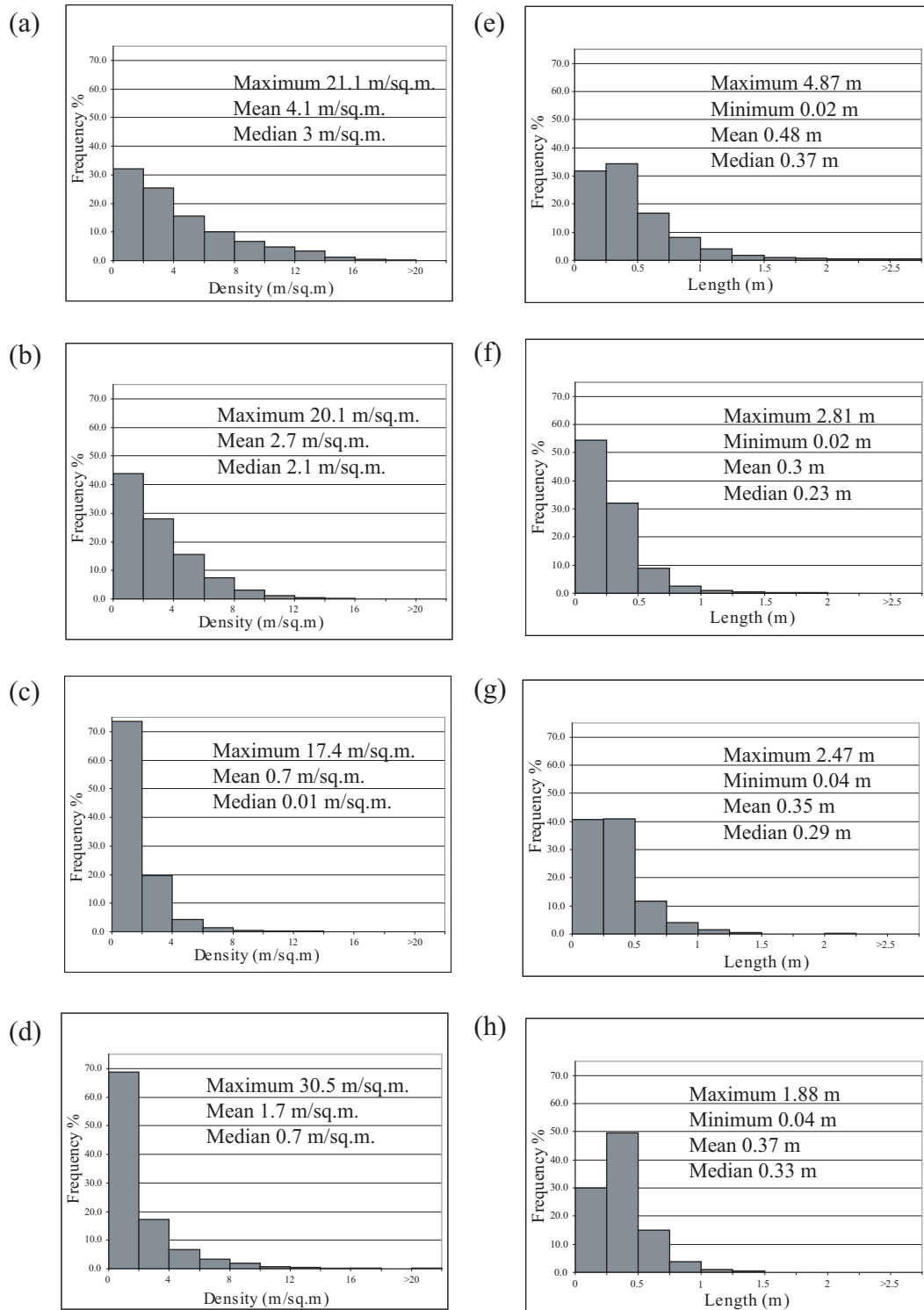


Figure 2.7. Histogram showing density distribution of (a) Longitudinal fractures (b) Transverse fractures (c) NNE oblique fractures and (d) WNW oblique fractures. Histogram showing length distribution of (e) Longitudinal fractures (f) Transverse fractures (g) NNE oblique fractures (h) WNW oblique fractures.

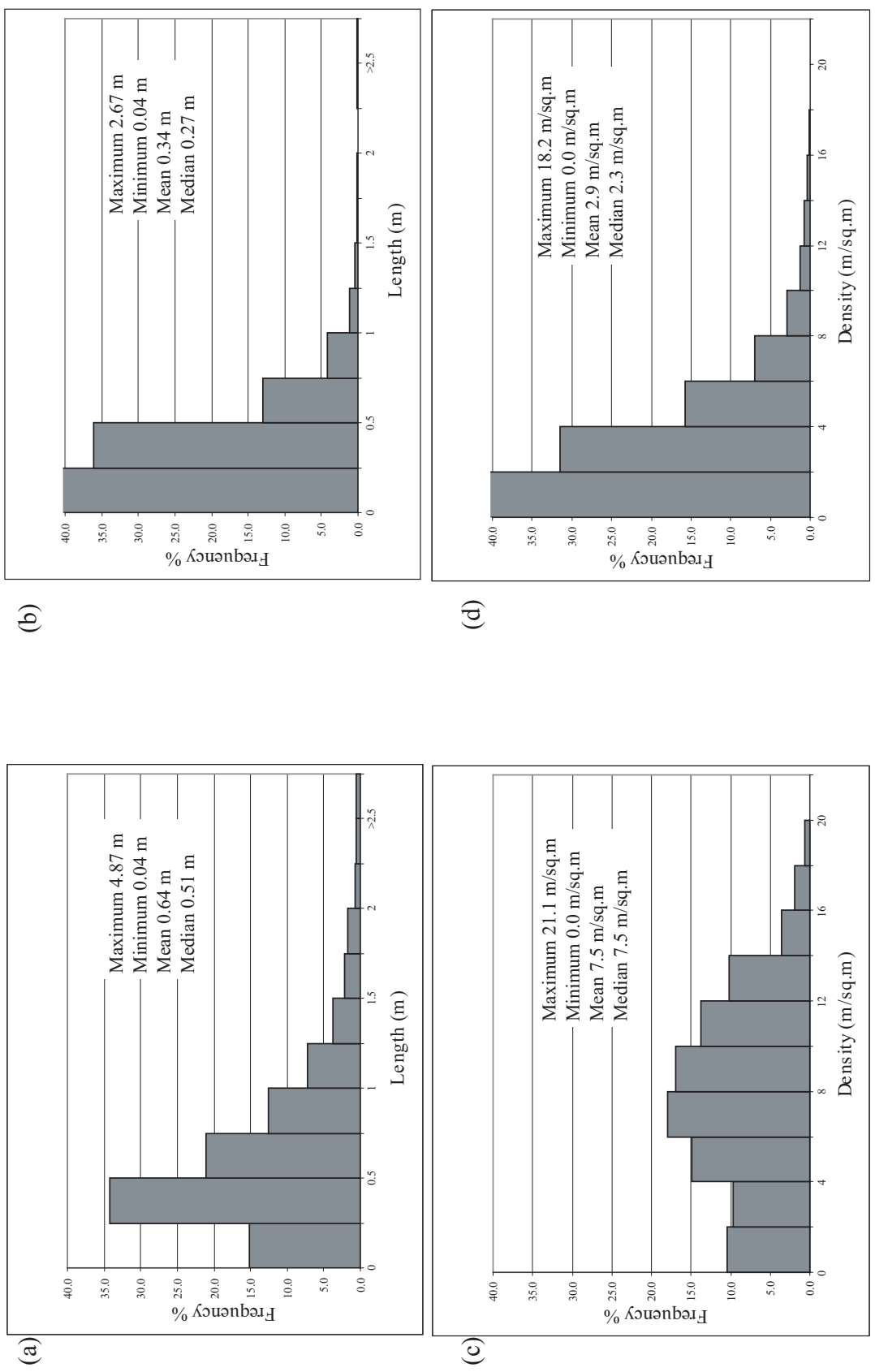


Figure 2.8: Length distribution of (a) longitudinal fractures of hinge locations; (b) longitudinal fractures of limb locations. (c) Density distribution of longitudinal fractures of hinge locations. (d) Density distribution of longitudinal fractures of limb locations.

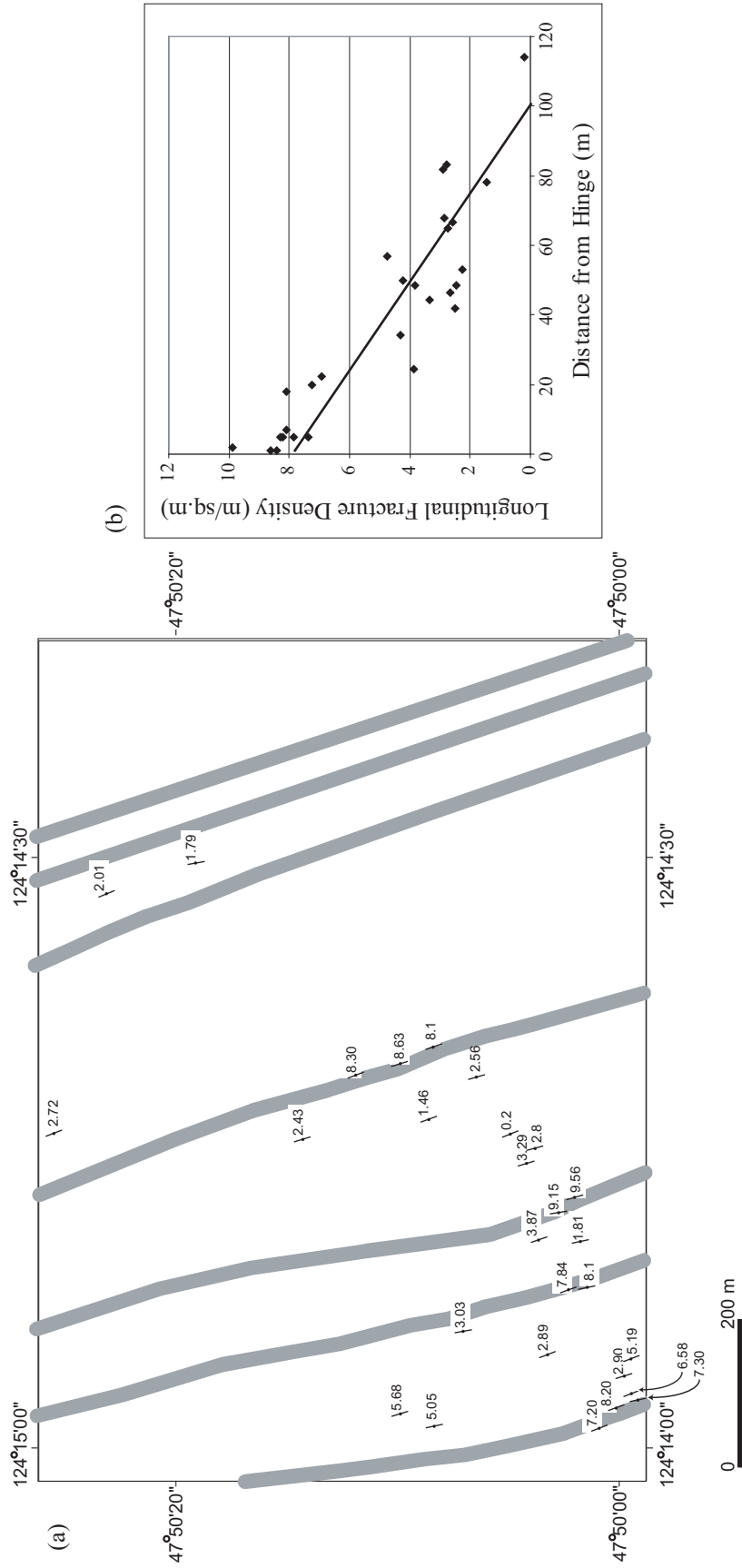


Figure 2.9. (a) Map showing the density of longitudinal fractures for all locations. The gray areas mark the locations of subtle hinge zones. The oriented line indicates the average strike of longitudinal fractures at each location and the number indicates the fracture density of Longitudinal Fractures. (b) Plot showing the variation of Longitudinal Fracture Density with Distance from the nearest hinge zone.

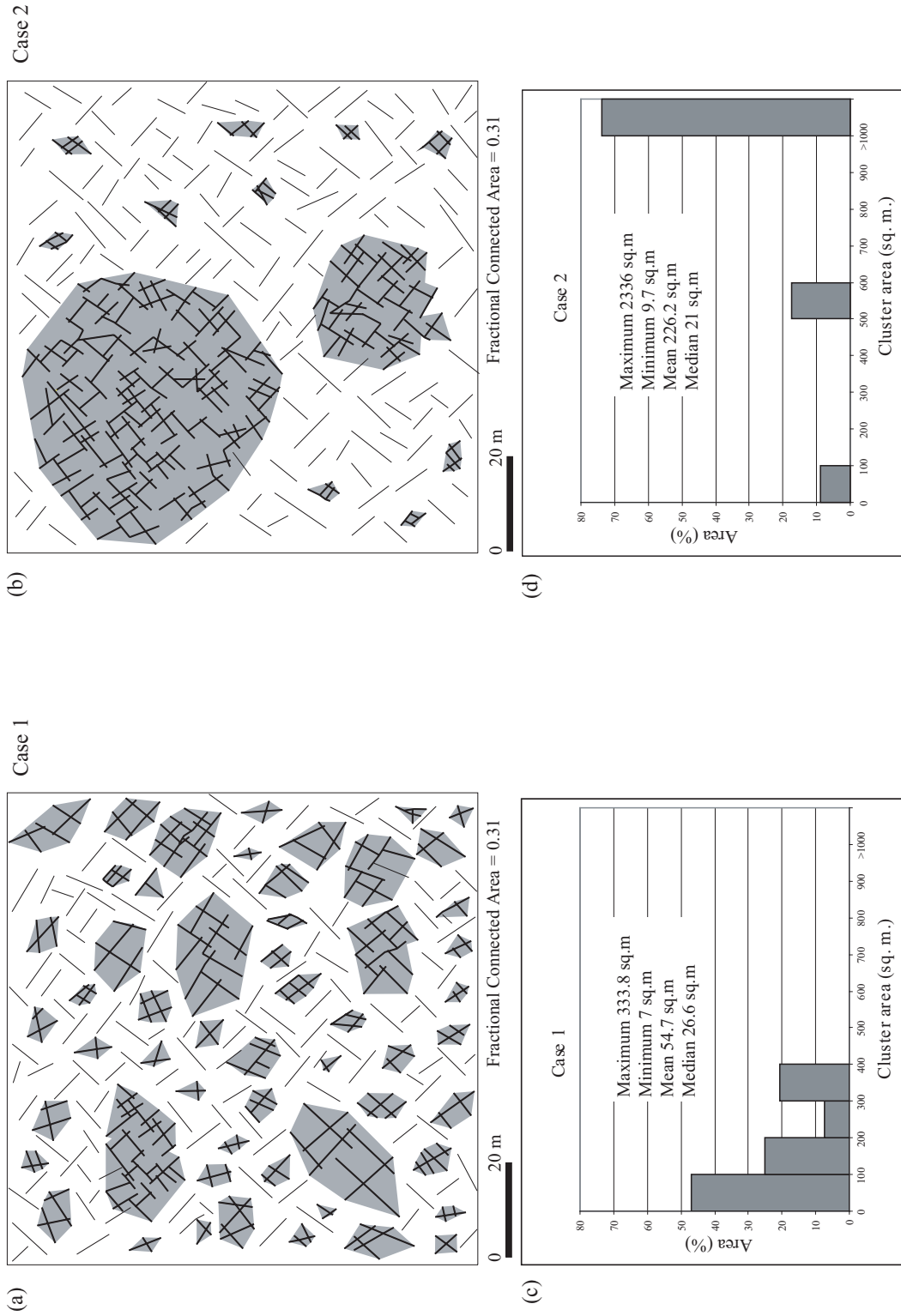


Figure 2.10: (a-b) Schematic fracture maps showing two areas with same fractional connected area. Gray polygons show the individual clusters for each case. (c) Histogram of distribution of cluster area for case 1 (d) Histogram of distribution of cluster area

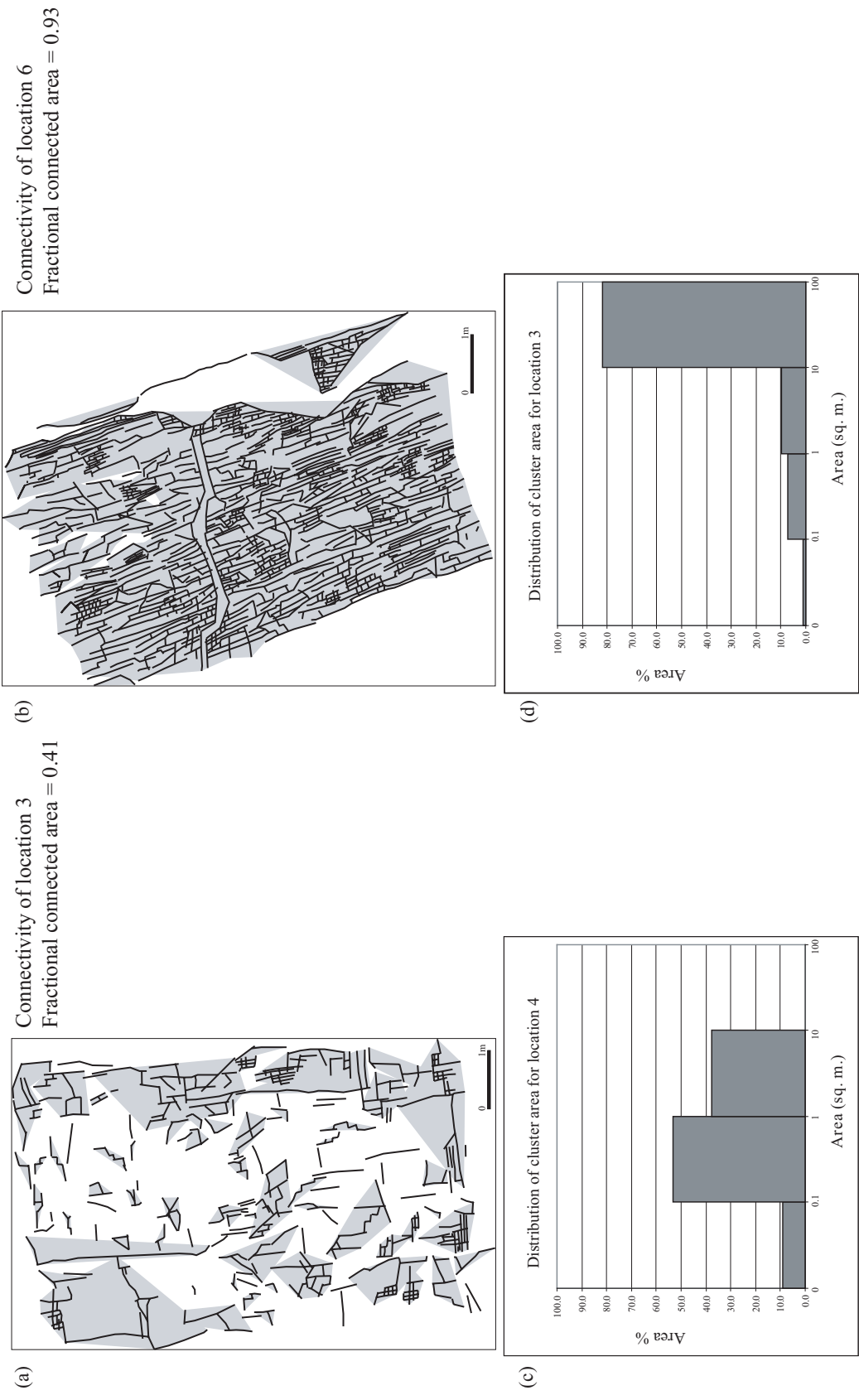


Figure 2.11 (a) Cluster areas (represented by gray polygons) for location 3 in figure 2.3 (limb location). (b) Cluster areas for location 6 in figure 2.3 (hinge location). (c) Histogram showing distribution of cluster areas for location 3. (d) Histogram showing distribution of cluster areas for location 6.

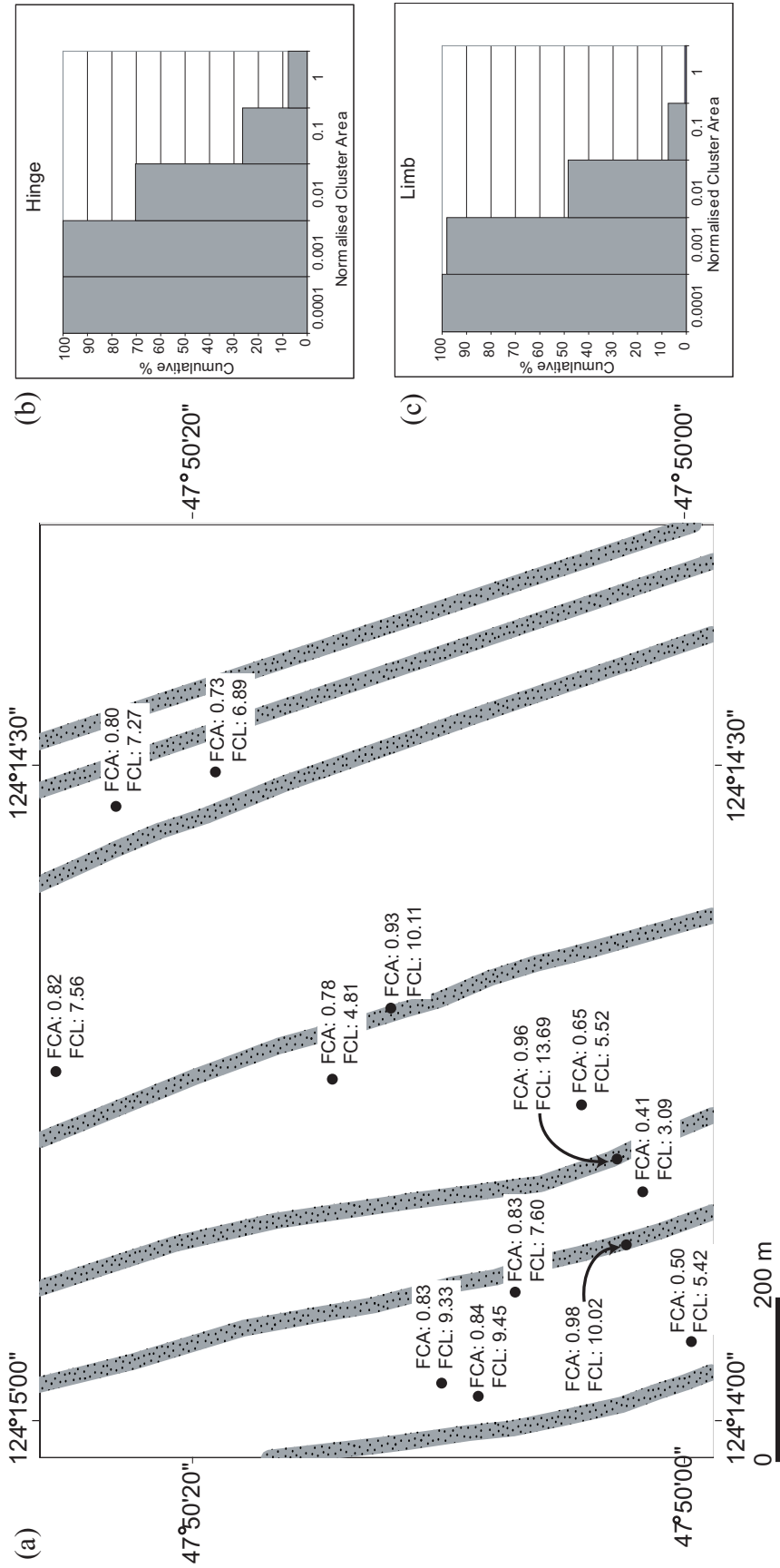


Figure 2.12. (a) Map showing Fractional Connected Areas (FCA) and Fractional Connected Lengths (FCL) for the Teton anticline. The gray areas mark the locations of hinge zones. (b) Frequency distribution of cluster area normalized by the respective study area for all hinge locations. (c) Frequency distribution of cluster area normalized by the respective study area for all limb locations.

CHAPTER 3:

FRACTURE SIMULATION

3.1 INTRODUCTION

3.2 PREVIOUS WORK IN FRACTURE SIMULATION

3.3 LOCAL FRACTURE SIMULATION METHOD

3.4 STRUCTURALLY CONTROLLED SIMULATION

3.5 REVIEW OF RESULTS OF FRACTURE SIMULATION

3.6 CONCLUSIONS

3.1 Introduction

Analysis of fractures using outcrop or subsurface data usually involves isolated and widely-spaced data points. Surface analysis is usually conducted on isolated outcrops, whereas subsurface analysis is limited to oriented core and/or borehole televiewer or log data from widely-spaced wells. Prediction of the fracture density and orientation in different parts of a subsurface structure requires the interpolation of fracture densities between these sparse data points.

Simulation of fracture is one method of interpolating between data points. The accuracy of fracture prediction is dependent on a simulation algorithm that incorporates all controls of fracture density and orientation for an area. Most existing methods of simulation, discussed in more detail in the next section, involve methods that simulate fracture parameters homogeneously over a local region. Therefore, these methods do not incorporate structural controls of fracture density. In this section, a method of regional simulation that extends these methods to regional simulation incorporating structural parameters is discussed. The methods are then used to simulate fracturing and connectivity for the Teton anticline which exposes Devonian and Mississippian carbonates in the frontal part of the Sawtooth Range in Montana. Fracture parameters vary with structural position on the structure, so that it provides a good analogue for many surface fractured reservoirs in the frontal parts of fold belts.

3.2 Previous work in fracture simulation

There are three main conceptual models to simulate fracture network geometry: (1) Stochastic Continuum Model (SC) (2) Channel Network Model (CN) and (3) Discrete Fracture Network Model (DFN),

In stochastic continuum model, heterogeneous media is treated as a random variable described through its statistical parameters and analyzed by statistical modeling techniques (e.g. Monte Carlo simulation). It has been used to model fractured media (Neuman, 1987) though more commonly used to model granular porous media (Smith and Freeze, 1979, Gutjahr, 1978). Channel network model depend on the length, width, apertures and hydraulic conductivities to simulate the hydraulic and transport properties of the channels or fractures. Discrete Fracture Network model is based on fracture characteristics and specific relation between the parameters like length, orientation, density, aperture termination relation and fracture shape.

The Stochastic Continuum and Channel Network models are mostly used for modeling groundwater flow and transport while the Discrete Fracture Network model is commonly used to simulate realistic geological realizations (Dershowitz et al., 1996). Dershowitz et al. reviewed the main conceptual DFN models (table A1) in terms of their applicability, advantages and disadvantages. The development of each model is based on specific relationships between characteristics such as location of fracture sets, termination and fracture shape. A

detail of various models used in fracture simulation is provided in the appendix table A1.

3.3 Local fracture simulation method

The basic geometric characteristics that are considered during the simulation of fracture networks are fracture location, size (defined by trace length in two dimensional studies) and orientation. Each set of fractures is simulated separately. The input data for fracture simulation is obtained from data collected in the field. Fracture data is sorted in different fracture sets based on orientation. Basic characteristics like fracture length and density are evaluated for each set separately.

Local simulation is done by choosing a region for simulation, such that the fracture characteristics of the chosen region can be represented by a sample map prepared in the field. In other words, the region must be structurally and lithologically congruent with the sample map. The sample map should also be devoid of 'no data' regions. Local fracture simulation achieved in this study is guided by the Baecher model (Baecher et al., 1977). The primary characteristics of the Baecher model are that the fracture centers are located uniformly in space using a Poisson process and the fractures are generated as discs with a given radius and orientation. In this study, the fractures simulated on the bedding plane as two-dimensional trace lengths, hence the shape and size of the fractures are

characterized by line length, instead of discs. In the present study the distribution of fracture location is guided by fracture density, which is a modification from Baecher model where the fracture centers are uniformly distributed.

The primary goal of the simulation is to obtain a fracture network for an unmapped area, using the data from a mapped area. The basic assumption in this simulation is that the spatial variations of fracture characteristics in the unmapped area are similar to that of the mapped area. Thus the first step of selecting an area of simulation is achieved based on the knowledge of local geology and its influence on fracturing. In the case of the Teton anticline, where the fracture characteristics are influenced by vicinity to hinge zone, the area of simulation is chosen such that the area is located at least 40m away from any hinges and also the area is within the same lithologic facies as the sample map. Following the selection procedure, a sequence of steps is carried out to transfer the fracture characteristics from the mapped area to the unmapped area, which is discussed in detail in the following sections.

Fracture size (or trace length) simulation

Fracture trace length of the sample area is determined from field mapping and fracture digitizing. Fracture length in the sample area is fitted to exponential distribution. The statistics of the length distribution are noted (e.g. maximum, minimum, mean, median and standard deviation). These distribution parameters

and the theoretical curves fitted to the distribution are used to guide the fracture length over the area of simulation. The detail of the process based on a hypothetical data set is described below:

Let's say sample area S1 is of dimension 10m * 10m, and has 100 fractures, with a maximum fracture length of 2m and a minimum of 0.25m (Figure 3.1 a, b). This data is used to generate a fracture simulation over area A1 of dimension 100m * 100m

Step 1: The length distribution of the fractures within the sample area is analyzed in detail. The equation of the curve fitted to the length distribution is extracted. All the statistical parameters are noted (figure 3.1 c, d).

Step 2: Corresponding to 100 fractures in the sample area, 10000 points are generated for the simulation area (100 fractures in 10*10m are proportional to 100*100= 10000 points in 100*100m area). Each point is assigned length values following the distribution equation extracted from the sample map. The equation is iterated within the range of values observed in the sample map. Thus the maximum, minimum, mean, median and standard deviation of the length values assigned to these points are the same as that of the sample map.

Step 3: From the sample map the length of each fracture is transferred to the fracture center points and then the fracture centers are interpolated over the sample area s1 to generate the fracture length grid. The interpolation is performed using the inverse distance weighted function given by the equation:

$$Z_k = \sum_{i=1}^n w_i Z_i \text{ (Shepard, 1968)}$$

Where Z_k is estimated based on the value of neighboring points Z_i at all points n , and Z_i is weighted based on its distance from the unknown point Z_k .

Thus w_i is given by:

$w_i = 1/d_{ik}$, where d_{ik} is the distance between the known point i and the unknown point k .

The cell size for the interpolated grid is 1cm (figure 3.2a)

Similarly, for the simulation area, the length values from the generated points are interpolated to generate a length map for area A1. The interpolation parameters used for the simulation area is same as that of the sample map. The cell size for the interpolated grid over area A1 is 10cm (figure 3.2b).

Step 4: The semi-variogram of length grid for the sample map is fitted to a theoretical semi-variogram curve. The theoretical semi-variogram is a function describing the degree of spatial dependence of a random field. It is defined as the expected squared increment of the values between two locations. It is given by the equation:

$\Gamma(h) = (1/2n(h)) \sum_{i=1}^{n(h)} (X(Z_i + h))^2$, (Matheron, 1963) where n is the number of pairs separated by distance h (also known as the lag). Thus comparing the semi-variogram of the sample and simulation grid will provide a good estimate of spatial variation of the variable that is simulated. The semi-variogram of the

simulation map is derived and compared to the semi-variogram of the sample map, to estimate the closeness of match (figure 3.2c).

Fracture location simulation

Fracture sites or center points are generated as a function of fracture density. Fracture density is calculated by two proposed methods, which are: (a) summation of length over area (D_l) and (b) number of fractures over area (D_n) (Mauldon et al. 2001). A fracture density (D_l) grid for the sample area is generated by evaluating the density value of each cell within the grid, by summing all fracture lengths within a prescribed search radius centered at the cell, divided by the search area (Gross et al., 2000). The density (D_n) grid is also generated by calculating the number of fracture centers within a prescribed search radius centered at the cell, divided by the search area. While D_n provides a good estimate of number of fracture in the system, D_l provides a more comprehensive estimate of density as it is sensitive to both the number and length of fractures. Hence D_n is used to simulate fracture location and D_l is used to verify the goodness of match. The density information of the sample map is used to generate the density grid for the simulation area and finally the length and density information of each cell is used to create the fracture site.

The detailed process of determining the fracture location is as follows:

Step 1: The fracture density (D) grid for sample area S1 is generated using the following equation:

$$D_1 = (\sum_{i=1}^n L_n)/A$$

where, L_n is the length of fracture within a search radius and A is the circular area (figure 3.3a).

Fracture density is also calculated as the number of fractures per unit area. In this method, fracture centers are used to count the fractures. Fracture density is given by number of fractures within the prescribed search radius divided by the circular area.

$$D_n = n/A$$

where n is the number of fracture within a search radius and A is the circular area.

The cell size for the above grids is 1cm (figure 3.4a).

Step 2: The density grids of the sample area are characterized by using semi-variogram. The range and sill of the semi-variogram is noted and an experimental semi-variogram is fitted to the data. The range and sill derived from the data are used to create the density distribution for the simulation area. The semi-variogram curve becomes asymptotic at a certain level, the distance where the curve first flattens is the range and the value at which the curve attains the range is called the sill. This generates the fracture density grid for the simulation area (figure 3.4 b, c, d).

Step 4: Dividing the density grid (D_n) by the circular area (calculated from the search radius used for the density grid), the grid is converted to fracture number grid.

Step 5: The resulting fracture number grid is converted to an integer grid, such that each square unit has a whole number value (n) assigned to it.

Step 6: The resulting grid is resampled to a coarser grid such that cell size of the grid is equivalent to the search radius used to derive the density grid.

Step 7: For each unit area n numbers of points are generated as fracture sites. The points are generated using Poisson point process that is given by the equation:

$$P(a) = e^{-m}[(m^a)/\text{Factorial}(a)]$$

where m = average number of random occurrences per interval, P is the probability of occurrence of “ a ” in the interval.

Thus the fracture sites are generated randomly within the unit square area, while the number of fracture sites for each square unit is controlled by the fracture density. These fracture sites are the fracture centers of the simulated fractures (figure 3.5).

Fracture orientation simulation

The fracture orientation data for the simulated fractures is calculated based on von Mises distribution (Davis, 1986). This is a circular equivalent of a normal

distribution and is characterized by two parameters: mean direction and standard deviation. The mean direction and dispersion or spread of the strike direction is obtained by evaluating the resultant vector of field data given by the following equation:

$$R = [(\sum_{i=1} \cos\theta_i)^2 + (\sum \sin\theta_i)^2]^{(1/2)} \quad (\text{Engelder and Delteil, 2004})$$

where, the strike of fracture is assumed to be unit vector at an angle θ .

$$x_i = \cos\theta_i \quad y_i = \sin\theta_i.$$

The resultant length R is standardized by dividing R by the number of observations n. The standardized resultant length R' varies between 0 and 1, where larger the value of R' more tightly bunched are the observations.

Generating simulated fractures

After evaluating the mean and dispersion of direction, the orientation for simulated fractures are assigned to each fracture site. The orientation can be assigned to the sites randomly within the dispersion range. Considering the orientation of one set of fractures will be within a tight range of dispersion, a random distribution within the range is reasonable. In case of wide dispersion, orientation must be assigned according to the rose-diagram statistics of the sampled fracture set. Each fracture site is also assigned a fracture length from the underlying length grid. The area of simulation is populated with fracture sites

(points), where the each site has a value for fracture orientation and length attached to it. Using the length and orientation data a fracture is generated at each site, the site location point being the center of the fracture (figure 3.6). After generating the simulated fractures, the density (D_1) grid is generated for the simulated fractures (figure 3.3b). The variogram of density (D_1) grid generated from the sample map that is generated from the simulated fractures is compared to check the closeness of match (figure 3.3c).

3.4 Structurally controlled simulation

In naturally fractured reservoirs, fracture size, orientation or density are commonly not homogeneous isotropic properties and vary with lithology and structural position. Integration of the structural controls on fracture intensities notably modifies the simulated fracture network while enhancing its connectivity.

Field studies for the Teton anticline suggest that the key structural control that is postulated to be important for longitudinal fractures is distance from the hinge. Transverse fractures are generally more homogeneously distributed, but they do appear to increase slightly in the vicinity of regional fracture sets (figure 3.7). Therefore, in order to correctly predict fracture patterns and density around a macroscopic structure, it is necessary to incorporate these structural controls into the simulation process.

The structural controls of fracture parameters were incorporated into the simulation by using fracture density data from sample map as the primary data and using the relation of fracture density to proximity to a feature as a secondary variable. This is done by using the function of collocated cokriging to simulate fracture density for the entire structure.

Collocated cokriging is a method of coupling the primary data with a secondary variable and relies on the strength of the relationship between the primary and secondary data. The method is applicable in situations where the secondary variable is more continuously sampled than the primary variable, so that in places of lack of primary data, the relation between the primary and secondary variable, expressed in the form of correlation coefficient, can be used to supplement for the primary data. This method is widely used in a variety of applications. Examples include velocity modeling from well data, time to depth conversion, heterogeneity modeling, seismic data integration in stochastic earth model and permeability modeling from densely sampled porosity data (Lee and Xu, 2000, Dubrule, O., 1998, Lamy et. al., 1999, Dubrule, O. and Haldorsen, H.H., 1986).

The method starts by identifying the secondary variable that is more densely sampled and can be used to supplement the primary data. In the case of the Teton anticline, it is inferred from the field observations that the longitudinal fracture density decreases with distance from hinge. The correlation coefficient is

calculated between the fracture density and proximity to fold hinge. The cell value of ‘proximity to hinge’ is available as a continuous value for the entire ‘area to be simulated’, hence making it a perfect secondary variable that can be used for collocated cokriging. A semi-variogram model of the primary variable, i.e. fracture density in this case, is derived. Finally the semi-variogram model of the primary variable, the grid of the secondary variable and the correlation coefficient is used to generate a fracture density simulation for the entire structure.

The secondary variable semi-variance model is assumed to be proportional to the primary attribute semi-variance model, thus the correlation coefficient is used as the constant of proportionality. The density value of the target cell is estimated using the following equation:

$$Z_x = \lambda_{z1}Z_1 + \lambda_{z2}Z_2 + \lambda_{z3}Z_3 + \beta_{T0}T_0 \quad (\text{Xu et al., 1992})$$

Where Z_x is the density to be estimated for the target cell, Z_1, Z_2, Z_3 , are the density values at the neighboring cells, $\lambda_{z1}, \lambda_{z2}, \lambda_{z3}$, are the weight of the density value for the respective location, determined based on the semi-variance model of build for the density distribution, T_0 is the value of secondary variable at the target cell and β_{T0} is the weight of the secondary variable based on the correlation coefficient.

Some key features of collocated cokriging is that (i) the secondary attribute should be continuously sampled or the sampling must be dense and uniform enough to yield a meaningful continuous grid with simple interpolation;

(ii) the accuracy of the estimate is strongly dependent on the correlation coefficient as it controls the scaling between primary and secondary data, hence careful estimation of the correlation coefficient is critical to get an accurate estimation; (iii) the secondary attribute will have less influence in the estimation if the correlation coefficient is less than 0.5. Thus to effectively use the influence of structural position on fracture density or any similar relationship, it is important to identify a factor that has a strong influence on the fracture parameter; (iv) it is important to understand the physical meaning of the correlation; and (v) this method of simulation honors the primary data, which is the fracture density values from the sample map and at the same time integrates the spatial correlation of the variations of the secondary data, but the integration depends only on correct linear correlation model.

In case of Teton anticline, the density of longitudinal fractures to proximity to hinge yielded a correlation coefficient of 0.88, which ensures a reasonably good correlation of density to hinge for the entire structure. Using the correlation coefficient, 'proximity of hinge' grid and semi-variogram model for fracture density derived from the sample maps (figure 3.8), the fracture density grid of the simulation area is generated (figure 3.9). After estimating the fracture density for the entire structure, fracture center points are generated using Poisson's point process described in the previous section.

The length distribution for the same set of fracture yielded a correlation coefficient of 0.5 when plotted against proximity to hinge. Thus, unlike the fracture density map, the length of longitudinal fractures did not exhibit any systematic spatial variation with respect to the hinge. The average length of longitudinal fractures plotted against distance from hinge shows a clustered pattern. The plot exhibits two clusters, which can be interpreted as the points within a distance of 0 to 25m from the hinge exhibits a high average length ranging from 0.6 to 0.8m while the fractures away from the hinge exhibit a low average length ranging from 0.3 to 0.5m (Figure 3.10a). The cumulative length distribution of longitudinal fractures from all the hinge locations and that from all the limb locations are plotted separately. The length grid of an area within 25m from hinge is prepared using the length distribution of hinge locations and then the procedure is repeated for the area away from hinge (>25m from hinge) (Figure 3.11a, b). Finally the grids are merged to generate a unified length grid for the entire area (figure 3.11c). After generating fracture sites or center points (using the simulated fracture density grid) and the length grid, the length for each fracture center is extracted from the underlying fracture length grid. The orientations of fractures are assigned according to the mean orientation and standard deviation of longitudinal fracture set observed in the sample maps. At this point each row of attribute table of fracture center has information about the

length and orientation of respective fractures. Finally this information is used to generate simulated fracture for each fracture center.

Transverse fractures do not show any systematic relation with respect to the hinges, but do exhibit a weak relation with respect to the regional fractures (figure 3.7). The density of transverse fracture is high in the vicinity of regional fractures and decreases away from it. The cross plot of distance from regional fractures to distance away from regional fractures yields a correlation coefficient of 0.7. Thus the transverse fractures were simulated using the density grid of transverse fracture as the primary variable, the distance from regional fracture as secondary variable and correlation coefficient of 0.7.

The spatial distribution of oblique fractures did not exhibit any relation with the major structure, thus the simulation of oblique sets were done using the average density, length and orientation values for different sets.

3.5 Review of results of fracture simulation

Fracture simulation for the Teton anticline is performed using the field data and structural relations derived from field measurements. Several sets of fractures are observed in Teton anticline, the two most dominant set of fractures being (1) the longitudinal set, parallel to the fold axis and (2) the transverse set, perpendicular to fold axis. The density of the longitudinal set shows positive correlation with the fold hinges, i.e. the density increases with proximity to fold

hinge. The longitudinal fracture set exhibits an increased density within the hinge zone while the density decreases rapidly approximately 40m away from the fold hinge (figure 3.7a). The transverse set on the other hand, shows no systematic change in density with respect to the fold hinges, rather positive relation is exhibited between density of the transverse set and proximity to regional fractures (figure 3.7b), though this relation is much more feeble than the relation between longitudinal fracture set and distance from the fold hinges. For all other sets of fractures no correlation between density and any structural feature was identified. The oblique fracture sets comprises of less than 8% of the total fracture length and/or number, hence have minimal influence on the overall fracture pattern. All the fracture data used for simulation was collected from the same lithologic unit to take out the influence of lithology on fracture parameters.

A series of 13 large and 18 small maps were used for fracture simulation. The density map of the sample and simulated longitudinal fractures for the same area are compared visually to see the similarity of the maps (figure 3.12 and Appendix figure A1 – A7). Longitudinal fractures of all the locations exhibits a good match with the sample maps. Average density and length for longitudinal set of fractures from each location are recorded from the sample and simulated fracture maps and cross plotted (figure 3.13) to compare the results. Both the plots yielded a high correlation coefficient. The point to note is that the trend line in the plot has a slope of 46° for both length and density cross plot, which indicates that

the simulated and sample fracture distribution matched very well. The length distribution of sample fractures versus the simulated fractures is plotted as cumulative distribution in figure 3.13. In both the plots 90% of all the fractures are less than 50cm in length and a few fractures are 2m or greater in length.

Transverse fractures from the simulated and sampled map are compared in the same way. Visual comparison of the sample and simulated fracture density (figure 3.14 and Appendix figure A8 – A14) reveals similar pattern of fracture distribution. The cross plot of density values of sample versus simulated fractures exhibits a high correlation coefficient (figure 3.15), though the slope of the trend line fitted through the data show approximately 3° departure from 45°, indicating that the match between sample and simulated fractures are less perfect than that for the longitudinal fractures. This is because the coefficient used for density simulation of transverse fractures was 0.7, which implies that the structural relation used for simulation of this set was weaker compared to that of the longitudinal set. Cumulative plot of length distribution reveals a close match of the sample and simulated fractures (figure 3.15).

In case of oblique fractures the result of comparison between the sample and simulation shows match when all the locations are taken together, but some of the individual locations exhibit a poor match, although the overall statistics are comparable. This is because the simulation is based on field data only which is sparsely located. The density distribution of oblique fractures in sample and

simulated maps is demonstrated in figures 3.16 and Appendix figures A15 – A21 and the length distribution of the same is shown in figure 3.17.

The average length, density and orientation of longitudinal, transverse and oblique sets of fractures are summarized in table 2, 3 and 4 respectively. The average density calculated as the total length of fractures within the study area divided by area. The comparison clearly shows that the simulated longitudinal fractures exhibit the closest match with the sample map while the oblique fractures exhibit the least match. This difference signifies the importance of incorporating structural factor in fracture simulation.

Table 3.1: Comparison chart of longitudinal fracture parameters

Location	Average length		Density		Orientation	
	Sample	Simulation	Sample	Simulation	Sample	Simulation
M01	0.27	0.3	2.90	3.2	163	166
M02	0.7	0.68	7.84	7.93	160	163
M03	0.65	0.62	8.30	8.55	159	159
M04	0.31	0.30	2.01	2.2	158	160
M05	0.45	0.6	5.68	5.33	163	164
M06	0.43	0.44	3.29	3.42	163	162
M07	0.43	0.41	1.79	1.65	170	167

M08	0.38	0.38	2.72	2.74	164	164
M09	0.42	0.45	5.05	5.55	168	172
M10	0.4	0.4	3.03	3.49	170	170
M11	0.64	0.62	2.43	2.38	163	166
M12	0.39	0.41	1.81	1.76	168	166
M13	1.07	1.2	9.15	10.7	171	175

Table 3.2: Comparison chart of transverse fracture parameters

Location	Average length		Density		Orientation	
	Sample	Simulation	Sample	Simulation	Sample	Simulation
M01	0.29	0.33	3.02	3.46	87	80
M02	0.21	0.24	1.63	1.87	75	70
M03	0.12	0.15	1.59	1.87	82	76
M04	0.35	0.39	5.14	5.5	76	80
M05	0.33	0.42	2.99	3.91	74	73
M06	0.21	0.28	1.55	2.06	80	71
M07	0.4	0.41	4.17	4.26	89	85
M08	0.35	0.36	3.12	3.21	75	80
M09	0.44	0.44	4.43	4.4	79	78
M10	0.41	0.42	4.44	4.71	86	82

M11	0.53	0.53	2.56	2.6	99	81
M12	0.29	0.33	1.32	1.4	83	80
M13	0.15	0.2	0.89	1.07	86	84

Table 3.3: Comparison chart of oblique fracture parameters

Location	Average length		Density		Orientation	
	Sample	Simulation	Sample	Simulation	Sample	Simulation
M01 NNE	0.42	0.32	0.41	0.35	31	30
NNW	0.33	0.43	1.07	0.42	112	122
M02 NNE	0.39	0.39	0.74	0.37	37	26
NNW	0.53	0.31	0.43	1.37	120	125
M03 NNE	0.24	0.39	0.61	0.32	37	33
NNW	0.28	0.41	0.4	0.36	113	120
M04 NNE	0.31	0.32	0.48	0.34	39	30
NNW	0.28	0.36	0.44	0.45	125	120
M05 NNE	0.54	0.45	0.63	0.42	54	32
NNW	0.22	0.37	0.03	0.43	128	120
M06 NNE	0.33	0.4	1.3	0.45	32	29
NNW	0.28	0.33	0.4	0.33	117	123
M07 NNE	0.37	0.23	0.63	0.99	17	16.5

NNW	0.37	0.35	2.85	0.27	107	118
M08 NNE	0.32	0.35	0.99	0.43	35	33
NNW	0.42	0.38	1.58	0.47	117	121
M09 NNE	0.24	0.32	0.17	0.28	7	29
NNW	0.12	0.36	0.01	0.41	110	119
M10 NNE	0.57	0.31	0.3	0.3	38	29
NNW	0.39	0.29	0.68	0.32	109	120
M11 NNE	0.4	0.4	0.42	0.46	28	38
NNW	0.5	0.34	0.35	0.45	123	120
M12 NNE	0.3	0.42	0.31	0.44	29	30
NNW	0.28	0.4	0.21	0.37	116	122
M13 NNE	0.56	0.33	3.45	0.53	22	30
NNW	0.31	0.33	0.61	0.53	118	119

The final test of simulation lies in comparing the connectivity of the sample data and the simulated fracture pattern. Connectivity of the sample fracture maps and simulated fracture maps for the same locations are evaluated. Connectivity is evaluated in terms of cluster size and fractional connected area. The result of the comparison is summarized in table 5. The results show that the difference in fractional connected area between the sample and simulated map is within 5% (except in places where there area no-data zone within the sample

area), which implies that the connectivity pattern of the fracture network is well preserved in the simulation procedure. Connected groups of fractures in sample and simulated maps are shown in figures 3.18 and Appendix figure A22 – A28. Histogram plots of fractional connected area for the sample maps and that of the simulated maps (extracted using the sample map area) are shown in figure 3.19. The plot shows that in both the cases most of the connected areas are less than 5sq.m Both in sample and simulated maps, the hinge locations have high fractional connected areas. Four sets of fractures that are simulated separately contribute to the connectivity of fracture network. Of the four sets, two sets (longitudinal and transverse sets) were simulated using structural controls. Two oblique sets were simulated using the average density and length distribution for the entire area. Since the latter sets are less dominant for the entire area, they have less contribution to the connectivity pattern, so the fractional connected area of the sample and simulated maps yielded a good match even though the oblique sets were simulated using the average bulk values for the entire structure. The cluster size of the sample and simulated fractures showed a good match in 7 out of 6 large sample maps. This is most likely attributed to the method of calculation of cluster size. The value of cluster size is depended only on the largest cluster of the study area, so the simulation method was able to re-generate the connected pattern of the fracture network, but did not necessarily recreate the largest cluster of a specific area.

Table 3.4: Comparison chart of connectivity

Location	Cluster size		Fractional Connected Area	
	Sample	Simulation	Sample	Simulation
M01	0.06	0.06	0.5	0.62
M02	0.41	0.55	0.98	0.99
M03	0.76	0.4	0.93	0.89
M04	0.2	0.2	0.8	0.77
M05	1	0.9	0.85	0.97
M06	0.3	0.3	0.65	0.65
M07	0.3	0.28	0.73	0.69
M08	0.6	0.1	0.82	0.78
M09	0.98	0.83	0.84	0.88
M10	0.9	0.4	0.83	0.81
M11	0.9	0.6	0.78	0.77
M12	0.15	0.1	0.41	0.37
M13	0.98	0.92	0.96	0.92

3.6 Conclusions

This approach of simulation of fracture network using structural controls gave good results concerning the spatial distribution of fractures. This model allows generation of networks with characteristics that closely mimics natural network observed in the outcrops. Although the simulation relies on simple inputs, it allows incorporation of structural controls for producing variation of

fracture characteristics across the structure. The simulation successfully reproduced fracture density ranging from very low density in the limb areas and progressively high density in the hinge zones. This property of fracture density variation is inferred from detailed field studies and used as a guide for fracture simulation.

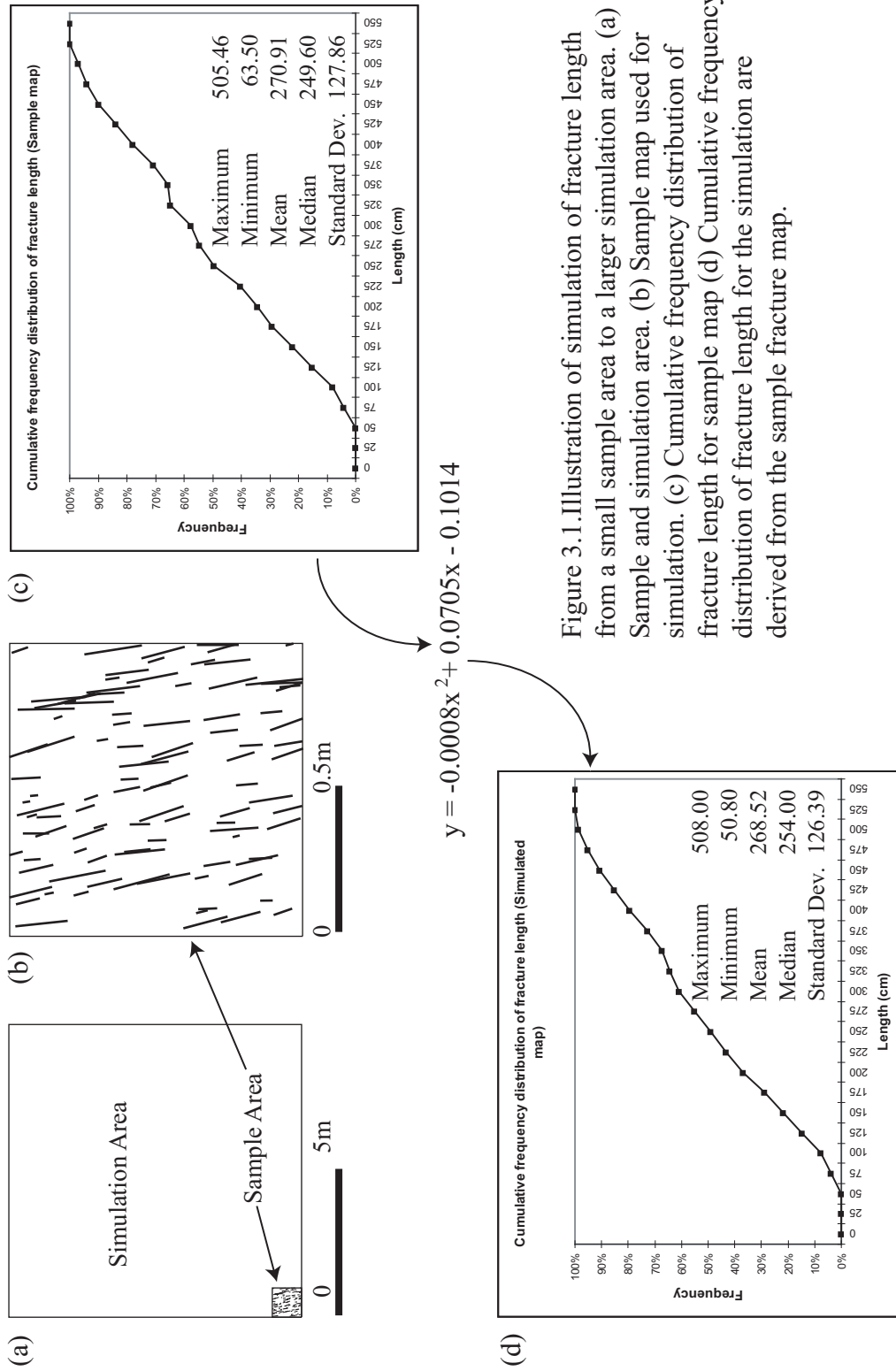


Figure 3.1. Illustration of simulation of fracture length from a small sample area to a larger simulation area. (a) Sample and simulation area. (b) Sample map used for simulation. (c) Cumulative frequency distribution of fracture length for sample map (d) Cumulative frequency distribution of fracture length for the simulation area derived from the sample fracture map.

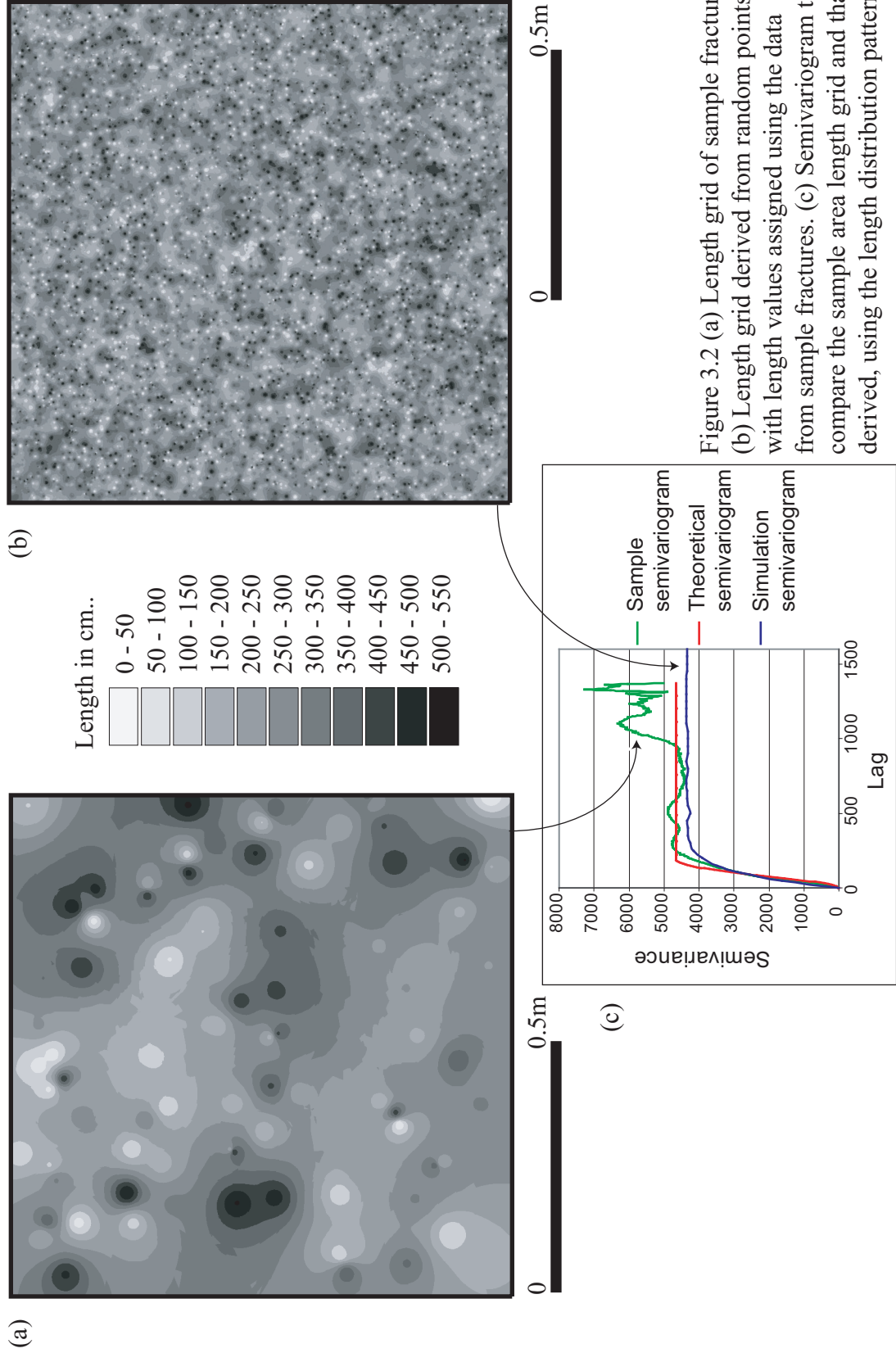
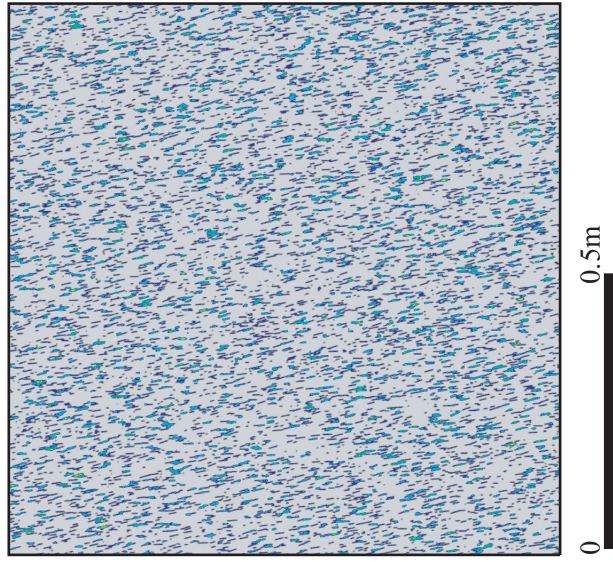
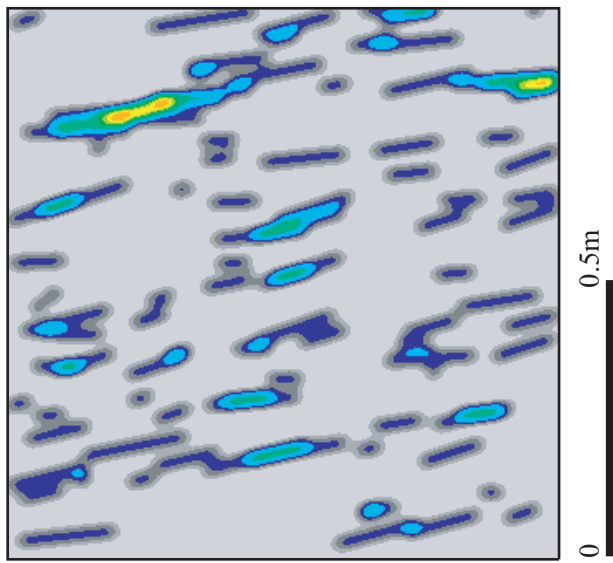
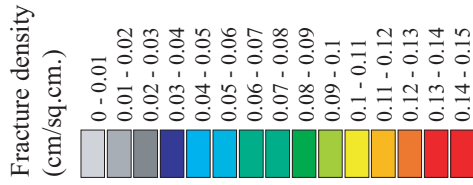


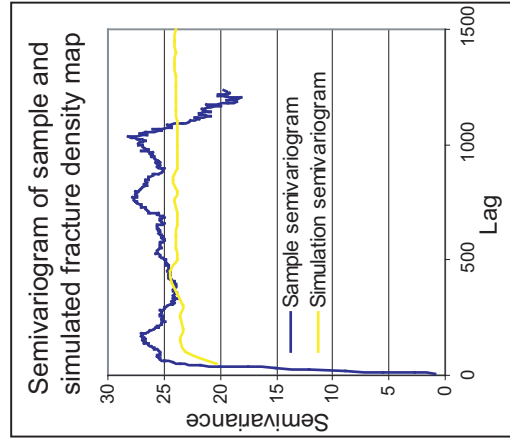
Figure 3.2 (a) Length grid of sample fractures (b) Length grid derived from random points with length values assigned using the data from sample fractures. (c) Semivariogram to compare the sample area length grid and that derived, using the length distribution pattern.



(a)



(b)



(c)

Figure 3.3. (a) Density grid of sample map calculated as the summation of length within a circular search area. (b) Density grid of simulated fractures. (c) Semivariogram derived from the sample fracture density grid and simulated fracture density grid to compare the closeness of result.

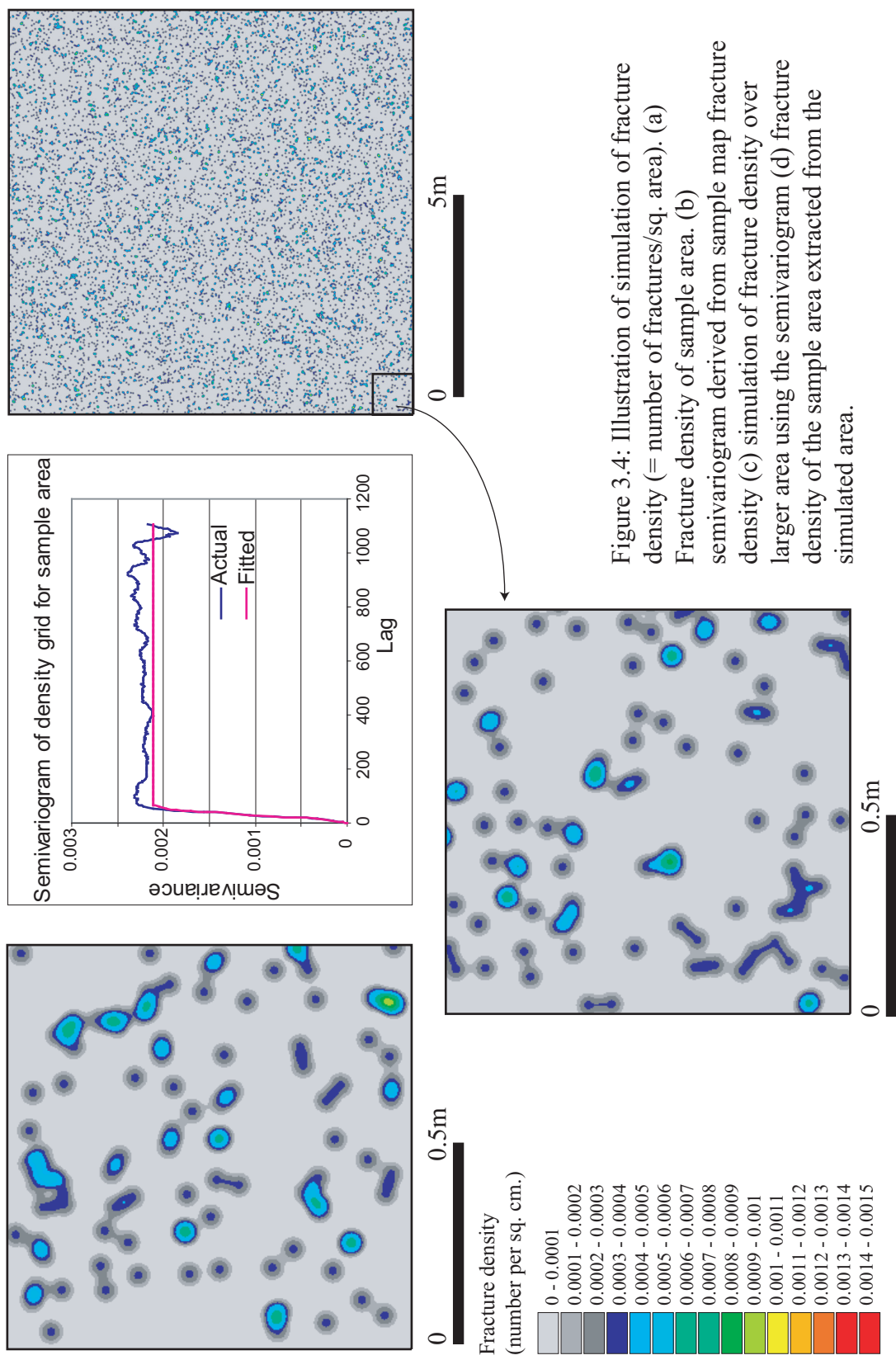


Figure 3.4: Illustration of simulation of fracture density (= number of fractures/sq. area). (a) Fracture density of sample area. (b) Semivariogram derived from sample map fracture density (c) simulation of fracture density over larger area using the semivariogram (d) fracture density of the sample area extracted from the simulated area.

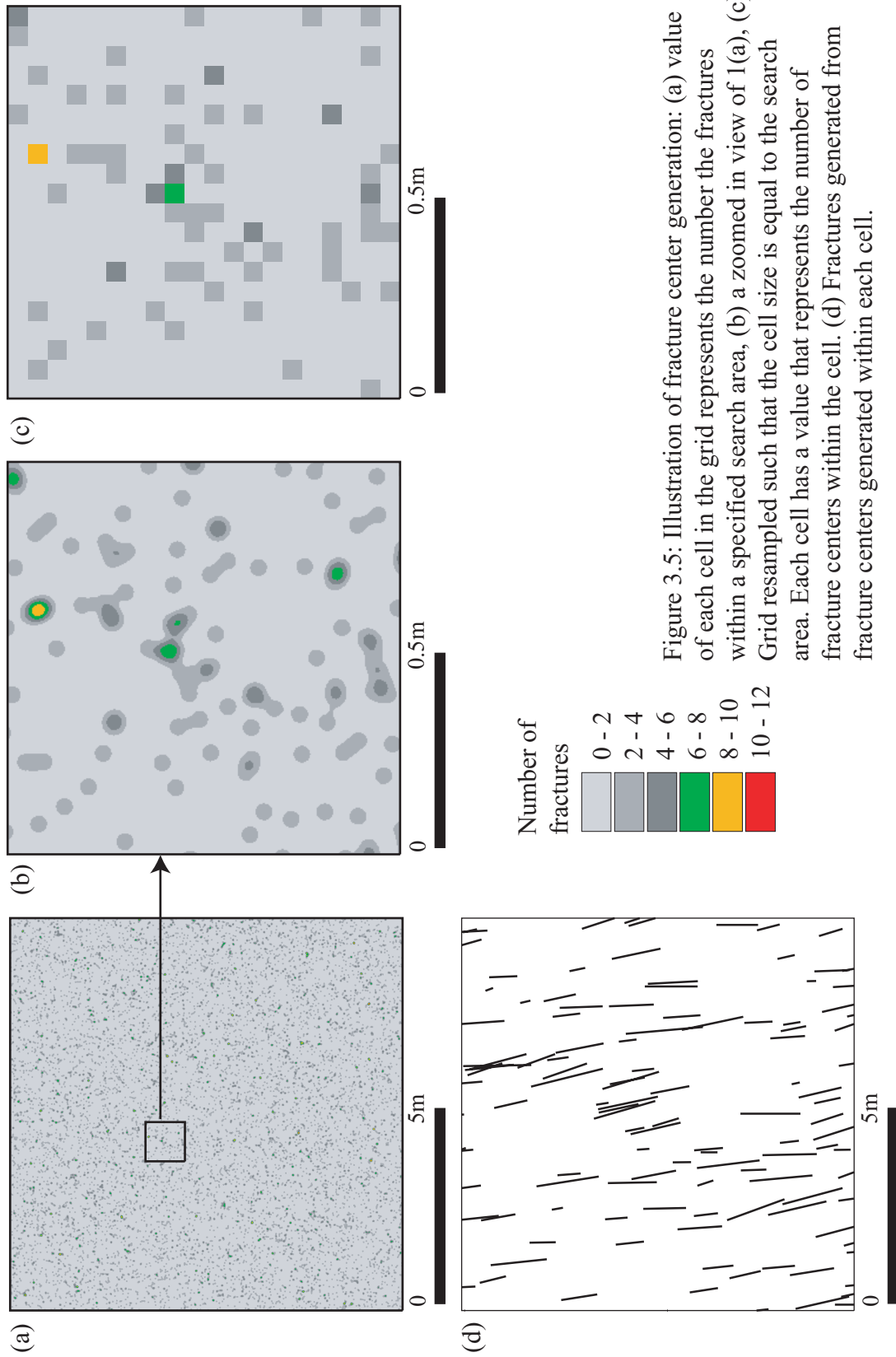


Figure 3.5: Illustration of fracture center generation: (a) value of each cell in the grid represents the number the fractures within a specified search area, (b) a zoomed in view of 1(a), (c) Grid resampled such that the cell size is equal to the search area. Each cell has a value that represents the number of fracture centers within the cell. (d) Fractures generated from fracture centers generated within each cell.

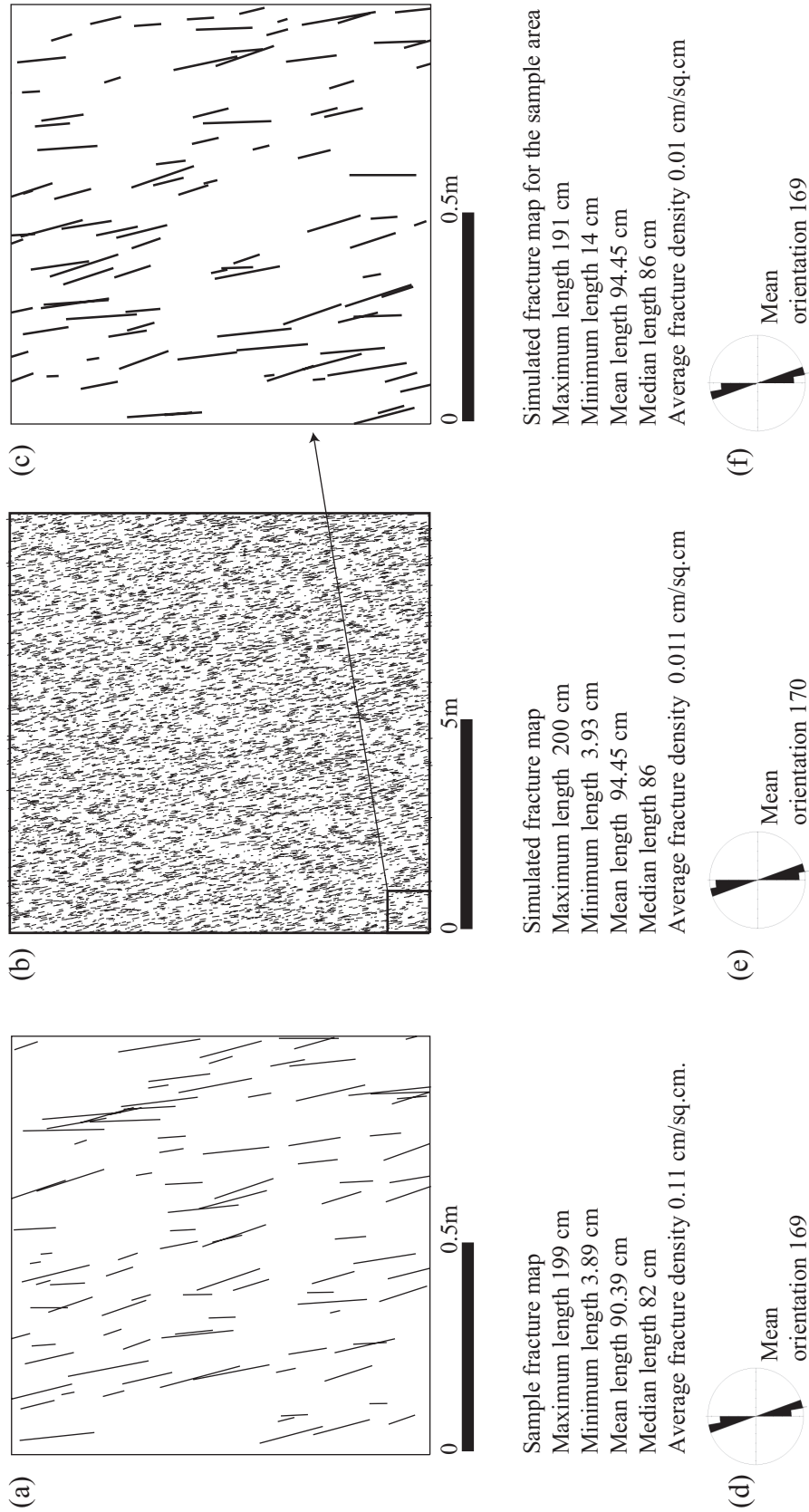


Figure 3.6: (a) Sample fracture map used for simulation. (b) Simulated fracture map.(c) Simulated fracture map zoomed in to the area of sample map. (d) Mean orientation of sample fractures.(e) Mean orientation of simulated fractures. (f) Mean orientation of simulated fractures extracted from the sample area.

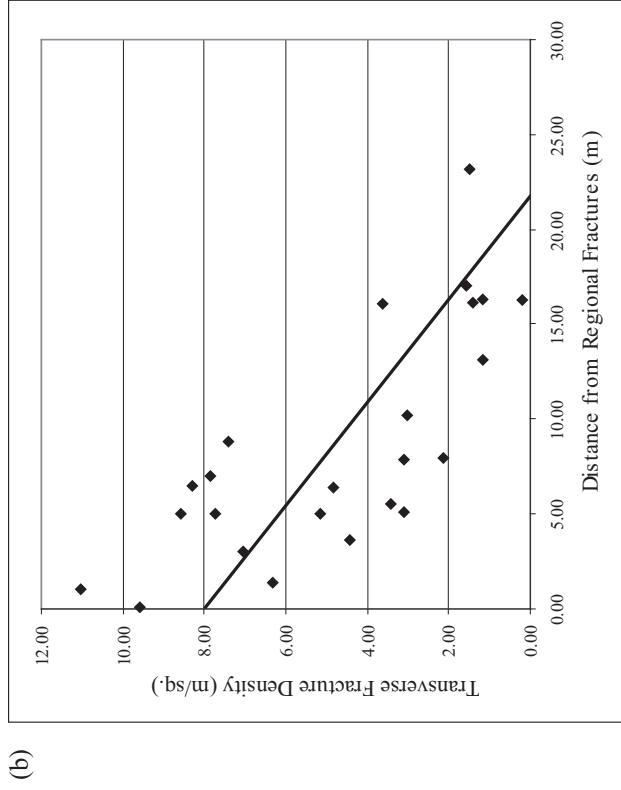
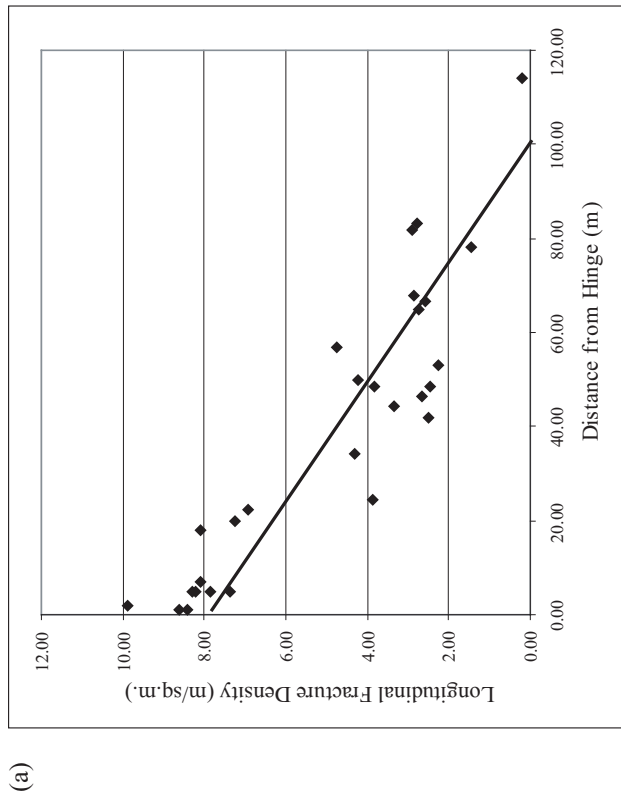


Figure 3.7: Plots showing variation of density of (a) longitudinal fractures with respect to subtle hinges of Teton anticline and (b) transverse fractures with respect to the regional fractures of the area.

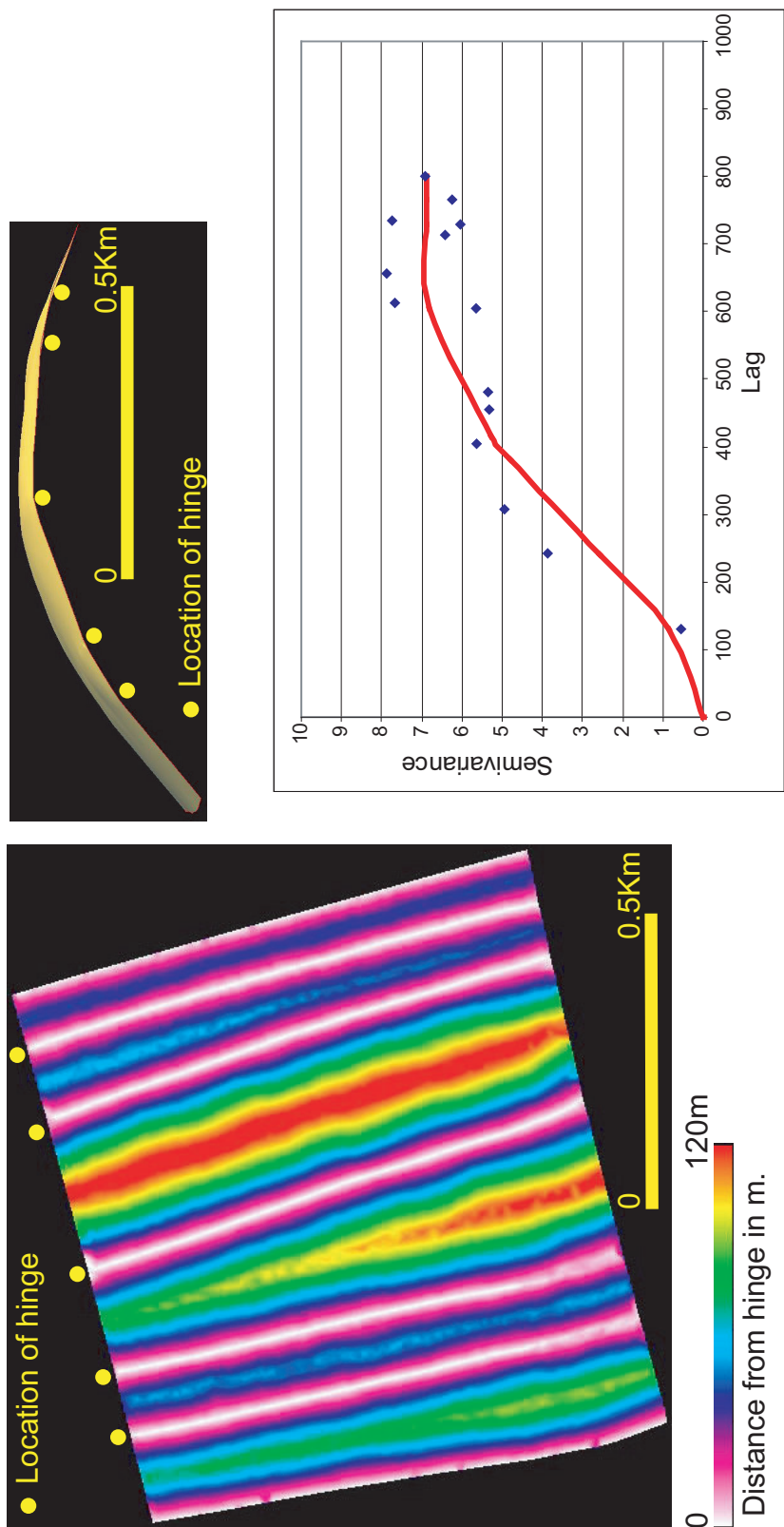


Figure 3.8. (a) Top view of Teton anticline, color coded by distance from hinge. (b) Profile of Teton anticline, yellow dots marking the location of subtle hinges. (c) Theoretical curve fitted through longitudinal fracture density.

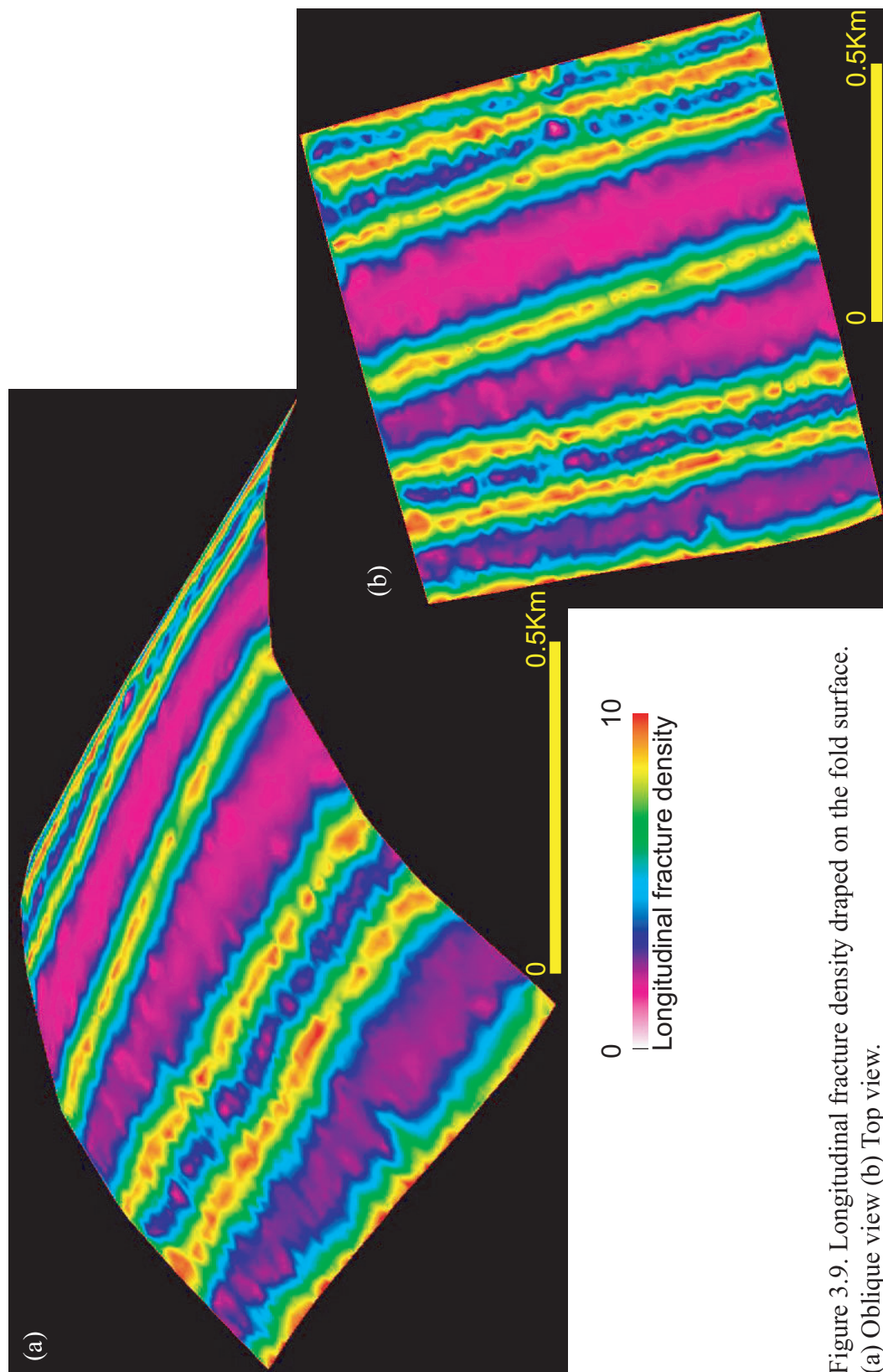


Figure 3.9. Longitudinal fracture density draped on the fold surface.
(a) Oblique view (b) Top view.

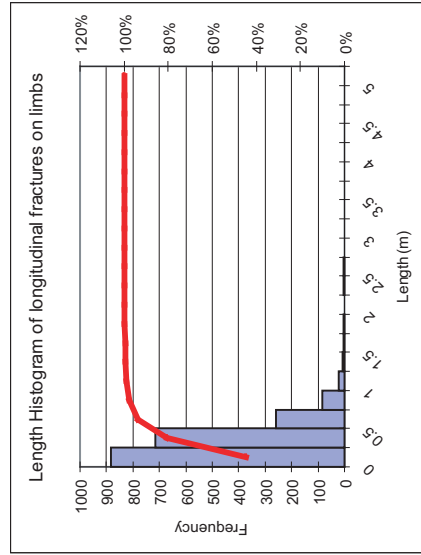
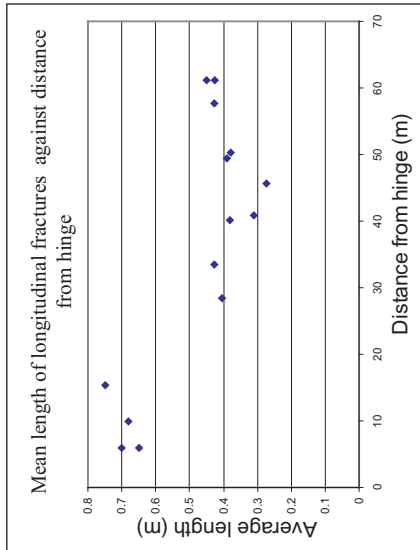
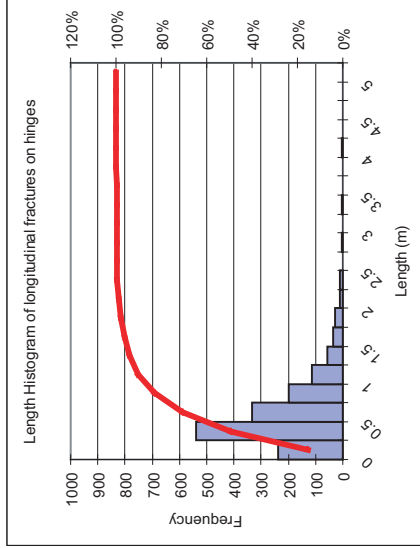


Figure 3.10. Length distribution of longitudinal fractures. (a) Mean length of sample locations plotted against distance from hinge of each location. (b) Length distribution of longitudinal fractures on hinges. (c) Length distribution of longitudinal fractures on limbs

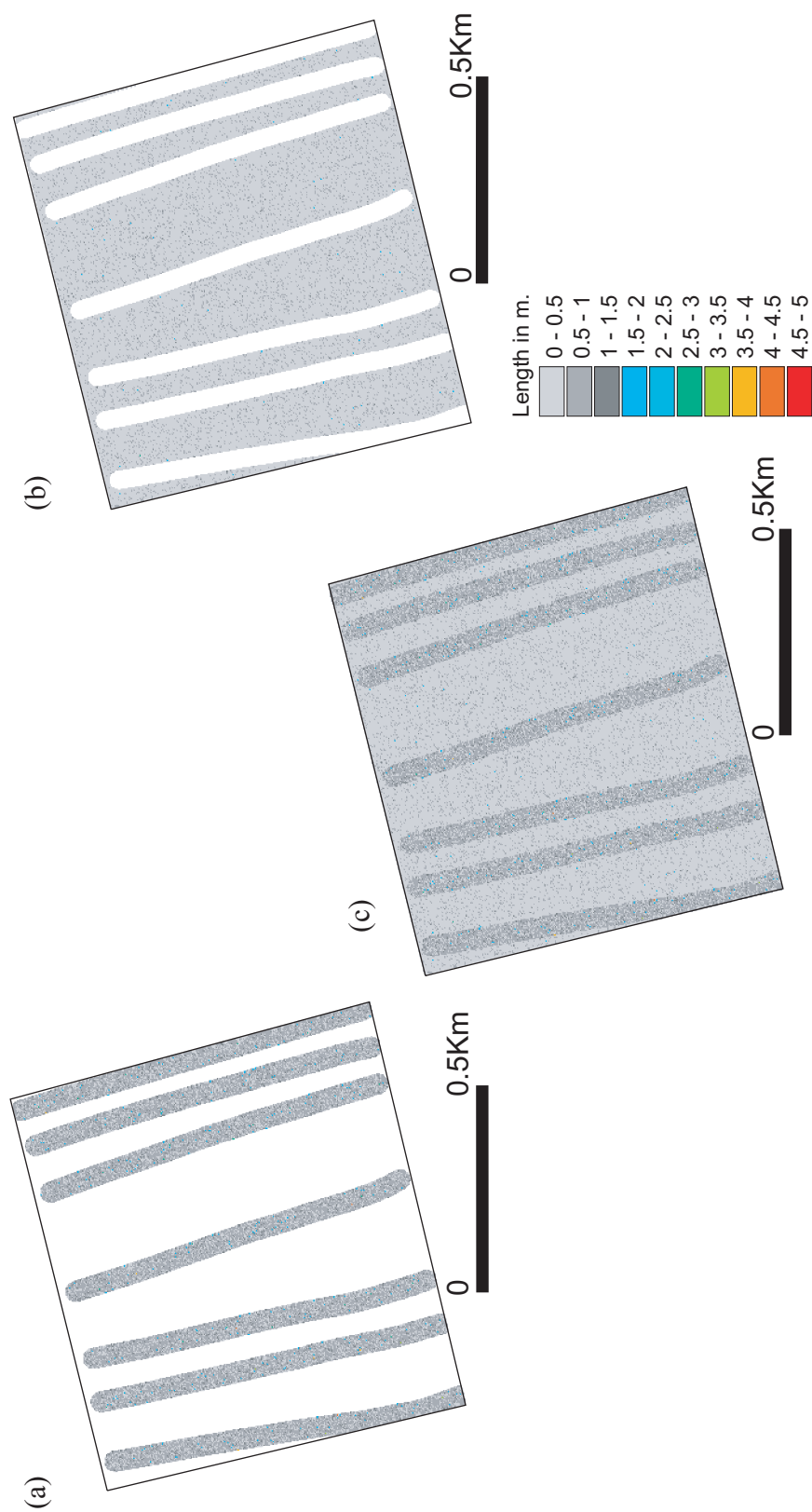


Figure 3.1.1. Simulated length grids. (a) Length grid for the area within 25m from the hinges. (b) Length grid for area at least 25m away from hinge. (c) Integrated length grid for the entire structure.

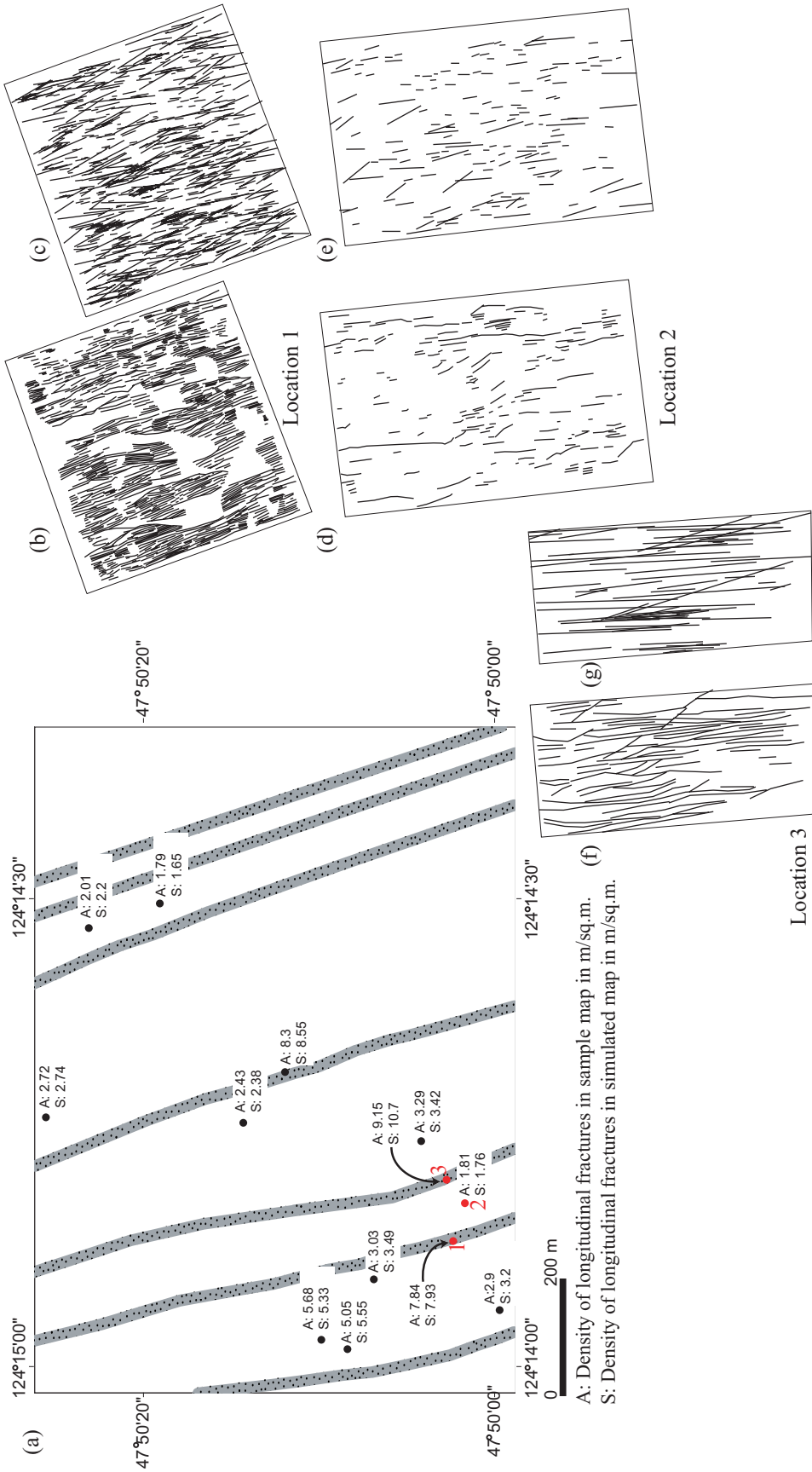


Figure 3.12: (a) Index map showing the location of hinges and longitudinal fracture density (in m/sq.m) for simulated and sample maps. Fracture map and respective simulation of longitudinal set of locations marked in red are displayed in figures b through g. Location 1 and 3 area hinge locations while location 2 is a limb location. (b) Longitudinal fracture map of location 1. (c) Simulated longitudinal fracture map of location 1. (d) Longitudinal fracture map of location 2. (e) Simulated longitudinal fracture map of location 2. (f) Longitudinal fracture map of location 3. (g) Simulated longitudinal fracture map of location 3.

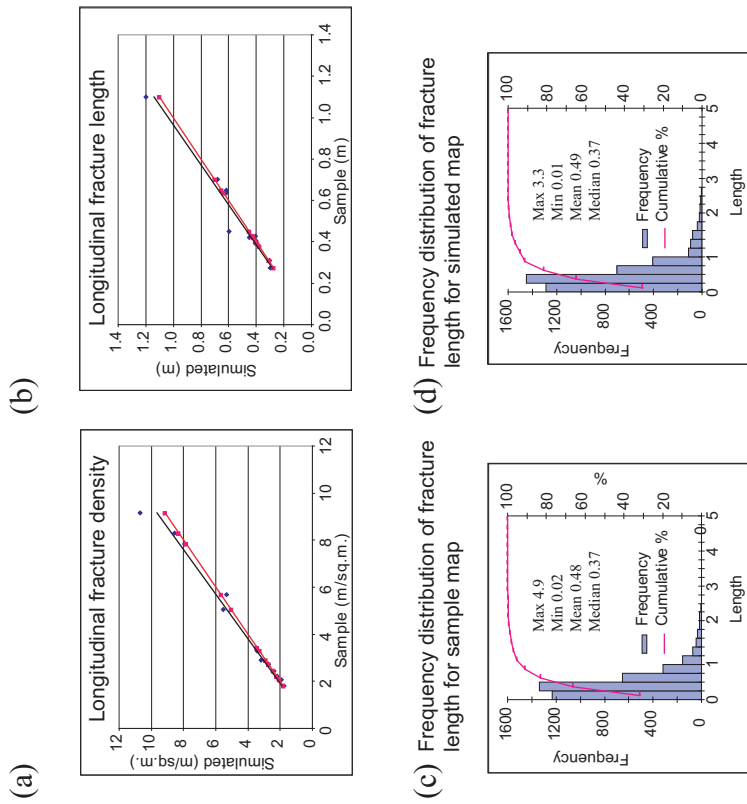


Figure 3.13: (a) Plot of density of sample versus simulated fractures for all the locations. Red line in the plot is a line of 45 degree slope, black line is the trend line fitted to data points. (b) Plot of length of sample versus simulated fractures for all the locations. Red line in the plot is a line of 45 degree slope, black line is the trendline fitted to data points. (c) Frequency distribution of length for longitudinal fractures of sample maps. (d) Frequency distribution of length for longitudinal fractures of simulated maps.

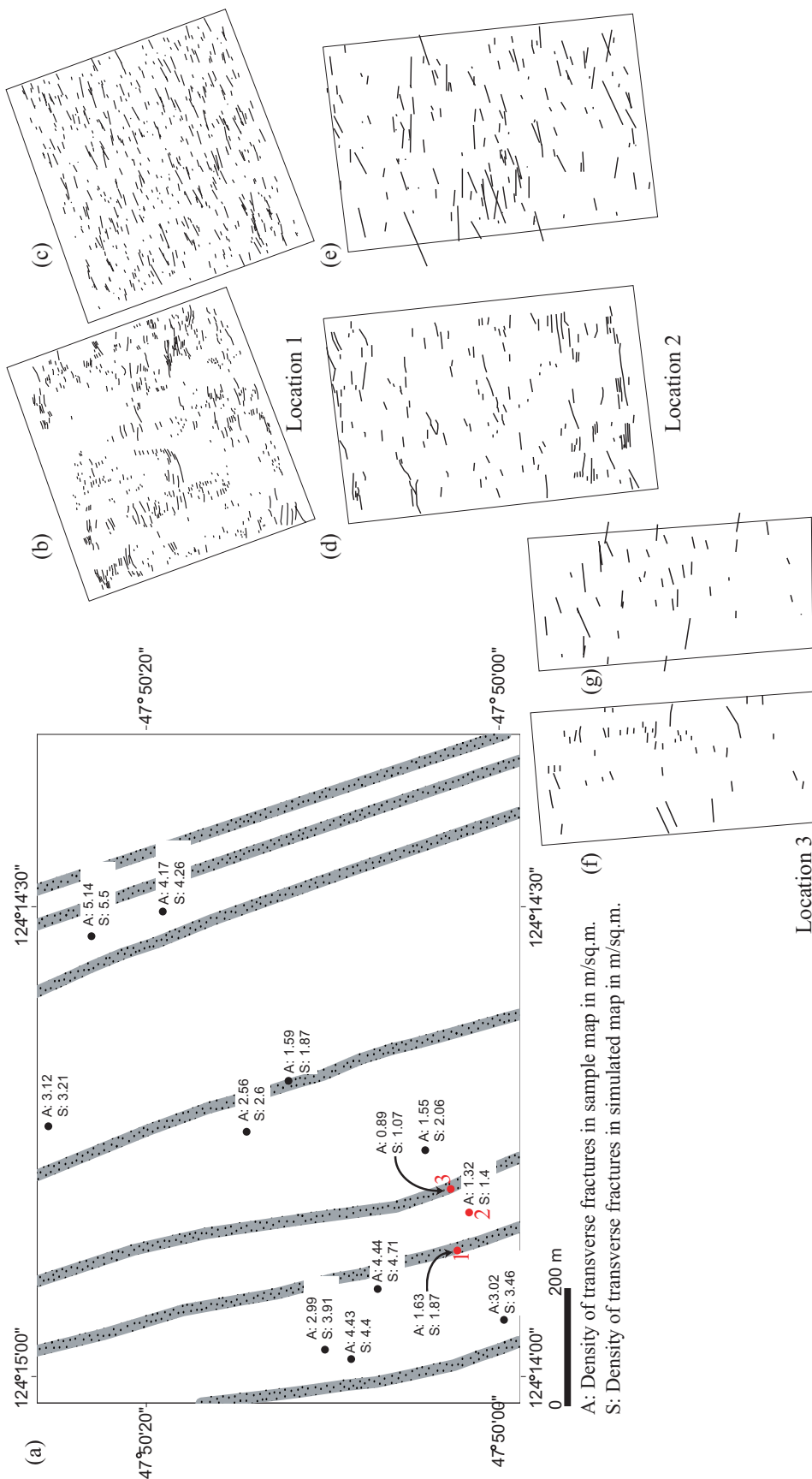


Figure 3.14: (a) Index map showing the location of hinges and transverse fracture density (in m/sq.m) for simulated and sample maps. Fracture map and respective simulation of transverse set of locations marked in red are displayed in figures b through g. Location 1 and 3 are hinge locations while location 2 is a limb location. (b) Transverse fracture map of location 1. (c) Simulated transverse fracture map of location 1. (d) Transverse fracture map of location 2. (e) Simulated transverse fracture map of location 2. (f) Transverse fracture map of location 3. (g) Simulated transverse fracture map of location 3.

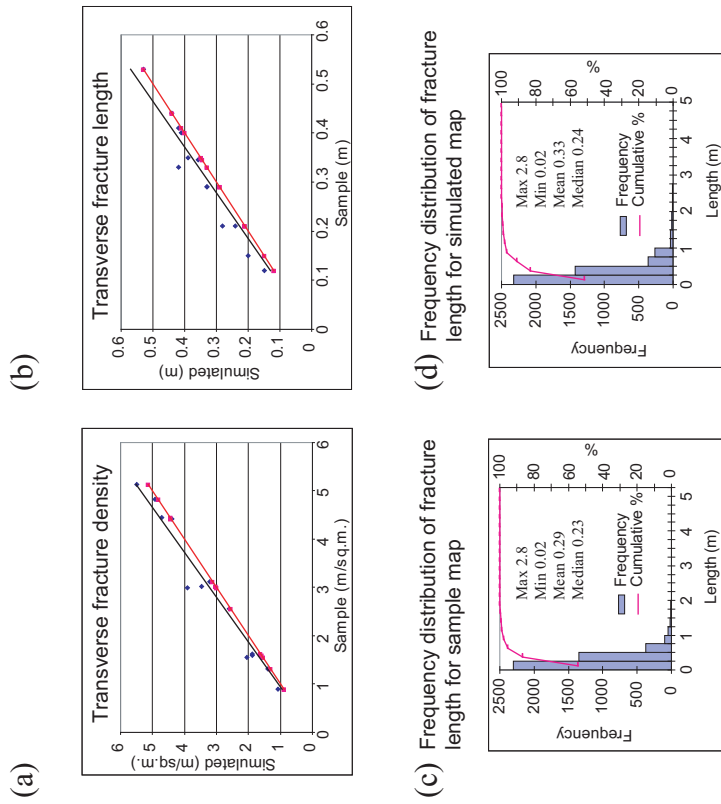


Figure 3.15: (a) Plot of density of sample versus simulated fractures for all the locations. Red line in the plot is a line of 45 degree slope, black line is the trend line fitted to data points. (b) Plot of length of sample versus simulated fractures for all the locations. Red line in the plot is a line of 45 degree slope, black line is the trend line fitted to data points. (c) Frequency distribution of length for transverse fractures of sample maps. (d) Frequency distribution of length for transverse fractures of simulated maps.

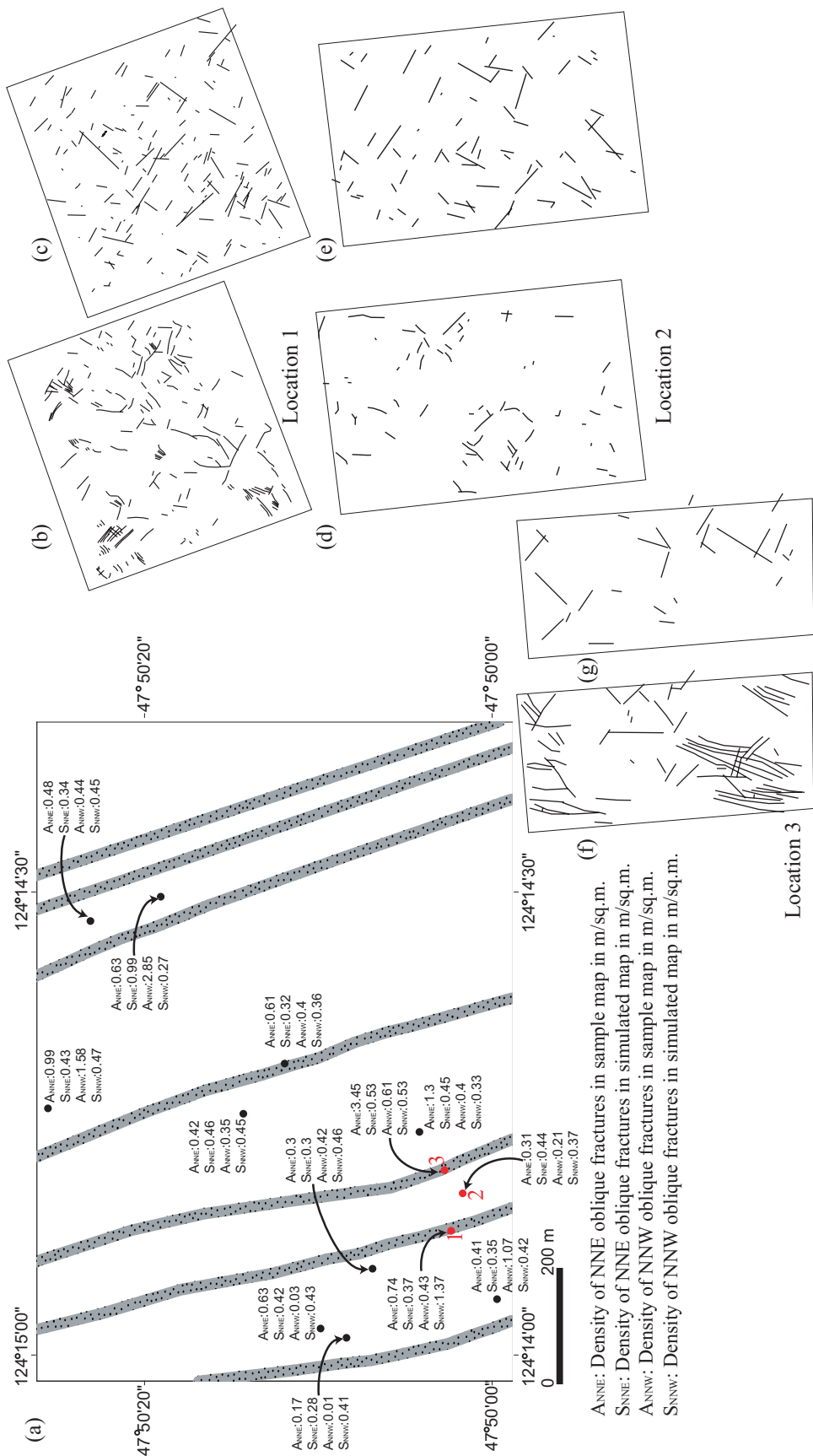
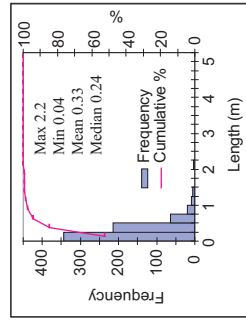
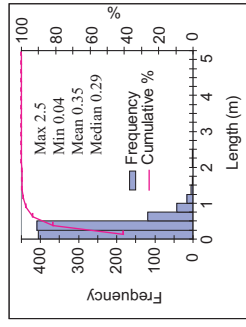


Figure 3.16: (a) Index map showing the location of hinges and oblique fracture density (in m/sq.m) for simulated and sample maps. Fracture map and respective simulation of oblique set of locations marked in red are displayed in figures b through g. Location 1 and 3 are hinge locations while location 2 is a limb location. (b) Oblique fracture map of location 1. (c) Simulated oblique fracture map of location 1. (d) Oblique fracture map of location 2. (e) Simulated oblique fracture map of location 2. (f) Oblique fracture map of location 3. (g) Simulated oblique fracture map of location 3.

(a) Frequency distribution of NNE oblique fracture length for sample maps (b) Frequency distribution of NNE oblique fracture length for simulated maps



(c) Frequency distribution of NNW oblique fracture length for sample maps (d) Frequency distribution of NNW oblique fracture length for simulated maps

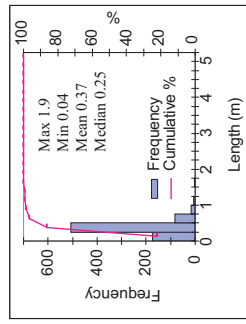
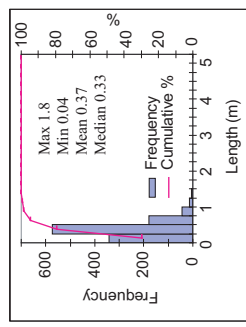


Figure 3.17: (a) Frequency distribution of length for NNE oblique fractures of sample maps. (b) Frequency distribution of length for NNE oblique fractures of simulated maps. (c) Frequency distribution of length for NNW oblique fractures of sample maps. (d) Frequency distribution of length for NNW oblique fractures of simulated maps.

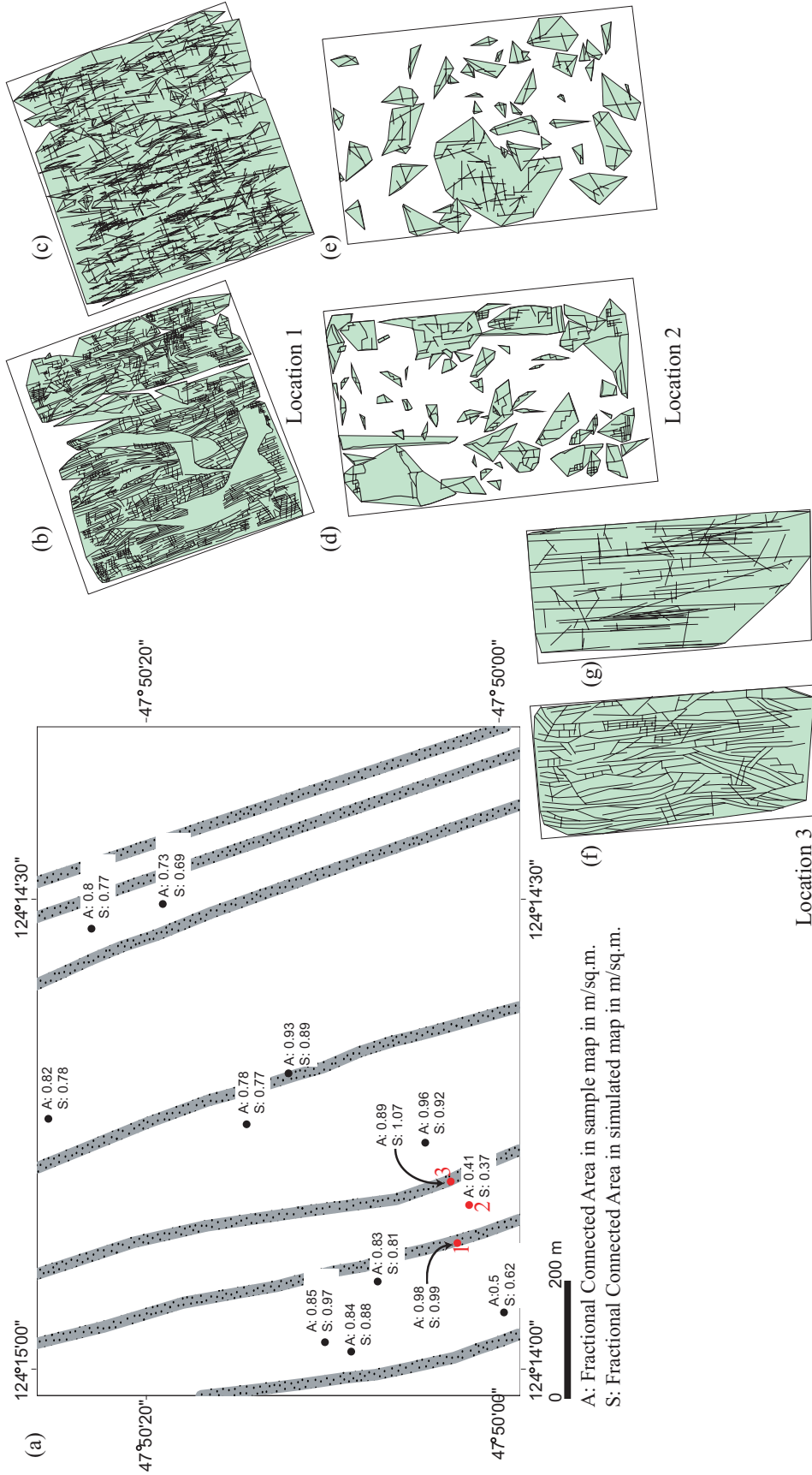


Figure 3.18: (a) Index map showing the location of hinges and Fractional Connected Area for simulated and sample maps. Fracture map and respective simulation of all sets of locations marked in red are displayed in figures b through g. Location 1 and 3 are hinge locations while location 2 is a limb location. (b) Simulated connectivity map of location 1. (d) Connectivity map of location 2. (e) Simulated connectivity map of location 3. (f) Connectivity map of location 2. (g) Simulated connectivity map of location 3.

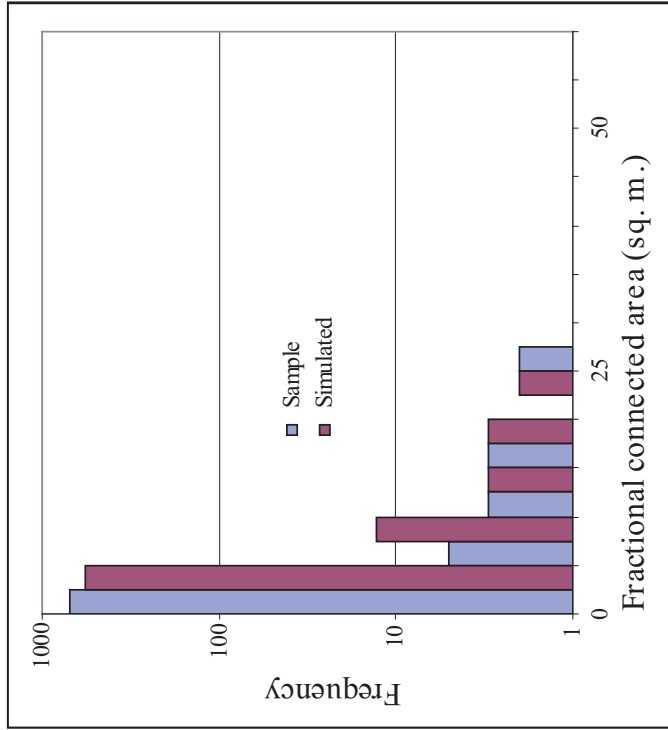


Table:
Fractional Connected Area (sq. m.)

	Sample	Simulated
Mean	0.6	0.7
Median	0.06	0.08
St. Dev	3.2	3.2

Figure 3.19: Histogram of fractional connected area from all the sample maps and the simulated fractures extracted using the sample map area. The statistics for the same is recorded in the adjacent table.

CHAPTER 4:

FRACTURE DISTRIBUTION OF CANYONLANDS

GRABEN AREA

4.1 INTRODUCTION

4.2 STRUCTURAL BACKGROUND OF CANYONLANDS

4.3 FRACTURE CHARACTERISTICS IN THE

CANYONLANDS

4.4 STRUCTURAL CONTROLS OF FRACTURES IN THE

CANYONLANDS

4.5 FRACTURE CONNECTIVITY IN THE CANYONLANDS

4.6 CONCLUSIONS

4.1 Introduction

Fracture patterns associated with normal faults were studied in the Graben area of Canyonlands National Park, Utah. High quality exposures of fractures in the Cedar Mesa Sandstone mappable using remote sensing data were available for the area. The normal faults mapped in the area were obtained from a Utah Geological Survey map (Hintze, et al., 2000) (Figure 4.1). Data was primarily obtained from high resolution (60 cm) Quickbird satellite images from Digital Globe, which collects black and white, four band multispectral color images. The images used for this study were orthorectified, pan sharpened natural color image of 60cm resolution. Orthorectification is an image processing technique used to eliminate terrain and panoramic distortion and provide better horizontal accuracy. Pan-sharpening is a resampling method that increases the resolution of multispectral image data by using a high resolution panchromatic image. Such high resolution image enables identification of any fractures longer than 60cm. The fractures are formed in the Cedar Mesa sandstone, which is aeolian sandstone with surface exfoliation. The fractures identified on the Quickbird image are the only scale of fractures that are present on the bedding plane of the uppermost unit of Cedar Mesa sandstone. The image obtained from the digital image library was used as a base map for identifying fractures (Figure 4.2c). The fractures in the Canyonlands area range in length from a few tens of meters to a few kilometers.

Field work was carried out to provide a ground check for remote sensing data and also to record the vertical extent of the fractures. The fractures that are exposed in the map view are contained within the Cedar Mesa sandstone unit. Data collection in the field focused on fracture length, orientation, type of fracture and termination characteristics of different sets of fractures to understand the sequence of fracturing.

Fractures mapped were often not continuous due to erosion. Thus patches of continuously mapped area were selected and all analyses were limited within these areas to eliminate noise in the data. The locations of all measurement stations are shown in Figure 4.2. Various fracture parameters (length, orientation, density), along with fracture network connectivity properties of the mapped fractures were analyzed and studied in detail to understand the variation of these parameters with respect to distance from the normal faults in the Canyonlands area.

4.2 Structural Background of Canyonlands

The Canyonlands are located within the Paradox basin, which was formed due to the collapse of the pre-Pennsylvanian basement along pre-existing NW trending faults. The most active period of subsidence extended from mid-Pennsylvanian to late Triassic, (Baars and Doelling, 1987). The lowermost unit of the paradox basin is the Paradox Formation, which consists of cyclic evaporites,

black shales and carbonates (Baars et al., 1967). The sedimentary section above the Paradox Formation consists of the Pennsylvanian Honker Trail Formation, the Pennsylvanian-Permian lower Cutler beds and the Permian Cedar Mesa Sandstone (Condon, 1997). The grabens in the Needles district of the Canyonlands National Park were formed as the Colorado River eroded the sedimentary overburden down to the Pennsylvanian evaporites. Thus the erosion of the canyon removed downdip confinement and allowed gravity driven extension of the overburden resulting in the formation of normal faults and related fractures (McGill and Stromquist, 1975).

The canyonlands grabens are a series of northeast-southwest trending normal faults along the southeastern side of the Colorado River (Figure 4.1). It has been estimated (based on the downcutting rate of the Colorado River) that the graben development began ca. 0.5Ma (McGill and Stromquist, 1975). The major grabens exhibit a wide variety of fault linkages and transfer zones (Trudgill and Cartwright, 1994).

4.3 Fracture characteristics in the Canyonlands

Fractures in this area extend from a few meters to several hundred meters in length. The smallest fracture identified from the digital image was 0.87m and the largest fractures extend to 814.2m (figure 4.3). Fracture orientations measured at the outcrops are displayed on rose diagrams and equal angle stereographic net

projections (Figure 4.4, 4.5, 4.6). Based on the fracture plots, several sets of fractures were identified with two most dominant sets that are parallel and perpendicular to the regional normal faults. The set parallel to the normal fault is oriented NE-SW and the set perpendicular to the fault is oriented ESE-WNW. A close look at the orientation data reveals that there is a spatial variation within the most dominant sets. Assuming a dispersion of 20° , the fault parallel set can be divided in two subsets, a 14° set and a 30° set. The fracture set with 14° average strike is more dominant in the northeastern part of the study area and the density decreases towards the west and south of the study area, where the 30° set is more dominant (figure 4.4). Similar observations are made within the fault normal set of fractures. This set is divided into a 121° set and a 137° set. The fracture set with 121° average orientation has a higher density in the northeastern part of the study area, whereas the 137° fracture set is more dominant in the southern and western part of the area (figure 4.5). A generalized pattern that can be inferred from the observations of fracture orientation is that the 121° set is co-associated with the 14° set and the 137° set is co-associated with the 30° set. Similar observations were made by Lorenz and Cooper, (2001), in fractures within the Entrada sandstone in the Salt Valley anticline, Utah which is about 80miles north of the Canyonlands graben area. This spatial variation of fracture orientation may be related to the episodic dissolution or movement of evaporites resulting in the rotation of fractures (Lorenz and Cooper, 2001). All the fracture sets are sub-

vertical and are perpendicular to sub-horizontal bedding, which has an orientation of 218/02W. In subsequent discussions, the 14° and 30° sets are grouped together and referred to as fault parallel fractures while the 121° and 137° sets are grouped together and referred to as fault perpendicular fractures.

For each fracture set, the distributions of length and fracture density were analyzed (figure 4.7, 4.8, 4.9, 4.10). Fracture density grids were generated for each fracture set, where the value of each cell in the grid is calculated as the summed lengths of all fractures of that set within a circular search radius, divided by the search area (Figure 2.5). The sequence of fracturing as observed in the field exhibits that the fracture perpendicular to the fault almost always terminates at the fracture parallel to the fault. Figure 4.11a shows a field photograph exhibiting this relationship, within an interlayer of Cedar Mesa sandstone. The same relation of termination is also observed in the Quickbird images (Figure 4.11b). Thus the relation of fracture termination is consistent at multiple scales.

The fault parallel fractures were found to have a significantly higher length and average density than the fault normal fractures. Map pattern of fracture density values for different sets is shown in figure 4.12, 4.13. The densities of both fault parallel and fault normal fractures sets exhibit spatial heterogeneity which is primarily tied to the structural position.

4.4 Structural controls of fractures in the Canyonlands

There are two main structural controls of fracture densities in the Canyonlands area: (1) distance from faults, and (2) radial distance from fault tips.

Distance from Faults

The fracture density of dominant sets of fractures, i.e. the fault parallel and fault normal sets, exhibit systematic variation with respect to distance from normal faults. The averaged fracture density within an area of every 5m from the fault trace was plotted against distance from fault (Figure 4.8a, b). Both of the dominant sets exhibit high fracture density in the vicinity of the fault, and the density decreases away from the fault trace. The curve shows a stepped pattern indicating that within a narrow zone around the fault the density is high, but away from the fault zone, the density decreases gradually. Again, approximately 300m away from the fault, the density decreases rapidly and eventually decreases to the lowest density value farthest from the fault.

This relationship of the fracture densities of sets parallel to the normal fault can be attributed to the fact that the NE-SW faults formed due to slip on pre-existing fractures. The faults in the Canyonlands Graben nucleated on pre-existing fractures and then possibly increased in length by mechanical interaction of slipped fractures (Moore and Schultz, 1999). Thus the faults may have formed where the fracture density was high, eventually resulting in a map pattern of high

density of fault parallel fractures in the vicinity of the normal faults. The fault normal set, on the other hand, was formed due to stress rotation within the stress shadow zone of the large normal faults (Katternhorn et al., 2000). Therefore, one interpretation of the spatial pattern of fracture density with respect to faults is that the fault parallel fractures formed before the normal faults and the fault normal fractures were formed synchronously with the normal faults under the same regional stress state.

Distance from Fault Tips

To study the variation of density with distance from fault tips, the locations of all fault linkages and fault terminations within the study area were marked by points and the distance of each cell was calculated as the minimum radial distance from the point (figure 4.14d). A cross plot was generated for the density of fault parallel set and distance from fault linkage and/or termination points (Figure 4.14e). The plots show comparatively lower densities within 15m of the linkage and then the density increases, remains high within ~200m from the termination points and then decreases gradually. A similar plot was made with the fault normal set (Figure 4.14f) but no systematic relation was observed.

The state of stress at the fault tip leads to an increase in the formation of secondary fractures leading to linkage of faults (Martel and Pollard, 1989, Trudgill and Cartwright, 1994). Relay structures develop when two fault segments

propagate into an overlapping configuration and further lateral propagation is inhibited by the interaction of stress fields around the overlapping fault tips (Peacock and Sanderson, 1991, Seagall and Pollard, 1980). Progressive increase in displacement gradient near the locked fault tips results in the rotation of the ramp between the overlapped segments. Several of these overlapping and rotated fault segments are observed within the study area. Therefore, one should expect higher fracture densities in the immediate vicinity of these fault tips. One explanation of the low density values in the vicinity of fault linkages is probably due to a high rate of erosion in these areas, which can be attributed to the increased fracturing at fault tips.

4.5 Fracture connectivity in the Canyonlands

Cluster analysis is performed on the fracture networks to evaluate the connectivity pattern of fractures. Due to the presence of multiple sets of fractures, and at least of one set of fractures (the fault-parallel set) being extensive in size, the connectivity within each fault block is very high (Figure 4.15). In all the blocks the fracture maps are completely connected to yield a fractional connected area of 1. Thus the fracture connectivity in this case is controlled dominantly by the length of the fault parallel fracture set that has an average length 80m, which is 43 to 72% higher than any adjacent fracture sets. The fractures parallel and perpendicular to normal faults exhibit a spatial relation with the normal faults

with the density of both sets high within a zone adjacent to the fault and then decreasing dramatically beyond that zone. This relation has some control on the connectivity pattern which is inferred from the density pattern of the connected fractures. Fractional connected length, which is effectively the density of connected group of fractures, is evaluated as a grid (Figure 4.16a). The map pattern of the density grid exhibits high values located near the fault. Figure 4.16b shows a plot of fractional connected length averaged over 5m distance from the fault against distance from fault. The plot reveals that the fractional connected length decreases gradually with distance from fault then at a distance of approximately 200m there is a sudden drop in connectivity. This pattern is consistent with the spatial distribution of fault parallel set that shows a drop in density approximately 200m away from the fault tip. The connectivity of the fracture network being controlled by the length of the fault parallel fractures exhibits similar spatial variation, i.e., the fracture connectivity is high in the vicinity of normal faults, and decreases dramatically at a distance of 200m.

4.6 Conclusions

Fracture patterns in the Canyonlands area can be grouped into two major sets and four minor sets. The primary fracture sets are parallel and perpendicular to the regional NE-SW trending normal faults. The fracture set parallel to the normal fault exhibits spatial variation of strike. The orientation of this set changes

from an average of 014° in the northeastern part of the study area to 030° towards the south and western part of the study area (towards the Colorado river). A similar relation is also observed in the set perpendicular to normal fault, i.e. the 121° set is dominant in the northeastern part and the 137° set is dominant towards the south and western part of the study area. Similar observation in the Salt valley anticline was attributed to episodic movement of salt in the subsurface (Lorenz and Cooper, 2000).

Major fracture sets in the area were formed in the same stress regime. The normal faults nucleated on the pre-existing fault parallel fractures and later increased in length by interaction with slipped fractures, while the fault normal fractures formed within the stress shadow zone of the normal faults due to local stress rotation. This evolution of fractures resulted in a relationship between the fracture density and distance from the normal faults. The density of the two major sets of fractures and the overall fracture connectivity exhibit high values in the vicinity of the faults and decrease gradually with distance from the faults.

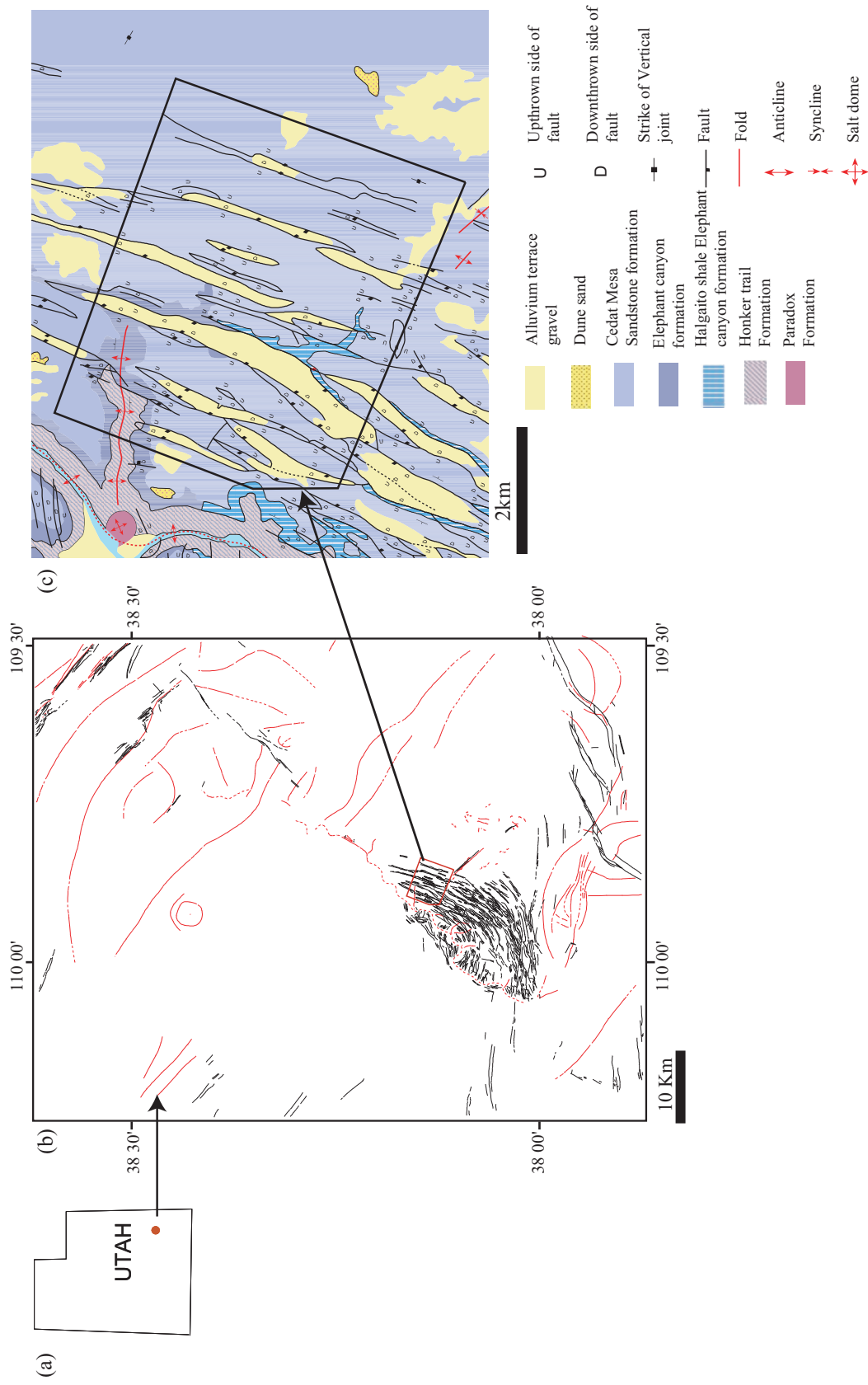


Figure 4.1: (a) Location of study area marked by a red dot on state map of Utah. (b) Generalized structure map of Canyonland area ((Hintze, 2000) (c) Generalized geologic map of study area (Hintze, 2000).

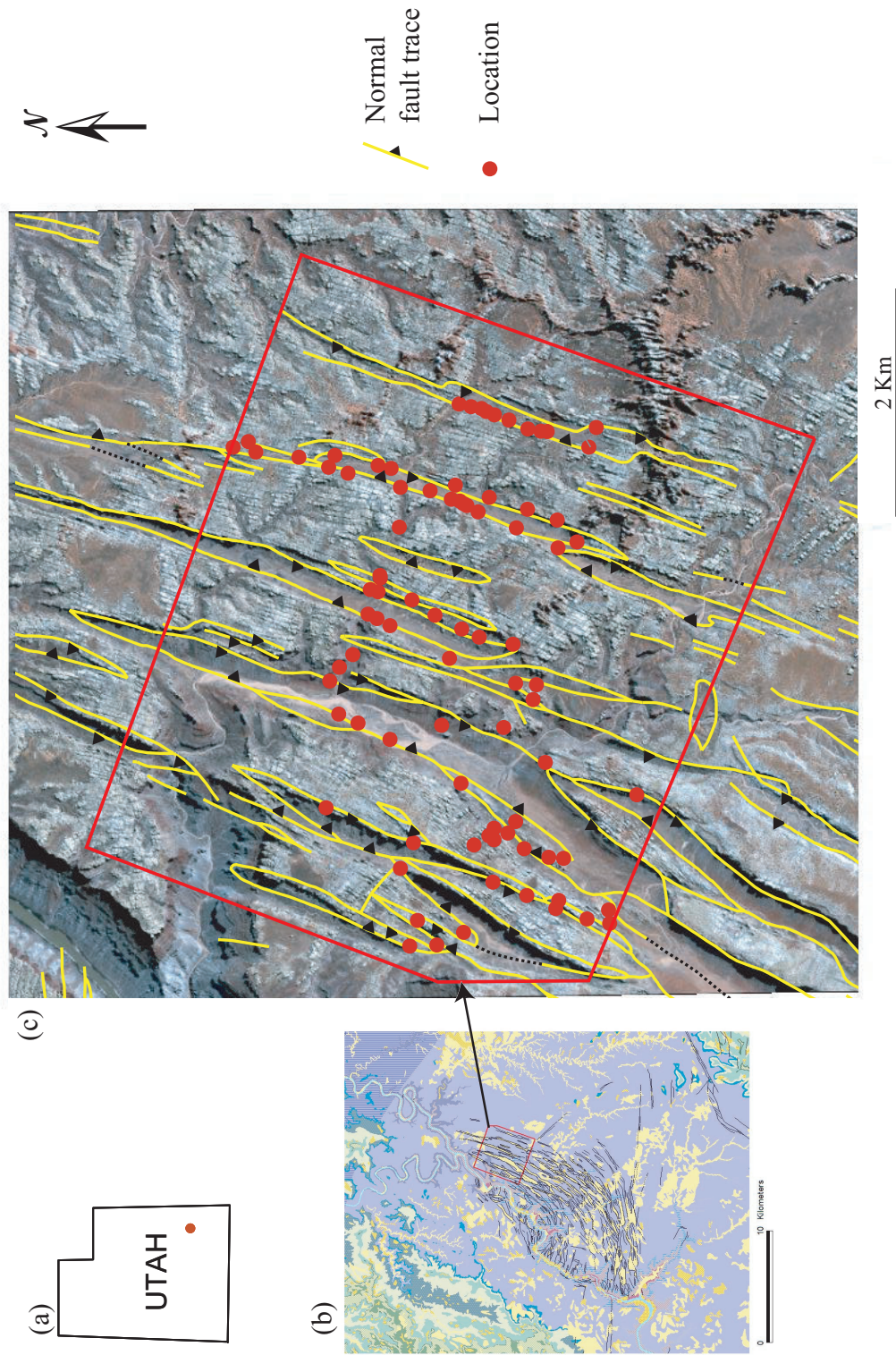


Figure 4.2. (a) Location of Canyonlands needles district in Utah. (b) General geologic map of the study area, red boundary showing the extent of the study area. (c) Location of fracture data measurement on 60cm resolution Quickbird image. The yellow lines on the image indicate traces of normal faults in the area, acquired from Utah geological survey, (Hintze et al., 2000)

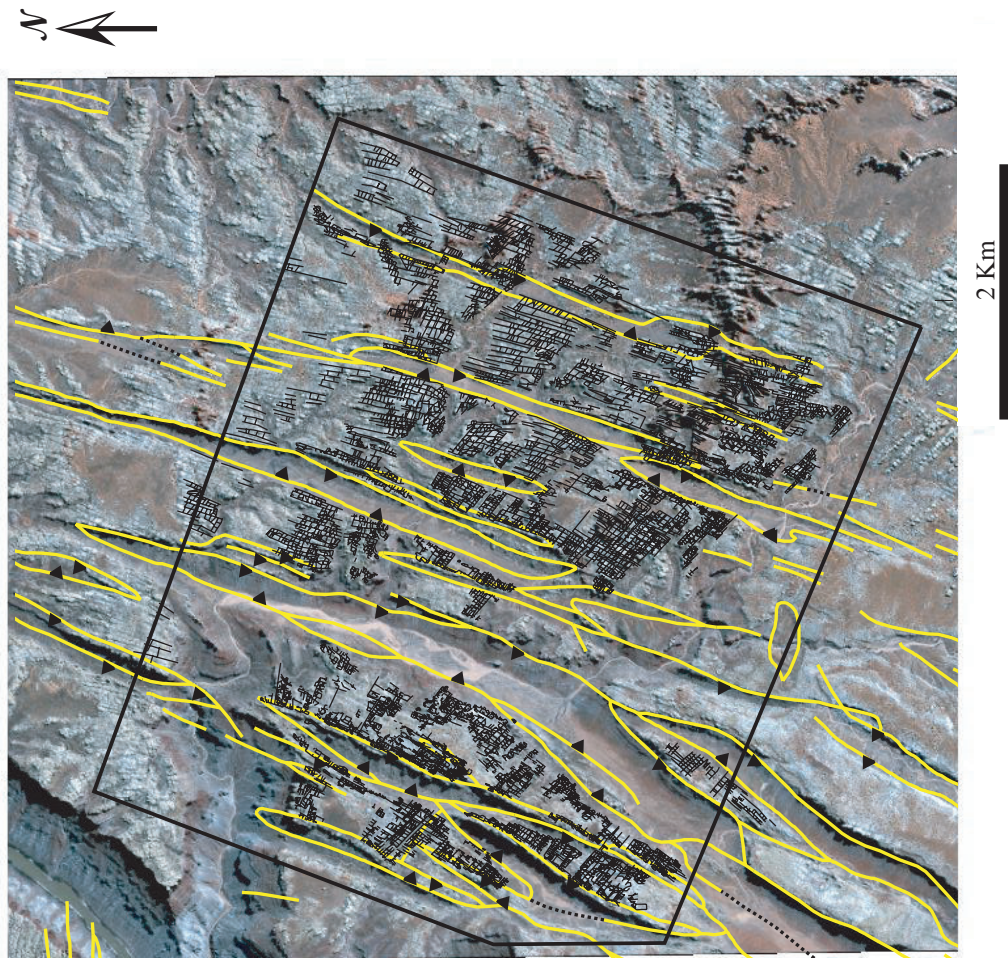


Figure 4.3. Fractures mapped on 60cm resolution Quickbird image. The yellow lines on the image indicate traces of normal faults in the area, acquired from Utah geological survey, (Hintze et al., 2000)

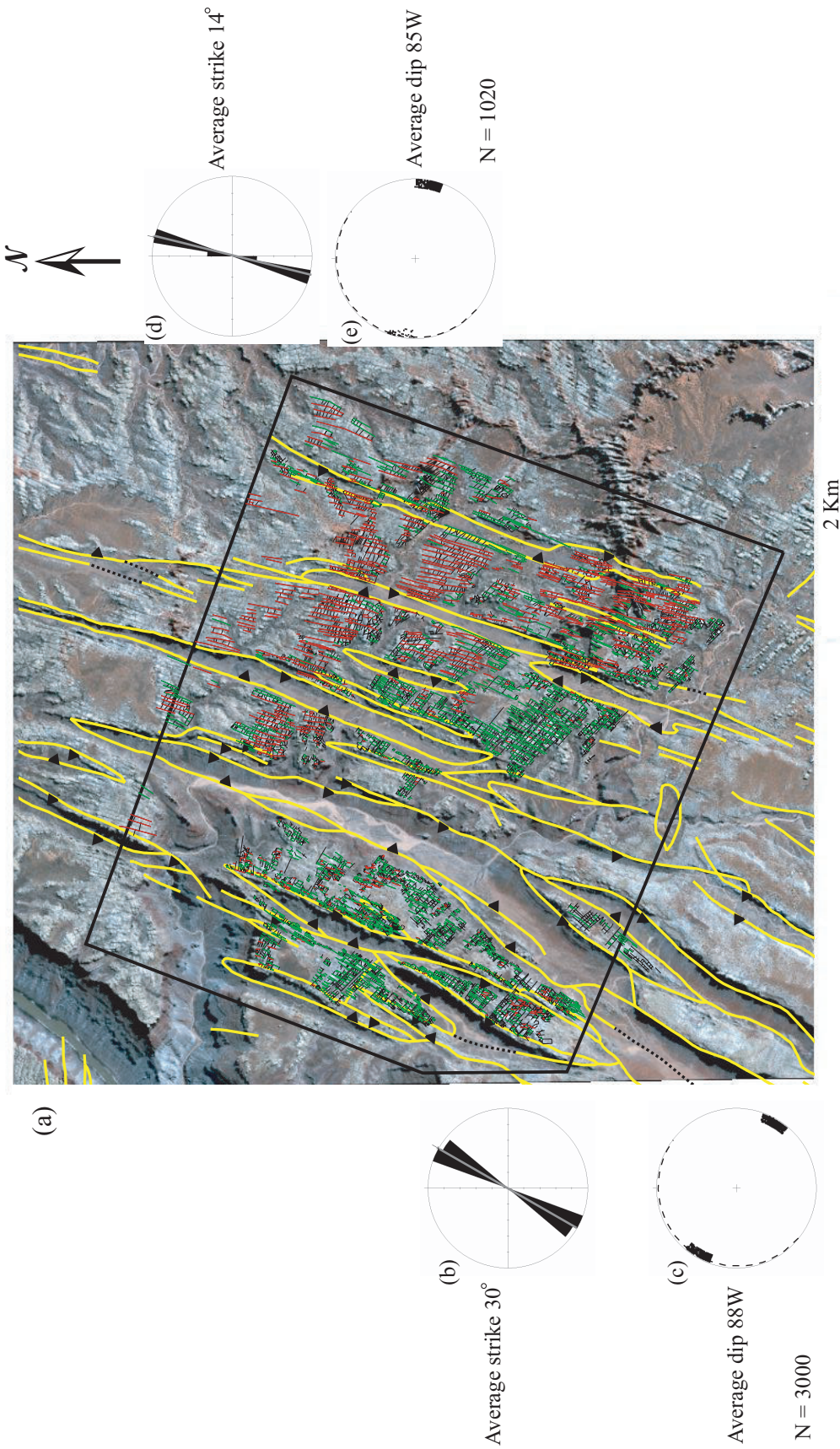


Figure 4.4. Fractures mapped on 60cm resolution Quickbird image. The yellow lines on the image indicate traces of normal faults in the area, acquired from Utah geological survey, (Hintze et al., 2000). Red lines indicating fractures striking 14° and green lines indicating fractures striking 30°. (b) Rose diagram showing strikes of 30° set. (c) Equal area stereographic plots showing poles to planes of 30° set. (d) Rose diagram showing strikes of 14° set. (e) Equal area stereographic plots showing poles to planes of 14° set.

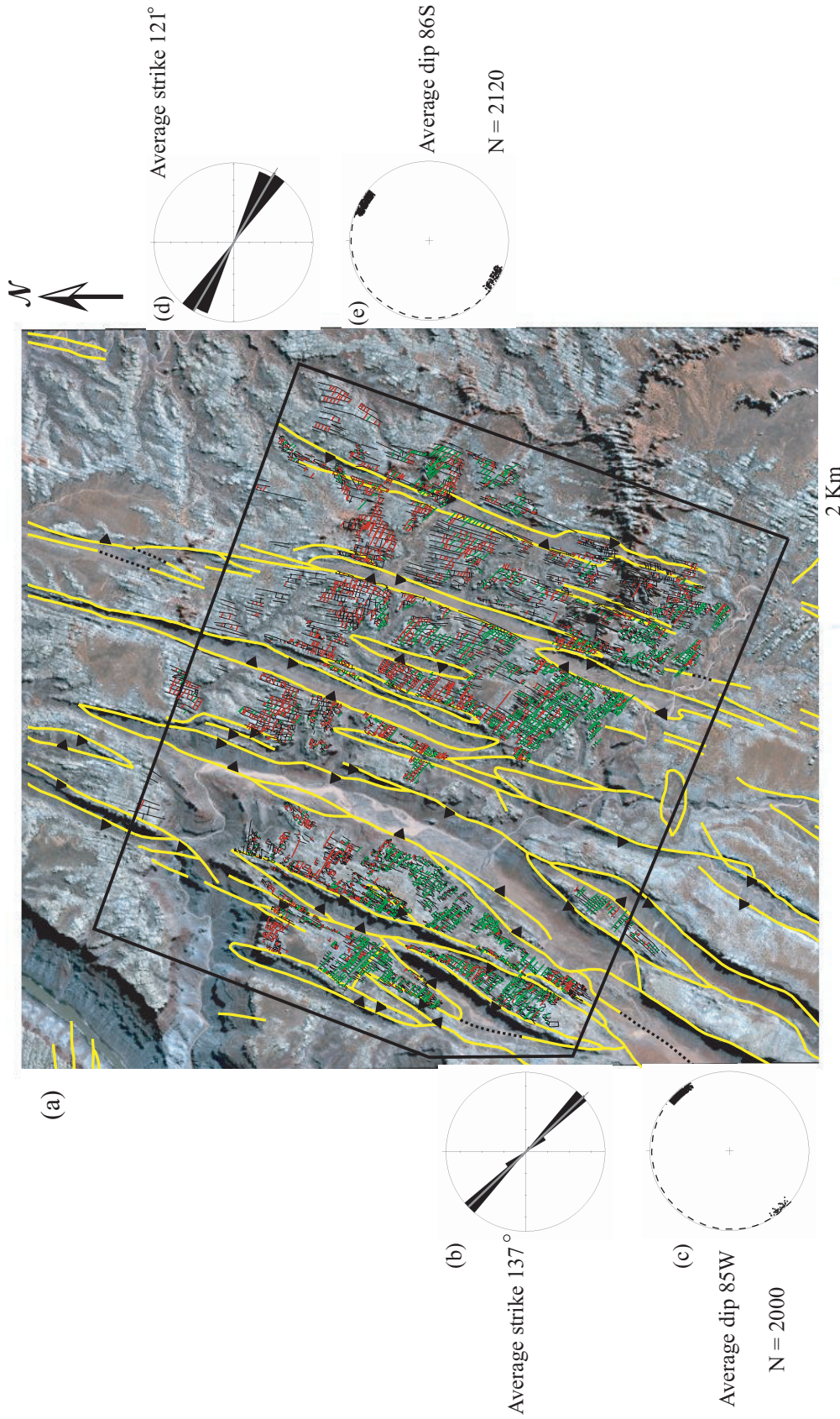


Figure 4.5. Fractures mapped on 60cm resolution Quickbird image. The yellow lines on the image indicate traces of normal faults in the area, acquired from Utah geological survey, (Hintze et al., 2000). Red lines indicating fractures striking 121° and green lines indicating fractures striking 137°. (b) Rose diagram showing strikes of 137° set. (c) Equal area stereographic plots showing poles to planes of 137° set. (d) Rose diagram showing strikes of 121° set. (e) Equal area stereographic plots showing poles to planes of 121° set. N: Number of fractures

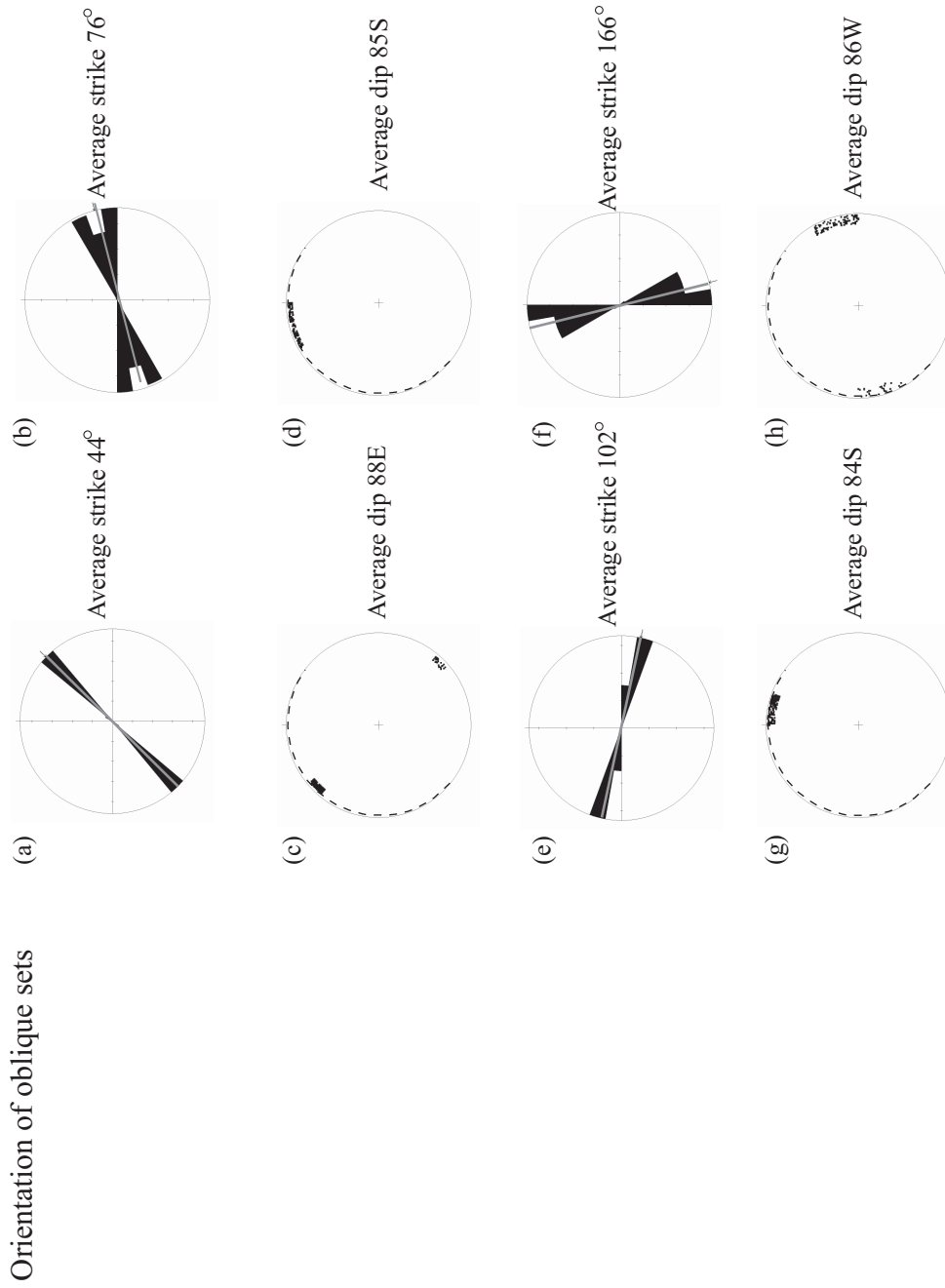


Figure 4.6 Orientation of oblique sets. a-b. Rose diagrams showing the strikes of (a) 44° and (b) 76° fracture set. c-d. Equal area stereographic plots showing poles to planes of fractures and great circle for bedding. (c) 44° (d) 76° fracture. e-f. Rose diagrams showing the strikes of (e) 102° and (f) 166° fracture set. g-h. Equal area stereographic plots showing poles to planes of fractures and great circle for bedding. (g) 102° (h) 166° fracture set.

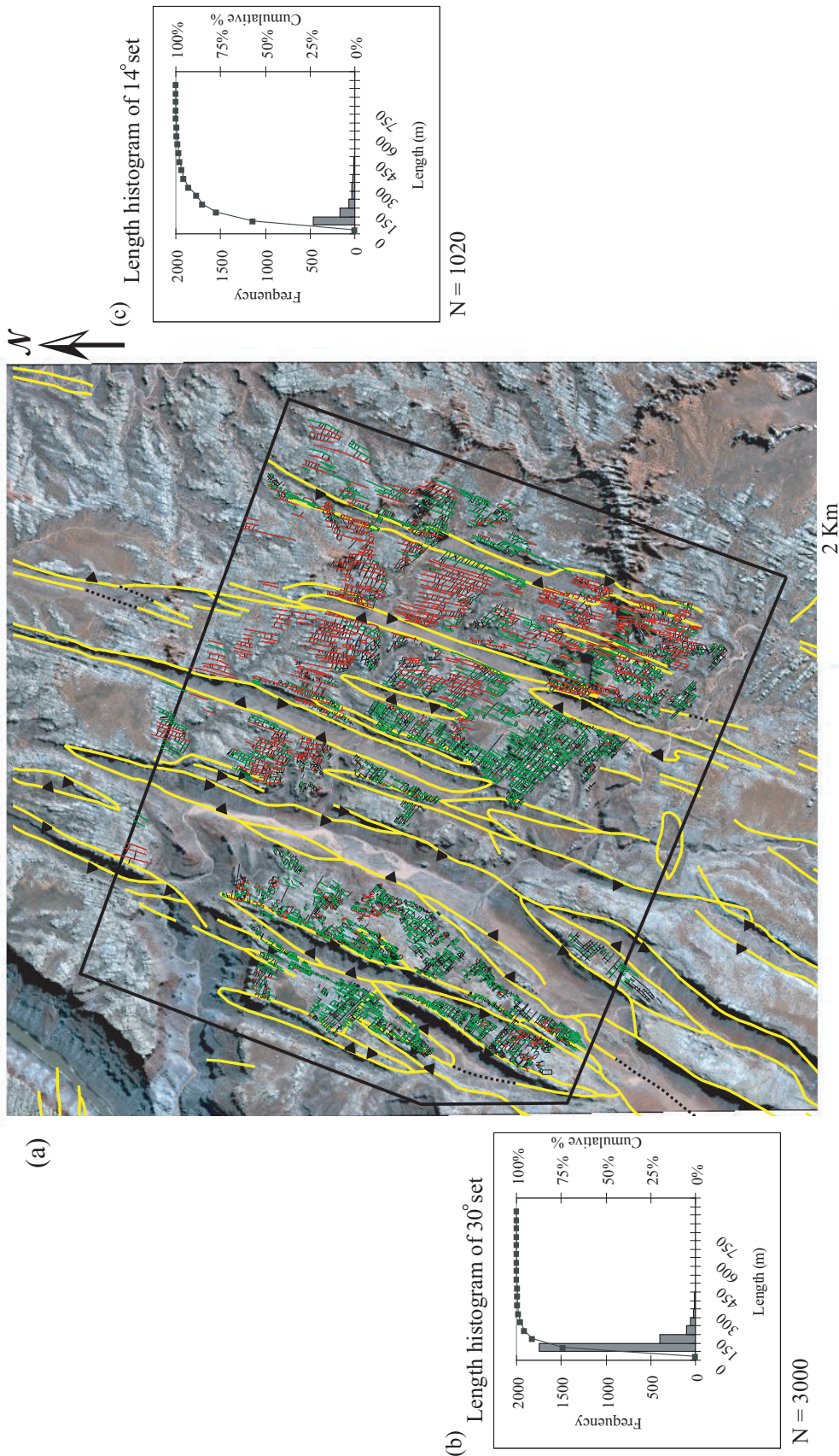


Figure 4.7. Fractures mapped on 60cm resolution Quickbird image. The yellow lines on the image indicate traces of normal faults in the area, acquired from Utah geological survey, (Hintze et al., 2000). Red lines indicating fault parallel fractures striking 14° and green lines indicating fault parallel fractures striking 30°. (b) Length histogram of 14° set. (c) Length histogram of 30° set.

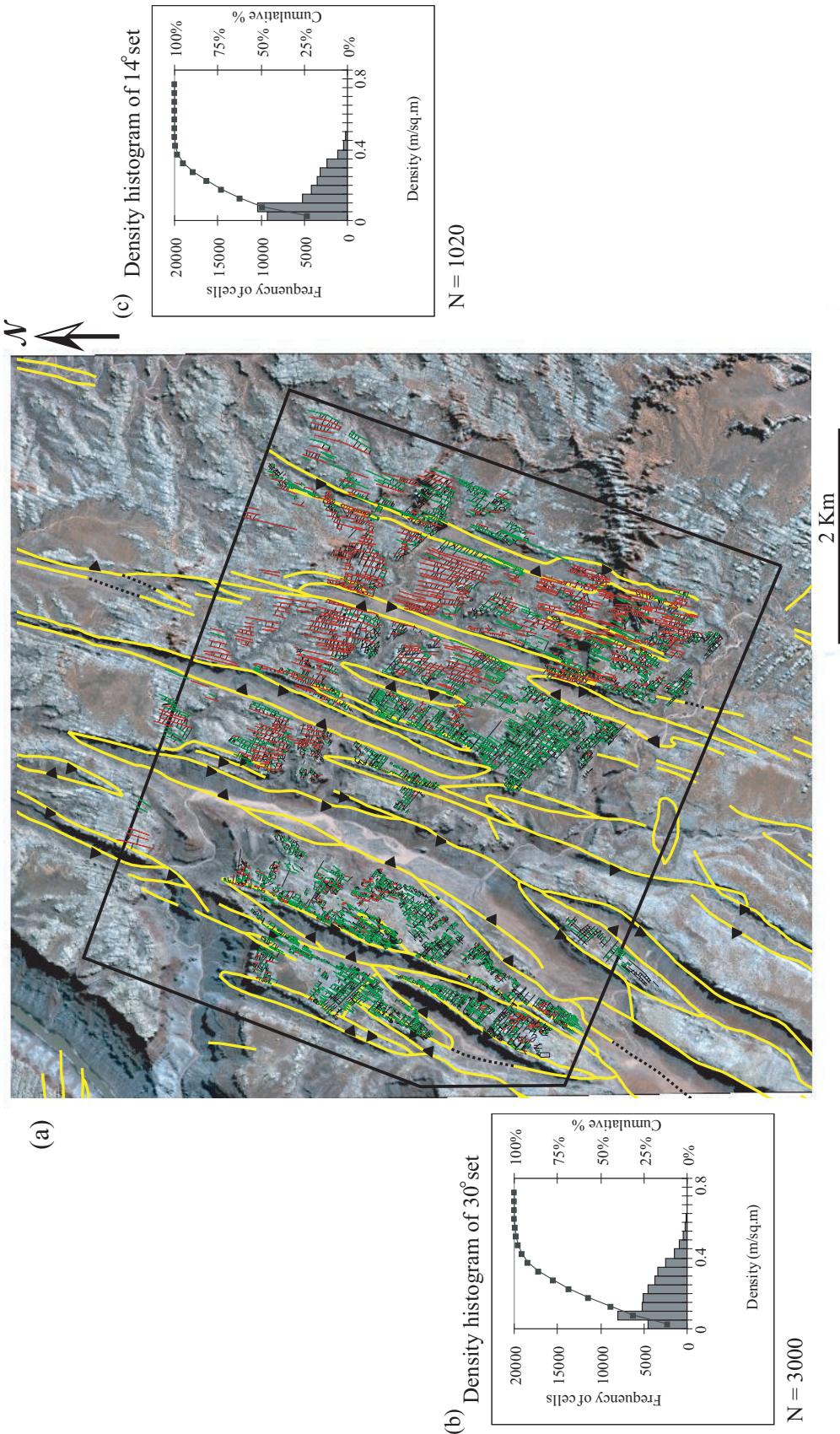


Figure 4.8. Fractures mapped on 60cm resolution Quickbird image. The yellow lines on the image indicate traces of normal faults in the area, acquired from Utah geological survey, (Hintze et al., 2000). Red lines indicating fault parallel fractures striking 14° set and green lines indicating fault parallel fractures striking 30° set. (b) Density histogram of 14° set. (c) Density histogram of 30° set.

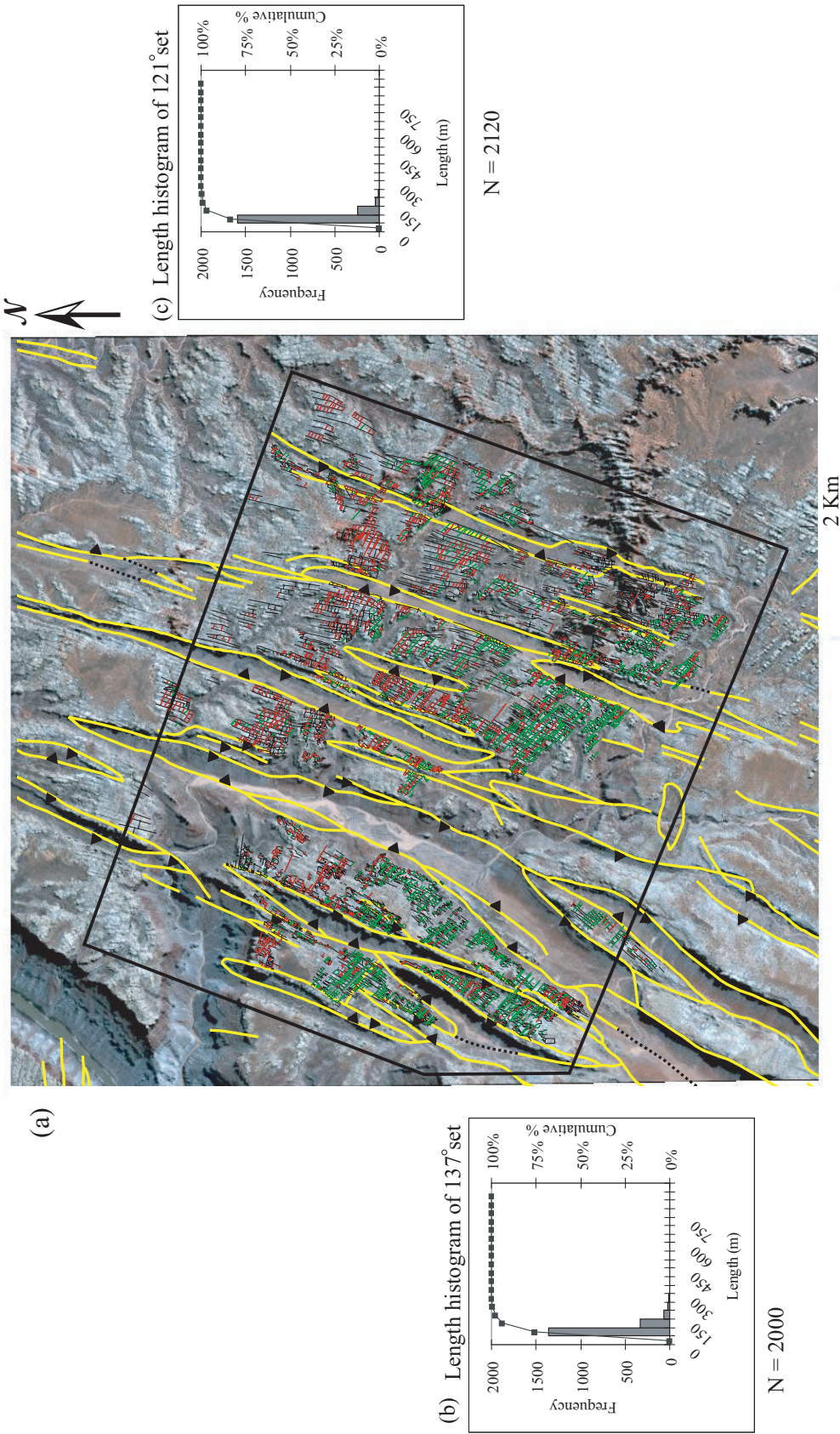


Figure 4.9. Fractures mapped on 60cm resolution Quickbird image. The yellow lines on the image indicate traces of normal faults in the area, acquired from Utah geological survey, (Hintze et al., 2000). Red lines indicating fault normal fractures striking 121° and green lines indicating fault normal fractures striking 137°. (b) Length distribution of 137° set. (c) Length distribution of 121° set. N: Number of fractures

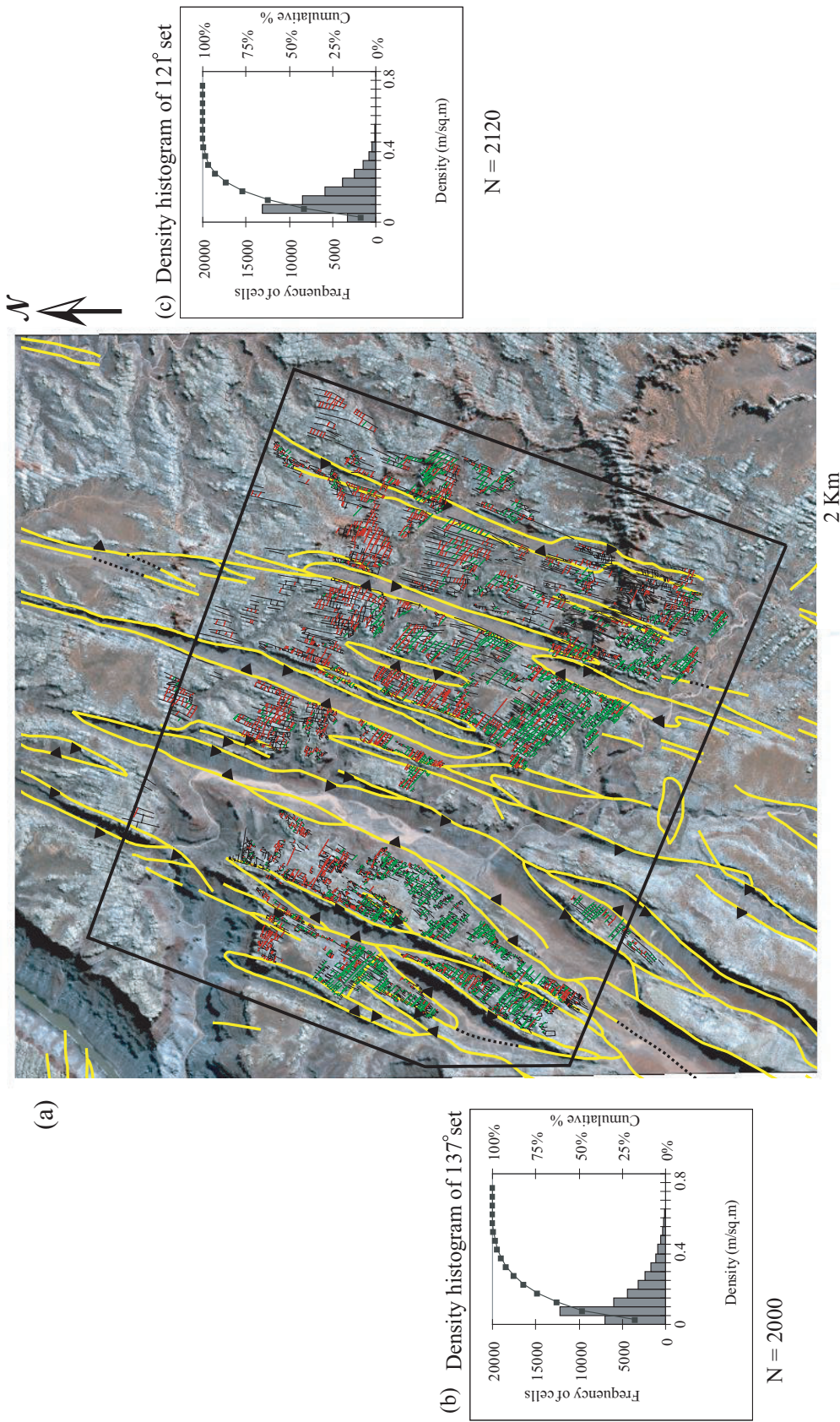


Figure 4.10. Fractures mapped on 60cm resolution Quickbird image. The yellow lines on the image indicate traces of normal faults in the area, acquired from Utah geological survey, (Hintze et al., 2000). Red lines indicating fault normal fractures striking 121 and green lines indicating fault normal fractures striking 137. (b) Density distribution of 137° set. (c) Density distribution of 121° set. N: Number of fractures

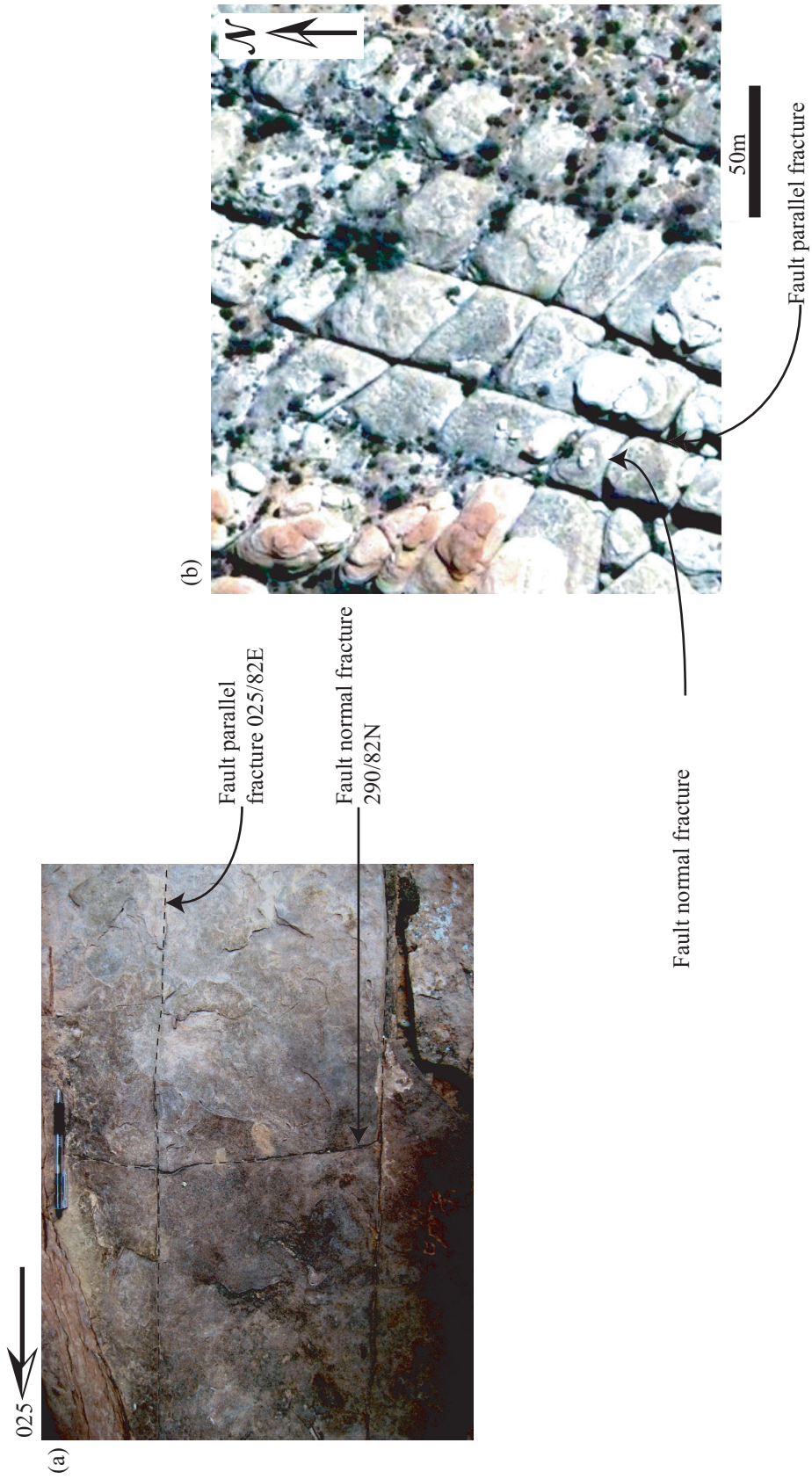


Figure 4.11 Fault parallel and fault normal fractures exposed on the surface of an interlayer within Cedar Mesa sandstone. Pen (15cm) in photograph for scale. Point to note is that the termination of fault normal fracture against fault parallel set. (b) Same relation of termination is observed in remotely sensed image.

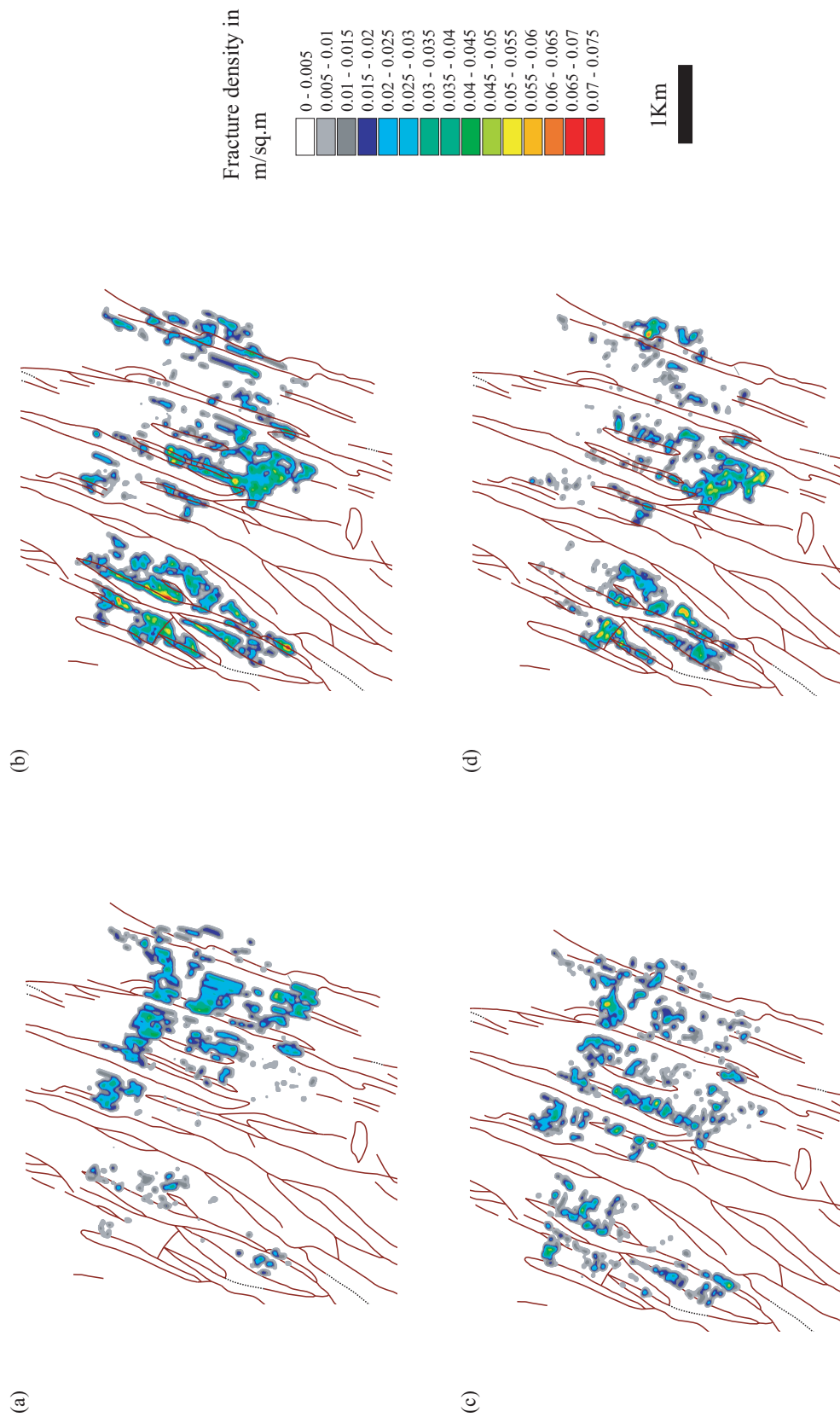


Figure 4.12. Map showing density distribution of fault parallel and fault normal fracture set. (a) Fault parallel (14°) fracture set (b) Fault parallel (30°) fracture set (c) Fault normal (121°) fracture set and (d) Fault normal (137°) fracture set.

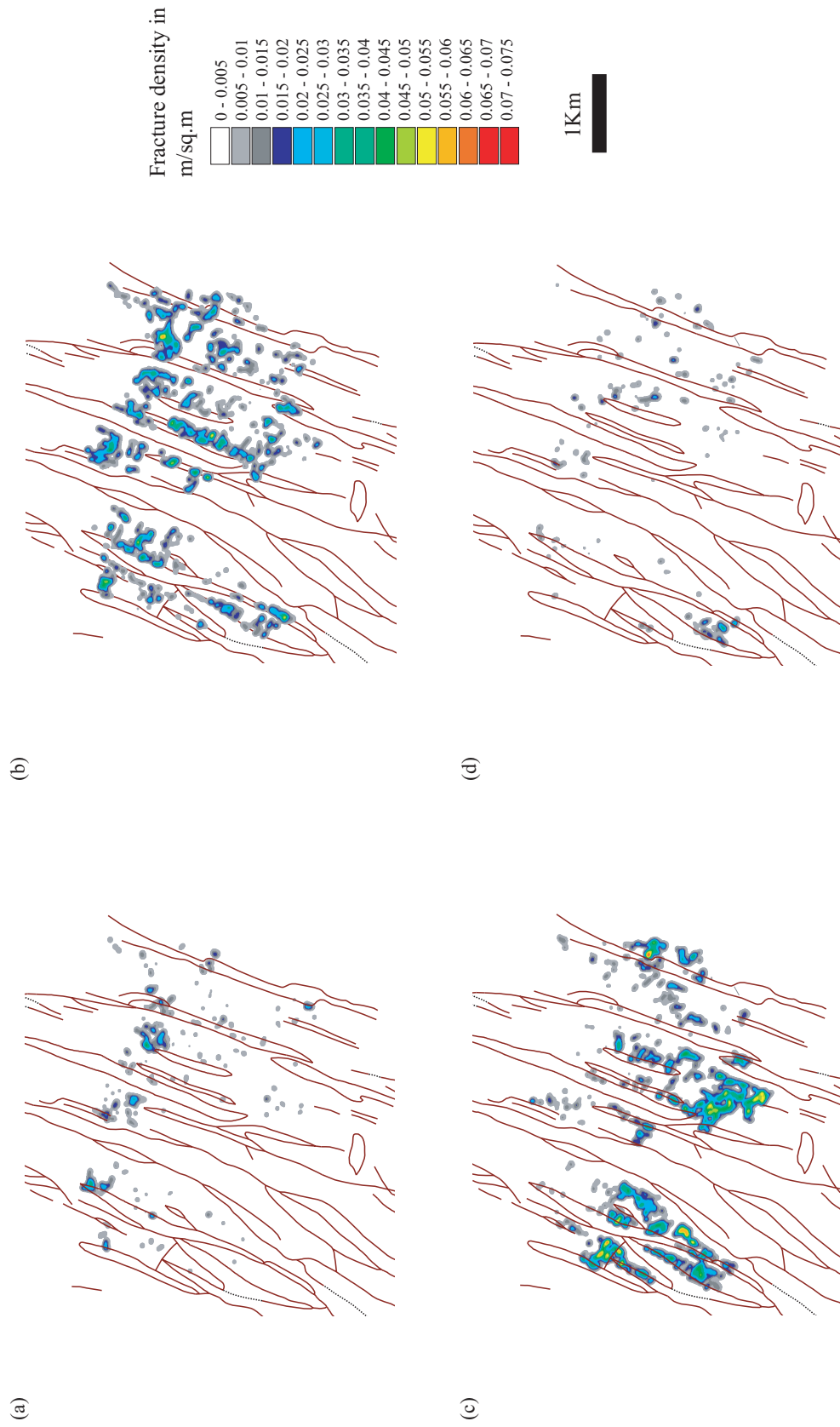


Figure 4.13. Map showing density distribution (a) 44° fracture set (b) 76° degree fracture set (c) 102° fracture set and (d) 166° fracture set.

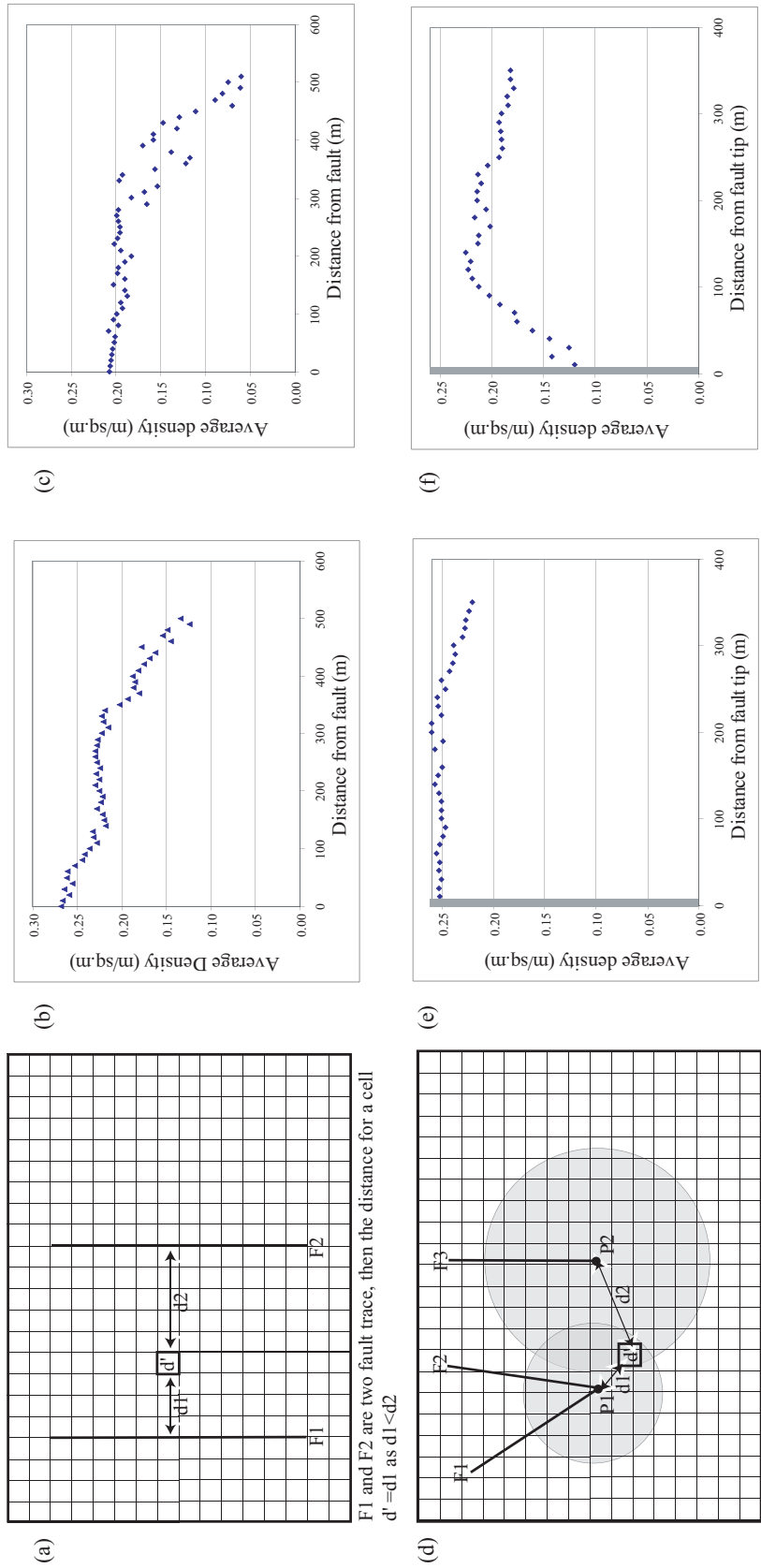


Figure 4.14. (a) Schematic diagram showing distance calculation from fault traces. (b) Plot of fault parallel fracture Density against Distance from nearest fault. (c) Plot of fault normal fracture Density against Distance from nearest fault. (d) Schematic diagram showing distance calculation from fault intersection and/or tip. (e) Plot of fault parallel fracture Density against Distance from nearest fault tip; gray area marks the no-data region. (f) Plot of fault normal fracture Density against Distance from nearest fault tip; gray area marks the no-data region.

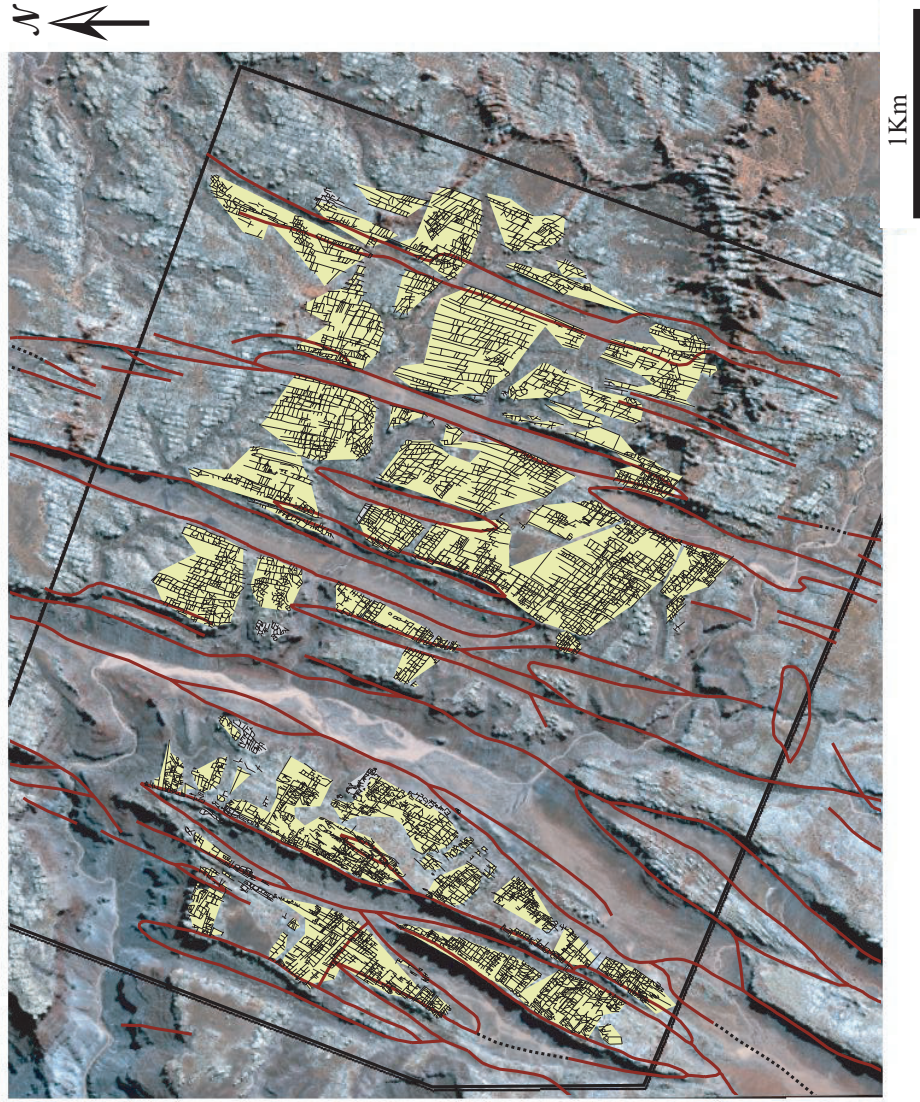


Figure 4.15. Fracture connectivity patterns in Canyonlands area. The yellow polygons represent the connected area, the red lines are traces of normal faults, and the black lines are the traces of connected group of fractures.

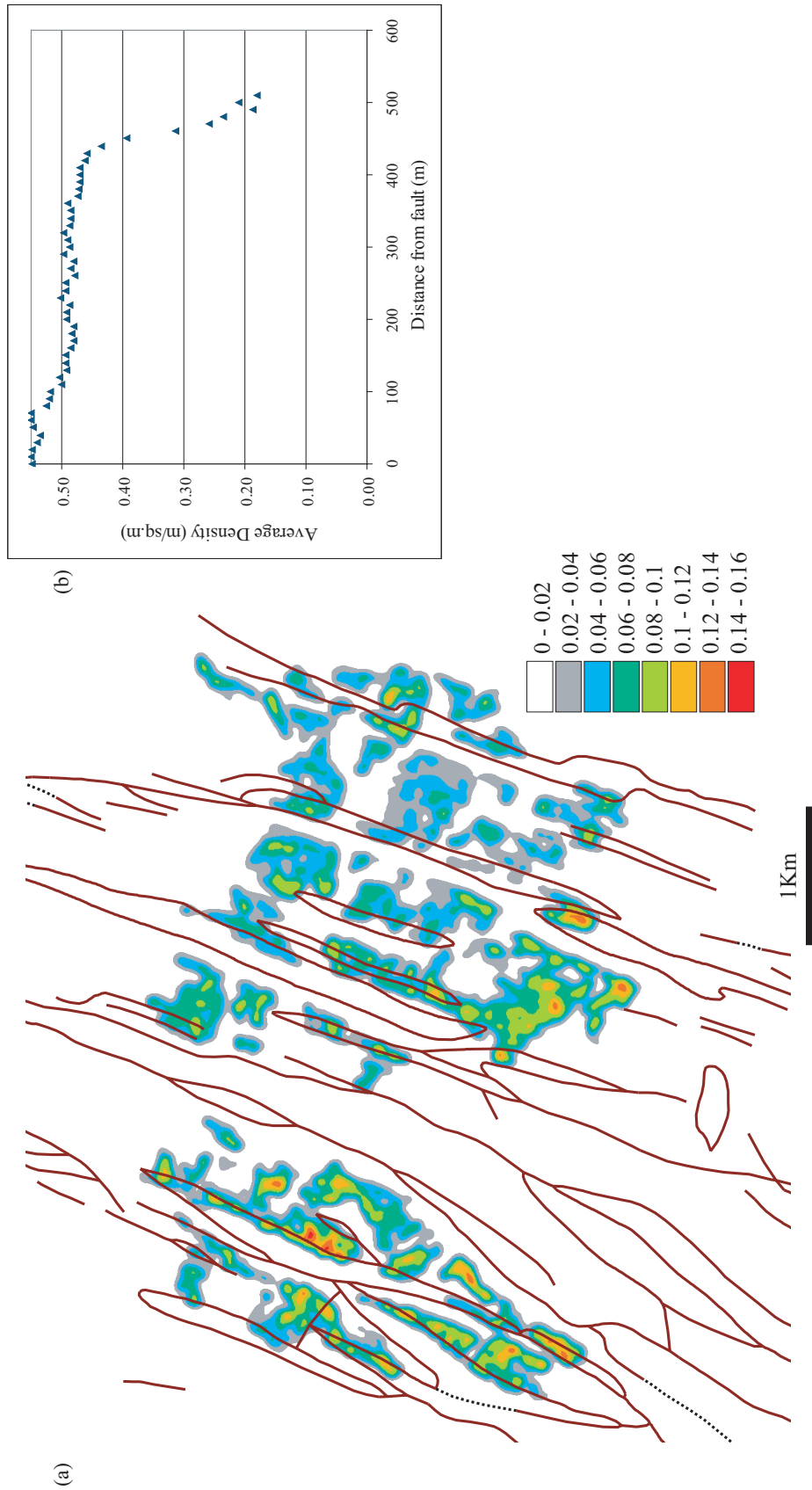


Figure 4.16. (a) Map showing density distribution of connected fractures (b) Plot showing Fractional connected length (connected fracture density) against Distance from normal fault

CHAPTER 5:

FRACTURE CONNECTIVITY

5.1 INTRODUCTION

5.2 APPROACH

5.3 METHODOLOGY

5.4 SINGLE FRACTURE SET

5.5 TWO FRACTURE SETS, ONE SET DOMINANT

5.6 TWO FRACTURE SETS, BOTH SET VARYING

5.7 CONNECTIVITY PATTERN FROM OUTCROP

EXAMPLES

5.8 CONCLUSIONS

5.1 Introduction

Fluid flow in fractured rocks is controlled by an interconnected pattern of conductive fractures. Therefore, the identification and characterization of the key parameters that influence the connectivity of fracture networks is important in understanding the patterns of fluid flow in fractured rocks. In most fractured reservoirs, the flow is predicted based on dual permeability models that incorporate the matrix and fracture permeabilities. The fracture permeability is usually the more dominant component, so that an accurate prediction of this component is important in developing a successful model.

The fracture permeability is determined by only a small fraction of fractures within a fracture system that are interconnected to form a continuous permeable network. Due to limited subsurface data availability, it is difficult to build precise reservoir models with explicit information about the fracture geometry, so that the fracture geometry is usually summarized by a limited number of parameters. Therefore, it is critical to know the fracture parameters that have the most dominant influence on connectivity of the fracture network.

The problem can be addressed using multiple approaches. First detailed analysis of fractured outcrops can provide surface analogues which can be used to model subsurface reservoirs. Second, simulations of fracture networks can be conducted for different scenarios to predict the influence of different parameters in controlling fracture connectivity.

In this section a detailed study of fracture networks is conducted to investigate the evolution of fracture connectivity with varying geometric properties. A series of simulated fracture maps are generated to identify the factors influencing connectivity of fracture systems.

5.2 Approach

Fracture connectivity is sensitive to the geometry and characteristics of individual fractures. Connectivity also depends on the spatial distribution of different fracture sets (Balberg and Binenbaum, 1983; Balberg et al., 1991; Odling et al., 1999). Increasing fracture propagation leads to the formation of clusters or connected fractures. Field studies (Rouleau and Gale, 1985; Odling, 1992, 1993, 1997; Gillespie et al., 1993; Bloomfield, 1996; Castaing et al., 1996) suggest that connectivity and clustering are dependent on fracture lengths, densities, dispersion, and spacing. In general, connectivity increases as (1) an increasing number of fractures of the same set are added to the system, (2) the length of the fractures increases (3) the orientation of fractures in a set exhibits a higher degree of dispersion, or (4) fractures of multiple sets are added to the system.

A series of fracture simulations are modeled to investigate the influence of all four characteristics on the fracture network, and to identify the relative contribution of each factor towards network connectivity. All simulations are

conducted in two-dimensions, and all simulated fractures are assumed to be open and have the same length/aperture ratio. In real situations, some fracture sets will be more conductive than others, but this factor is not considered in the simulations. Because the combination of the key parameters can result in an almost infinite number of possibilities, only three specific settings that relate to real observations are considered.

The simulations are compared to natural examples of natural fractures seen in outcrops and also with published fracture maps gathered to establish the effects of different fracture parameters on connectivity in natural fracture systems. Integration of simulated fracture maps with surface analogues of natural fracture system provides an overview of the fracture geometry and interaction of a range of fracture systems.

5.3 Methodology

GIS based software is used to simulate 2D fracture maps within a constant area in this study. The simulation was conducted for three main types of fracture systems (Figure 5.1): (1) A single fracture set with varying length, spacing and angular dispersion; (2) Two sets of fractures with one dominant set of fracture of constant length and spacing, and a second set with varying lengths, spacing and orientations connecting the dominant set of fractures; and (3) Two sets of fractures, with both sets varying in length, density and orientation. In the past,

connectivity has been quantified by cluster size (Odling, 1997), which measures the length of the largest connected group of fractures as a proportion of the total fracture length in the network. In this study, the extent of clustering and connectivity is measured by the fractional connected area (FCA) defined as:

$$\text{FCA} = \frac{\text{Summed area of all connected clusters within the fracture network}}{\text{Total Sample Area}}$$

This parameter provides a measure of the extent to which the fractures within the system can drain the area in question. The simulated results are then compared to identify the influence of critical parameters on fracture connectivity.

5.4 Single fracture set

Straight line segments are generated at multiple stages to study influence of length, spacing and dispersion on fracture connectivity for a single set of fractures within a square area bounded by sides of length 1 (figures 5.2, 5.3, 5.4). The length and spacing of fracture are normalized by the side of the square, 1. At each stage, two of the three parameters are held constant and the third parameter is varied at regular intervals. Normalized length L^* ($=L/1$) is varied from 0.1 to 0.3 at an increment of 0.05, spacing is varied from 0.025 to 0.25 at an increment of 0.025 and dispersion is varied from 10 to 30° at increment of 5°.

For all the simulated fracture maps fractional cluster area is calculated to investigate the variation of connectivity with varying fracture parameters.

Furthermore, critical combinations of parameters at which complete connectivity is achieved (a) in the direction parallel to the average fracture trend and (b) in the direction perpendicular to the average fracture trend are studied.

For single fracture set of fractures a minimum dispersion of 10° is necessary to establish connectivity for most combinations of fracture lengths and spacing. Connectivity in a direction parallel to the average fracture orientation is most dependent on the lengths of the fractures, with good connectivity established at normalized lengths of 0.3, independent of the fracture spacing. This is an important consideration for natural fractures systems involving a single set of fractures.

Connectivity in directions both parallel and transverse to the fracture set requires the intersection of the independent fracture swarms through an optimum combination of dispersion, normalized length and normalized spacing. The relation between orientation, dispersion, minimum length and spacing of fracture networks required to trigger connectivity in lateral direction can be prescribed using the following equation:

$$L^* = S^*/\sin(\theta/2)$$

Where L^* is the minimum normalized length required for connectivity in lateral direction, S^* is the normalized spacing and θ is the angular dispersion within a single set of fractures.

The variation in the fractional connected area resulting from the simulations is displayed as plot of normalized spacing versus connectivity for different normalized lengths and dispersions, in figure 5.5. The value of the fractional connected area increases with increasing normalized length and dispersion, and decreasing spacing. The simulations with higher lengths and greater dispersions always result in higher fractional connected areas. The fractional connected area increases dramatically, when the fracture networks extend connectivity in the perpendicular direction. Therefore, the most critical factor appears to be the normalized spacing of the fractures. Significant connectivity is only attained when the normalized spacing drops below 0.1. Furthermore, the fractional connected area increases in a non-linear fashion below this spacing. Total connectivity is only attained below values of $S^* = 0.1$, except for very high dispersions.

5.5 Two fracture sets, one set dominant

In natural fracture system, two sets of fractures, with one systematic set and one less dominant set of cross fractures are commonly observed (Josnin et al., 2002, Rohrbaugh et al., 2002, Finn et al., 2003). The systematic set of fracture is a more planar, consistent in orientation and considerably greater in trace length due to earlier timing of formation (Finn et al., 2003). The cross fracture set, which

forms later, is limited in trace lengths and is generally confined between fractures of the pre-existing set.

To study the interaction of systematic fracture set and a second set of cross fractures at various orientation and length, two set of fractures were simulated by generating a series of equally spaced cross fractures between a set of systematic fractures that cross the entire sample area and have a constant spacing (S^*) of 0.1. A series of simulated fracture maps were generated by varying the length and orientation of cross fractures. Lengths of cross fractures were gradually increased until the fractures intersected the systematic fractures. The angle between the systematic fracture set and the cross fracture set varied from 15 to 90°. The strike of cross fractures had a dispersion of 4 to 5°. Connectivity of the fracture network for each orientation of cross joints was triggered at a certain length, i.e., the fractional connected area and cluster size yielded a value greater than 0; subsequently, the network became completely connected in both directions yielding a fractional connected area of 1 and finally at a greater length, all the fractures contributed to the connected network when the cluster size became 1. The length at which the fractional connected area and cluster size became greater than 1, and the length at which all the fractures became connected were unique different angles between the two fracture sets (figures 5.6 and 5.7).

The critical length of the cross fracture required for maximum connectivity is given by:

$$L^*_{X_{\max}} = S^*_1 / \sin\theta_{\min}$$

and the critical length of the cross fracture required to trigger fracture connectivity in a network is given by:

$$L^*_{X_{\min}} = S^*_1 / \sin\theta_{\max}$$

where L^*_x is the critical length of cross fracture, S^*_1 is the spacing of systematic fracture and θ_{\min} and θ_{\max} are minimum and maximum angle between the systematic and cross fracture, respectively. The table below summarizes the maximum and minimum acute angle for each set of cross fractures generated in the simulation and the expected range of length for which the network will achieve complete connectivity.

Table 5.1: Summary table of acute angle between systematic and cross fracture orientation (θ) (in degree) and the critical length (L_x) (in meter) of cross fracture.

The spacing between systematic fractures is constant at 1m.

θ_{\min}	θ_{\max}	Sin θ_{\min}	Sin θ_{\max}	$L_{X_{\max}}$	$L_{X_{\min}}$
15	19	0.26	0.33	3.86	3.07
30	34	0.50	0.56	2	1.79
45	49	0.71	0.75	1.41	1.33
60	64	0.87	0.90	1.15	1.11
75	79	0.97	0.98	1.04	1.02

90	94	1.00	1.00	1.00	1.00
----	----	------	------	------	------

The variation in fractional connected area and cluster size is shown against length for different angles between the two fracture sets. These maps show the dramatic change in connectivity at unique points (Figure 5.8a-f). Cross plot of angle between cross fracture and systematic fracture versus critical length at which the complete connectivity is attained is shown in figure 5.8g. The plot shows that the critical length for connectivity increases with a decrease in the angle between the systematic fractures and the cross fractures.

5.6 Two fracture sets, both set varying

Connectivity patterns of fracture networks where at least one set of fractures is systematic are relatively simple as the systematic fracture set provides the basic framework and presence of cross fractures enhance the connectivity in the lateral direction, i.e., in the direction perpendicular to systematic fractures. In areas where neither of the fracture sets are systematic, the fracture network yields complex connectivity patterns which are controlled by a combination of parameters of all the sets. A series of simulation is performed with two sets of fractures in which the density and length of both sets are changed systematically. In the first series of examples, two orthogonal sets of fractures are generated (figure 5.9-5.10) and then in the second series, the angle between the fracture sets

is reduced to 45° (figure 5.11-5.12). In all simulations, the length of one set is held constant, while the length of the other set and the density of both sets is increased systematically.

The results show increases in fracture connectivity with length, density, and an increase in the angle of intersection of the two sets. Graphical representation of results (figure 5.13) reveals that the increase in density of one set had a dramatic effect on connectivity when the length of the other set was short (0.1), while the change in connectivity was more subtle to insignificant when the length of the other set is long (0.3). The slope of curves for two series of simulations, are comparable, indicating that the effect of length and density on both the series are similar, but the absolute value of connectivity yielded by the networks is different. The orthogonal set of fractures yielded higher connectivity compared to fractures at a 45° angle of intersection, and the difference in connectivity values is greater at lower length and/or density.

5.7 Connectivity pattern from outcrop examples

The results of fracture simulation are compared to natural fracture to investigate the effects of spatial distribution of natural fractures on fracture network parameters. Although the simulated fractures are more uniformly distributed spatially, fracture geometries observed in several different outcrops exhibit patterns similar to those generated through fracture simulation. Examples

of natural fracture patterns from various sources ranging from personal field work to information gathered from published literature were used in this study.

Single fracture set

Fractures on the bedding surface of the Tensleep Formation (figure 5.14a) in the forelimb of Sheep mountain anticline (Bellahsen et al., 2006) exhibit a single set of ENE-WSW fracture with 10° dispersion in strike and average normalized spacing of 0.05 (approx.) and average normalized length of 0.24 (approx). The point to note in this photograph is that the fractures have low connectivity (fractional connected area of 0.06), and the connectivity is manifested only along the strike of the fractures. Despite the low spacing and high length due to the uniform sub-parallel orientation of the fractures, there is no connectivity in the direction perpendicular to the fractures because of the low dispersion, hence resulting in a low fractional connected area of 0.06. This result is consistent with the fracture simulation achieved a similar spacing, length and orientation dispersion exhibited in figure 5.14c with similar length, spacing and orientation dispersion and a low connectivity of 0.05.

Figure 5.14d-e shows an example of fractures in the Late Namurian (Carboniferous), Upper sandstone Group at Telpyn Point, Wales, U.K. There are several sets of fractures, but the most dominant set is a NS set with a strike dispersion of 13°, average normalized length of 0.21 and normalized spacing of

0.02. The map shows a clustering of fractures in the central part of the study area, where the fractures are much closely spaced ($S^* = 0.016$), whereas on either side, the spacing is 0.021. Connectivity of the NS set is extracted for the whole map. Fractional connected area for the entire study area yielded by the NS set is 0.1, but in the central part of the study area where the fractures are closely spaced ($S^*=0.016$), and the dispersion is higher, the fractional connected area is 0.35. This is because the close spacing and higher dispersion of the fractures triggers lateral connectivity that resulted in a higher total connectivity. However, the low dispersion of fracture orientations prevented complete connectivity in the area. This example establishes the fact that a single set of fracture can furnish connectivity where the fractures are closely spaced and there is dispersion in orientation significant enough to overcome the spacing.

Two fracture sets, one set dominant

Multiple sets of fracture increases the chances of connectivity. An example of fractures from Lompoc landing (Figure 5.15), California illustrates this fact. All the fractures in the figures are from the same outcrop, different sets of fractures are illustrated separately to demonstrate the contribution of systematic and cross fractures towards enhancing the connectivity. In Figure 5.15a-b, there are two sets of fractures, a NE set of average normalized length of 0.07 and dispersion 10° and a NNW set of normalized length 0.05 and dispersion 4° . These

two fracture sets form a few clusters yielding a fractional connected area of 0.024. None of the individual clusters are extensive enough to connect the entire study area. In figure 5.15c-d, the east-west striking systematic fractures are long and extensive, and connect the opposite ends of the study area in the E-W direction. The average normalized length of EW set is 0.3 and the dispersion 30° . Due to the extensive length and higher dispersion, the network yielded fractional connected area of 0.41, but the connectivity is extended only along the strike of the fractures and the clusters still do not connect the entire area. In figure 5.15d-e, all the fracture sets together yielded a fractional connected area of 1 and formed a continuous fracture network that cover the entire study area. This example illustrates that although the secondary sets have very low lengths and high spacing, that because they are at two sets are at high angles to the systematic set, the dramatically increase the connectivity to cover the entire area.

Examples of two sets of fractures with a set systematic fractures connected by a perpendicular set of cross fractures are observed in several outcrops. Figures 5.16 show two examples, from the Nashpoint limestone, Wales (figure 5.16a-b) (Josnin, et. al., 2002), and from the Jurassic limestone formation of Llantwit Major, Wales (figure 5.16c) (Rohrbaugh et. al., 2002).

Fractures in Nashpoint limestone consist of two orthogonal sets of fractures (figure 5.16a-b). In this example the NS fractures striking 175° are much longer (average length =0.4) compared to the EW fracture striking 88° (average

length = 0.28m) and also the NS set is more closely spaced (spacing = 0.02). This is an example where one set (NS set) is a systematic set of fracture extending across the study area, whereas an orthogonal set of cross fractures (EW set) is contributing toward enhancing the lateral connectivity, thus leading to a fractional connectivity of 1.

A similar case is observed in the pavement of limestones within the early Jurassic Porthkerry Formation (Figure 5.16c; (Rohrbaugh, et al., 2002). In this example there are two orthogonal sets, with one systematic set striking 165° and a cross set striking 75° . The fracture network exhibits complete connectivity, due to the high angle between the two sets, in spite of the short lengths and relatively high spacing of the second set. A simulation is shown in Figure 5.16d, where the network exhibits complete connectivity even though second set (cross fractures) were of short length and high spacing.

Figure 5.17a-b, exhibits fractures on the flank of Salt Valley Anticline, in the Entrada sandstone, Utah, where two sets of fractures, unlike the fractures in Nashpoint limestone or Porthkerry Formation, are intersecting at a low angle. In this example two sets of fractures are present only in the western part of the study area hence a connected pattern is manifested only in the western part. But even where two sets are present, and the fractures of both sets are closely spaced, the low angle of intersection of two sets resulted in low connectivity. A low angle of

intersection of two sets requires a high length of the cross set to build network connectivity.

Two fracture sets, both sets varying

In Figure 5.18a-b, there are two dominant sets of fractures in the Tensleep sandstone, a NW-SE set of strike 329° with an average dispersion of 12° and an ENE-WSW set of strike 72° with an average dispersion of 11° . The angle between two sets is 76° . The average normalized length of the ENE-WSW set is 0.1 and the normalized spacing is 0.06, whereas for the NW-SE set, the average normalized length is 0.09 and the normalized spacing is 0.06. Thus this fracture pattern is an example of two fracture sets, at a high angle to each other, where both sets show similar spacings and lengths. The fractional connected area of the network is 1, indicating complete connectivity. The important characteristic in this fracture network is that although both sets have relatively low lengths, the average length is higher than the spacing of for each set, and this results in a high connectivity. This is consistent with the results yielded by the two sets of simulated fractures shown in figure 5.18f, where the length of two orthogonal sets are higher than the spacing of the respective sets.

Figure 5.19 shows fractures in Mississippian carbonates on the western flank of Teton anticline, Montana. All the maps consist of several sets of fractures, but there are two dominant sets that control the connectivity of study

area. The fracture map in figure 5.19a, exhibits two sets of fractures where NW-SE set is the dominant set with a density of 8.3m/sq.m and normalized length of 0.1. The fractional connected area is 0.93 and the fractures connect the opposite ends of the sample area. The fracture map of 6.39b, shows two dominant sets of fractures where both sets are of similar length but the density of the EW set is double that of the NW set resulting in several fracture clusters, but none of the clusters are extensive enough to cover the entire area. A simulation of this example is shown in figure 5.19d, where there are two sets of fractures of similar length, but the density of the EW set is double that of NS set. The difference in connectivity between figures 5.19a and 5.19b is because in figure 5.19a there is one fracture set, the NW-SE set that is long and closely spaced forming the backbone of the network and all other sets are enhancing the connectivity in direction perpendicular to the main set, whereas in figure 5.19b, none of the sets are dominant and the orthogonal sets of fracture result in only moderate clustering. In figure 5.19c, all the fracture sets have very low density, with the northwest set having the highest fracture density of 1.8m/sq.m (NW set), resulting in low fractional connected area of 0.41. An example from the simulated maps exhibits how the low length and fracture density resulted in low fracture connectivity.

5.8 Conclusions

Fracture simulation designed to analyze the controls of different fracture parameters (variations in fracture strike, density and length) on fracture network connectivity reveals certain parameters are more dominant in controlling the connectivity. Simulations with one set of fractures show that increases in length, density and dispersion all result in higher fracture-parallel connectivity, but the increase in density is the most important in increasing fracture-normal connectivity, especially, where the dispersion in fracture strike is very low.

Simulations of two sets of fractures reveal that the density, length and the difference in angle between the two sets play dominant role in achievement of complete connectivity. In cases where one set of fracture is a systematic set and extends through the entire length of the study area, there is a critical combination of length of the second set and the angle between the two sets that results into complete connectivity. In cases where both set of fractures have varying length and density, the influence of increasing density of one set had a dramatic effect on connectivity when the length of the other set was short, while the change in connectivity was more subtle to insignificant when the length of the other set is long. The network also showed higher connectivity with increasing angular difference between two sets.

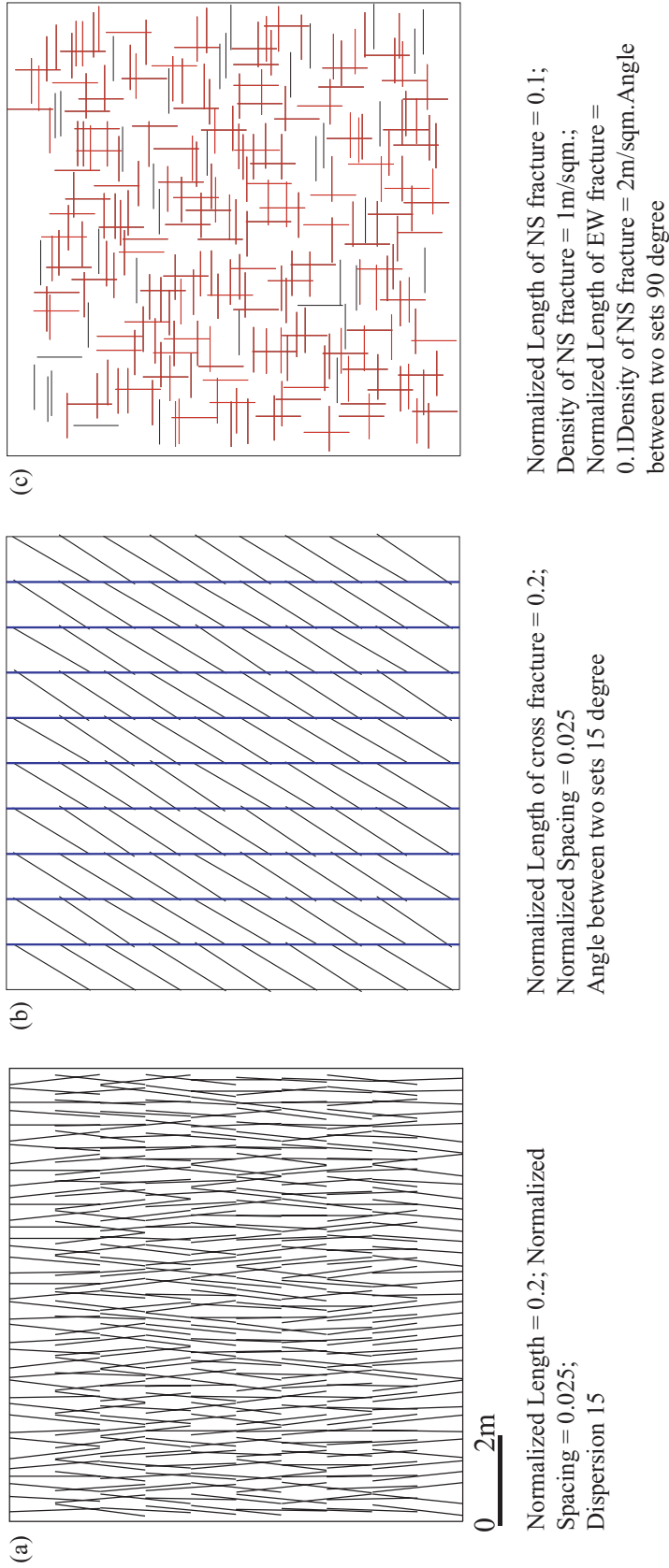
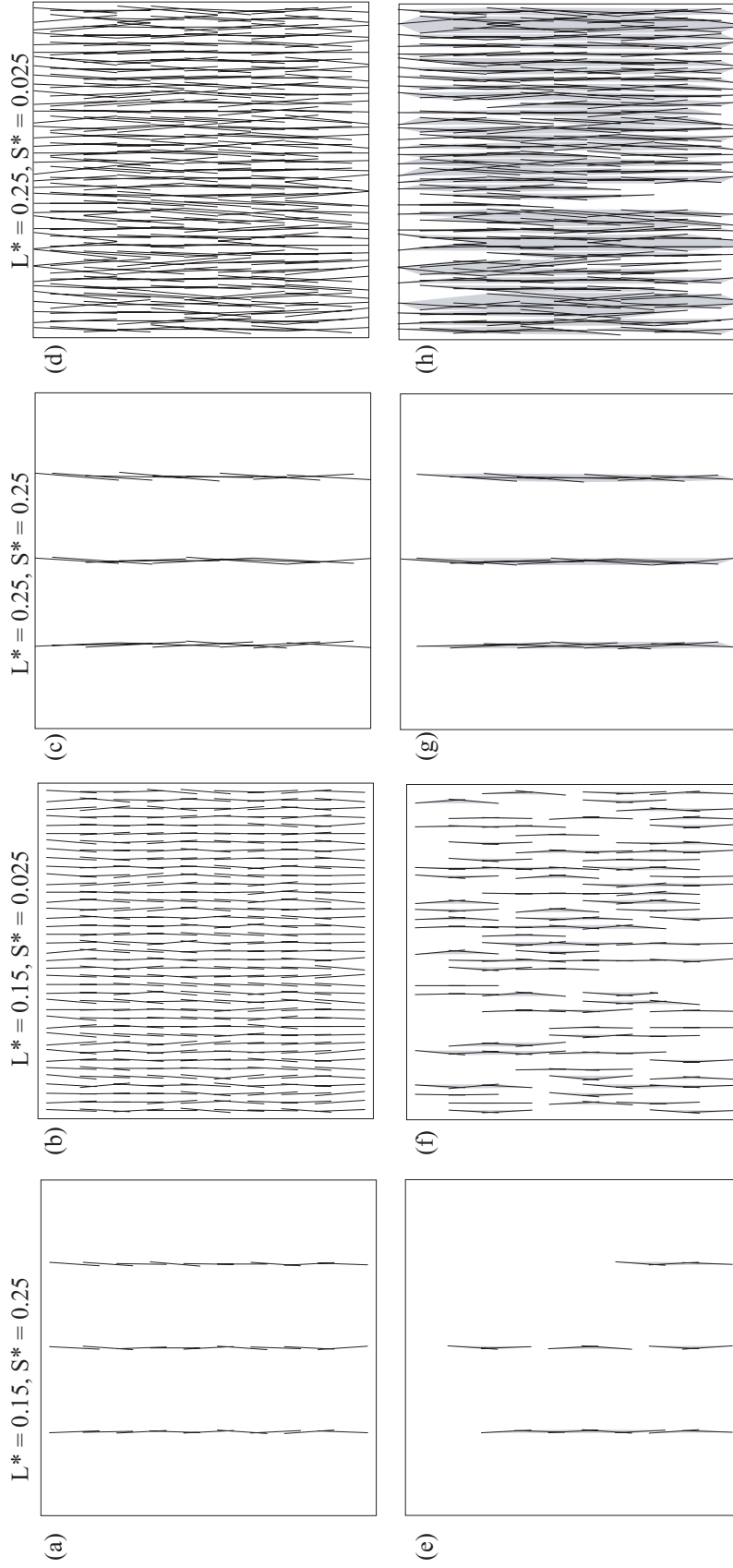


Figure 5.1. (a) Single set of fracture with an angular dispersion of 15 degree. (b) Two sets of fractures with one dominant set extending across the study area and a second set of cross fractures developed in between the dominant set. (c) Two orthogonal set of fractures where both sets are dominant.



Dispersion 10 degree

Figure 5.2. Examples from single set of simulated fractures with 10 degree dispersion in strike, varying between 175 to 185 degree. (a-d) Single set of fracture with varying length and spacing. (e) Fracture cluster extracted from 5.2a. (f) Fracture cluster extracted from 5.2b. (g) Fracture cluster extracted from 5.2c. (h) Fracture cluster extracted from 5.2d. L^* : Normalized length; S^* : Normalized spacing.

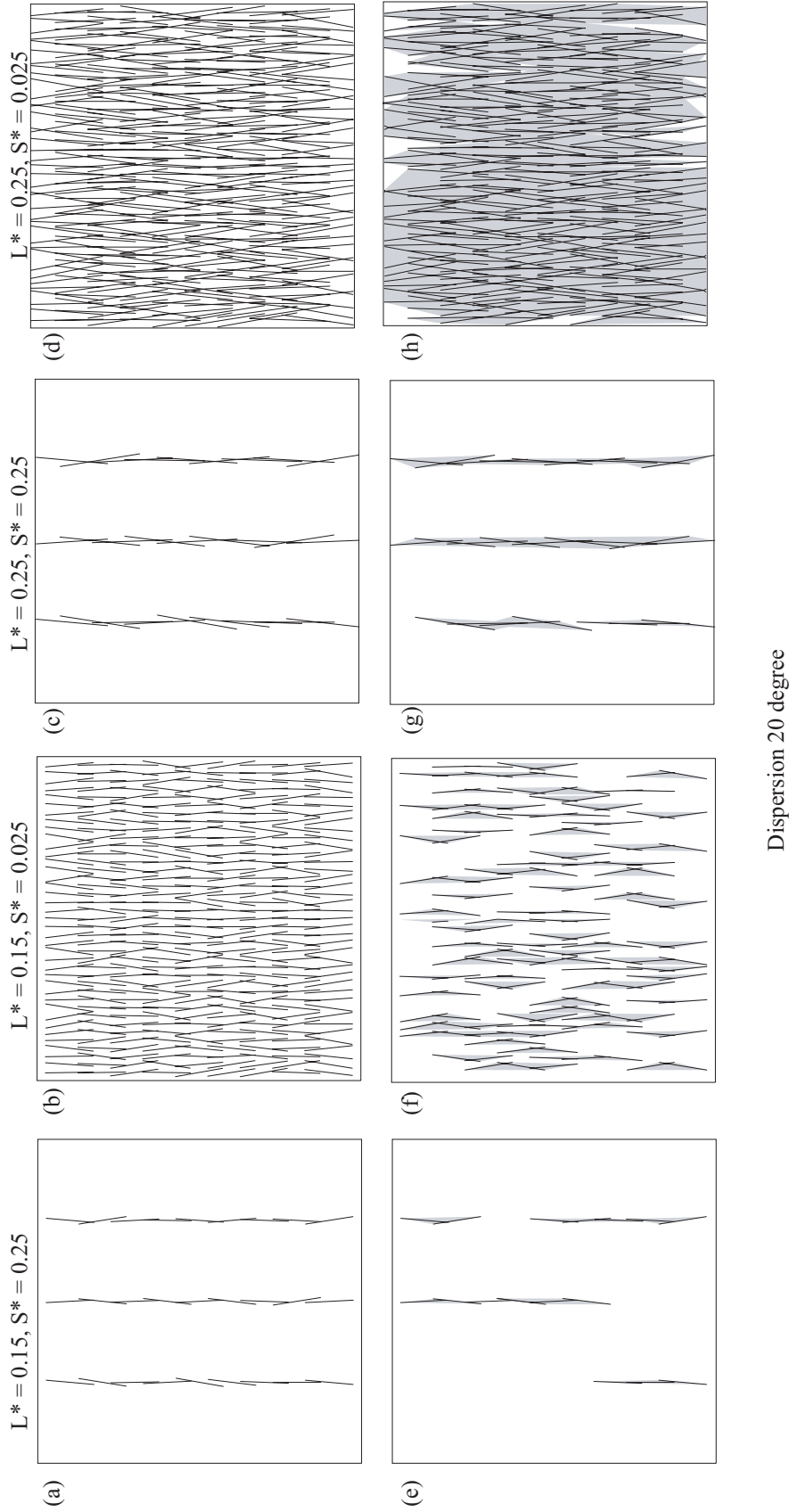
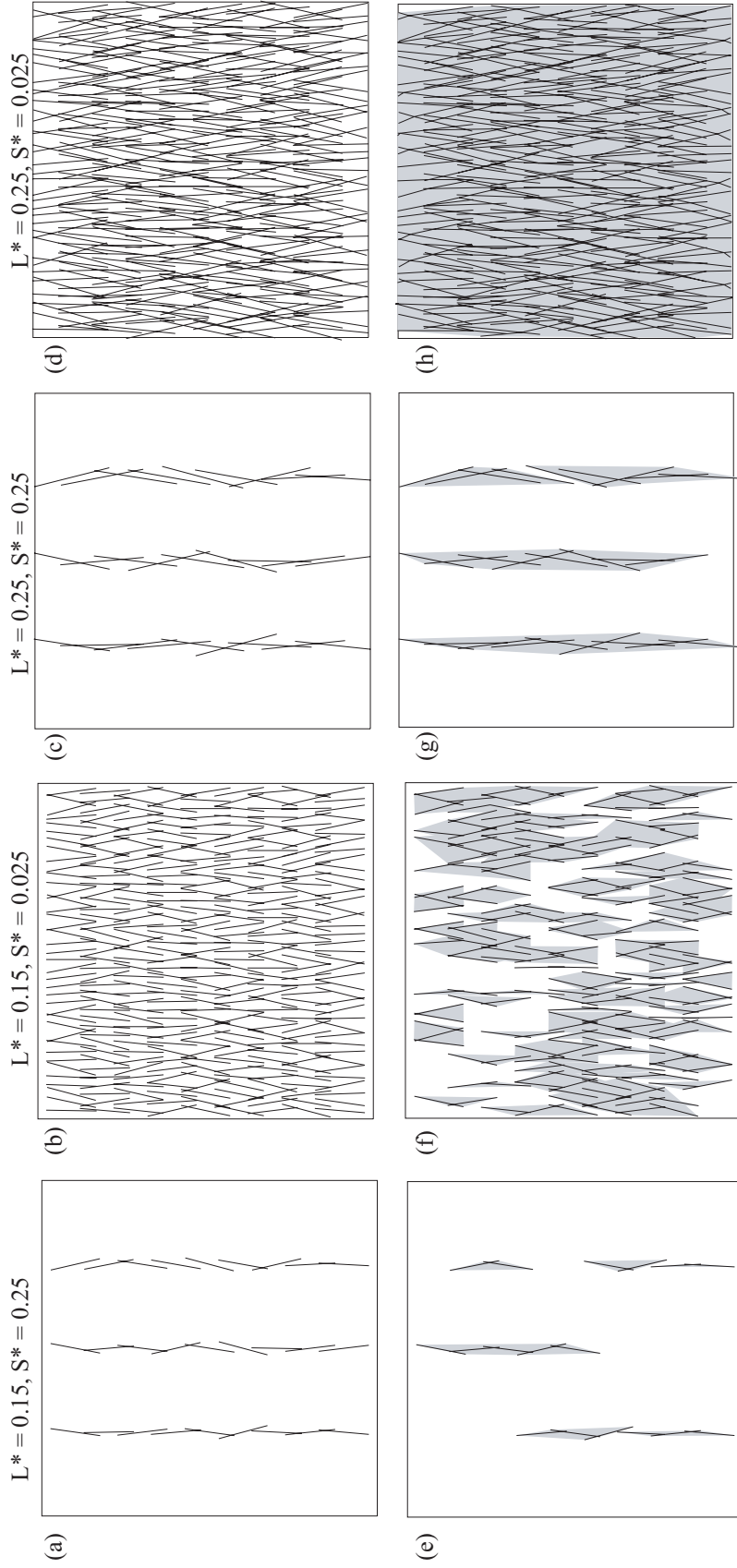


Figure 5.3. Examples from single set of simulated fractures with 20 degree dispersion in strike, varying between 175 to 185 degree. (a-d) Single set of fracture with varying length and spacing. (e) Fracture cluster extracted from 5.3a. (f) Fracture cluster extracted from 5.3b. (g) Fracture cluster extracted from 5.3c. (h) Fracture cluster extracted from 5.3d. L*: Normalized length; S*: Normalized spacing.



Dispersion 30 degree

Figure 5.4. Examples from single set of simulated fractures with 30 degree dispersion in strike, varying between 165 to 195 degree. (a-d) Single set of fracture with varying length and spacing. (e) Fracture cluster extracted from 5.4a. (f) Fracture cluster extracted from 5.4b. (g) Fracture cluster extracted from 5.4c. (h) Fracture cluster extracted from 5.4d. L^* : Normalized length; S^* : Normalized spacing.

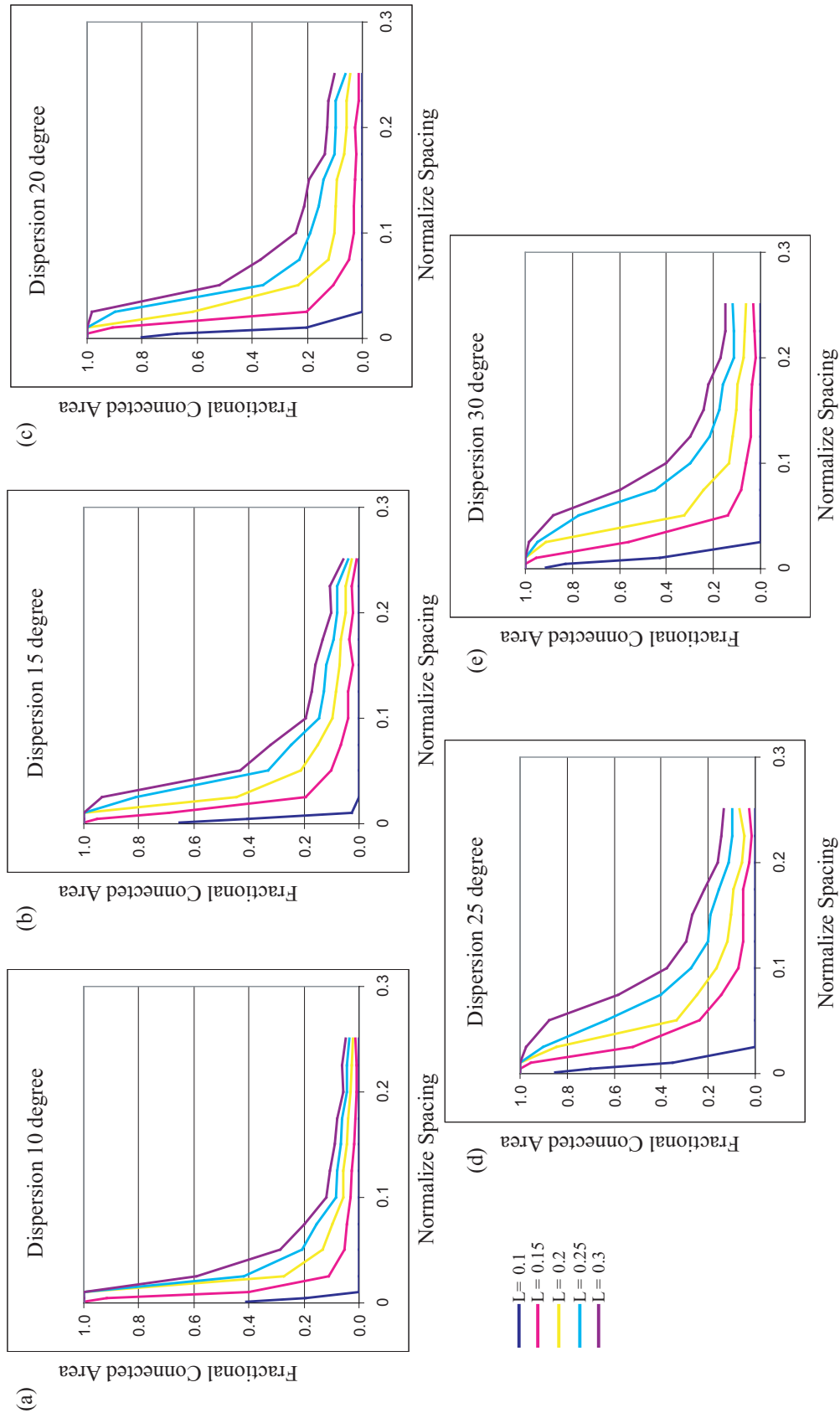


Figure 5.5. Plot of Spacing vs. Fractional Connected Area for varying length and orientation. The curve for varying length in each plot is color coded. L : Normalize length of fracture.

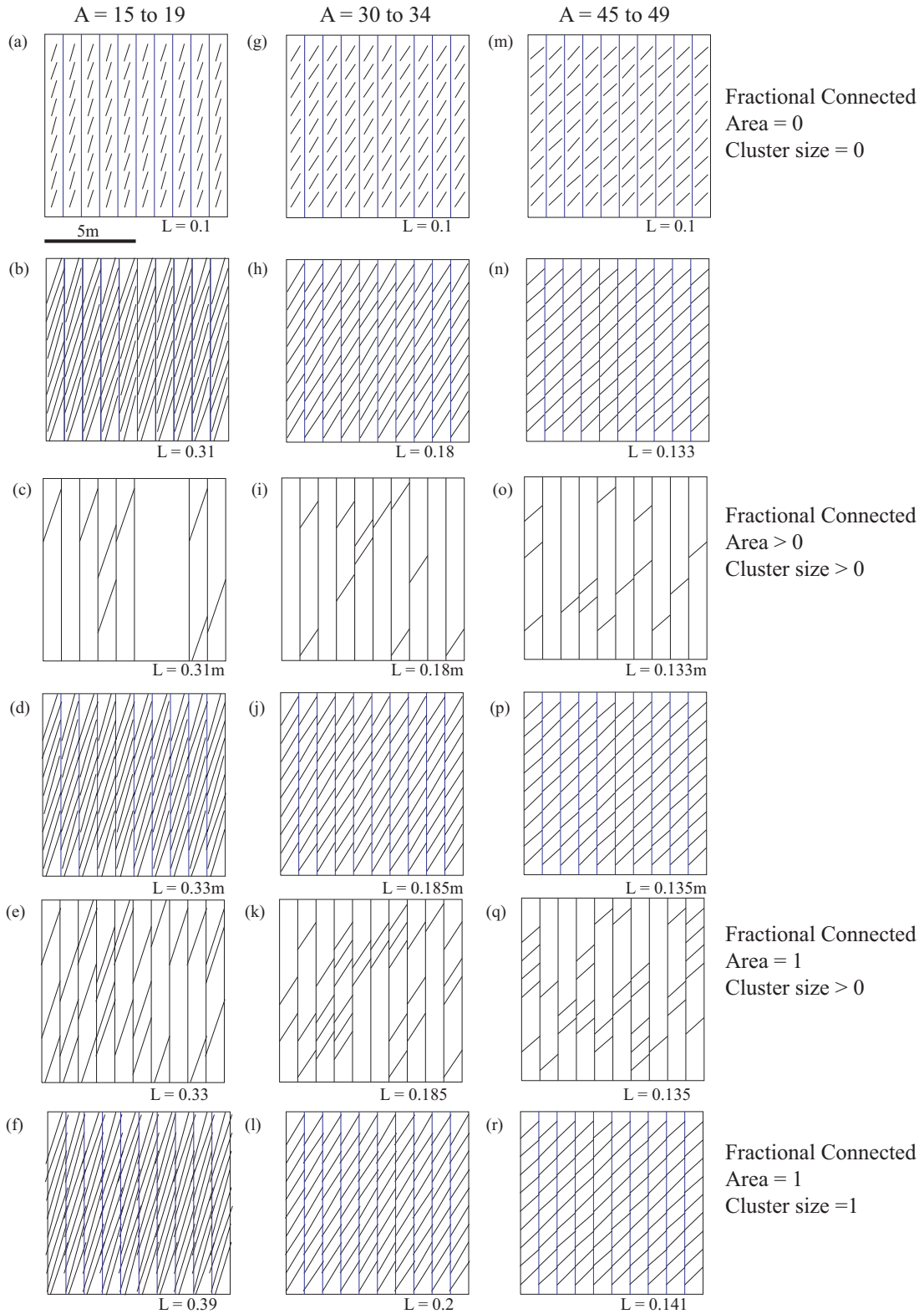


Figure 5.6. (a-f) Simulation of two sets of fractures, angle between 2 sets ranges from 15 to 19 degree. (g-l) Angle between 2 sets range from 30 to 34 degree. (m-r) Angle between 2 sets range from 45 to 49 degree. L: Normalized length of cross fractures; A: Angle between two sets in degrees.

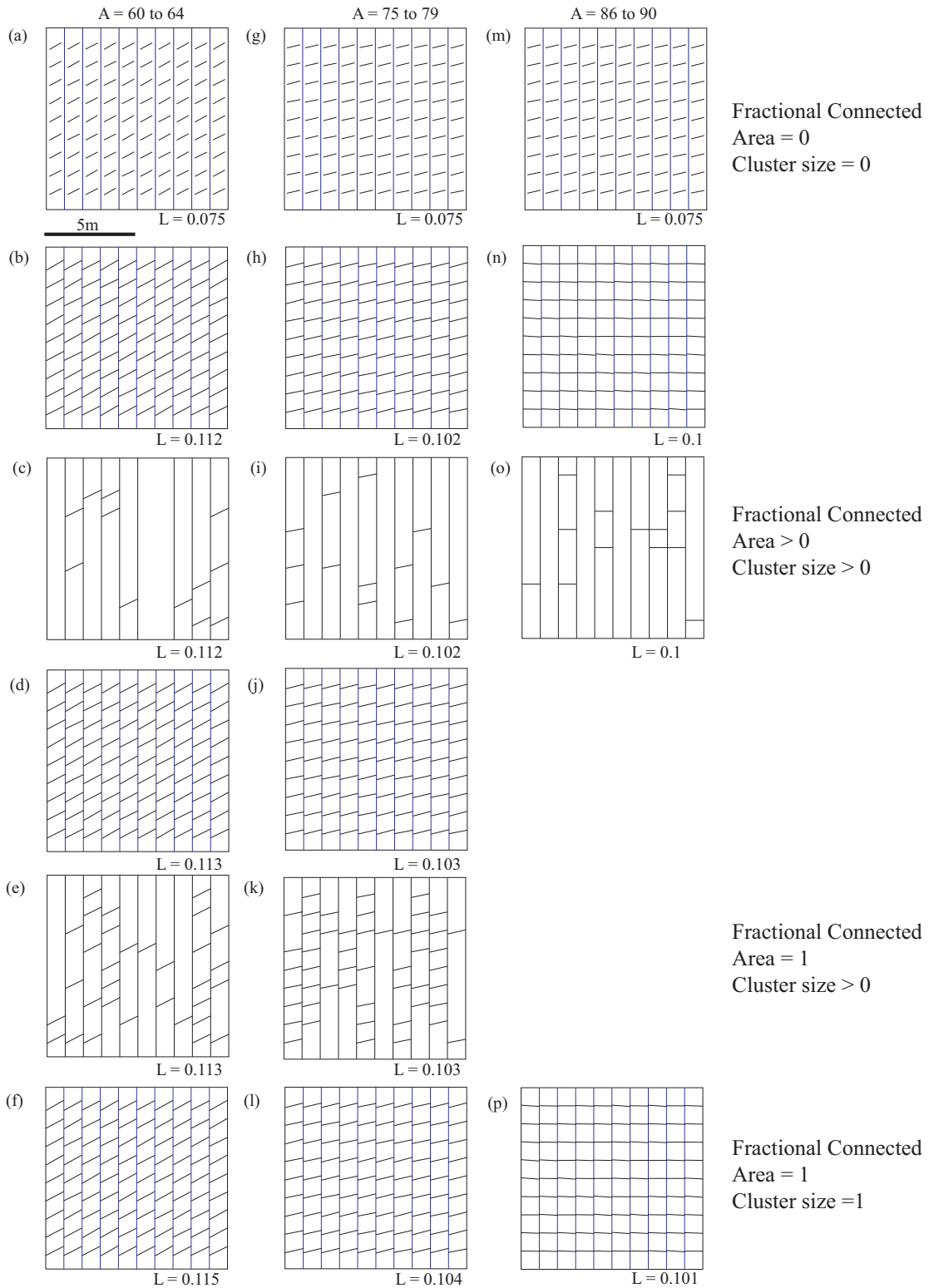


Figure 5.7. (a-f) Simulation of two sets of fractures, angle between 2 sets ranges from 60 to 64 degree.(g-l) Angle between 2 sets range from 75 to 79 degree.(m-p) Angle between 2 sets range from 86 to 90 degree. L: Normalized length of cross fractures; A: Angle between two sets in degrees.

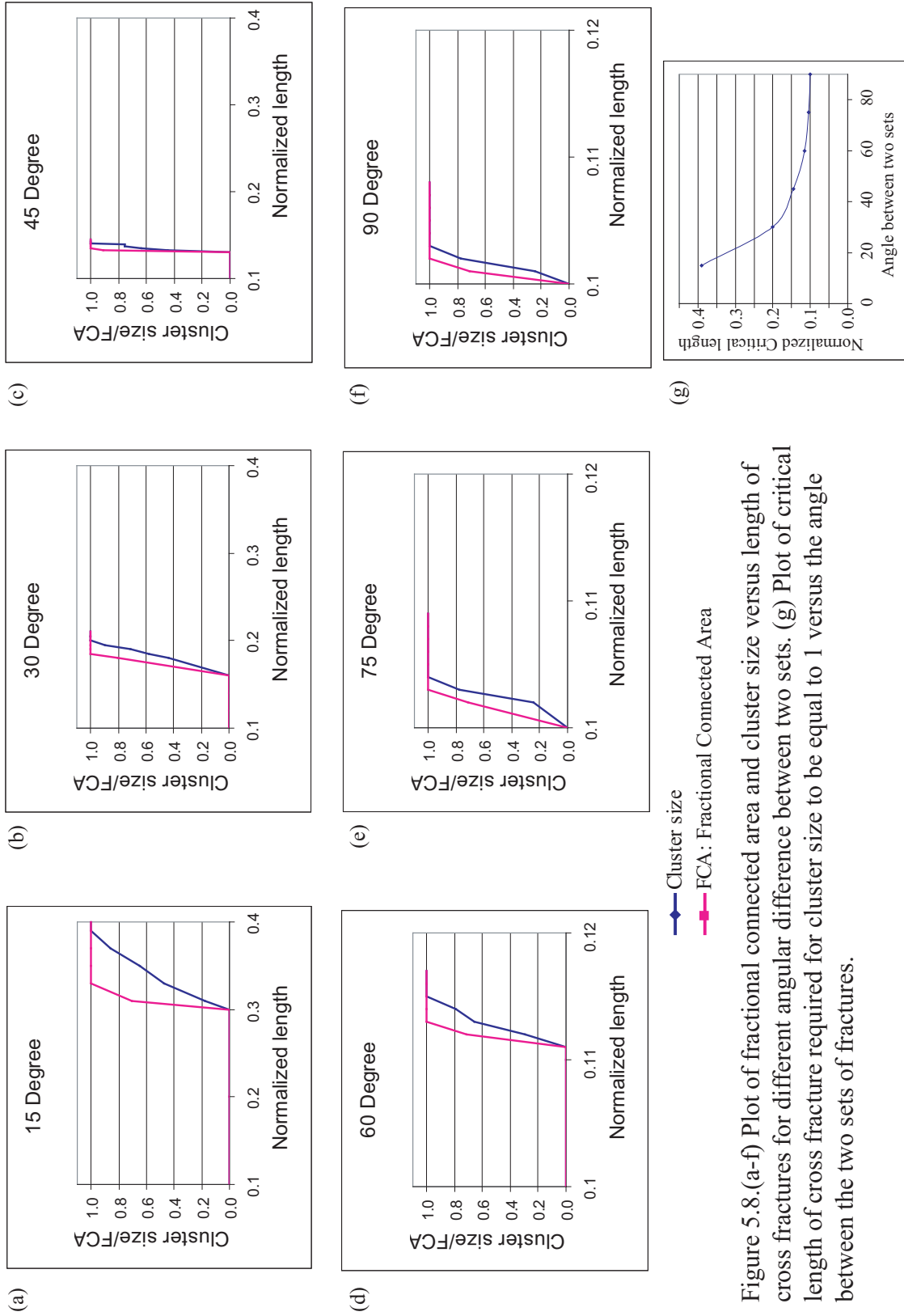


Figure 5.8.(a-f) Plot of fractional connected area and cluster size versus length of cross fractures for different angular difference between two sets. (g) Plot of critical length of cross fracture required for cluster size to be equal to 1 versus the angle between the two sets of fractures.

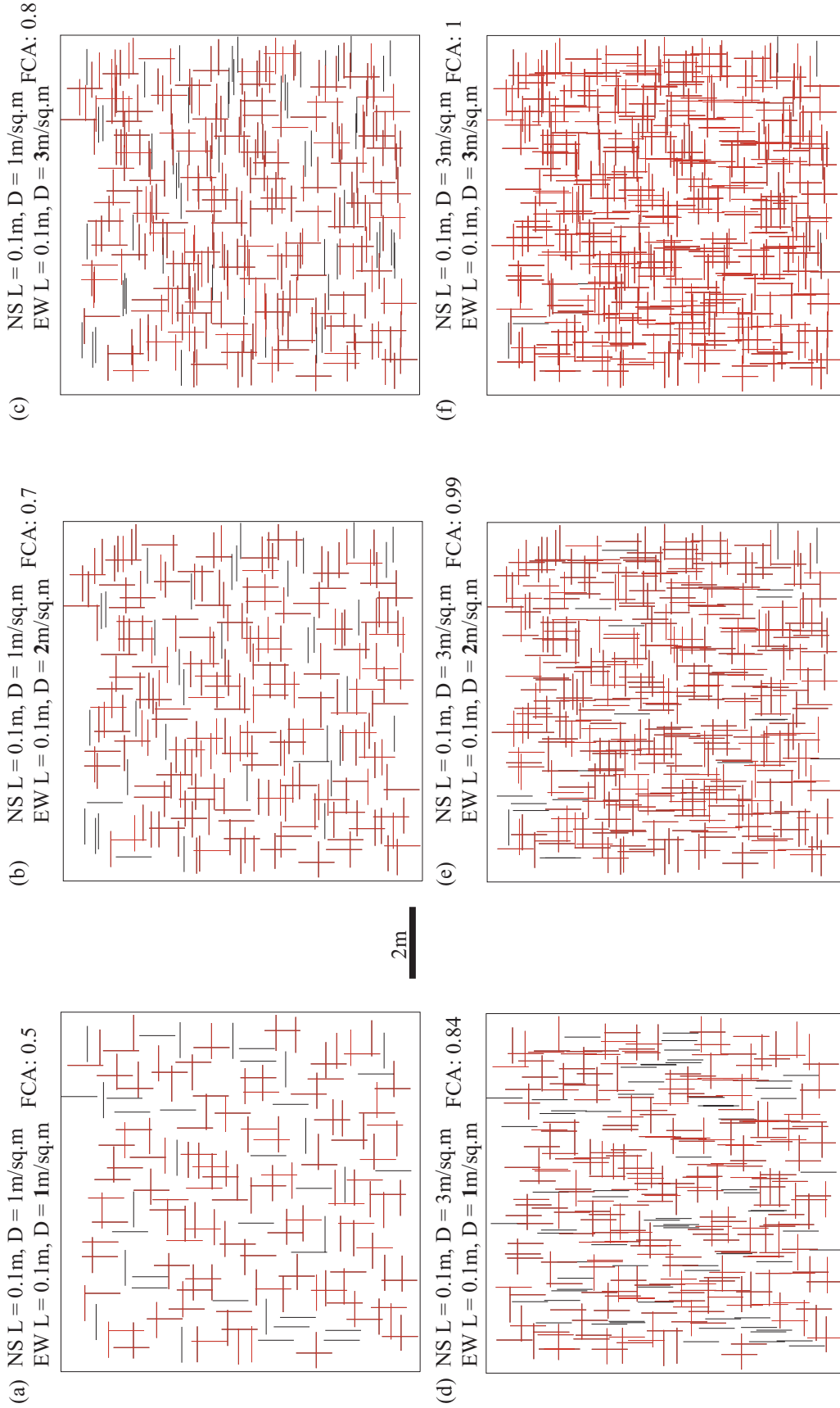


Figure 5.9. Simulation of two orthogonal set of fractures. Normalized length of EW and NS fracture is 0.1. Red lines indicate the connected group of fractures. (a-c) Density of NS set 1m/sq.m and density of EW set vary from 1 to 3m/sq.m. (d-f). Density of NS set 3m/sq.m and density of EW set vary from 1 to 3m/sq.m. FCA: Fractional Connected Area.

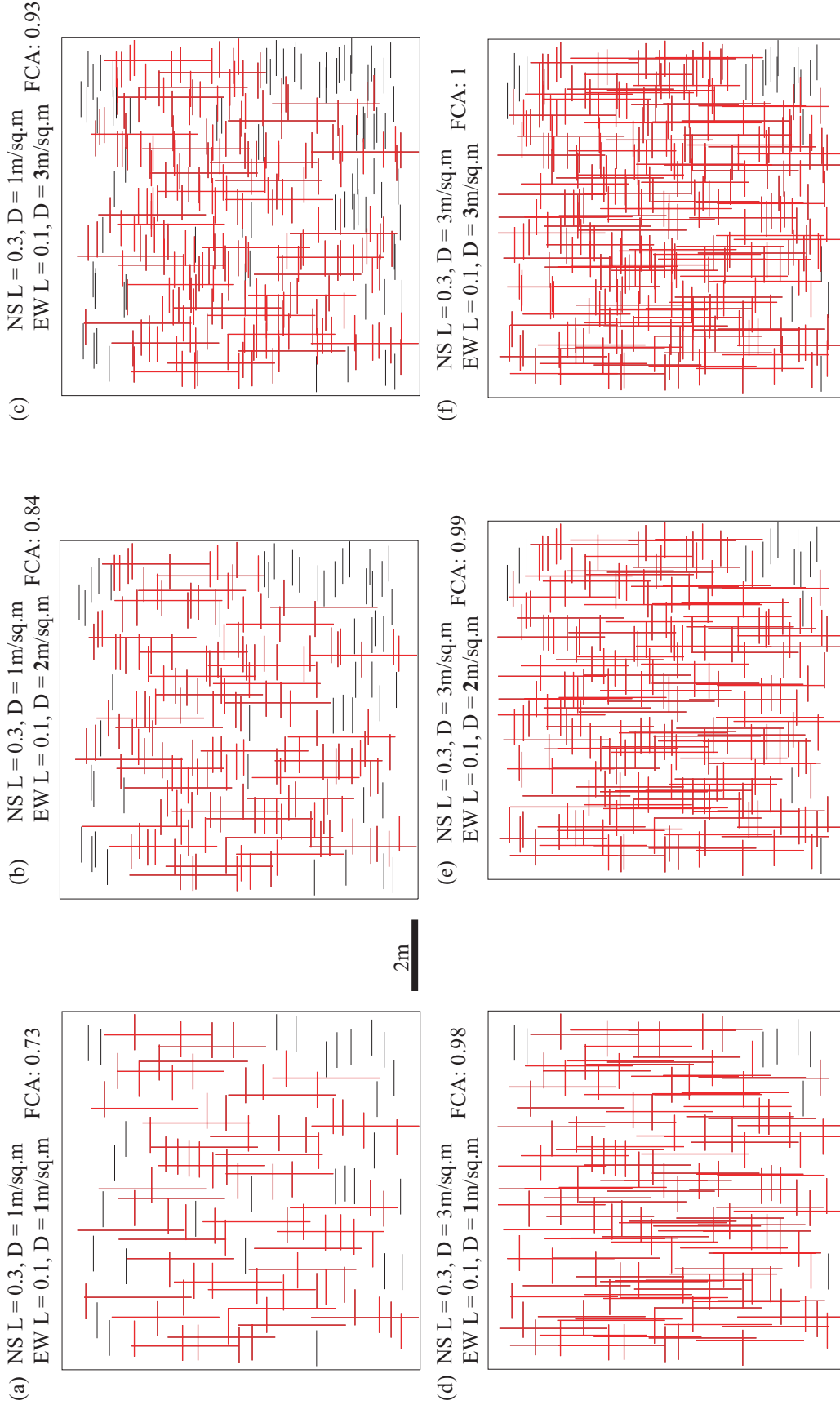


Figure 5.10. Simulation of two orthogonal set of fractures. Normalized length of EW set is 0.1 and NS set is 0.3. Red lines indicate the connected group of fractures. (a-c) Density of NS set 1m/sq.m and density of EW set vary from 1 to 3m/sq.m. (d-f) Density of NS set 3m/sq.m and density of EW set vary from 1 to 3m/sq.m. FCA: Fractional Connected Area.

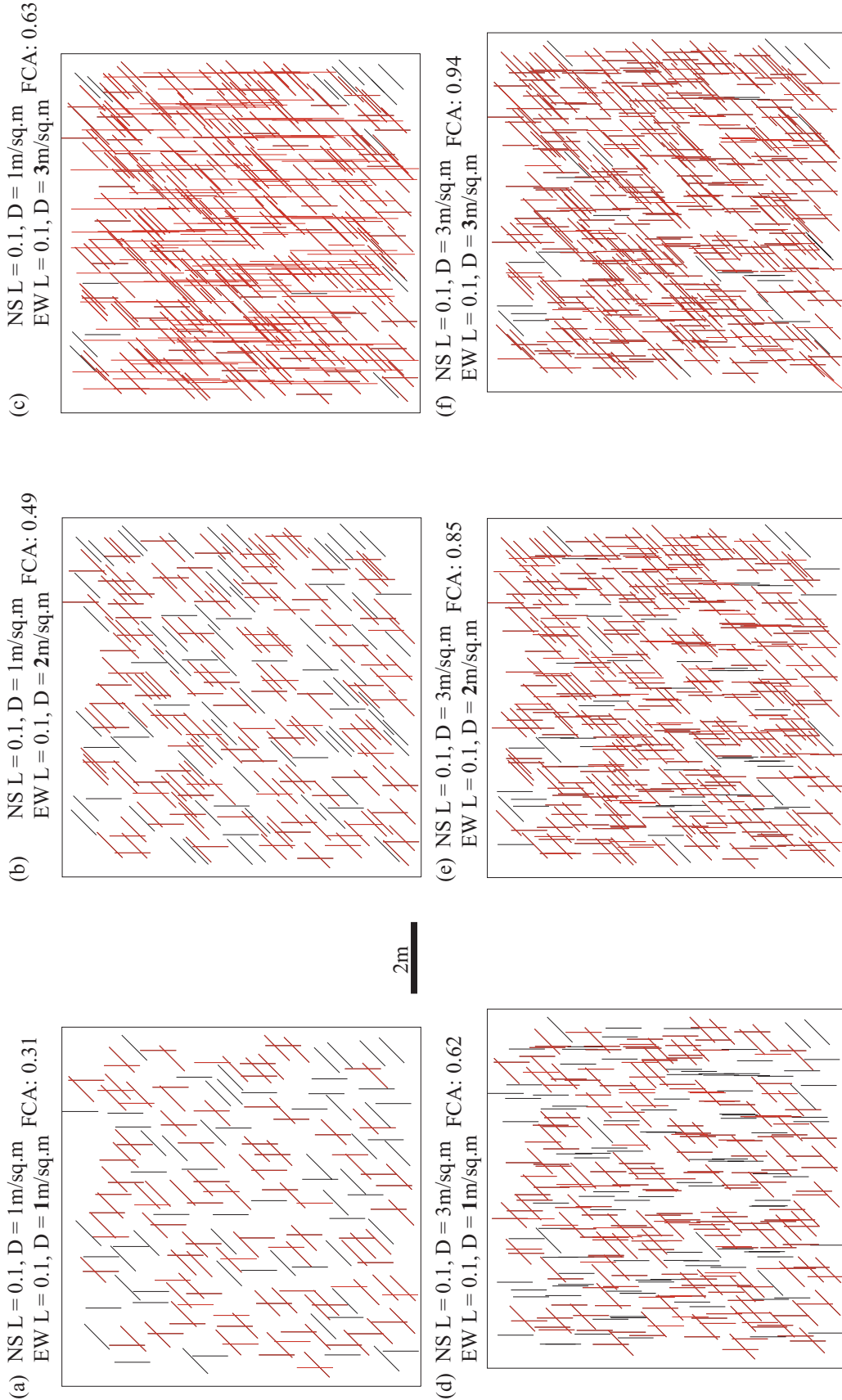


Figure 5.11. Simulation of two sets at 45 degrees. Length of EW and NS set is 0.1. Red lines indicate the connected group of fractures. (a-c) Density of NS set 1m/sq.m and density of EW set vary from 1 to 3m/sq.m. (d-f) Density of NS set 3m/sq.m and density of EW set vary from 1 to 3m/sq.m. FCA: Fractional Connected Area.

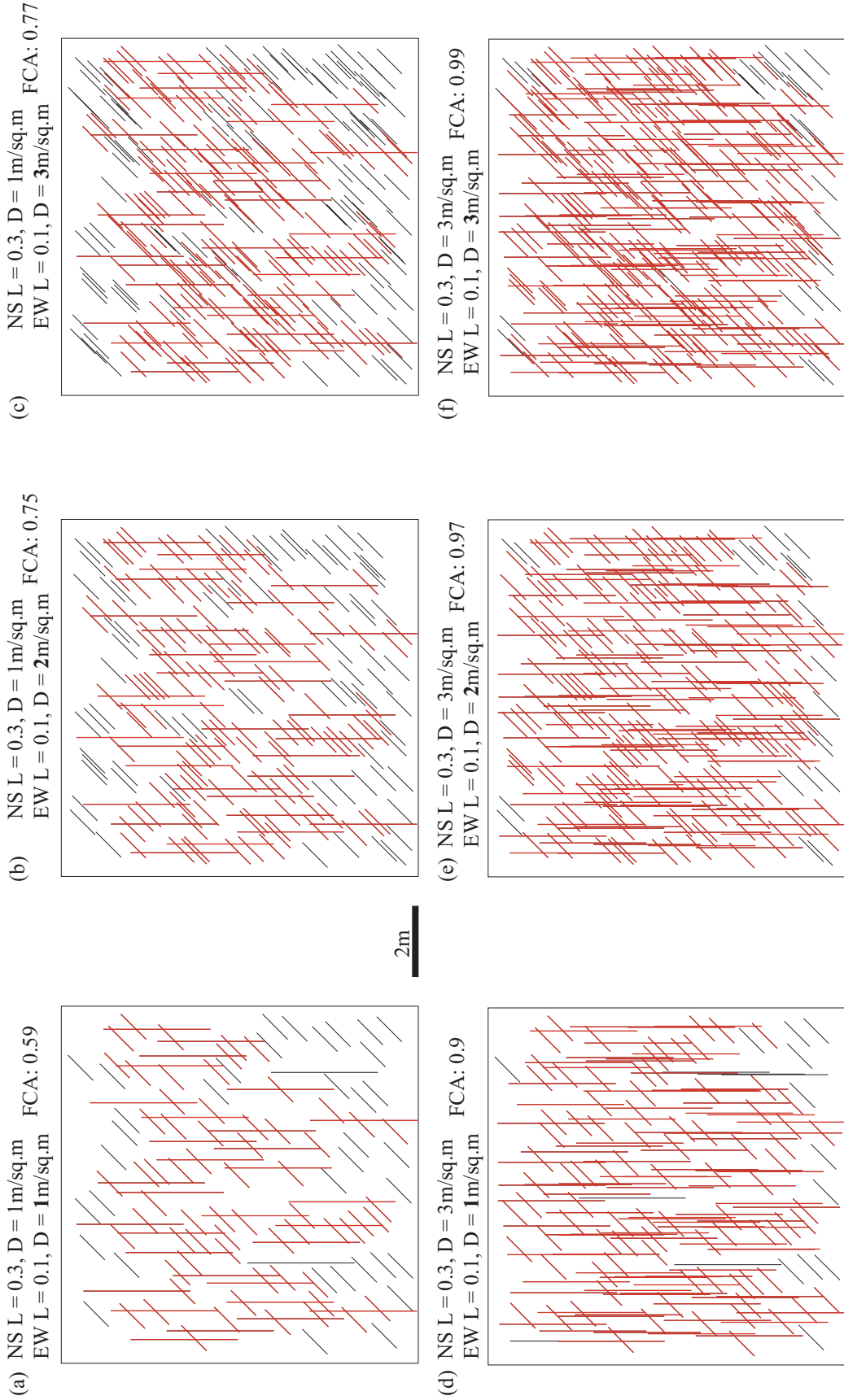


Figure 5.12. Simulation of two sets at 45 degrees. Length of EW set is 0.1 and NS set is 0.3. Red lines indicate the connected group of fractures. (a-c) Density of NS set 1m/sq.m and density of EW set vary from 1 to 3m.sq.m. (d-f) Density of NS set 3m/sq.m and density of EW set vary from 1 to 3m/sq.m. FCA: Fractional Connected Area.

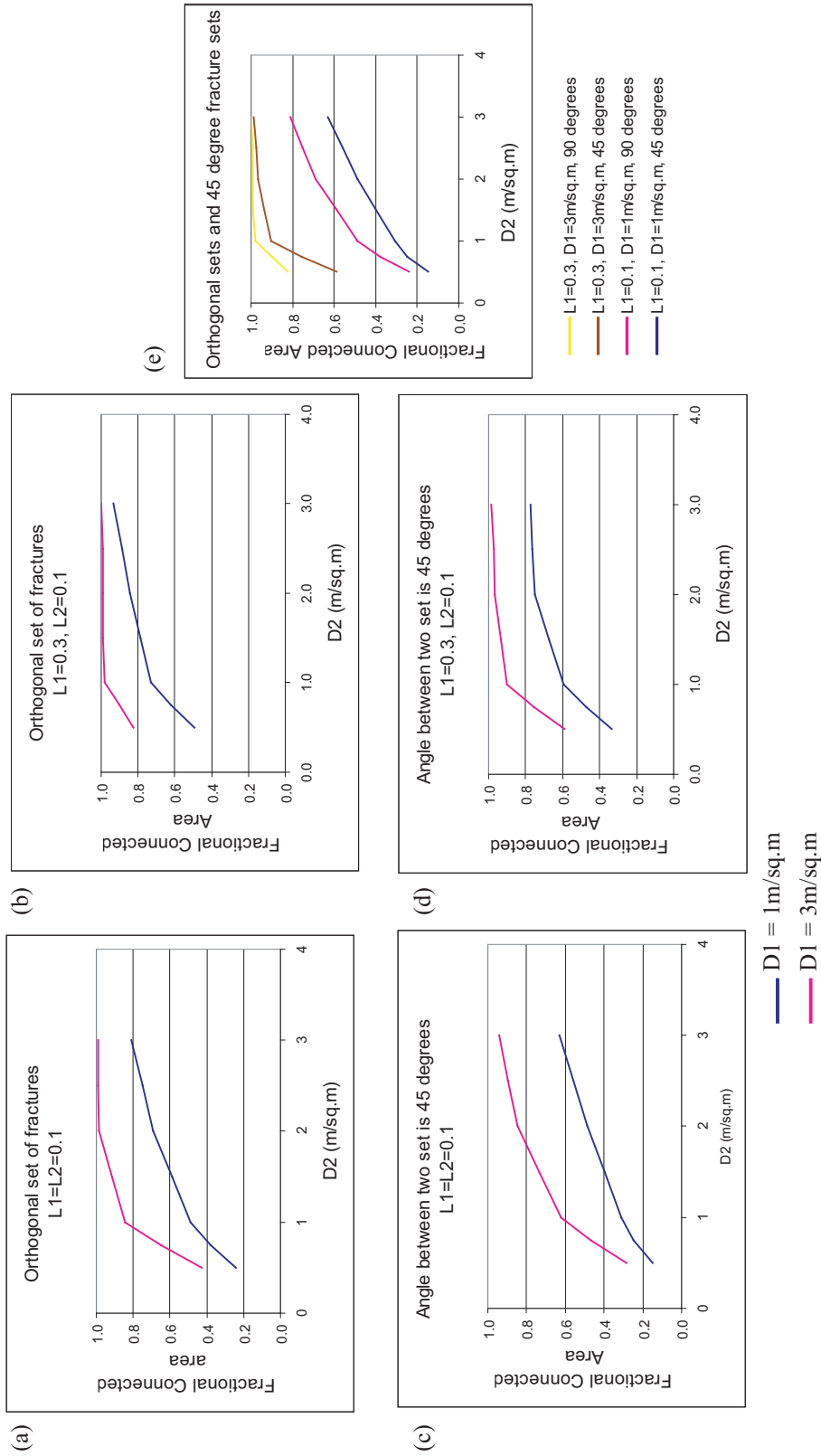


Figure 5.13. Graphical representation of simulation results for two sets of fractures with changing length and density. Plots of D2 versus Fractional Connected Area. (a) Orthogonal sets with normalized length of both sets is 0.1 (b) Orthogonal sets with normalized length of $L1=0.3$ and $L2=0.1$. (c) 45 degree sets with normalized length of both sets is 0.1. (d) 45 degree sets with normalized length of $L1=0.3$ and $L2=0.1$. (e) Orthogonal set and 45 degree set plotted together, curves color coded for varying $L1$ and $D1$. $L1$: Normalized length of NS set; $D1$: Density of NS set; $D2$: Normalized length of EW set; $D2$: Density of EW set.

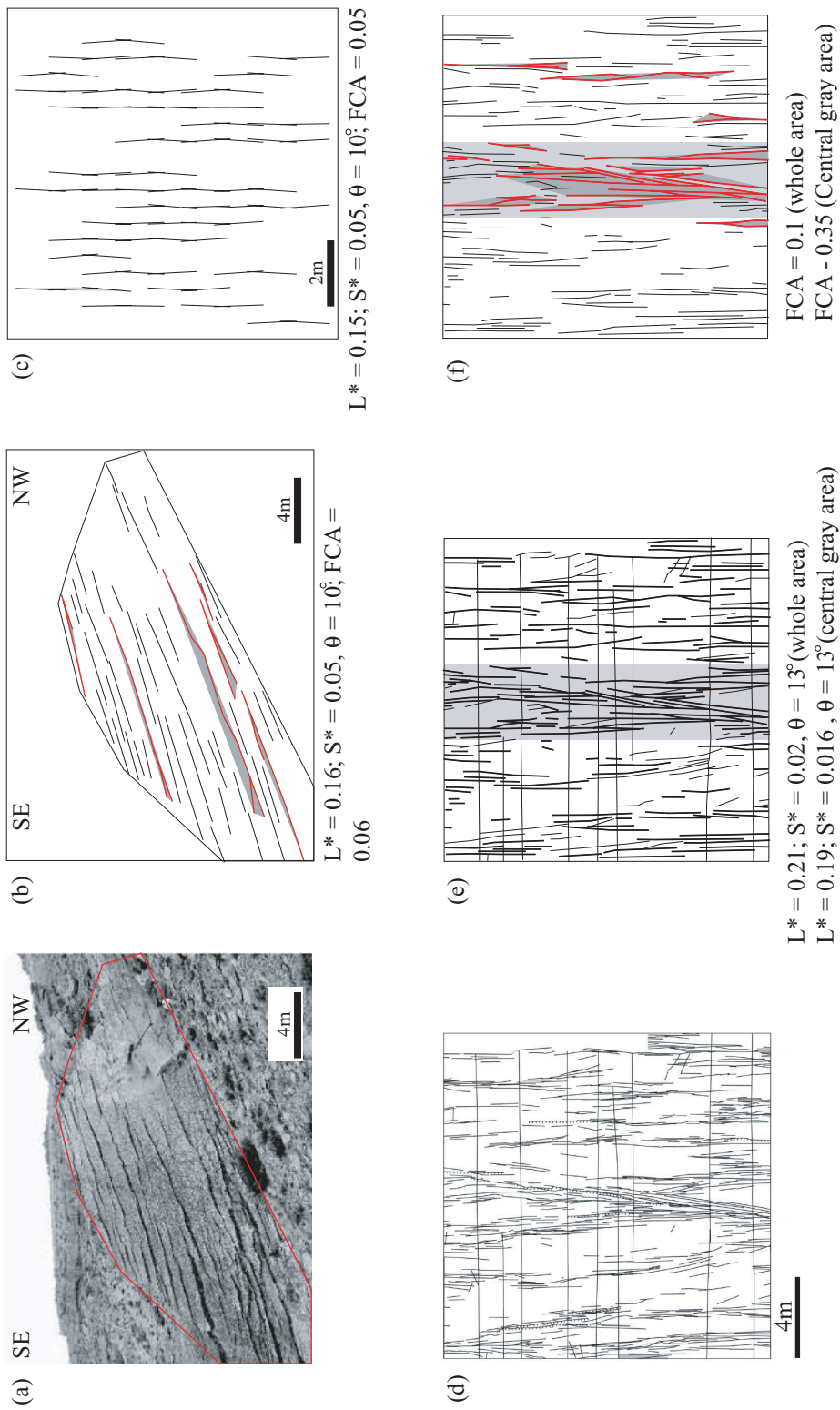


Figure 5.14. (a) Fractures hosted in Tensleep sandstone (Bellahsen et al., 2006). (b) Fracture cluster extracted from photo 5.14a. Red lines indicate fractures contributing to the cluster. (c) Simulated fractures with low strike dispersion. (d) Fractures hosted in Carboniferous sandstone at Telpyn point, Wales, UK, (Rohrbaugh et al., 2002). (e) Anastomosing fracture pattern in Entrada sandstone, Utah, (Lorenz and Cooper, 2000). θ : Dispersion of strike orientation.

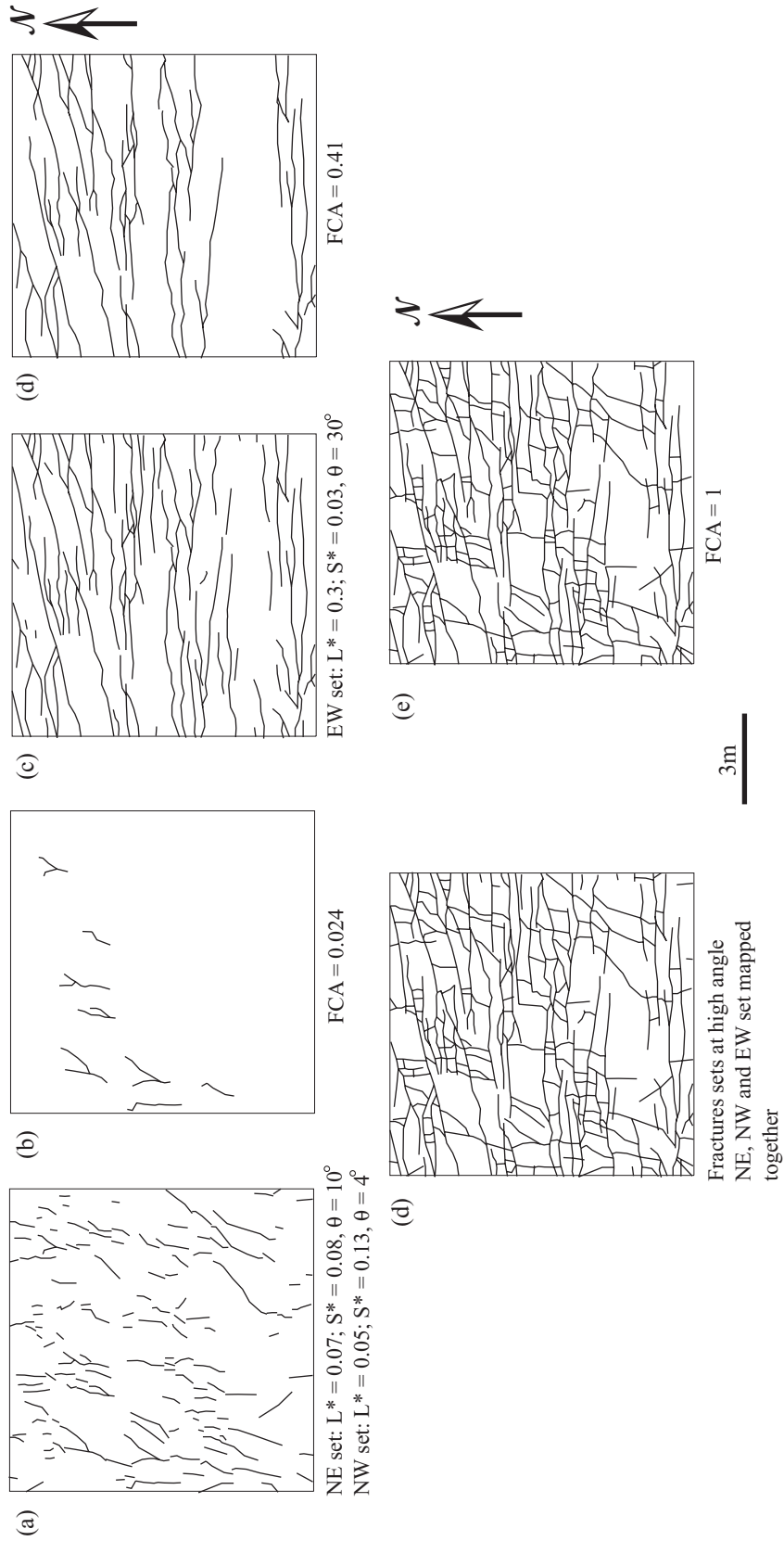


Figure 5.15. Natural fractures in Lompoc Landing, California. (a) NS trending fractures. (b) Connected group of NNW-SSE and NE-SW trending fractures. (c) EW trending fractures. (d) Connected group of EW trending fractures. (e) Fracture network consisting of all fracture sets. (f) Connected group of fractures constituted of all set of fractures. θ : Dispersion of strike within a single set.

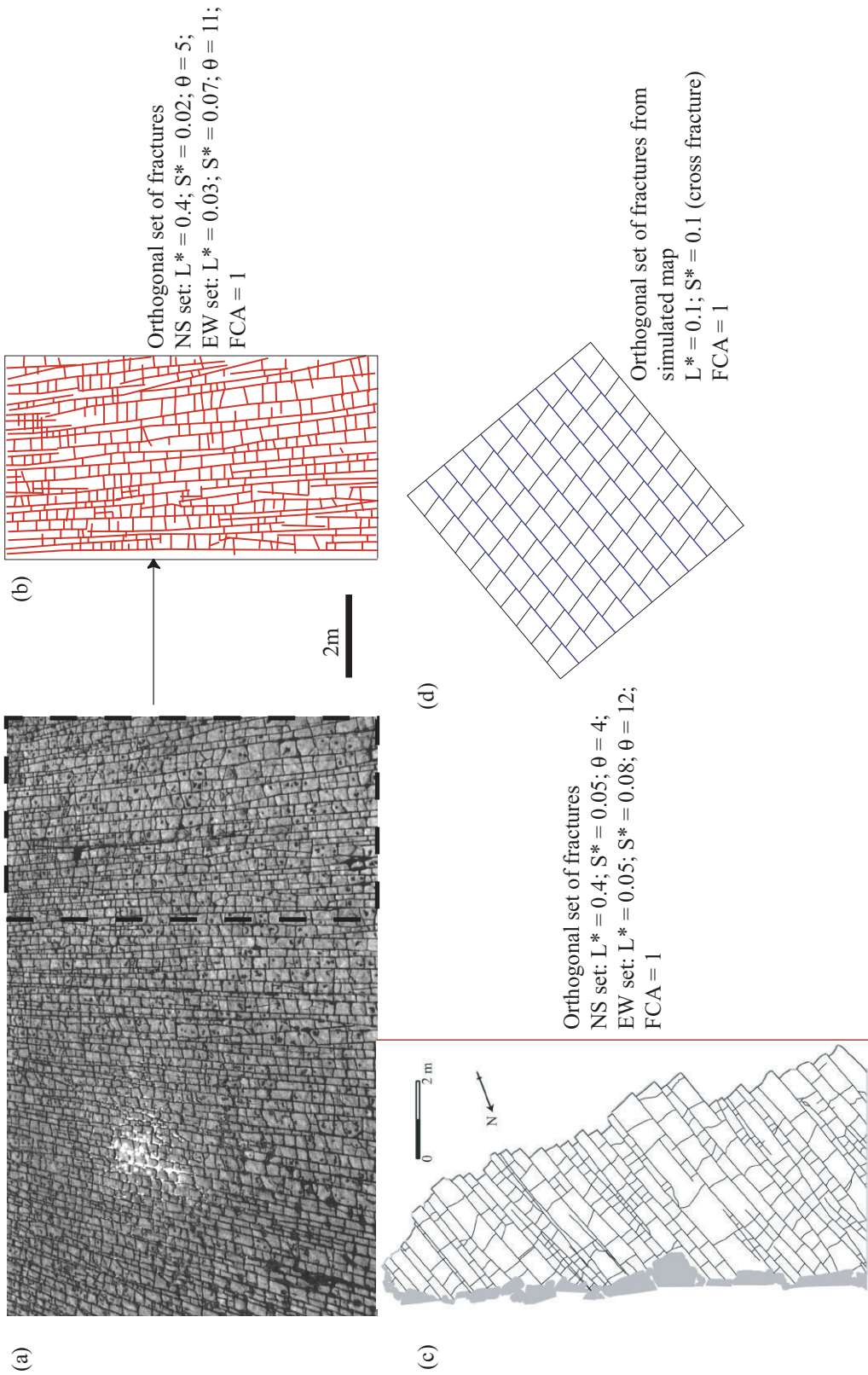


Figure 5.16. (a) Natural fractures hosted in Nashpoint limestone, (Josnin et. al., 2002). (b) Fracture trace of a part of the pavement marked by dotted lines in 5.16a (c) Fractures in Jurassic limestone formation, Llanwit Major, Wales, (Rohrbaugh et al., 2002). (d) Simulated fractures intersecting at high angle. θ : Dispersion of strike orientation.

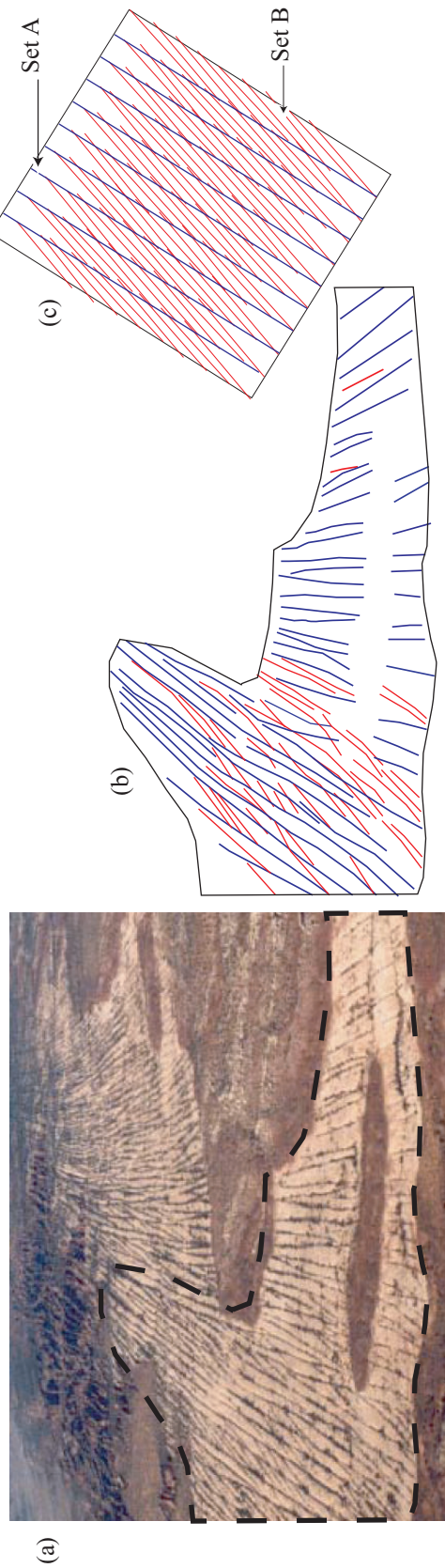


Figure 5.17. (a) Two sets of fractures intersecting at low angle on the flank of Salt Valley Anticline. Some fractures are traced out on the photograph to highlight the angular relation between intersecting fractures. (b) Fracture traces from part of figure 5.17a marked by a dotted line. Two sets of fractures represented by blue and red line. (c) Two sets of simulated fractures intersecting at low angles.

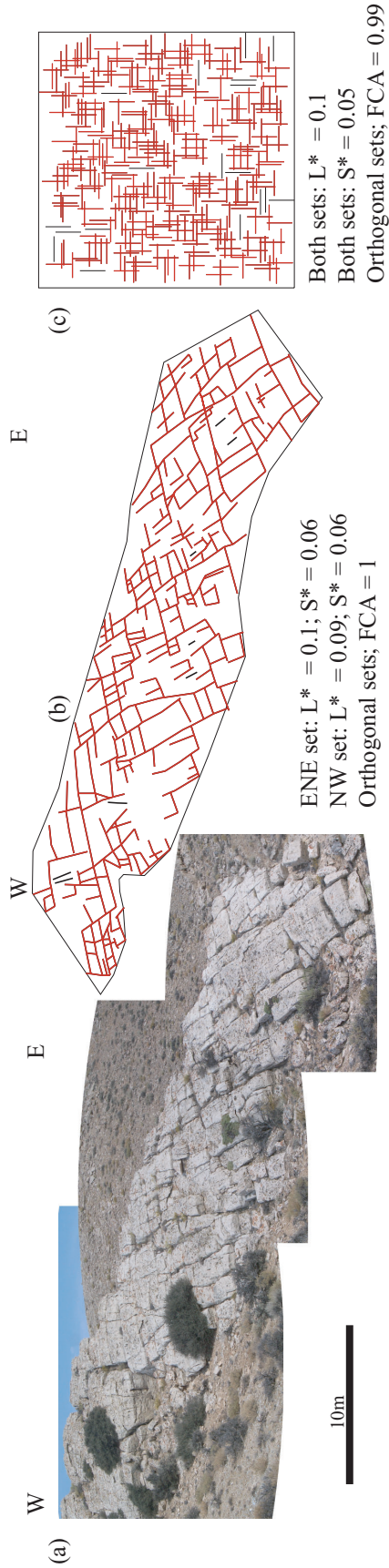


Figure 5.18. (a) Two sets of fractures at high angle, hosted in Tensleep sandstone. (b) Fracture traces of the pavement shown in figure 5.18a. Red lines represent fractures that belong to the fracture cluster. (c) Example from simulation of a condition similar to 5.18a.

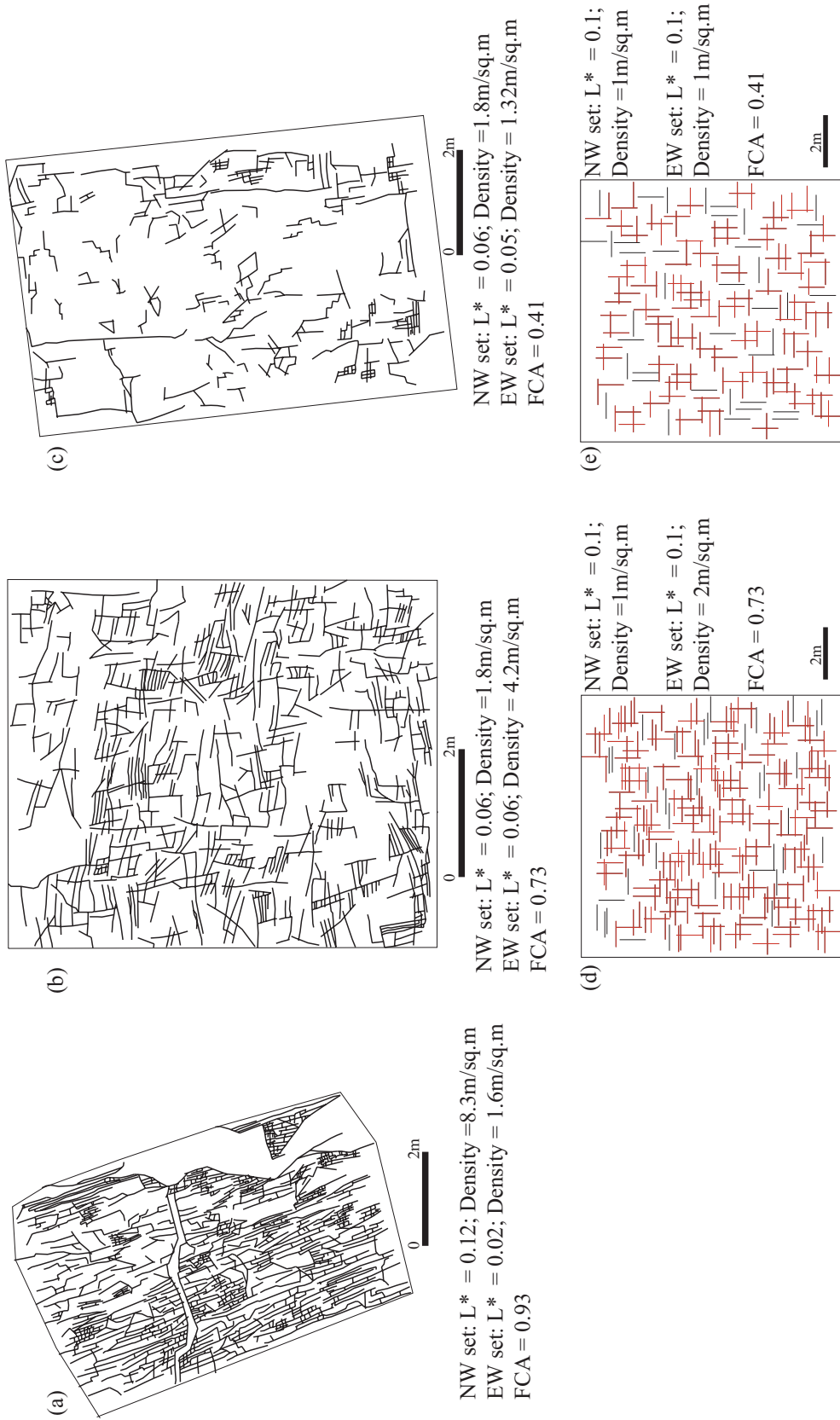


Figure 5.19. Fractures hosted in carbonate unit of western flank of Teton anticline. (a) One dominant set of fracture resulting into continuous connected network. (b) Several set of fractures resulting into connected pattern but not continuous pathway. (c) Low fracture density resulting into low connectivity despite of multiple set of fractures. (d-e) Examples from simulated map.

REFERENCES

- Ackermann, R.V., and Schlische, R.V., 1997, Anticlustering of small normal faults around larger faults: *Geology*, v.25, n.12, p. 1127-1130.
- Anderson, J.L., Osborne, R.H., and Palmer, D.F., 1983, Cataclastic rocks of the San Gabriel fault; an expression of deformation at deeper crustal levels in the San Andreas fault zone: *Tectonophysics*, v.98, n.3-4, p. 209-251.
- Baecher, G.B., Lanney, N.A., and Einstein, H.H., 1978, Statistical description of rock properties and sampling: *Proceedings of the 18th U.S. Symposium on Rock Mechanics*, 5C1-8
- Baecher, G.B., 1983, Statistical analysis of rock mass fracturing: *Mathematical Geology*, v.15, n.2, p. 329-348.
- Bahat, D., 1988, Early single-layer and late multi-layer joints in Lower Eocene chalks near Beer Sheva, Israel: *Annales Tectonicae*, v. 2, p. 3-11.
- Bai, T., and Pollard, D.D., 2001 Fracture spacing in layered rocks: a new explanation based on the stress reduction: *Journal of Structural Geology*, v. 22, p. 43-57.
- Bally, A.W., Gordy, P.L., and Stewart, G.A., 1966, Structure, seismic data and orogenic evolution of southern Canadian Rocky Mountains: *Bulletin of Canadian Petroleum Geology*, v.14, n.3, p.337-381.
- Barton C.C., 1995, Fractal analysis of scaling and spatial clustering of fractures, *in* Barton, C.C., and La Pointe, P.R., eds., *Fractals in the earth sciences*: New York, New York, Plenum Press, p.141-178.
- Barton, C.M., 1978, Analysis of joint traces: *Proceedings of the 19th U.S. Symposium on Rock Mechanics*, American Institute of Mining Engineers, pp. 39-40.
- Bebbington, M., Vere-Jones, D., and Zheng, X., 1990, Percolation Theory; a model for rock fracture?: *Geophysical Journal International*, v. 100, p. 215-220.
- Becker, A., and Gross, M.R., 1996 Mechanisms for joint saturation in mechanically layered rocks: An example from southern Israel: *Tectonophysics*, v. 257, p. 223-237.

Belfield, W.C., 1998, Incorporating spatial distribution into stochastic modeling of fractures: multi-fractals and Levy-stable statistics: *Journal of Structural Geology*, v. 20, p. 473-486.

Bellahsen, N., Fiore, P., and Pollard, D.D., 2006, The role of fractures in the structural interpretation of Sheep Mountain Anticline, Wyoming: *Journal of Structural Geology*, v.20, pp. 850-867.

Berkowitz, B., 1995, Analysis of Fracture Network Connectivity Using Percolation Theory: *Mathematical Geology*, v. 27, p.467-483.

Berkowitz, B., and Balberg, I., 1993, Percolation Theory and Its Application to Groundwater Hydrology: *Water Resources Research*, v. 29, p. 775-794.

Blanchet, P.H., 1957, Development of fracture analysis as exploration method: *American Association of Petroleum Geologists*, v. 41, n.8, p. 1748-1759.

Bonham Carter, G. F., 1994, *Geographic Information Systems for Geoscientists: Modeling with GIS*: Oxford, United Kingdom, Pergamon Press, 398 p.p.

Byerlee, J.D., 1993, Model for episodic flow of high pressure water in fault zones before earthquakes: *Geology*, v.21, n.4, p. 303-306.

Caine, J.S., Evans, J.P., and Forster, C.B., 1996, Fault zone architecture and permeability structure: *Geology*, v.24, p. 1025-1028.

Chelidze, T. L., 1986, Percolation Theory as a Tool for Imitation of Fracture Process in Rocks: *Pure and Applied Geophysics*, v. 124, p. 731-748.

Chester, F.M., and Logan, J.M., 1986, Implications for mechanical properties of brittle faults from observations of the Punchbowl fault zone, California: *Pure and Applied Geophysics*, v.124, n.1-2, p.79-106.

Condon, S.M., 1997, *Geology of the Pennsylvanian and Permian Cutler Group and Permian Kaibab Limestone in the Paradox Basin, southeastern Utah and southwestern Colorado*. U.S. Geological Survey Bulletin, 2000-P, 46.

Cooke, M.L., 1997, Fracture localization along faults with spatially varying friction: *Journal of Geophysical Research*, v.102, n.B10, p. 22425-22434.

Cowie, P.A., Sornette, D., Vanneste, C., 1995, Multifractal scaling properties of a growing fault population: *Geophysical Journal International*, v.122, n.2, p.457-469.

Cruden, D.M., 1977, Describing the size of discontinuities: *International Journal of Rock Mechanics and Mining Sciences and Geomechanical Abstracts*, v.14, p.133-137.

Cruikshank, K.M., and Aydin, A., 1994, Role of fracture localization in arch formation, Arches National Park, Utah: *Geological Society of America Bulletin*, v.106, n.7, p. 879-891.

Cruikshank, K.M., Zhao, G., and Johnson, A.M., 1991, Analysis of minor fractures associated with joints and faulted joints: *Journal of Structural Geology*, v.13, n.8, p.865-886.

Daly, C., and Mueller, D., 2004, Characterization and modeling of fractured reservoir: Static model: 9th European Conference on the Mathematics of Oil Recovery, (A024), Cannes, France.

Davis, J.C., 1973, *Statistical data analysis for geologist*: Wiley, New York, New York, 550p.

Dershowitz, W.S., Lee, G., Geier, J., Foxford, T., La Pointe, P., and Thomas, A., 1998, FracMan version 2.6 interactive discrete feature data analysis, geometrical modeling and exploration simulation, user documentation, Report 923 – 1089, Golder Associates Inc., Seattle, Washington.

Dershowitz, W.S., and Herda, H.H., 1992, Interpretation of fracture spacing and intensity: *in* Tillerson, J.R., and Wawersik, W.R., eds., *Proceedings of the 33rd U.S. Symposium on Rock Mechanics*: Rotterdam, Balkema, pp. 19-30.

Dershowitz, W.S. and Einstein, H.H., 1988, Characterizing rock joint geometry with joint system models: *Rock Mechanics and Rock Engineering*, v. 21, n. 1, pp. 21-51.

Dreuzy, J.R., Darcel, C., Davy, P., and Bour, O., 2004, Influence of spatial correlation of fracture centers on the permeability of 2D fracture networks following a power law length distribution: *Water Resources Research*, v. 40, n. 1, pp. 11.

Dershowitz, W.S., 1984, Rock joint systems: Ph.D., Thesis, MIT, Cambridge, MA.

Dershowitz, W.S., 1979, A probabilistic model for the deformability of jointed rock masses: M.S. Thesis, MIT, Cambridge, MA.

Dreuzy, J.R., Davy, P., and Bour, O., 2001, Hydraulic properties of 2D fracture networks following a power law length distribution: 1, Effective connectivity: *Water Resources Research*, v. 37, n. 8, pp. 2065-2078.

Deutsch, C.V., and Journel, A.G., 1992, *GSLIB, Geostatistical software library and user's guide*: Oxford University Press, London, 340p.

Dreuzy, J.R., Davy, P., and Bour, O., 2001, Hydraulic properties of 2D fracture networks following a power law length distribution: 2, Permeability of networks based on lognormal distribution of apertures: *Water Resources Research*, v. 37, n. 8, pp. 2079-2095

Dubrule, O., 1998, *Geostatistics in petroleum geology*, AAPG course note series #38, AAPG, Tulsa OK, 52p.

Dubrule, O., and Haldorsen, H.H., 1986, *Geostatistics for permeability estimation in reservoir characterization*, in Lake, L.W., and Carroll, H.B., eds.

Ehlen, J., 2000, Fractal analysis of joint patterns in granite: *International Journal of Rock Mechanics and Mining Sciences*, v. 37, p. 909-922.

Engelder, T. and Delteil, J., 2004, The orientation distribution of single joint sets: *in* Cosgrove, J. and Engelder, T., eds., *The initiation, propagation and arrests of joints and other fractures*. Geological Society of London Special Publication 231, pp. 285-297.

ArcGIS, 2006, *ArcMap Version 9.2*: Environmental Systems Research Institute, Inc., Redland, California.

Fischer, M.P., and Christensen, R.D., 2004, Insights into the growth of basement uplifts deduced from a study of fracture systems in the San Rafael monocline, east central Utah: *Tectonics*, v. 23, p. 1-14.

Fletcher, R.C., and Pollard, D.D., 1981, Anticrack model for pressure solution surfaces: *Geology*, v.9, n.9, p. 419-424.

Forster, C.B., and Evans, J.P., 1991 Hydrogeology of thrust faults and crystalline thrust sheets: results of combined field and modeling studies: *Geophysical Research Letters*, v.18, n.5, p. 979-982.

Friedman, 1969, Structural analysis, of fractures in cores from Saticoy field, Ventura county, California: *American Association of Petroleum Geologists*, v. 53, n.2, p.367-389.

Geier, J.E., Lee, K., and Dershowitz, W.S., 1989, Field validation of conceptual models for fracture geometry: *Rock Mechanics and Rock Engineering*.

Gervais, F., Gentier, S., and Chiles, J.P., 1995, Geostatistical analysis and hierarchical modeling of a fracture network in a stratified rock mass: In Myer, Cook, Goodman and Tsang eds., *Fracture and jointed rock masses*, Balkena, Rotterdam.

Gillespie, P.A., Johnston, J.D., Loriga, M.A., McCaffrey, K.L.W., Walsh, L.L., and Watterson, L., 1999, Influence of layering on vein systematics in line samples, *in* McCaffrey, K.J. W., et al., eds. *Fractures fluid flow in and mineralization*: Geological Society of London, Special Publication 155, p.35-56.

Gillespie, P.A., Howard, C.B., Walsh, J. J., and Watterson, J., 1993, Measurement and characterization of spatial distributions of fractures: *Tectonophysics*, v.226, p.113-141.

Goddard, J.V., and Evans, J.P., 1995, Chemical changes and fluid-rock interaction in faults of crystalline thrust sheets, northwestern Wyoming, USA: *Journal of Structural Geology*, v.17, n.4, p. 533-547.

Golf-Racht, T.D. van, 1982, *Fundamentals of reservoir engineering*: Amsterdam, Netherlands, Elsevier Science Publication Co., 710pp.

Gross, M.R., Bahat, D., and Becker, A., 1997, Relations between jointing and faulting based on fracture spacing ratios and fault slip profiles: A new method to estimate strain in layered rocks: *Geology*, v.25, n.10, p.887-890.

Gross, M.R., and Engelder, T., 1995, Strain accommodated by brittle failure in adjacent units of the Monterey Formation, U.S.A.: Scale effects and evidence for uniform displacement boundary conditions: *Journal of Structural geology*, v. 17, p. 1303-1318

Gross, M.R., 1995, Fracture partitioning: failure mode as a function of lithology in the Monterey Formation of coastal California: Geological Society of America Bulletin, v. 107, p. 779-792.

Gross, M.R., Fischer, M.P., Engelder, T., and Greenfield, R., 1995, Factor controlling joint spacing in interbedded sedimentary rocks: integrating numerical models with field observations from Monterey Formation, U.S.A., in Ameen, M.S. ed., Fractography: fracture topography as a tool in fracture mechanics and stress analysis: Geological Society Special Publication n. 2, p. 215-233.

Gross, M.R., 1993, The origin and spacing of cross joints: examples from the Monterey Formation, Santa Barbara Coastline, California: Journal of Structural geology, v. 15, p. 737-751.

Gueguen, Y., Chelidze, T., and Le Ravalec, M., 1997, Microstructures, Percolation Thresholds, and Rock Physical Properties: Tectonophysics, v. 279, p. 23-35.

Harris, J.F., Taylor, G.L., and Walper, J.L., 1960, Relation of deformational fractures in sedimentary rocks to regional and local structures: American Association of Petroleum Geologists, v. 44, n.12, p. 1853-1873.

Hennings, P.H., Olson, J.E., and Thompson, L.B., 2000, Combining outcrop data and three dimensional structural models to characterize fractured reservoirs: An example from Wyoming: American Association of Petroleum Geologists, v. 84, p. 830-849.

Higgs, N.G., 1981, Mechanical properties of ultrafine quartz, chlorite and bentonite in environments appropriate to upper-crustal earthquakes: PhD. Thesis, Texas A&M University, College Station, TX, 267p.

Harris, J.F., Taylor, G.L., and Walper, J.L., 1960, Relation of deformational fractures in sedimentary rocks to regional and local structures: American Association of Petroleum Geologists, v. 44, n.12, p. 1853-1873.

Hatton, C.G., Main, I.G., and Meredith, P.G., 1994, Non-universal scaling of fracture length and opening displacement: Nature, v. 367, pp. 160-162.

- Hennings, P.H., Olson, J.E., and Thompson, L.B., 2000, Combining outcrop data and three dimensional structural models to characterize fractured reservoirs: An example from Wyoming: American Association of Petroleum Geologists, v. 84, p. 830-849.
- Hintze, L.F., Willis, G.C., Laes, D.Y.M., Sprinkel, D.A. and Brown, K.D., 2000, Digital geologic map of Utah: Utah Geological Survey, scale 1:500000.
- Hoffman, W., Dunne, W.M., and Mauldon, M., 2004, Probabilistic-mechanistic simulation of bed normal joint patterns: *in* Cosgrove, J. and Engleder, T., eds., The initiation, propagation and arrests of joints and other fractures. Geological Society of London Special Publication 231, pp. 269-284.
- Huang, Q., and Angelier, J., 1989, Fracture spacing and its relation to bed thickness: Geological Magazine, v. 126, p. 355-362.
- Jolly, R.J.H., and Cosgrove, J.W., 2003, Geological evidence of patterns of fluid flow through fracture networks: examination using random realizations and connectivity analysis, *in* Ameen, M. ed., Fracture and in situ stress characterization of hydrocarbon reservoirs: Geological Society of London, Special Publication n. 209, p. 177-186.
- Josnin, J.Y., Jourde, H., Fenart, P., Bidaux, P., 2002, A three-dimensional model to simulate joint networks in layered rocks: Canadian journal of Earth Science, v. 39, pp. 1443-1455.
- Jourde, H., Flodin, E.A., Aydin, A., Durlifsky, L.J., and Wen, X., 2002, Computing permeability of fault zones in eolian sandstone from outcrop measurements: AAPG Bulletin, v. 86, n. 7, pp. 1187-1200.
- Kattenhorn, S.A., Aydin, A. and Pollard, D.D., 2000, Joints at high angles to normal fault strike: an explanation using 3-D numerical models of fault perturbed stress field: Journal of Structural Geology, v.22, p.1-23.
- La Pointe, P.R., 2002, Derivation of parent fracture population statistics from trace length measurements of fractal fracture populations: International Journal of Rock Mechanics and Mining Sciences, v. 39, p. 381-388.
- LaPointe, P.R., 1993, Pattern analysis and simulation of joints for rock engineering: In Comprehensive Rock Engineering, v. 13, Rock Testing and Site Characterizations, pp. 215-239.

La Pointe, P.R., and Hudson, J.A., 1985, Characterization and interpretation of rock mass joint pattern: Geological Society of America, Special Paper 199. 37p.p.

Lamy, P., Swaby, P.A., Rowbotham, P.S., Dubrule, O., and Hass, A., 1999, From seismic to reservoir properties with geostatistical inversion: SPE Reservoir Evaluation and Engineering, v.2, n.4, pp. 334 – 340.

Lisle, R.J., 1994, Detection of zones of abnormal strains in structures using Gaussian curvature analysis: American Association of Petroleum Geologists, v. 78, n.12 p. 1811-1819.

Mace, L., Souche, L., and Mallet, J.L., 2004, 3D Fracture modeling integrating geomechanics and geologic data: AAPG International Conference, Cancun, Mexico.

Matheron, G., 1963, Principles of geostatistics: Economic Geology, v.58, p. 1246-1266

Marrett, R., Ortega, O.J., Kelsey, C.M., 1999, Extent of power law scaling for natural fractures in rocks: Geology, v. 27, pp. 799-802.

Martel, S.J., and Boger, W.A., 1998, Geometry and mechanics of secondary fracturing around small three-dimensional faults in granitic rock: Journal of Geophysical Research, v.103, n.B9, p. 21299-21314.

Martel, S.J., Pollard, D.D, and Segall, P., 1988, Development of simple strike-slip fault zones, Mount Abbot Quadrangle, Sierra Nevada, California: Geological Society of America Bulletin, v.100, n.9, p. 1451-1465.

Martin, G.H., 1963, Petrofabric studies may find fracture porosity reservoirs: World Oil, v.156, p. 52-54.

Mauldon, M., Dunne, W.M., Rohrbaugh, M.B., 2001, Circular scanlines and circular windows: new tools for characterizing the geometry of fracture traces: Journal of structural geology, v. 23, p. 247-258.

Mauldon, M., Dershowitz, W., 2000, A multi-dimensional system of fracture abundance measures: Geological Society of America, Abstracts with programs, v. 32, n. 7, pp. A474.

Mauldon, M., 1998, Estimating mean fracture trace length and density from observations in convex windows: *Rock mechanics and Rock engineering*, v. 31, pp. 201-216.

McGill, G.E. and Stormquist, A.W., 1975, Origin of graben in the Needles District, Canyonlands National Park, Utah, in Fassett, J.E., ed., *Canyonlands country: Four Corner Geological Society, 8th Field Conference Guidebook*, p. 235-243.

McQuillan, H., 1974, Fracture patterns on Kuh-e Asmari anticline, southwest Iran: *AAPG Bulletin*, v. 58, n. 2. pp. 236-246.

McQuillan, H., 1973, Small scale fracture density in Asmari formation of southwest Iran and its relation to bed thickness and structural setting: *AAPG Bulletin*, v. 57, n. 2. p. 236-246.

Medwedeff, D.A., and Suppe, J., 1997, Multibend fault bend folding: *Journal of structural geology*, v. 19, n. 3-4, p. 279-292.

Mollema, P.N., and Antonellini, M., 1999, Development of strike-slip faults in the dolomites of the Sella Group, northern Italy: *Journal of Structural Geology*, v.21, n.3, p.273-292.

Moore, J.M., and Schultz, R.A., 1999, Processes of faulting in jointed rocks of Canyonlands National Park, Utah: *Geological Society of America Bulletin*, v.111, p. 808-822.

Mudge, 1972, *Structural geology of the Sun River Canyon and adjacent areas, Northwestern Montana: Geological Survey Professional Paper, 663B, U.S. Government printing office, Washington D.C., 52p.*

Narr, W., 1996, Estimating average fracture spacing in subsurface rock: *AAPG Bulletin*, v. 80, pp. 1565-1586.

Nelson, R.A., 1985, *Geologic analysis of naturally fractured reservoirs: Houston, Texas, Gulf Publishing, 320p.*

Nelson, R.A., 1975, Factors affecting orientation and distribution of regional fractures: *Geological Society of America, South Central Section, 9th Annual Meeting, Abstracts with Programs*, v.7, n.2, p. 221.

Nickelsen, R.P., and Hough, V.N.D., 1969, Jointing in south-central New York: reply: Geological Society of America Bulletin, v.80, n.5, p. 923-925.

Nickelsen, R.P., and Hough, V.N.D., 1967, Jointing in Appalachian plateau of Pennsylvania: Geological Society of America Bulletin, v.78, n.5, p. 609-629.

Odling, N.E., Gillespie, P., Bourguine, B., Castaing, C., Chiles, J.P., Christensen, N.P., Fillion, E., Genter, A., Olsen, C., Thrane, L., Trice, R., Aarseth, E., Walsh, J.J., and Watterson, J., 1999, Variations in fracture system geometry and their implications for fluid flow in fractured hydrocarbon reservoirs: Petroleum Geosciences, v. 5, pp. 373-384.

Odling, N. E., 1997, Scaling and connectivity of joint systems in sandstones from western Norway: Journal of Structural Geology, v. 19, p. 1251-1271

Odling, N.E., 1995, The development of network properties in natural fracture patterns: an example from the Devonian sandstones of Western Norway *in* Proceedings, International ISRM Symposium on Fractured and Jointed Rock Masses: Lake Tahoe, California, A.A., Balkema, Rotterdam, p.35-41.

Odling, N.E., 1992, Network properties of a two-dimensional natural fracture pattern: Pure and Applied Geophysics, v.138, n.1, p. 95-114.

Odling, N.E., and Webman, I., 1991, A “Conductance” mesh approach to the permeability of natural and simulated fracture patterns: Water Resources Research, v. 27, n. 10, pp. 2633-2643.

Ortega, O.J., and Marrett, R.A., 2000, Prediction of macrofracture properties using microfracture information, Mesaverde group sandstones, San Juan basin, New Mexico: Journal of Structural Geology, v. 22, p 571-587.

Ortega, O.J., Marrett, R.A., and Laubach, S.E., 2006, A scale independent approach to fracture intensity and average spacing measurements: AAPG Bulletin, v. 90, n. 2, pp. 193-208.

Peacock, D.C.P., Harris, S.D., and Mauldon, M., 2003, Use of curved scanlines and boreholes to predict fracture frequency: Journal of Structural Geology, v. 25, p. 109–119.

- Peacock, D.C.P., 2001, The temporal relationship between joints and faults: *Journal of Structural Geology*, v. 23, p. 329-341.
- Piteau, D.R., 1970, Geological factors significant to the stability of sloped cut in rocks: S. Af. Inst. Min. Met. Symposium Planning Open Pit Mines, Johannesburg, p. 33-53
- Price, N.J., 1966, Fault and joint development in brittle and semibrittle rocks: Oxford, United Kingdom, Pergamon Press, 176 pp.
- Priest, S.D., 1993, Fluid Flow in Discontinuities, *in* Discontinuity Analysis for Rock Engineering,: London, UK, Chapman and Hall, p. 340-381.
- Priest, S.D., and Hudson, J.A., 1981, Estimation of discontinuity spacing and trace length using scanline surveys: *International Journal of Rock Mechanics, Min. Sci., Gemech. Abstr.*, v.18, p. 183-137.
- Priest, S.D., and Hudson, J.A., 1976, Discontinuity spacings in rock: *International Journal of Rock Mechanics and Mining Sciences and Geomechanical Abstracts*, v. 13, p. 135 –148.
- Reches, Z., and Lockner, D.A., 1994, Nucleation and growth of faults in brittle rocks: *Journal of Geophysical Research*, v.99, n.B9, p. 18159-18174.
- Reiss, L.H., 1982, The reservoir engineering aspects of fractured formations: Houston, Texas, Gulf Publishing, 186p.
- Renshaw, C.E., and Park, J.C., 1997, Effect of mechanical interactions on the scaling of fracture length and aperture: *Nature*, v. 386, pp. 482-484.
- Reik, G.A., and Currie, J.B., 1974, A study of relations between rock fabric and joints in sandstone: *Canadian Journal of Earth Sciences*, v.11, n.9, p.1253-1268.
- Rives, T., Razack, M., Petit, J.P., and Rawsley, K.D., 1992, Joint spacing: analog and numerical simulations: *Journal of Structural Geology*, v.14, p. 925-937.
- Robinson, P.C., 1984, Numerical calculations of critical densities for lines and planes: *Journal of physics, A*, v.17, p. 2823-2830

- Robinson, P.C., 1983, Connectivity of fracture systems – a percolation theory approach: *Journal of physics, A*, v.16, p. 605-614
- Rohrbaugh, M.B., Dunne, W.M., and Mauldon, M., 2002, Estimating fracture trace intensity, density, and mean length using circular scanlines and windows: *American Association of Petroleum Geologists*, v. 86, p. 2089-2104.
- Rouleau, A., and Gale, J.E., 1985, Statistical characterization of the fracture system in the Stripa granite, Sweden: *International Journal of Rock Mechanics, Min. Sci. Gemech. Abstr.*, v. 22, p. 353-367.
- Scholz, C.H., and Anders, M.H., 1994, The permeability of faults: Open-File Report, U.S. Geological Survey, Report: OF 94-0228, p. 247-253.
- Shepard, D., 1968, A two-dimensional interpolation function for irregularly-spaced data: *Proceedings of the 1968 ACM National Conference*, p. 517-524.
- Sibson, R.H., 1977, Mechanics and effects of faulting: *Journal of the Geological Society of London*, v.133, n.Part 3, p. 175-275.
- Sinclair, S., 1980, Analysis of macroscopic fractures on Teton anticline, Northwestern Montana, M.S Thesis, Texas A & M, College station, TX, 102p.
- Smith, L., Forster, C., and Evans, J., 1990, Interaction of fault zones, fluid flow and heat transfer at the basin scale: *Hydrogeology, Selected papers*, v.2, p. 41-67.
- Smith, L., and Schwartz, F.W., 1984, An analysis of the influence of fracture geometry on mass transport in fractured media: *Water Resources Research*, v. 20, p. 1241-1252.
- Spooner, J.A., 1984, Field and laboratory study of fracture characteristics as a function of bed curvature in folded dolomites, Sawtooth mountains, Montana, M.S Thesis, University of Oklahoma, Norman, OK, 135p.
- Stauffer, D., 1985, Introduction to percolation theory: London, UK, Taylor and Francis, 190 p.p.
- Stearns, D., and Friedman, M., 1972, Reservoirs in fractured rock: *AAPG Memoir*, v. 16, n. 10, pp. 82-106.

- Stearns, D.W., 1968, Certain aspects of fractures in naturally deformed rocks. Rock Mechanics Seminar. R.E. Reick, Bedford, Terrestrial Sciences Laboratory, p. 97-118.
- Stearns, D. W. 1967. Certain aspects of fracture in naturally deformed rocks. *In*: Riecker, R. E. (ed.) *Rock Mechanics Seminar*. US Air Force Cambridge Research Laboratories, Contribution, AD 669375, p.97–118.
- Stearns, D.W., 1964, Macrofracture patterns on Teton anticline, northwest Montana (abs.): American Geophysical Union Trans., v.45, p. 107-108.
- Stone, D., 1984, Subsurface fracture maps predicted from borehole data: An example from the Eye-Dashaw Pluton, Atikokan, Canada: International Journal of Rock Mechanics, Scientific Geochemical abstract., v. 21, pp. 183-184.
- Suppe, J., 1983, Geometry and kinematics of fault-bend folding: American Journal of Science, v. 283, n. 7, pp. 684-721
- Taylor, W.L., Pollard, D.D., and Aydin, A., 1999, Fluid flow in discrete joint sets: Field observations and numerical simulations: Journal of Geophysical Research, v. 104, n. B12, pp. 28983-29006.
- Terzaghi, R.D., 1965, Sources of error in joint surveys: Geotechnique, v. 15, p. 287-304.
- Trudgill, B, and Cartwright, J., 1994, Relay-ramps forms and normal fault linkages, Canyonlands National Park, Utah: Geological Society of America Bulletin, v.106, p. 1143-1157.
- Underwood, C.A., Cooke, M.L., Simmon, J.A., and Muldoon, M. A., 2003, Straigraphic controls on vertical fracture patterns in Silurian dolomite, northeastern Wisconsin: American Association of Petroleum Geologists bulletin, v. 87, p. 121-142.
- Velde, B., Dubois, J., Touchard, G., Badri, A., 1990, Fractal analysis of fractures in rocks: the Cantor's dust method: Tectonophysics, v. 179, p. 345-352.
- Vermilye, J. M., and Scholz, C.H., 1995, Relation between vein length and aperture: Journal of Structural Geology, v. 17, n.3 pp. 423-434.

Willemsse, E.J.M., 1997, Segmented normal faults; correspondence between three-dimensional mechanical models and field data: *Journal of Geophysical Research*, v.102, n.B1, p.675-692.

Wall, B.R.G., Girbacea, R., Mesonjesi, A., Aydin, A., 2006, Evolution of fracture and fault-controlled fluid pathways in carbonates of the Albanides fold-thrust belt: *American Association of Petroleum Geologists*, v.90, n.8, p. 1227-1249.

Wu, H., and Pollard, D., 2002, Imaging 3-D fracture networks around boreholes: *AAPG Bulletin*, v. 86, n.4, pp. 593-604.

Wu, H., and Pollard, D.D., 1995, An experimental study of the relationship between joint spacing and layer thickness: *Journal of structural geology*, v. 17, p. 887-905.

Xu, C., Dowd, P.A., Mardia, K.V., and Fowell, R.J., 2006, A connectivity index for discrete fracture networks: *Mathematical Geology*, v.38, n.5, p. 611-634.

Zhang, X., and Sanderson, D.J., 1995, Anisotropic features of geometry and permeability in fractures rock masses: *Engineering Geology*, v. 40, pp. 65-75.

APPENDIX A

Table A1: Fracture simulation models, (Dershowtiz et al. 1999).

Model	Concept	Applicability	Advantages	Limitations
Orthogonal (Dershowitz and Einstein, 1988)	Fracture network simulated from 3 sets of unbounded orthogonal joints	Rock masses with completely defined rectangular rock blocks (mostly to hydrology)	Single geometry and treatment of data	Planar assumptions, limitation in the variation of fracture orientation
Baecher disk (Baecher et. al., 1978; Barton, 1978)	Generate fracture network from fracture centers that are distributed uniformly in space	Homogeneous rocks	Few field data available. Accurate in rock mechanics and hydraulics when a little is known	Do not simulate terminations of fractures; fractures must be planar.
Enhanced Baecher (Geier, et., al., 1989)	Generate fractures fracture centers located at random points in space. Intersections are calculated with pre-existing fractures	Fractured rock masses in which joint terminations are observed	Suited for simulation of connectivity of natural fracture population. Multiple intersections per fracture area possible	Fracture size distribution is not preserved; joints may be planar
BART (Dershowitz et. al., 1998)	Same principle as for the Enhanced Baecher	Fractured rock masses in which fracture terminations are observed	Quick simulation. Fracture size is preserved. Spatial	Fractures must be planar

	model, except that the center of fracture terminating at intersections is generated from point on fracture intersection		correlation in the simulated fracture population	
Veneziano (Veneziano, 1978)	Fracture network generated in 3 stochastic processes based on Poisson plane and Poisson lines	Suited for 100% persistent and unbounded fractures	Polygonal shapes are often observed in nature. More appropriate than orthogonal model for most cases, specially in case of coplanarity	Often fail to construct blocks. Intersection of fractures does not often match joint edges. Complex 3 D model
Dershowitz (Dershowitz , 1984)	Fracture network generated from 2 stochastic processes based on Poisson plane	Accurate for systems which exhibit distinct rock blocks bounded polygonal fractures and orientation dispersion	Model distinct rock blocks of various shapes, flexibility in the distribution of fracture orientations. Joint intersection at joint edges	Can generate large number of smaller polygons. Not so well fitted for coplanar fractures
Mosaic Tessellation (Dershowitz and Einstein, 1988)	Deterministic and/or stochastic generation of the blocks, then definition of fracture planes	Fracture systems resulting from a process of block formation (jointing in columnar basalt)	Manage non coplanarity, creation of the blocks first	Not so accurate in cases that do not display polyhedral blocks and polygonal fractures; blocks created first;

				indirect modeling of location, orientation and shape of fractures
Poisson Rectangle (Dershowitz, 1998)	Same concept as Enhanced Baecher except that fractures area rectangular	Same as Enhanced Baecher	Same as Enhanced Baecher	Specific conceptual model. Require a good knowledge of the rock mass geometry
Geostatistical (Gervais et. al., 1995)	Generate fractures according to a specified variogram	Describe the spatial behavior of regionalized variables of the fracture network	Account for a good spatial correlation	The size of the sampling area must be consequent compared to the study area
War Zone (Geier et. al., 1989)	Simulate higher densities of fractures between two major subparallel fractures	Simulation of fracture network in shear zones and in the surrounding rock mass	Binary model. Identify “ordinary zone” and “non-fractured zone”	Specific conceptual model. Require good knowledge of rock mass geometry
Non-Planar Zone (Dershowitz et. al., 1998)	Generate fractures along non-planar user defined surface	Simulation of fracture network along specified features (eg. Deformation zone)	Enhance rock zones with specific geometrical properties. Binary model	Require good knowledge of rock mass geometry
Levy-Lee Fractal (Geier et. al., 1989)	Generate clusters of smaller fractures around wider fractures	In combination with geometrical analysis: Hierarchical fracture trace model	Accounts for the chronology of fracture formation. Ability to generate a non-stationary	Do not consider the size and shape of the blocks delimited by the simulated

			fracture system with a set of parameters that remain constant throughout the generation system	fractures. Definition of the most appropriate fractal dimension.
Nearest-neighbour (Geier et. al., 1989)	Fractures are organized into primary, secondary and tertiary groups and area generated in this sequence	Can account for the generation of fracture network according to the theory of fracture genesis	Generate clusters of fractures around primary group. More explicit than Levy-Lee model if fractures can be classified	Must have enough data to assess the different groups and chronology.

APPENDIX B

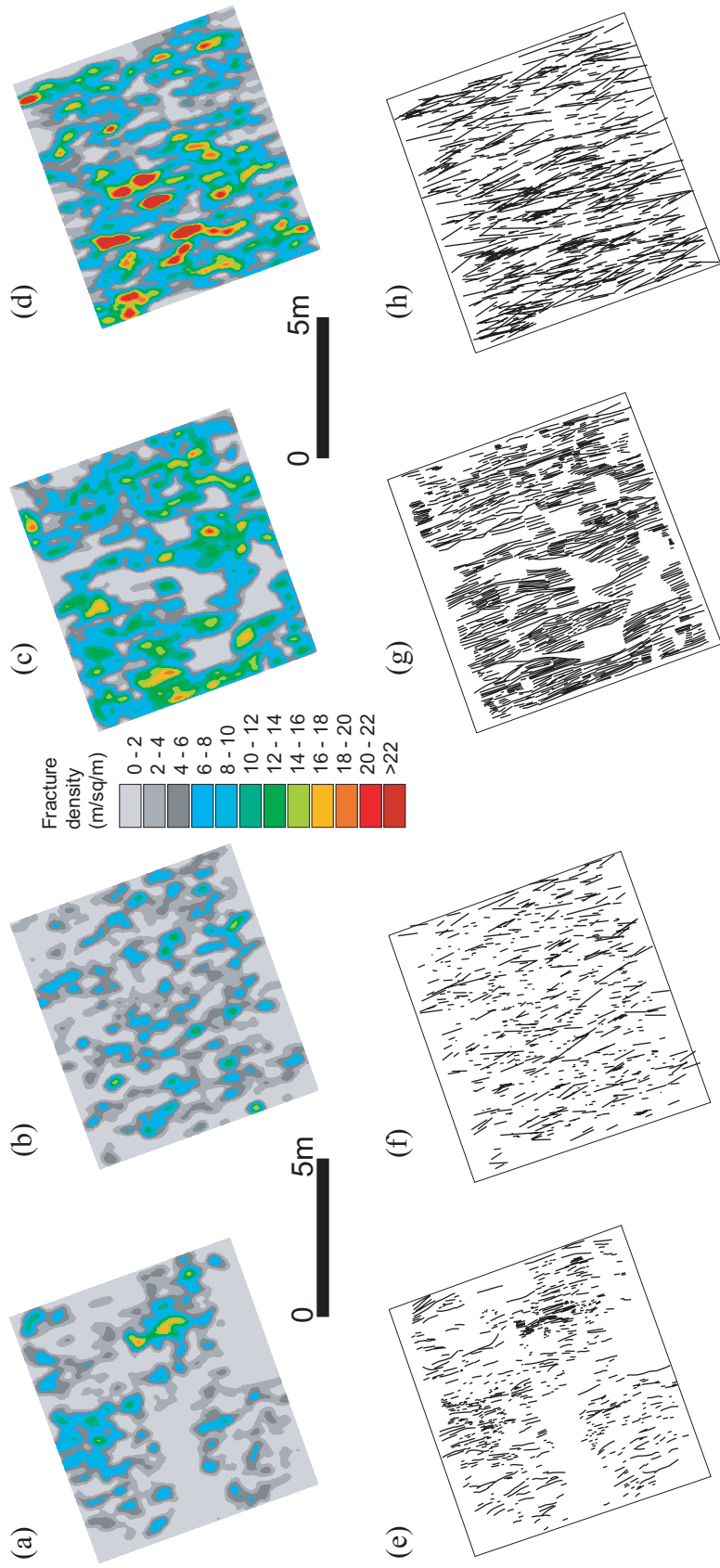


Figure A1: (a) Density map of longitudinal fractures for location M01. (b) Density map of simulated longitudinal fractures for location M01. The fractures for area M01 are extracted from the simulated map generated for the entire Teton anticline. (c) Density map of longitudinal fractures for location M02. (d) Density map of simulated longitudinal fractures for location M02. The fractures for area M02 are extracted from the simulated map generated for the entire Teton anticline. (e) Fracture map of longitudinal set for location M01. (f) Simulated fracture map of longitudinal set for location M01. (g) Fracture map of longitudinal set for location M02. (h) Simulated fracture map of longitudinal set for location M02.

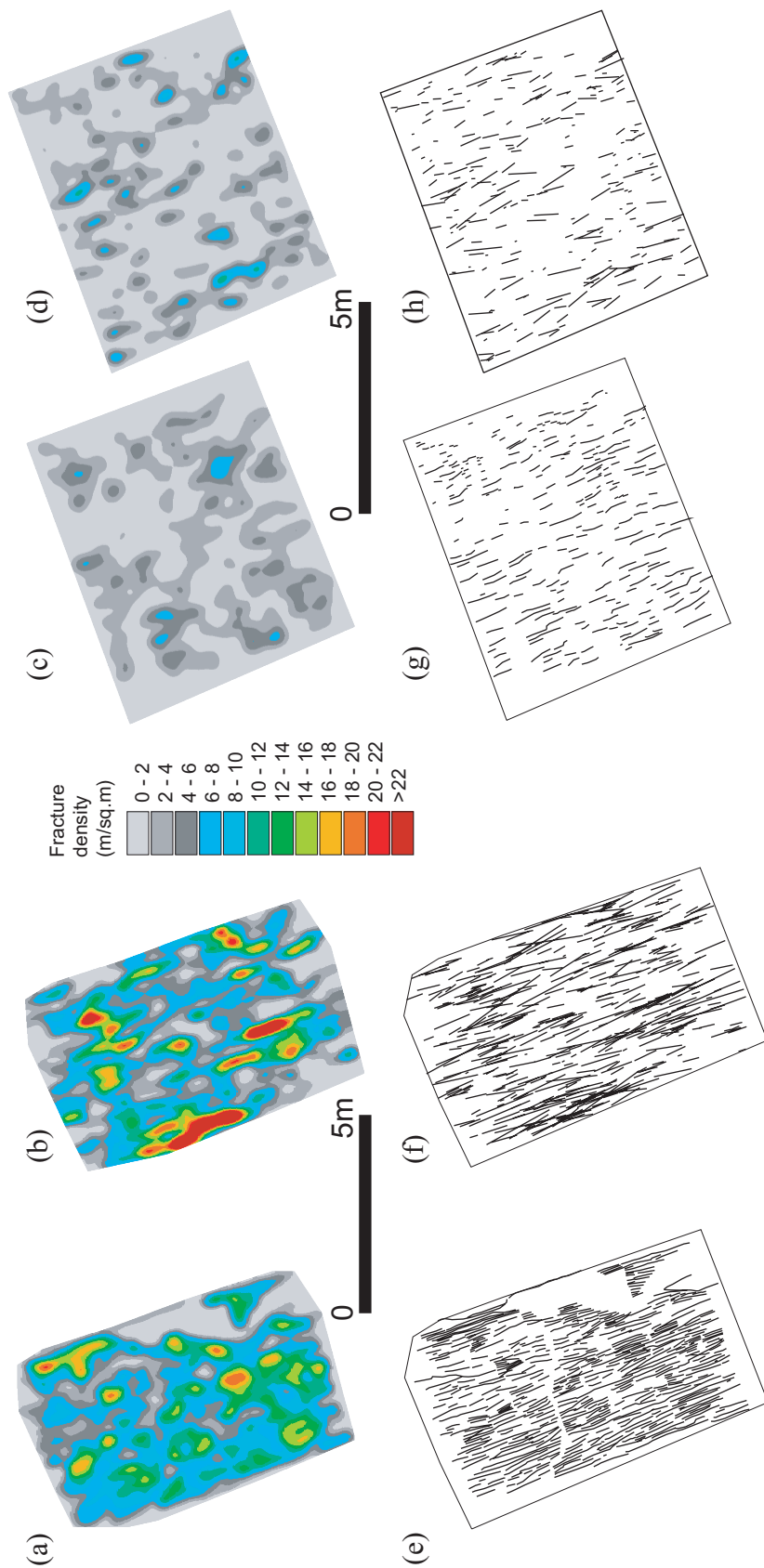


Figure A2: (a) Density map of longitudinal fractures for location M03. (b) Density map of simulated longitudinal fractures for location M03. The fractures for area M03 are extracted from the simulated map generated for the entire Teton anticline. (c) Density map of longitudinal fractures for location M04. (d) Density map of simulated longitudinal fractures for location M04. The fractures for area M04 are extracted from the simulated map generated for the entire Teton anticline. (e) Fracture map of longitudinal set for location M03. (f) Simulated Fracture map of longitudinal set for location M03. (g) Fracture map of longitudinal set for location M04. (h) Simulated fracture map of longitudinal set for location M04.

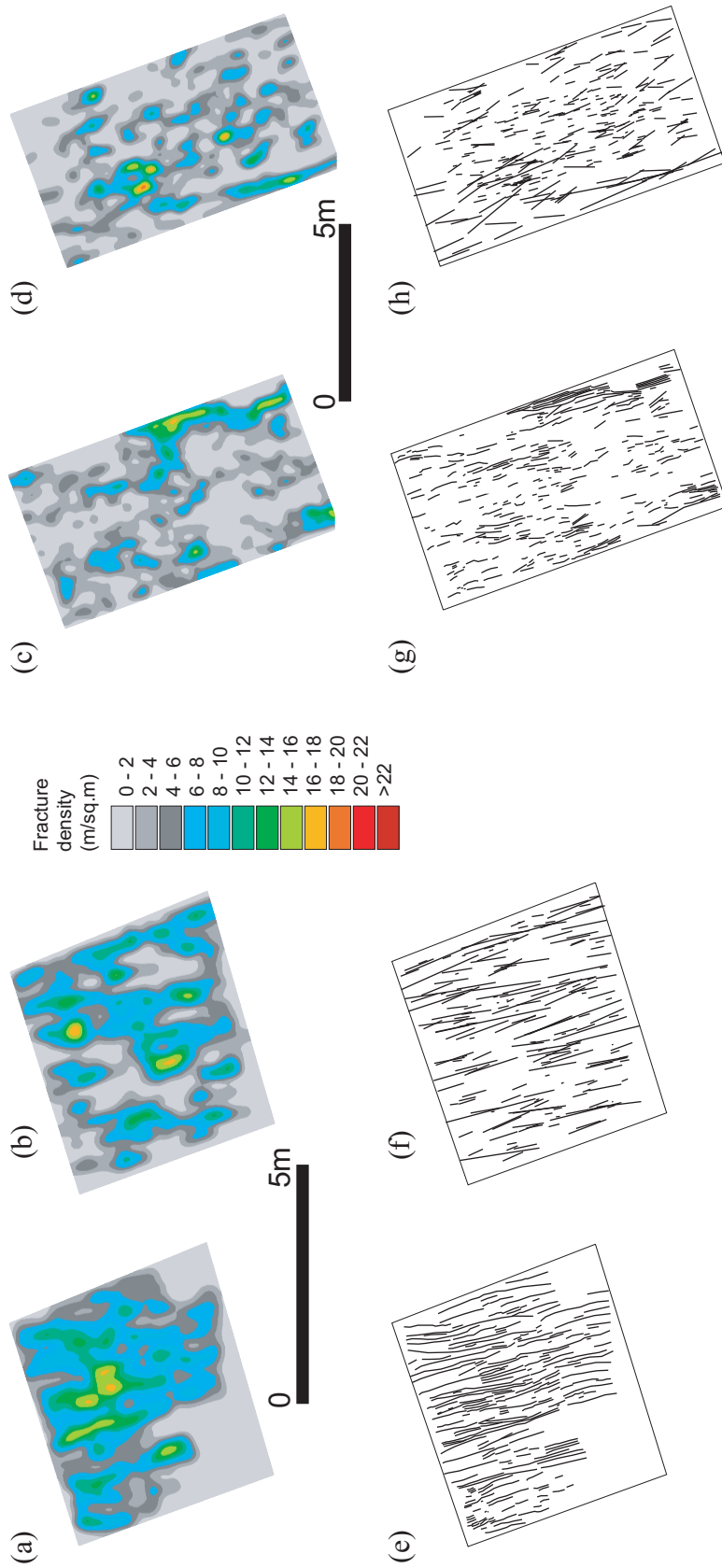


Figure A3: (a) Density map of longitudinal fractures for location M05. (b) Density map of simulated longitudinal fractures for location M05. The fractures for area M05 are extracted from the simulated map generated for the entire Teton anticline. (c) Density map of longitudinal fractures for location M06. (d) Density map of simulated longitudinal fractures for location M06. The fractures for area M06 are extracted from the simulated map generated for the entire Teton anticline. (e) Fracture map of longitudinal set for location M05. (f) Simulated Fracture map of longitudinal set for location M05. (g) Fracture map of longitudinal set for location M06. (h) Simulated fracture map of longitudinal set for location M06.

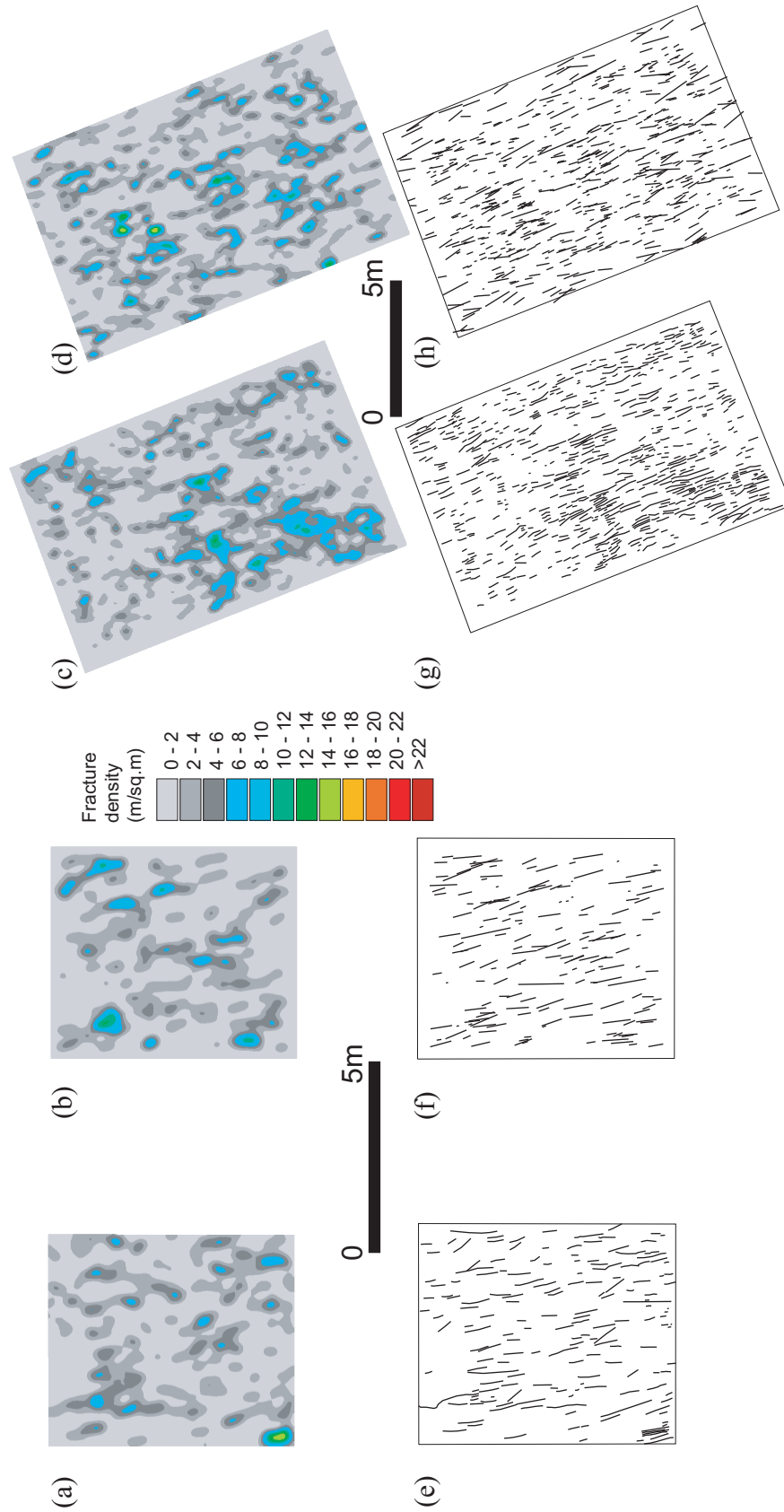


Figure A4: (a) Density map of longitudinal fractures for location M07. (b) Density map of simulated longitudinal fractures for location M07. The fractures for area M07 are extracted from the simulated map generated for the entire Teton anticline. (c) Density map of longitudinal fractures for location M8. (d) Density map of simulated longitudinal fractures for location M08. The fractures for area M08 are extracted from the simulated map generated for the entire Teton anticline. (e) Fracture map of longitudinal set for location M07. (f) Simulated fracture map of longitudinal set for location M07. (g) Fracture map of longitudinal set for location M08. (h) Simulated fracture map of longitudinal set for location M08.

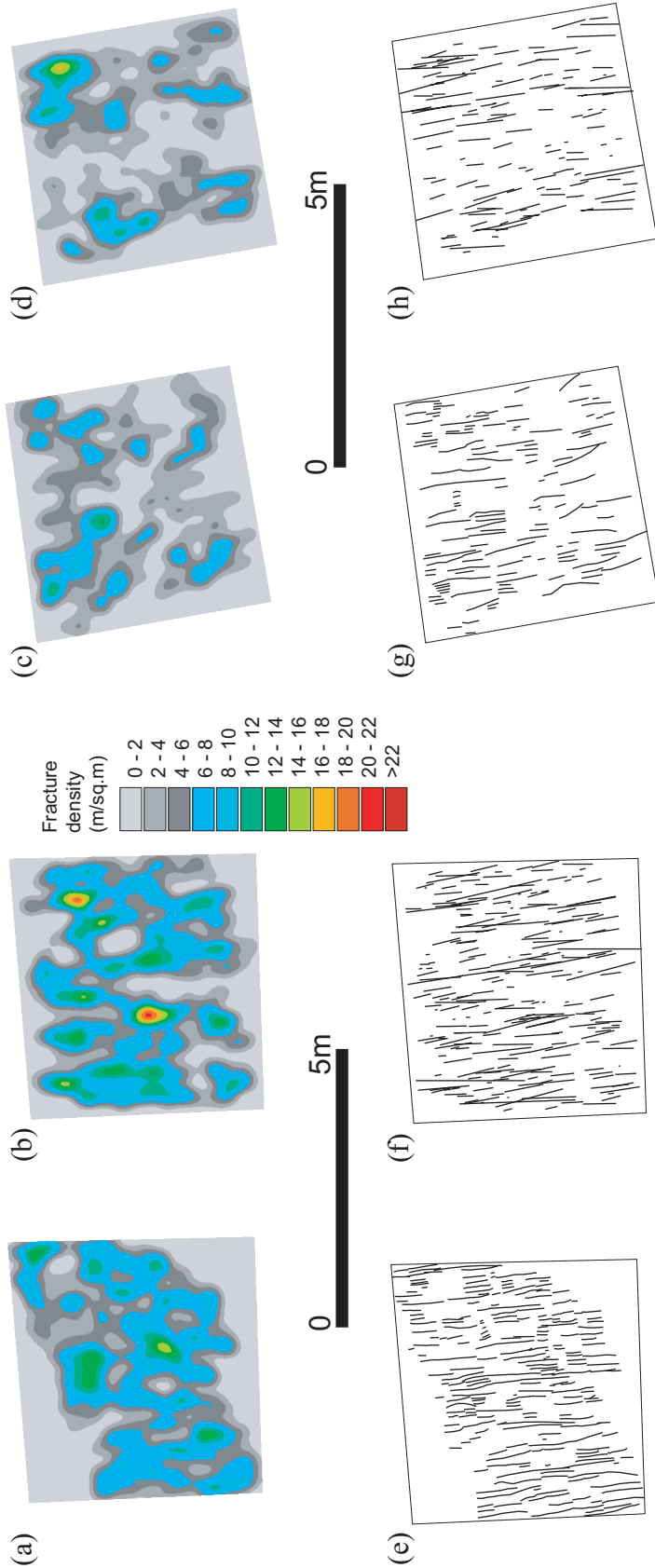


Figure A5: (a) Density map of longitudinal fractures for location M09. (b) Density map of simulated longitudinal fractures for location M09. The fractures for area M09 are extracted from the simulated map generated for the entire Teton anticline. (c) Density map of longitudinal fractures for location M10. (d) Density map of simulated longitudinal fractures for location M10. The fractures for area M10 are extracted from the simulated map generated for the entire Teton anticline. (e) Fracture map of longitudinal set for location M09. (f) Simulated fracture map of longitudinal set for location M09. (g) Fracture map of longitudinal set for location M10. (h) Simulated fracture map of longitudinal set for location M10.

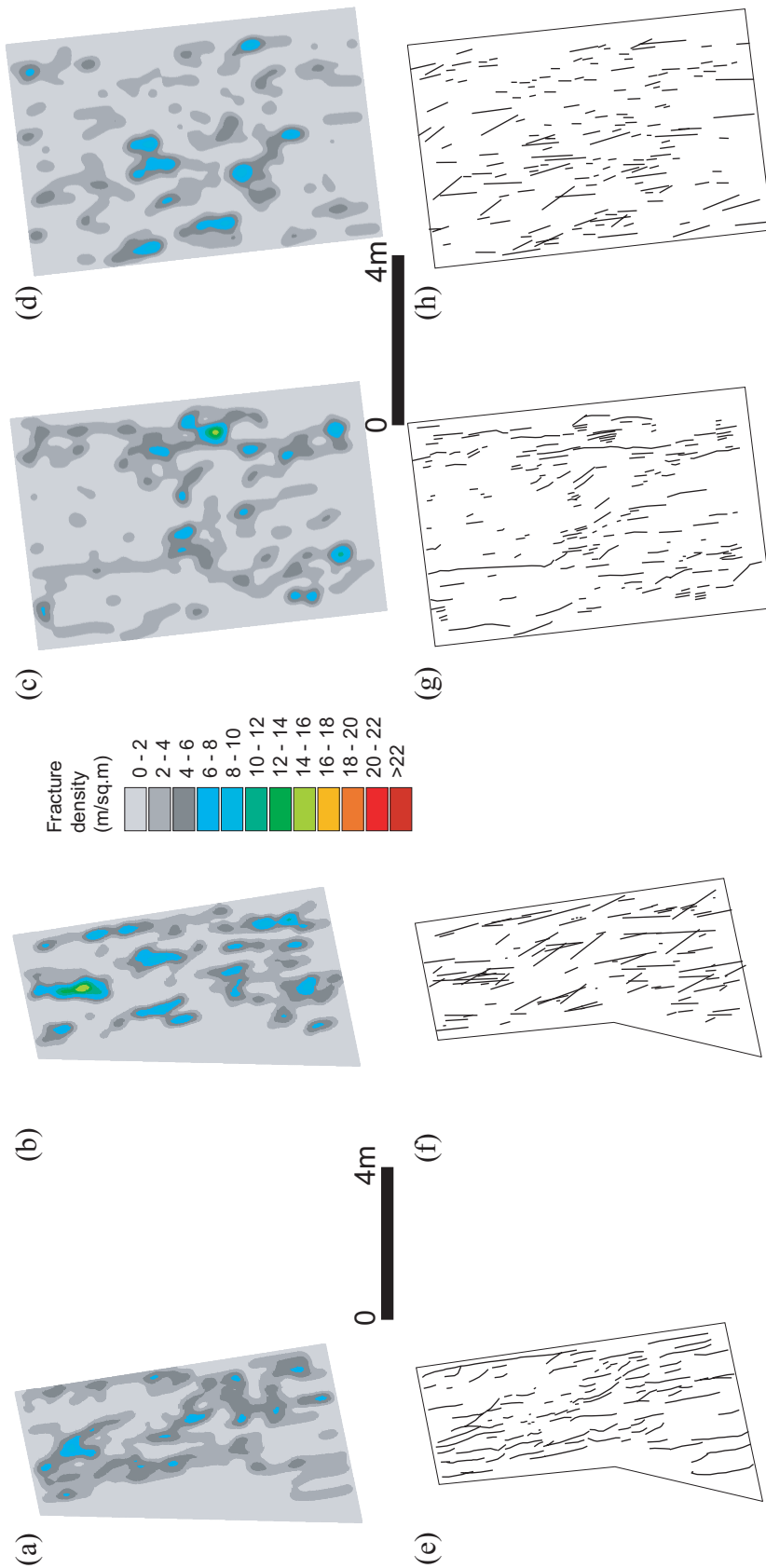


Figure A6: (a) Density map of longitudinal fractures for location M11. (b) Density map of simulated longitudinal fractures for location M11. The fractures for area M11 are extracted from the simulated map generated for the entire Teton anticline. (c) Density map of longitudinal fractures for location M12. (d) Density map of simulated longitudinal fractures for location M12. The fractures for area M12 are extracted from the simulated map generated for the entire Teton anticline. (e) Fracture map of longitudinal set for location M11. (f) Simulated fracture map of longitudinal set for location M11. (g) Fracture map of longitudinal set for location M12. (h) Simulated fracture map of longitudinal set for location M12.

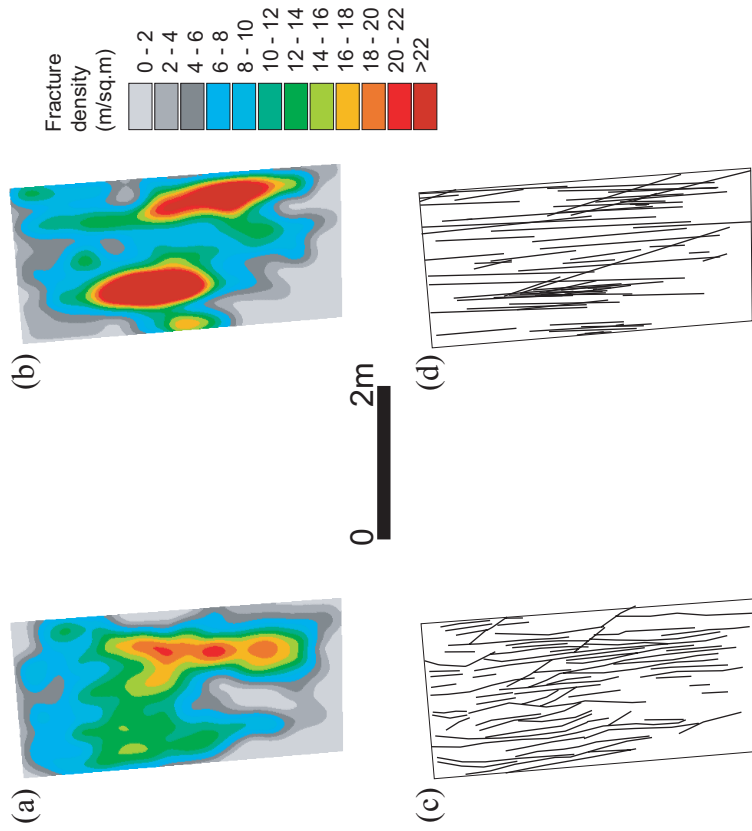


Figure A7: (a) Density map of longitudinal fractures for location M13. (b) Density map of simulated longitudinal fractures for location M13. The fractures for area M13 are extracted from the simulated map generated for the entire Teton anticline. (c) Fracture map of longitudinal set for location M13. (d) Simulated fracture map of longitudinal set for location M13.

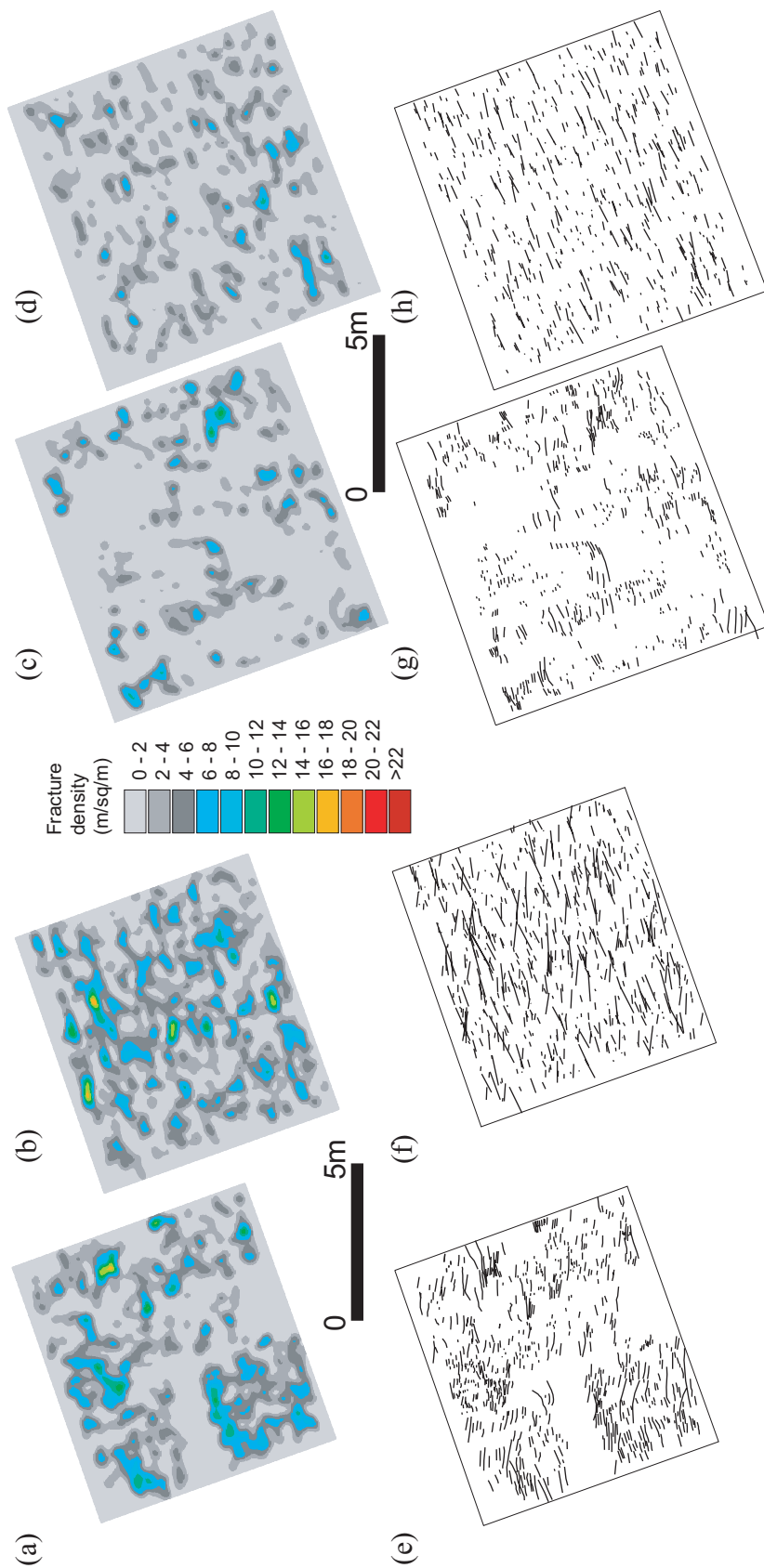


Figure A8: (a) Density map of transverse fractures for location M01. (b) Density map of simulated transverse fractures for location M01. The fractures for area M01 are extracted from the simulated map generated for the entire Teton anticline. (c) Density map of transverse fractures for location M02. (d) Density map of simulated transverse fractures for location M02. The fractures for area M02 are extracted from the simulated map generated for the entire Teton anticline. (e) Fracture map of transverse set for location M01. (f) Simulated fracture map of transverse set for location M01. (g) Fracture map of transverse set for location M02. (h) Simulated fracture map of transverse set for location M02.

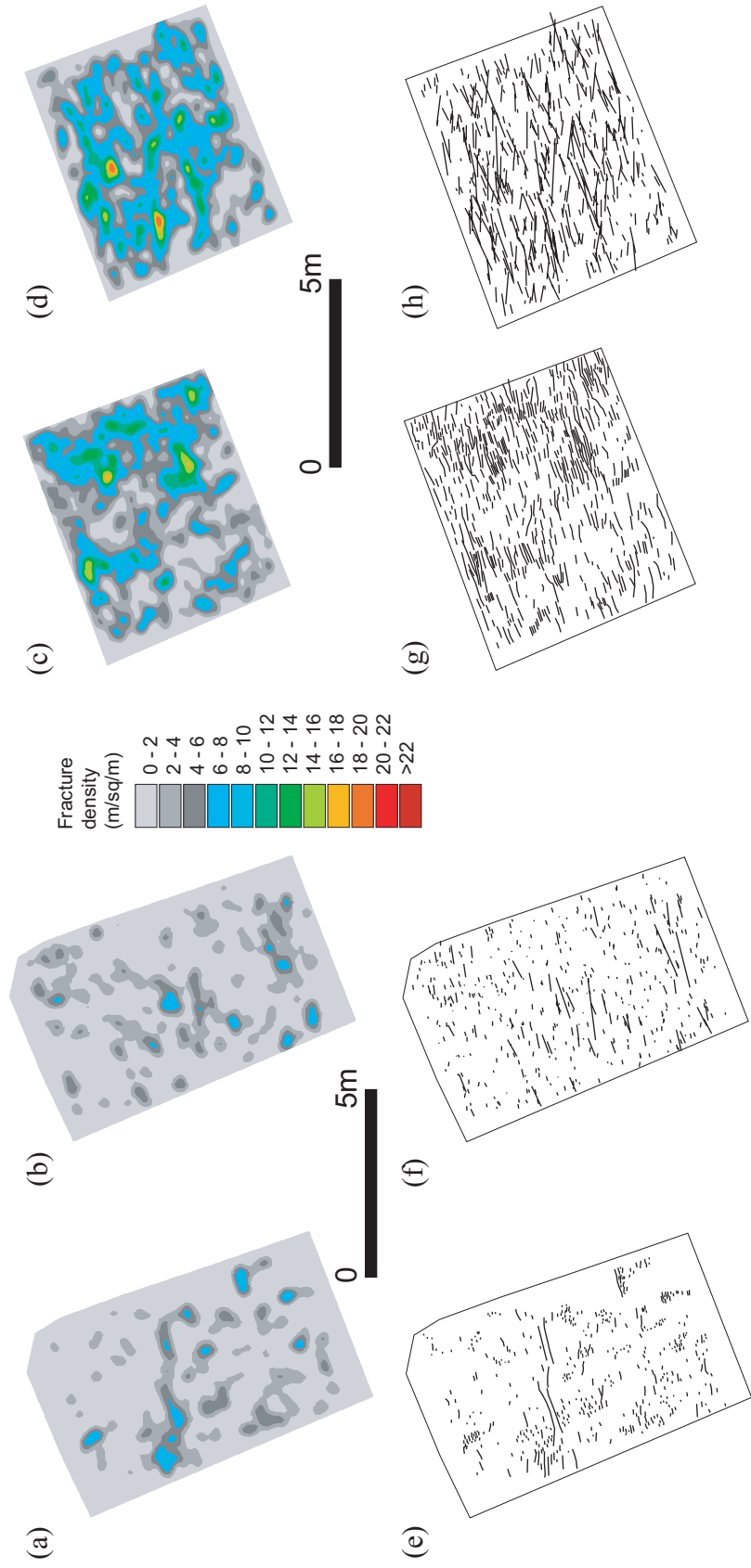


Figure A9: (a) Density map of transverse fractures for location M03. (b) Density map of simulated transverse fractures for location M03. The fractures for area M03 are extracted from the simulated map generated for the entire Teton anticline. (c) Density map of transverse fractures for location M04. (d) Density map of simulated transverse fractures for location M04. The fractures for area M04 are extracted from the simulated map generated for the entire Teton anticline. (e) Fracture map of transverse set for location M03. (f) Simulated fracture map of transverse set for location M03. (g) Fracture map of transverse set for location M04. (h) Simulated fracture map of transverse set for location M04.

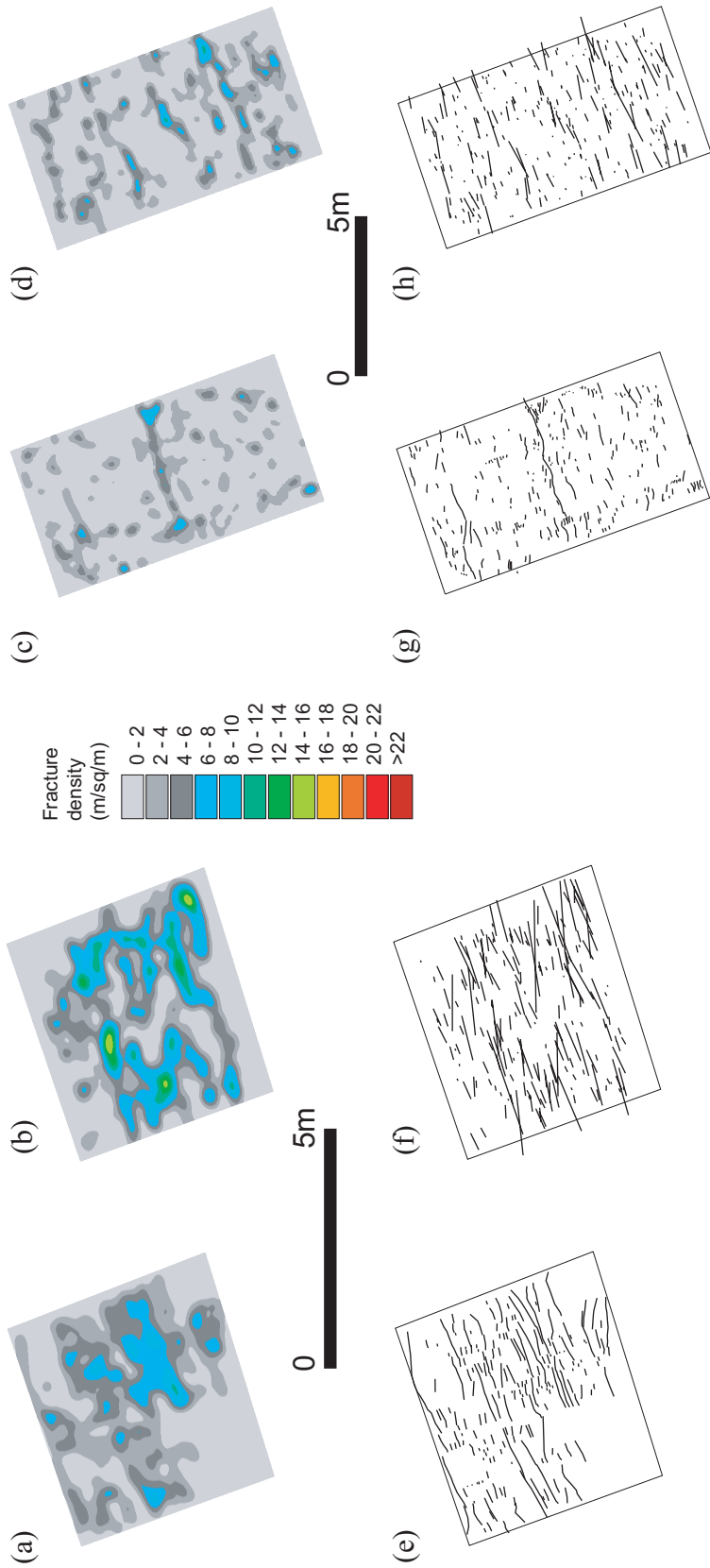


Figure A10: (a) Density map of transverse fractures for location M05. (b) Density map of simulated transverse fractures for location M05. The fractures for area M05 are extracted from the simulated map generated for the entire Teton anticline. (c) Density map of transverse fractures for location M06. (d) Density map of simulated transverse fractures for location M06. The fractures for area M06 are extracted from the simulated map generated for the entire Teton anticline. (e) Fracture map of transverse set for location M05. (f) Simulated fracture map of transverse set for location M05. (g) Fracture map of transverse set for location M06. (h) Simulated fracture map of transverse set for location M06.

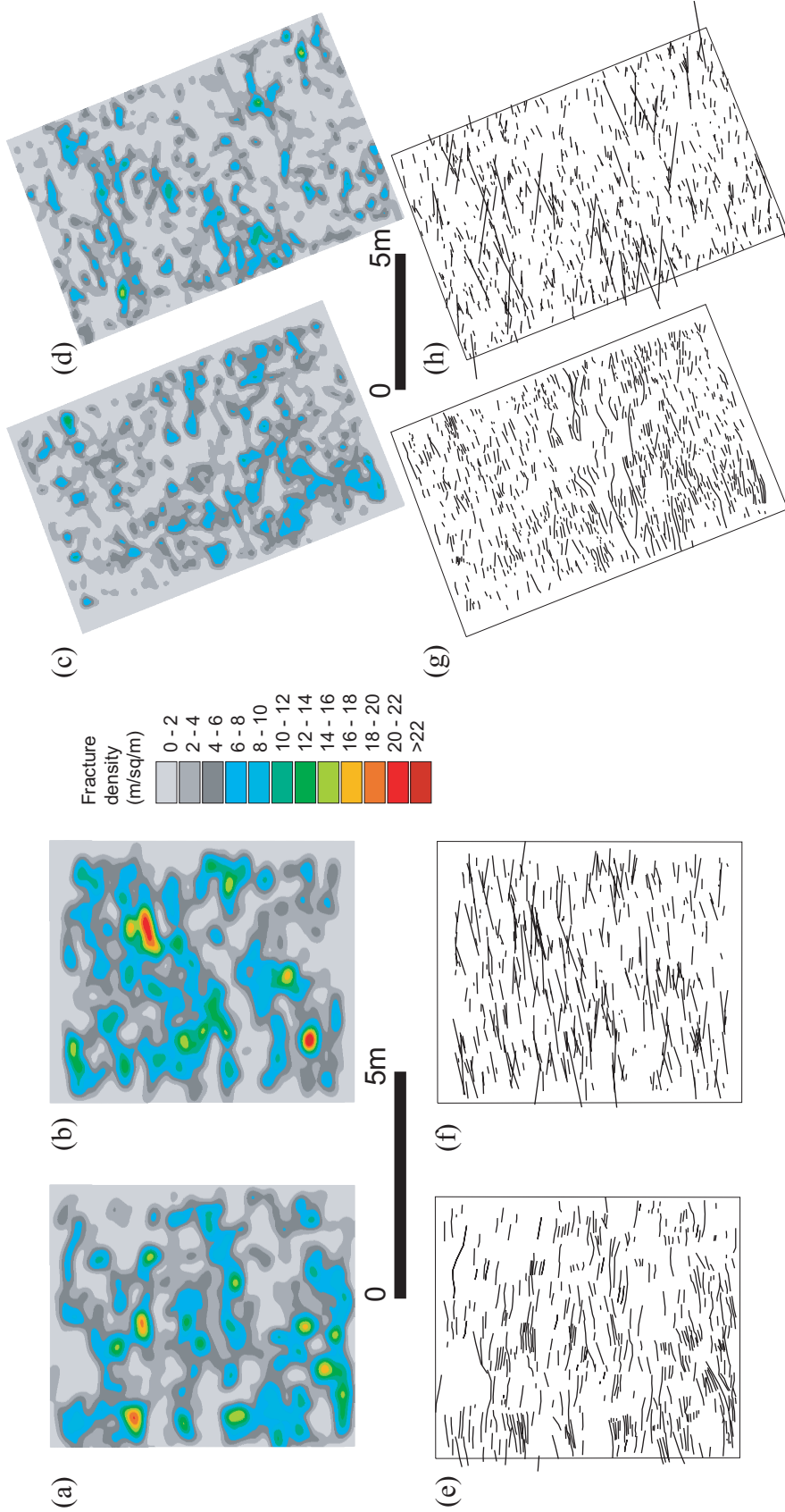


Figure A11: (a) Density map of transverse fractures for location M07. (b) Density map of simulated transverse fractures for location M07. The fractures for area M07 are extracted from the simulated map generated for the entire Teton anticline. (c) Density map of transverse fractures for location M08. (d) Density map of simulated transverse fractures for location M08. The fractures for area M08 are extracted from the simulated map generated for the entire Teton anticline. (e) Fracture map of transverse set for location M07. (f) Simulated fracture map of transverse set for location M07. (g) Fracture map of transverse set for location M08. (h) Simulated fracture map of transverse set for location M08.

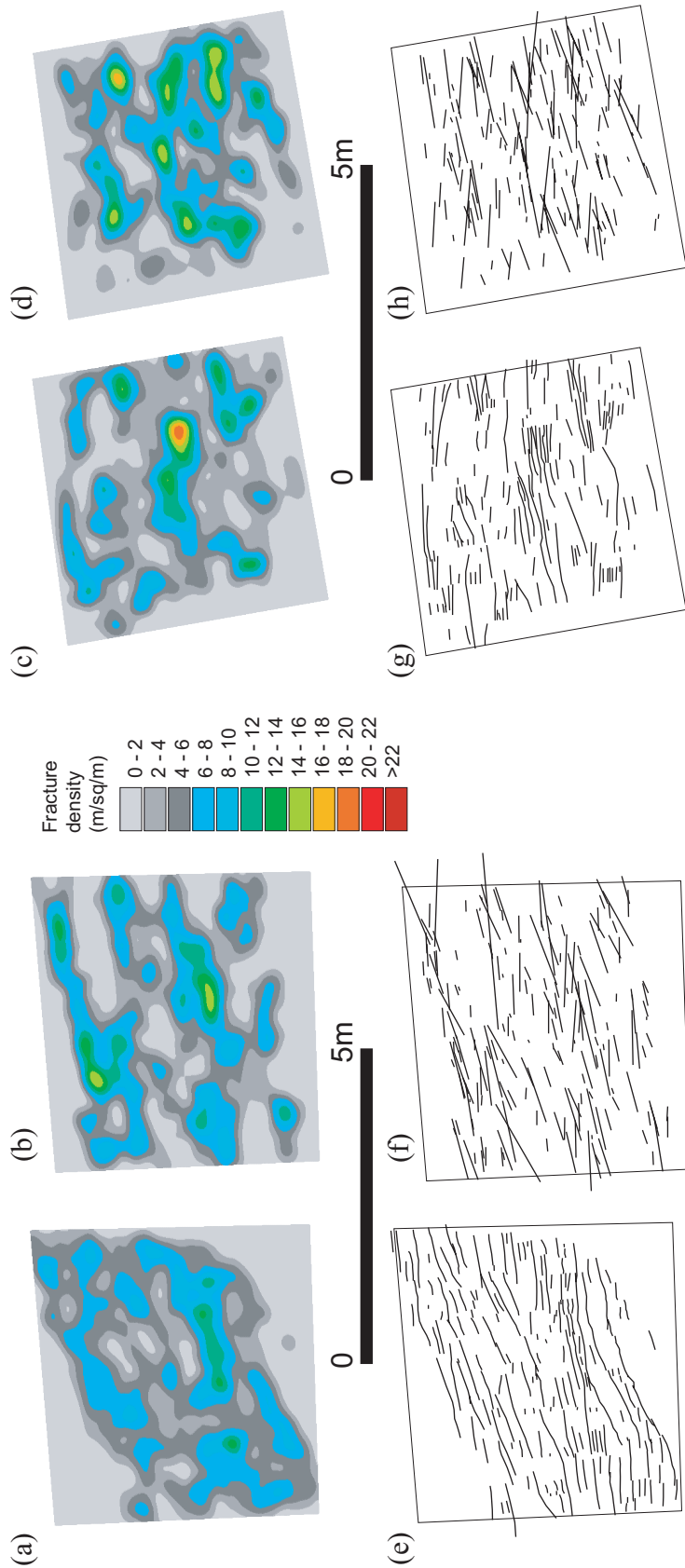
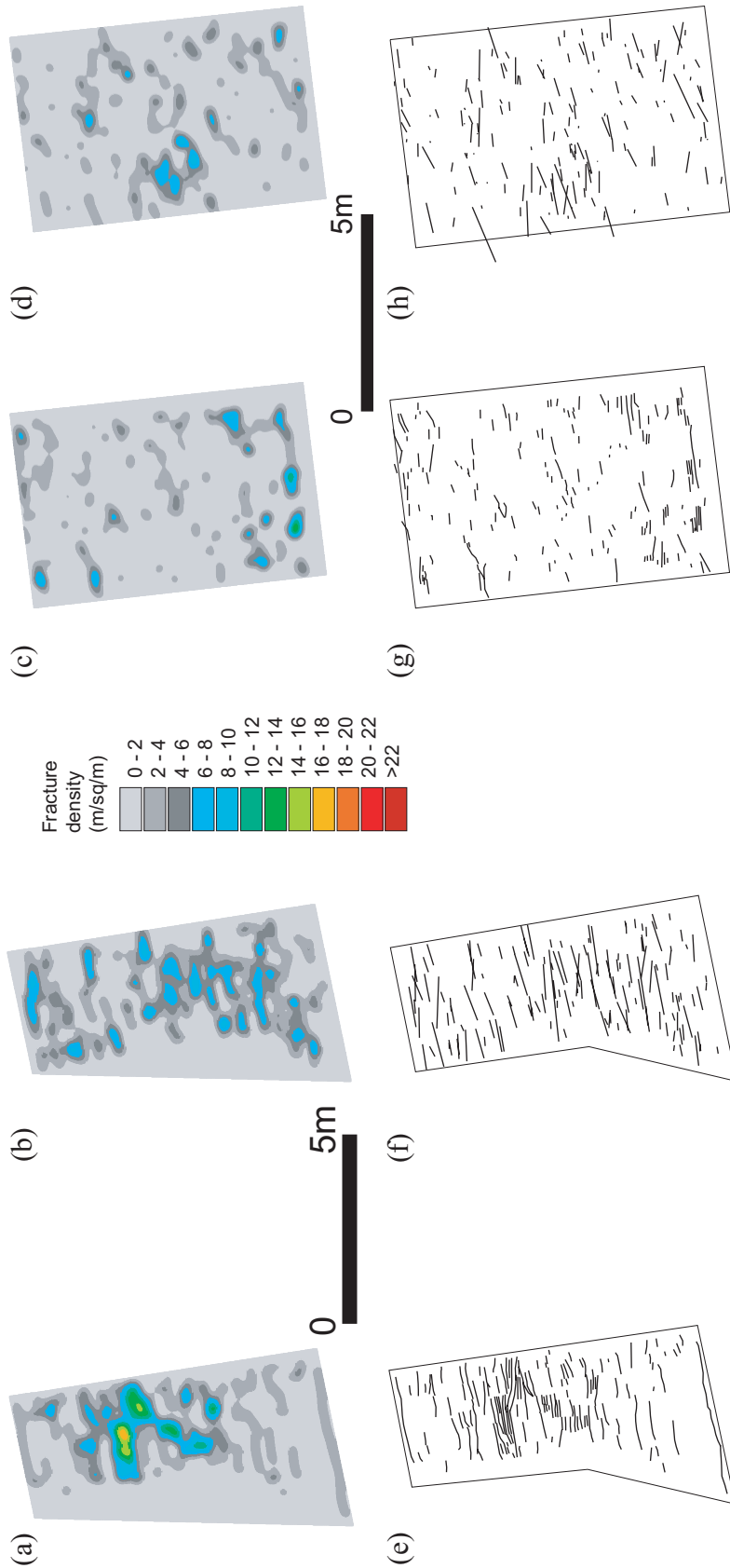


Figure A12: (a) Density map of transverse fractures for location M09. (b) Density map of simulated transverse fractures for location M019. The fractures for area M09 are extracted from the simulated fracture map generated for the entire Teton anticline. (c) Density map of transverse fractures for location M10. (d) Density map of simulated transverse fractures for location M10. The fractures for area M10 are extracted from the simulated fracture map generated for the entire Teton anticline. (e) Fracture map of transverse set for location M09. (f) Simulated fracture map of transverse set for location M09. (g) Fracture map of transverse set for location M10. (h) Simulated fracture map of transverse set for location M10.



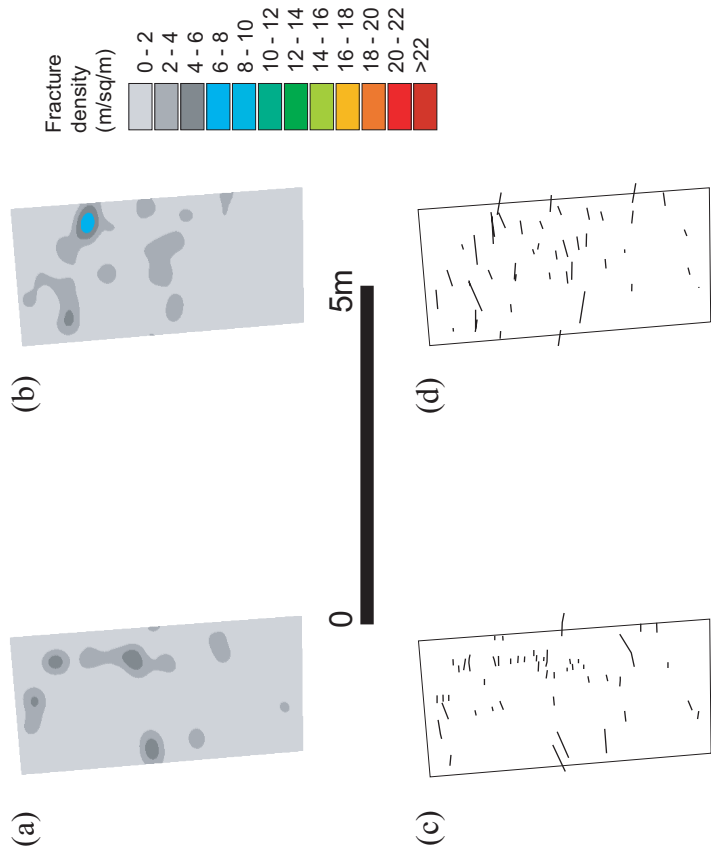


Figure A14: (a) Density map of transverse fractures for location M13. (b) Density map of simulated transverse fractures for location M13. The fractures for area M13 are extracted from the simulated map generated for the entire Teton anticline. (c) Fracture map of transverse set for location M13. (d) Simulated fracture map of transverse set for location M13. (e) Plot of density of sample versus simulated fractures for all the locations. Red line in the plot is a line of 45 degree slope, black line is the trendline fitted to data points. (f) Plot of length of sample versus simulated fractures for all the locations. Red line in the plot is a line of 45 degree slope, black line is the trendline fitted to data points. (g) Frequency distribution of length for transverse fractures of sample maps. (h) Frequency distribution of length for transverse fractures of simulated maps.

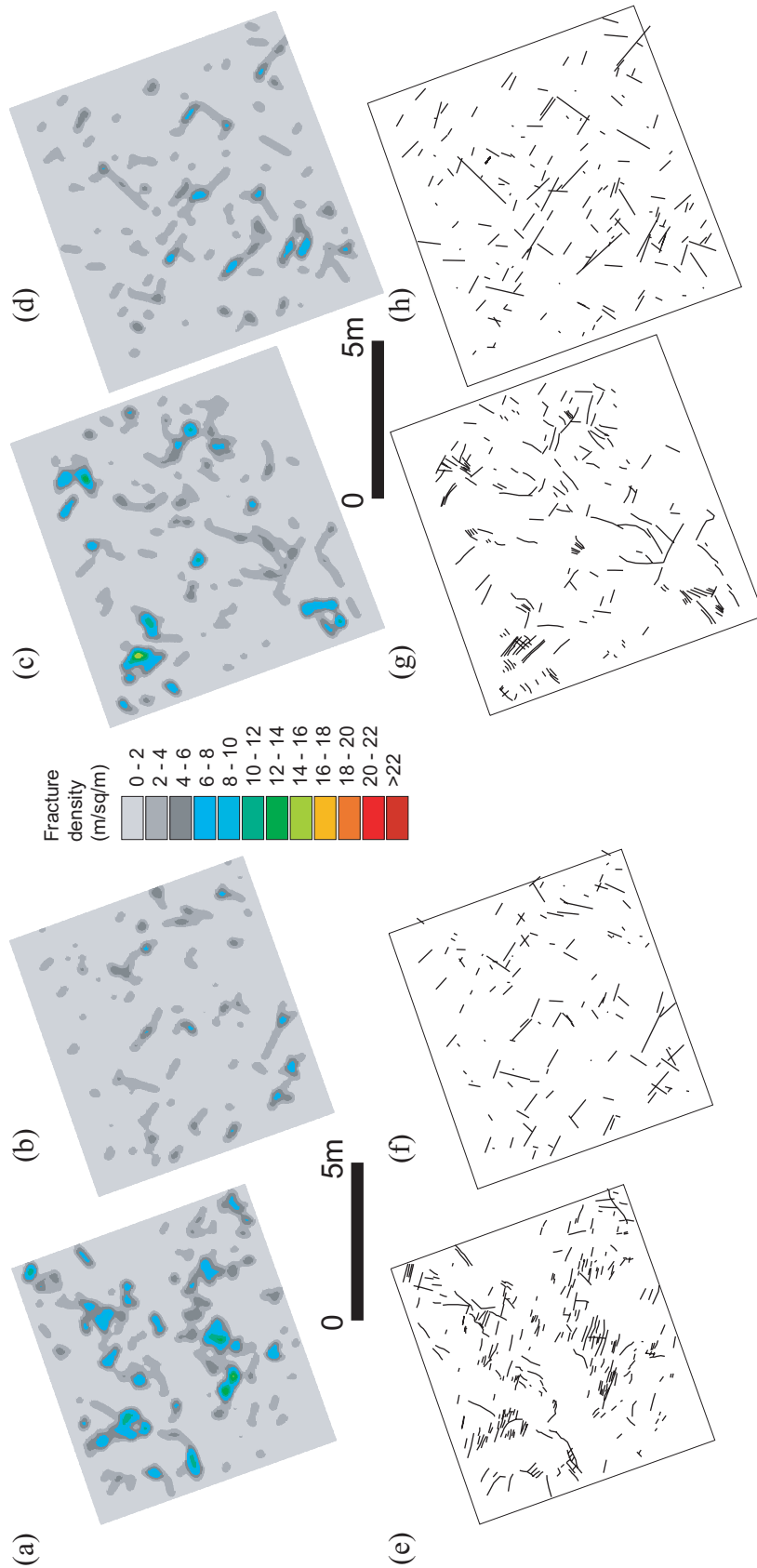


Figure A15: (a) Density map of oblique fractures for location M01. (b) Density map of simulated oblique fractures for location M01. The fractures for area M01 are extracted from the simulated map generated for the entire Teton anticline. (c) Density map of oblique fractures for location M02. (d) Density map of simulated oblique fractures for location M02. The fractures for area M02 are extracted from the simulated map generated for the entire Teton anticline. (e) Fracture map of oblique sets for location M01. (f) Simulated fracture map of oblique sets for location M01. (g) Fracture map of oblique sets for location M02. (h) Simulated fracture map of oblique sets for location M02.

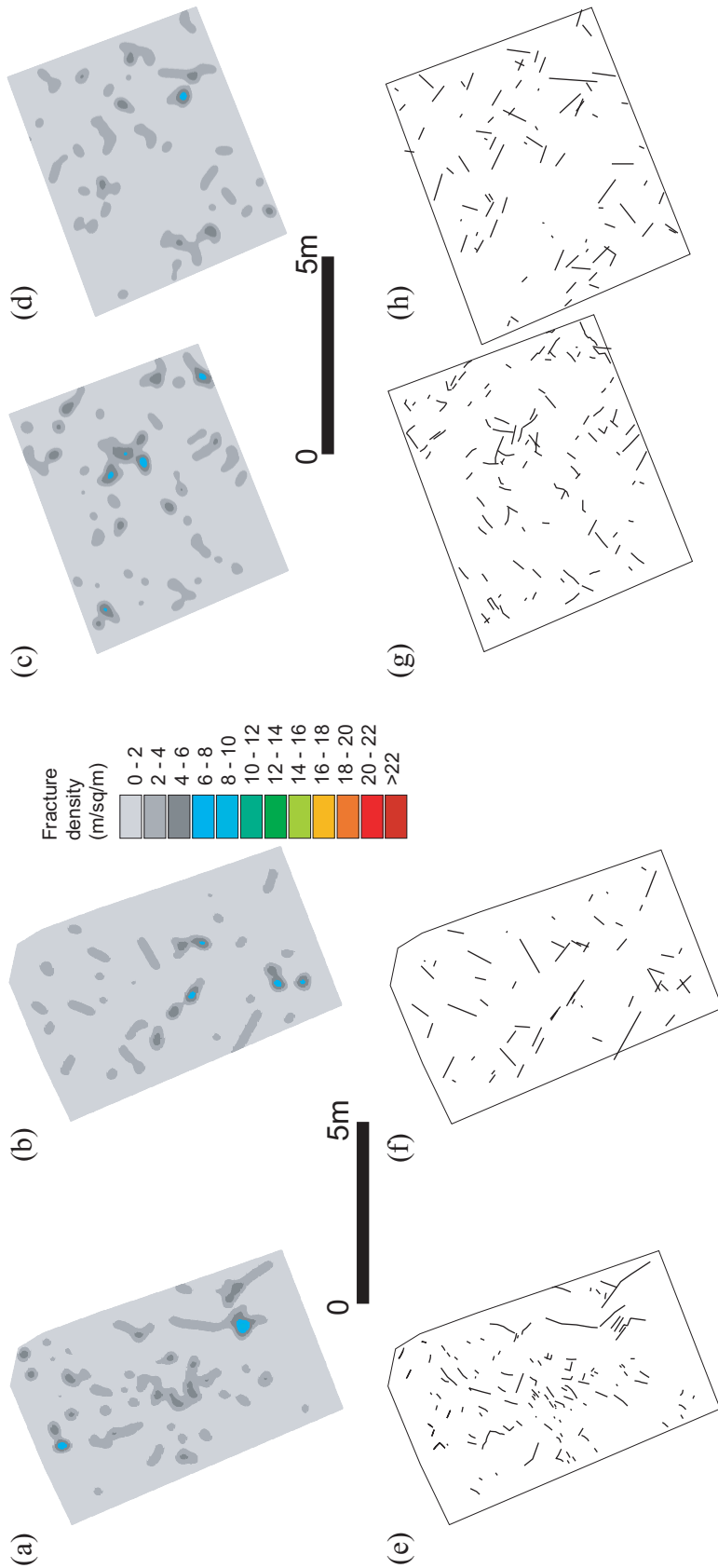


Figure A16: (a) Density map of oblique fractures for location M03. (b) Density map of simulated oblique fractures for location M03. The fractures for area M03 are extracted from the simulated map generated for the entire Teton anticline. (c) Density map of oblique fractures for location M04. (d) Density map of simulated oblique fractures for location M04. The fractures for area M04 are extracted from the simulated map generated for the entire Teton anticline. (e) Fracture map of oblique sets for location M03. (f) Simulated fracture map of oblique sets for location M03. (g) Fracture map of oblique sets for location M04. (h) Simulated fracture map of oblique sets for location M04.

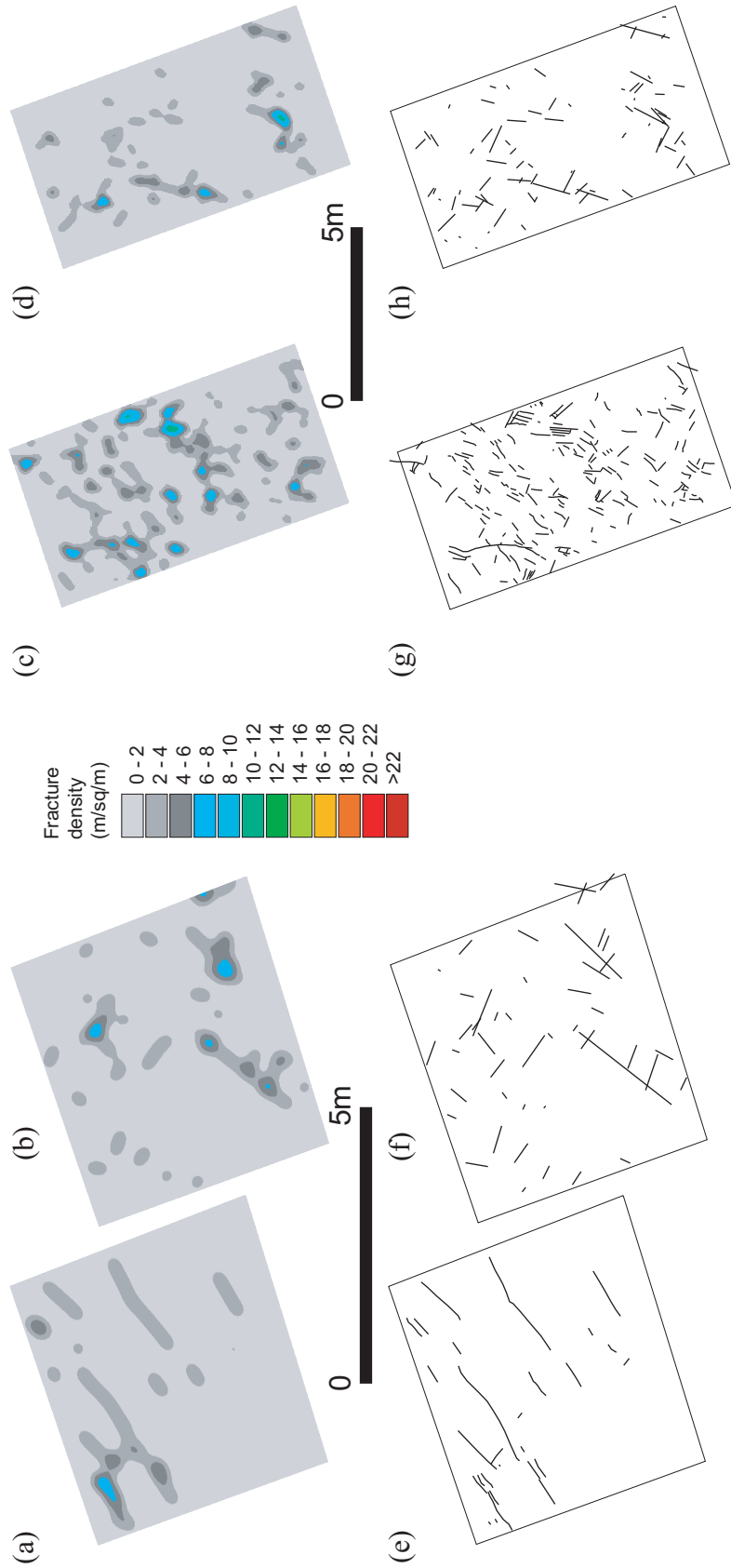


Figure A17: (a) Density map of oblique fractures for location M05. (b) Density map of simulated oblique fractures for location M05. The fractures for area M05 are extracted from the simulated map generated for the entire Teton anticline. (c) Density map of oblique fractures for location M06. (d) Density map of simulated oblique fractures for location M06. The fractures for area M06 are extracted from the simulated map generated for the entire Teton anticline. (e) Fracture map of oblique sets for location M05. (f) Simulated fracture map of oblique sets for location M05. (g) Fracture map of oblique sets for location M06 (h) Simulated fracture map of oblique sets for location M06.

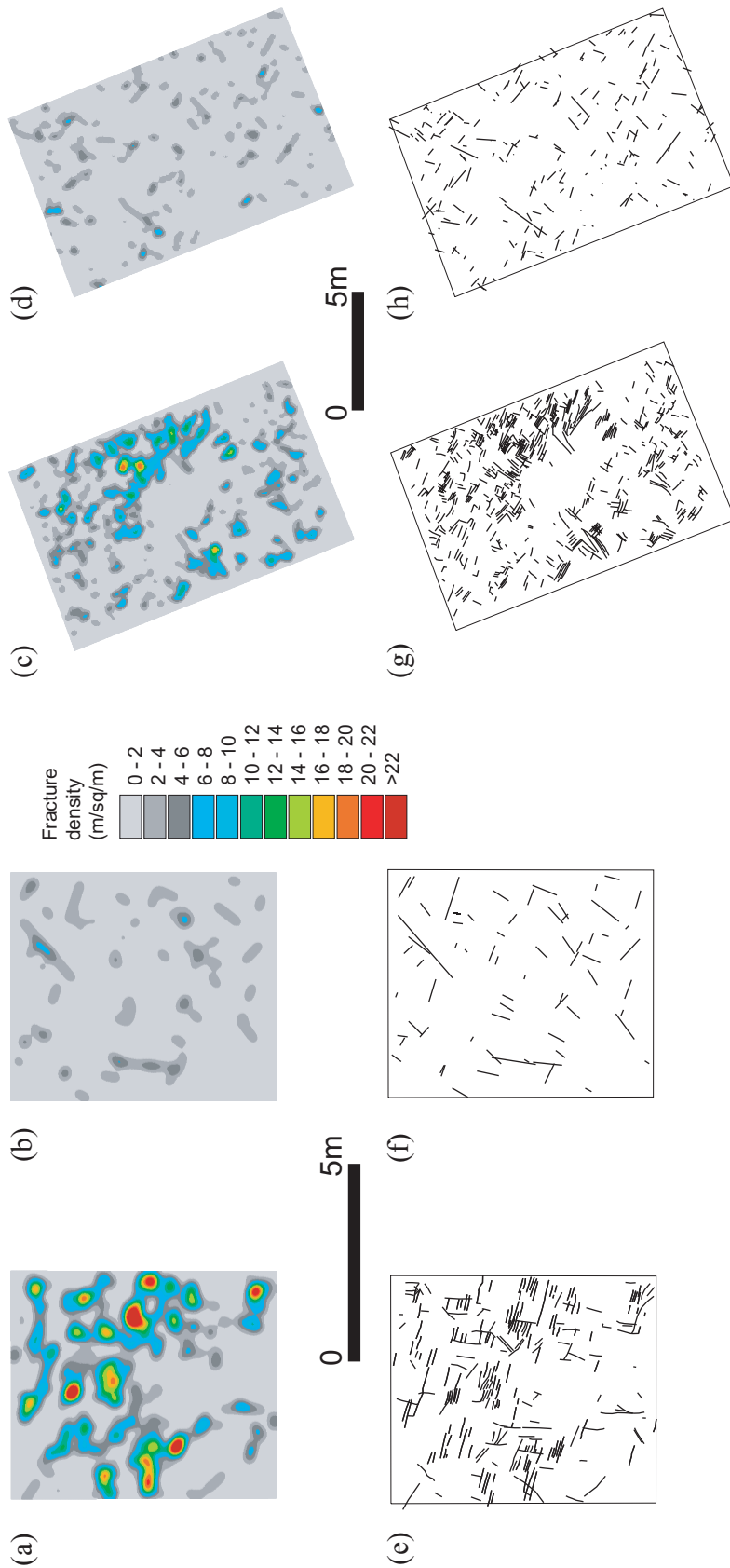


Figure A18: (a) Density map of oblique fractures for location M07. (b) Fractures for area M07 are extracted from the simulated map generated for the entire Teton anticline. (c) Density map of oblique fractures for location M08. (d) Fractures for area M08 are extracted from the simulated map generated for the entire Teton anticline. (e) Density map of oblique fractures for location M07. (f) Simulated fracture map of oblique sets for location M07. (g) Density map of simulated oblique fractures for the entire Teton anticline. (h) Simulated fracture map of oblique sets for location M08.

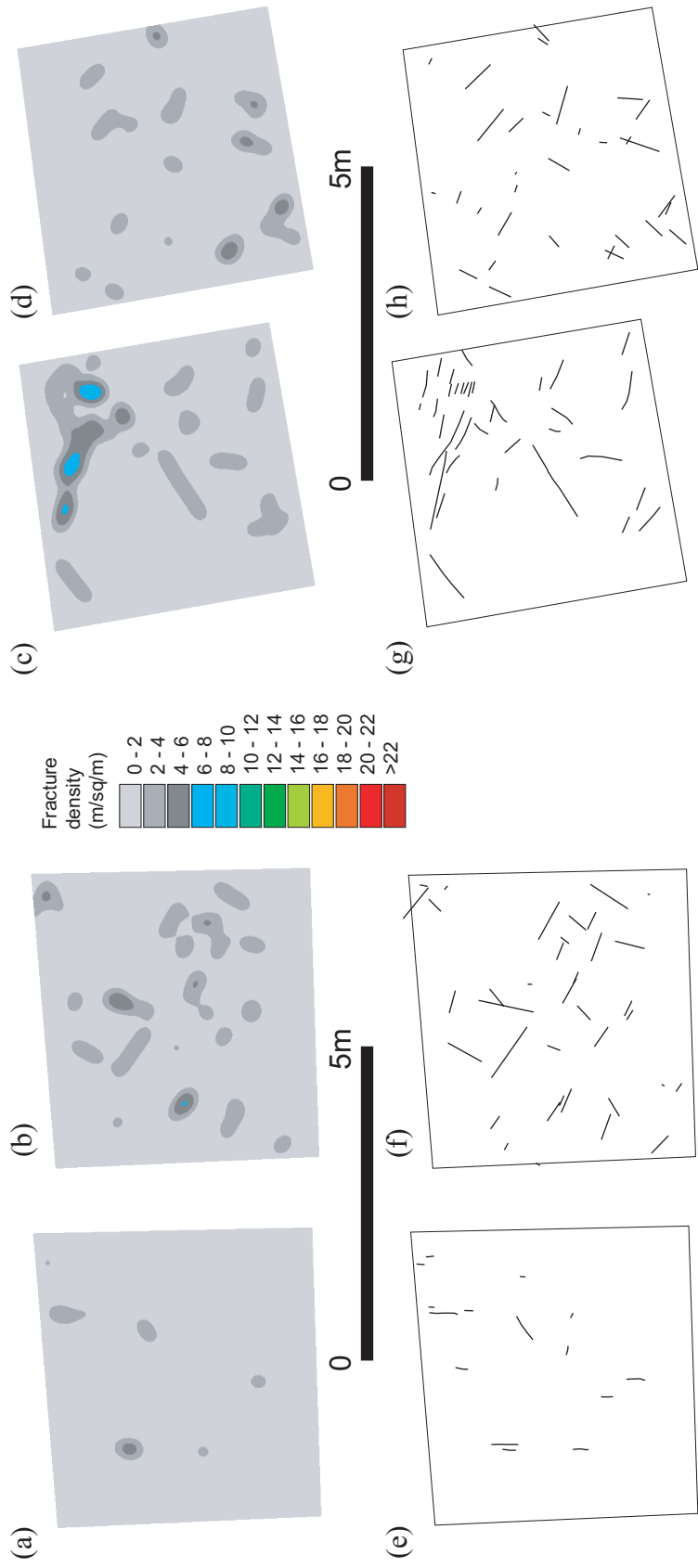


Figure A19: (a) Density map of transverse fractures for location M09. (b) Density map of simulated transverse fractures for location M09. The fractures for area M09 are extracted from the simulated map generated for the entire Teton anticline. (c) Density map of transverse fractures for location M10. (d) Density map of simulated transverse fractures for location M10. The fractures for area M10 are extracted from the simulated map generated for the entire Teton anticline. (e) Fracture map of transverse set for location M09. (f) Simulated fracture map of transverse set for location M09. (g) Fracture map of transverse set for location M10. (h) Simulated fracture map of transverse set for location M10.

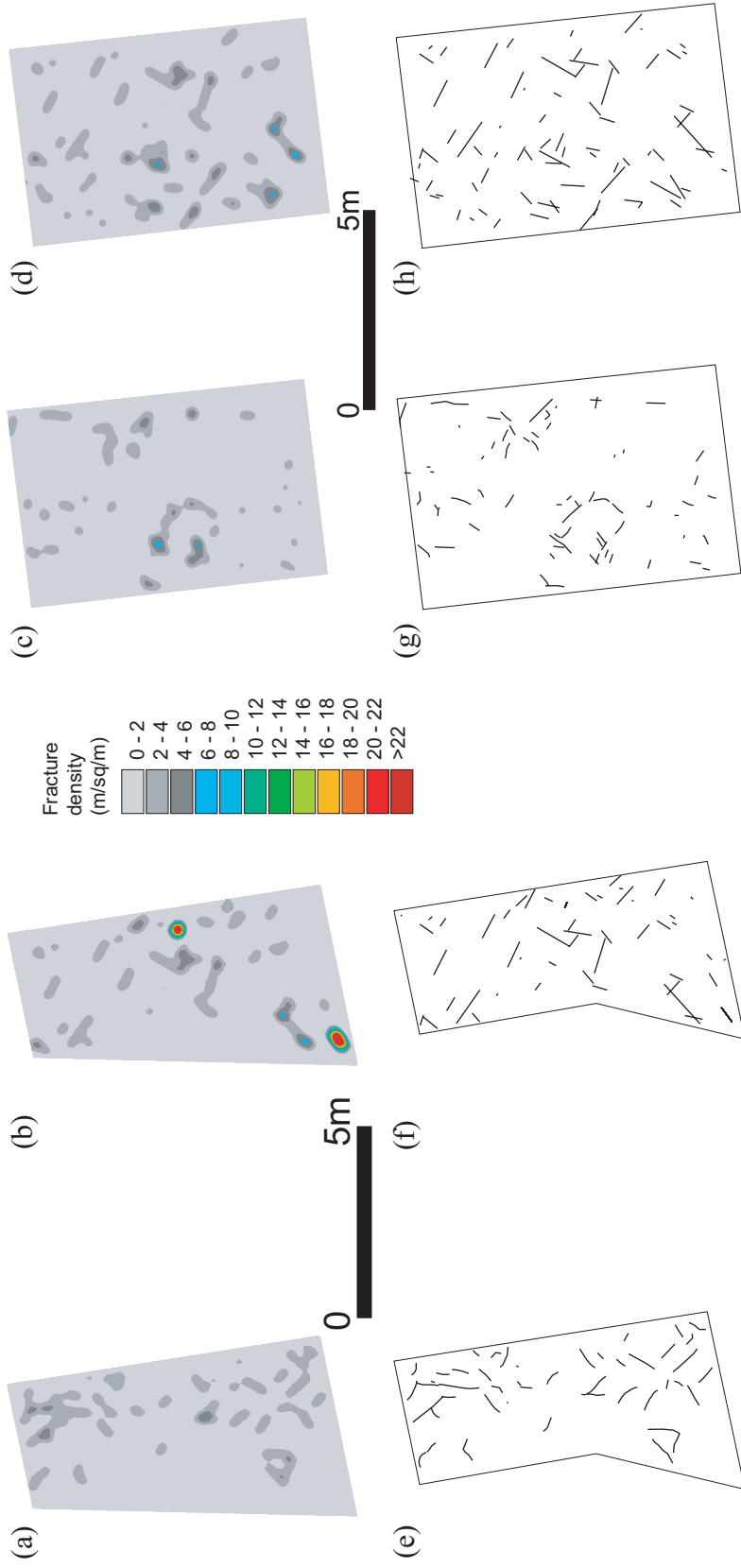


Figure A20: (a) Density map of oblique fractures for location M11. (b) Density map of simulated oblique fractures for location M11. The fractures for area M11 are extracted from the simulated map generated for the entire Teton anticline. (c) Density map of oblique fractures for location M12. (d) Density map of simulated oblique fractures for location M12. The fractures for area M12 are extracted from the simulated map generated for the entire Teton anticline. (e) Fracture map of oblique sets for location M11. (f) Simulated fracture map of oblique sets for location M11. (g) Fracture map of oblique sets for location M12. (h) Simulated fracture map of oblique sets for location M12.

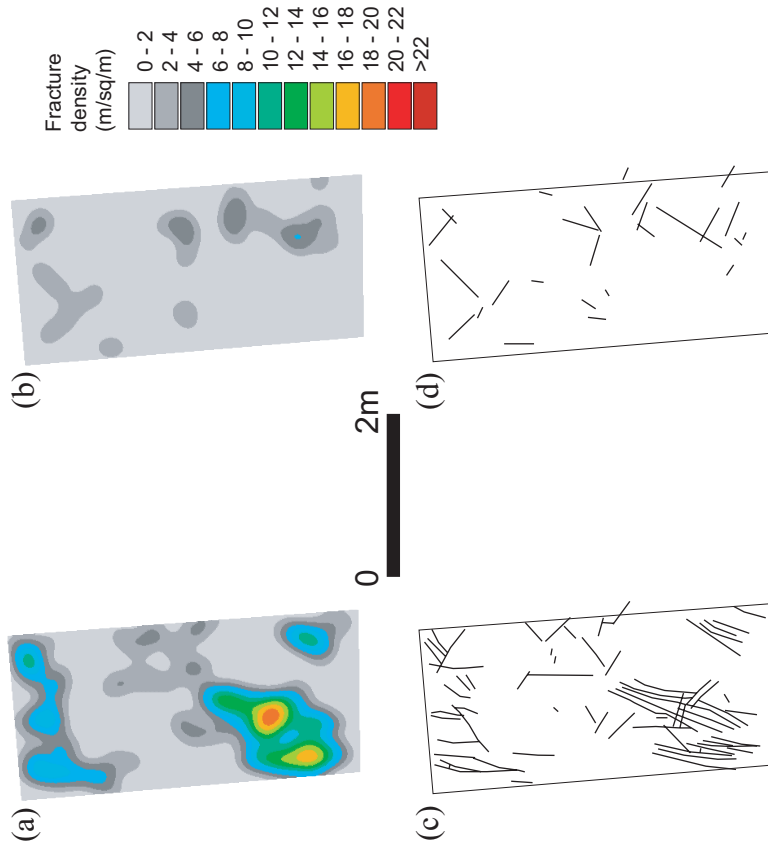


Figure A21: (a) Density map of oblique fractures for location M13. (b) Density map of simulated oblique fractures for location M13. The fractures for area M13 are extracted from the simulated map generated for the entire Teton anticline. (c) Fracture map of oblique sets for location M13. (d) Simulated fracture map of oblique sets for location M13.

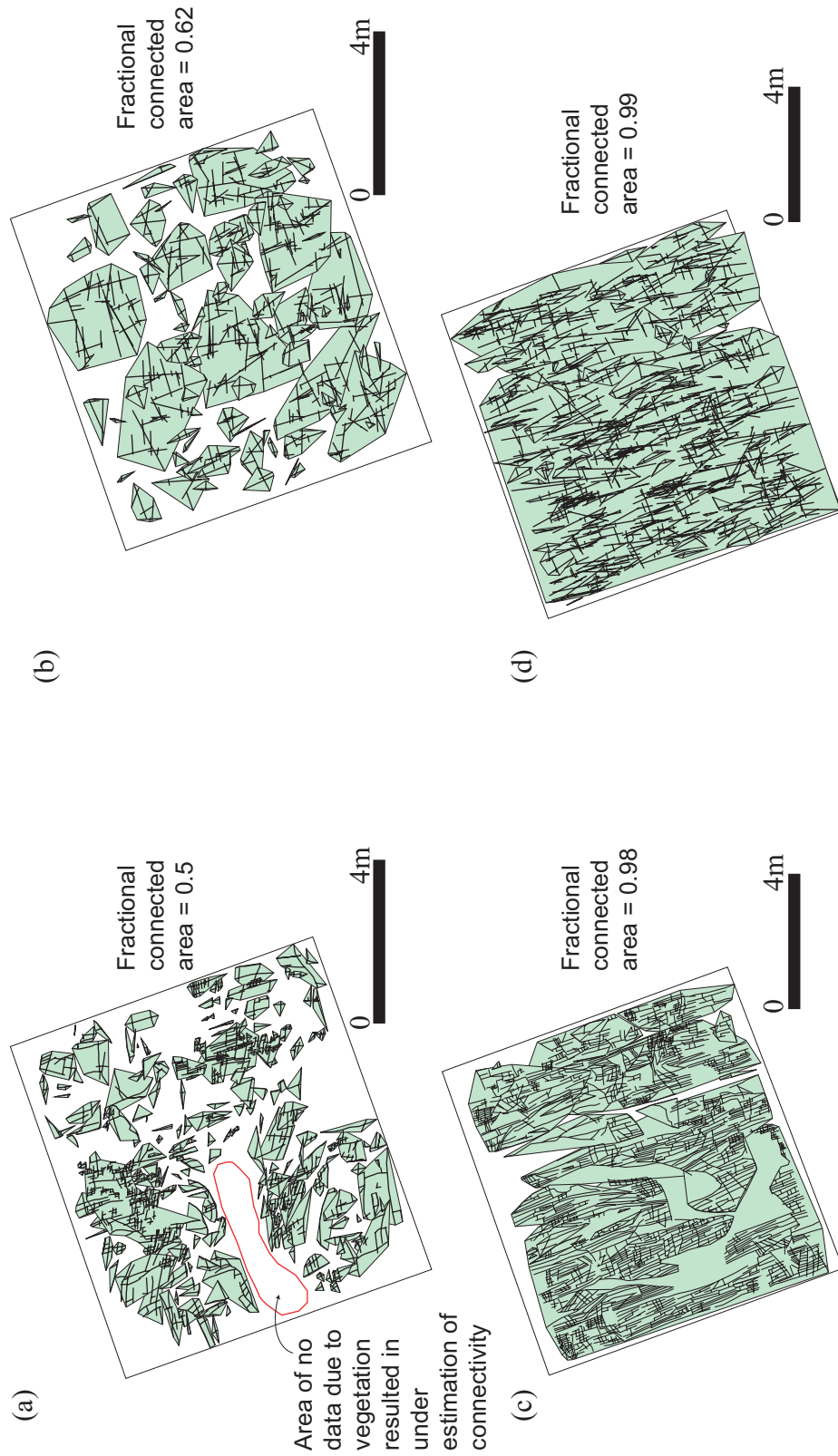


Figure A22: (a) Fracture cluster map for location M01. (b) Cluster map for fractures of location M01, extracted from the simulated map generated for the entire Teton anticline. (c) Fracture cluster map for location M02. (d) Cluster map for fractures of location M02, extracted from the simulated map generated for the entire Teton anticline.

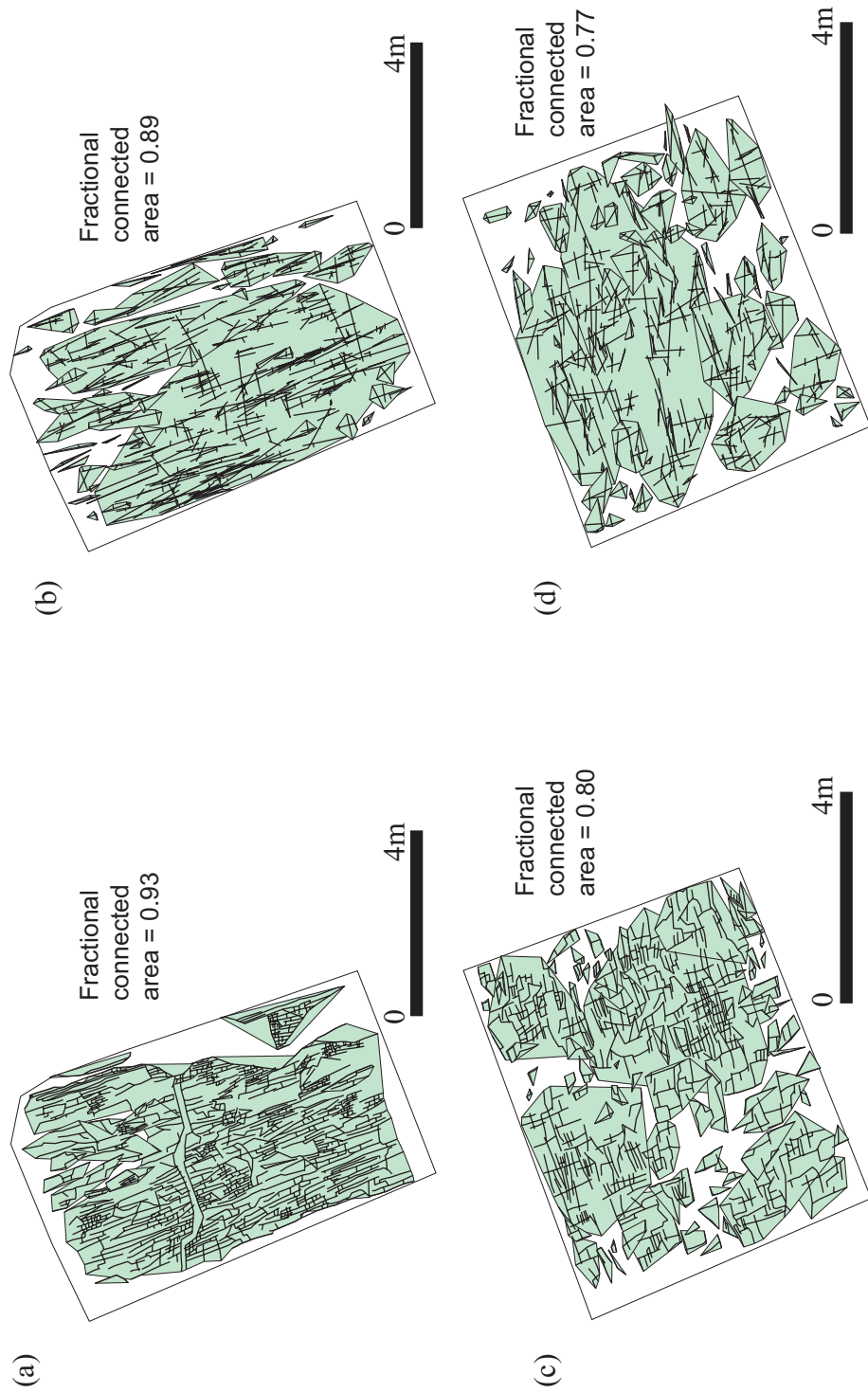


Figure A23: (a) Fracture cluster map for location M03. (b) Cluster map for fractures of location M03, extracted from the simulated map generated for the entire Teton anticline. (c) Fracture cluster map for location M04. (d) Cluster map for fractures of location M04, extracted from the simulated map generated for the entire Teton anticline.



Figure A24: (a) Fracture cluster map for location M05. (b) Cluster map for fractures of location M05, extracted from the simulated map generated for the entire Teton anticline. (c) Fracture cluster map for location M06. (d) Cluster map for fractures of location M06, extracted from the simulated map generated for the entire Teton anticline.



Figure A25: (a) Fracture cluster map for location M07. (b) Cluster map for fractures of location M07, extracted from the simulated map generated for the entire Teton anticline. (c) Fracture cluster map for location M08. (d) Cluster map for fractures of location M08, extracted from the simulated map generated for the entire Teton anticline.

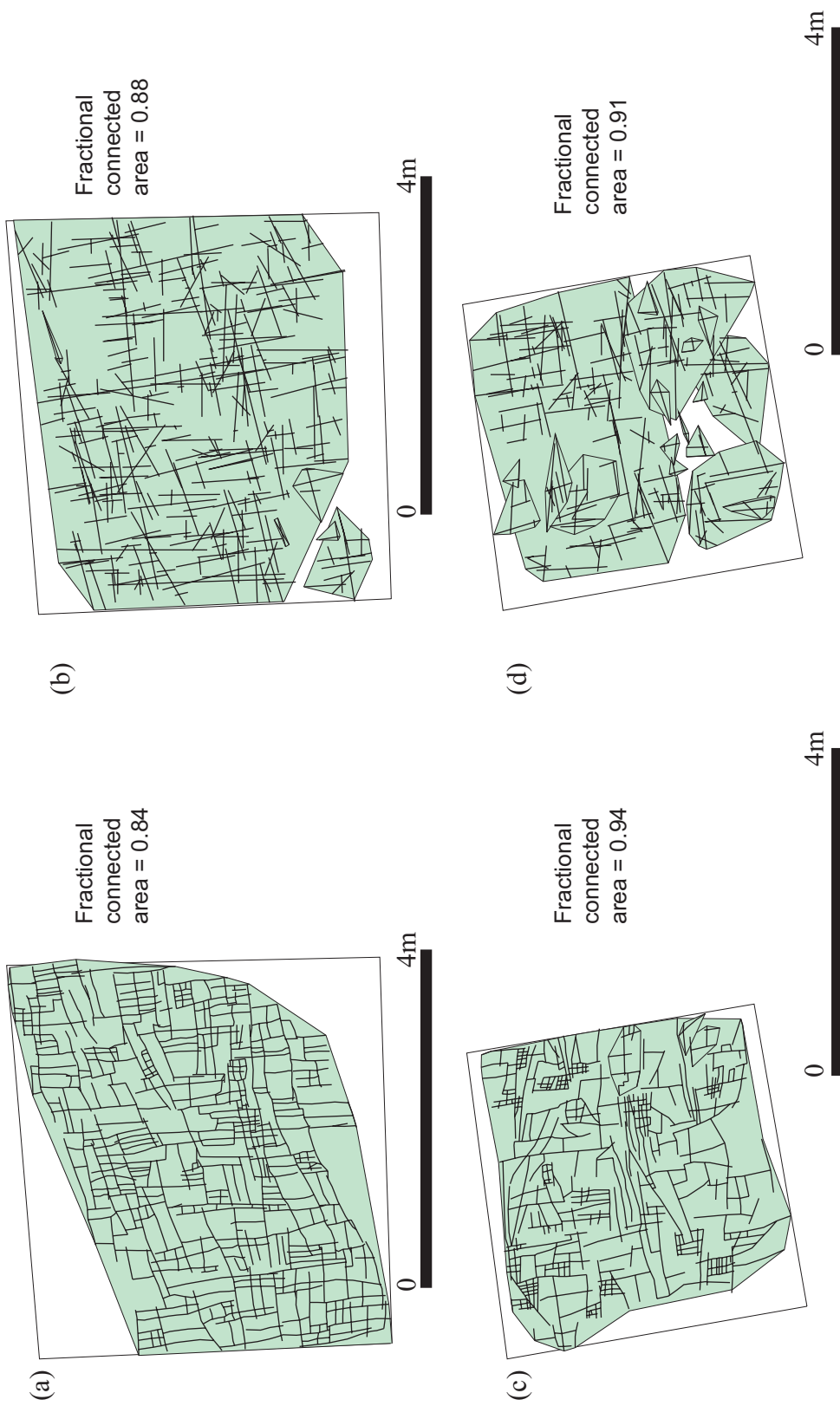


Figure A26: (a) Fracture cluster map for location M09. (b) Cluster map for fractures of location M09, extracted from the simulated map generated for the entire Teton anticline. (c) Fracture cluster map for location M10. (d) Cluster map for fractures of location M10, extracted from the simulated map generated for the entire Teton anticline.

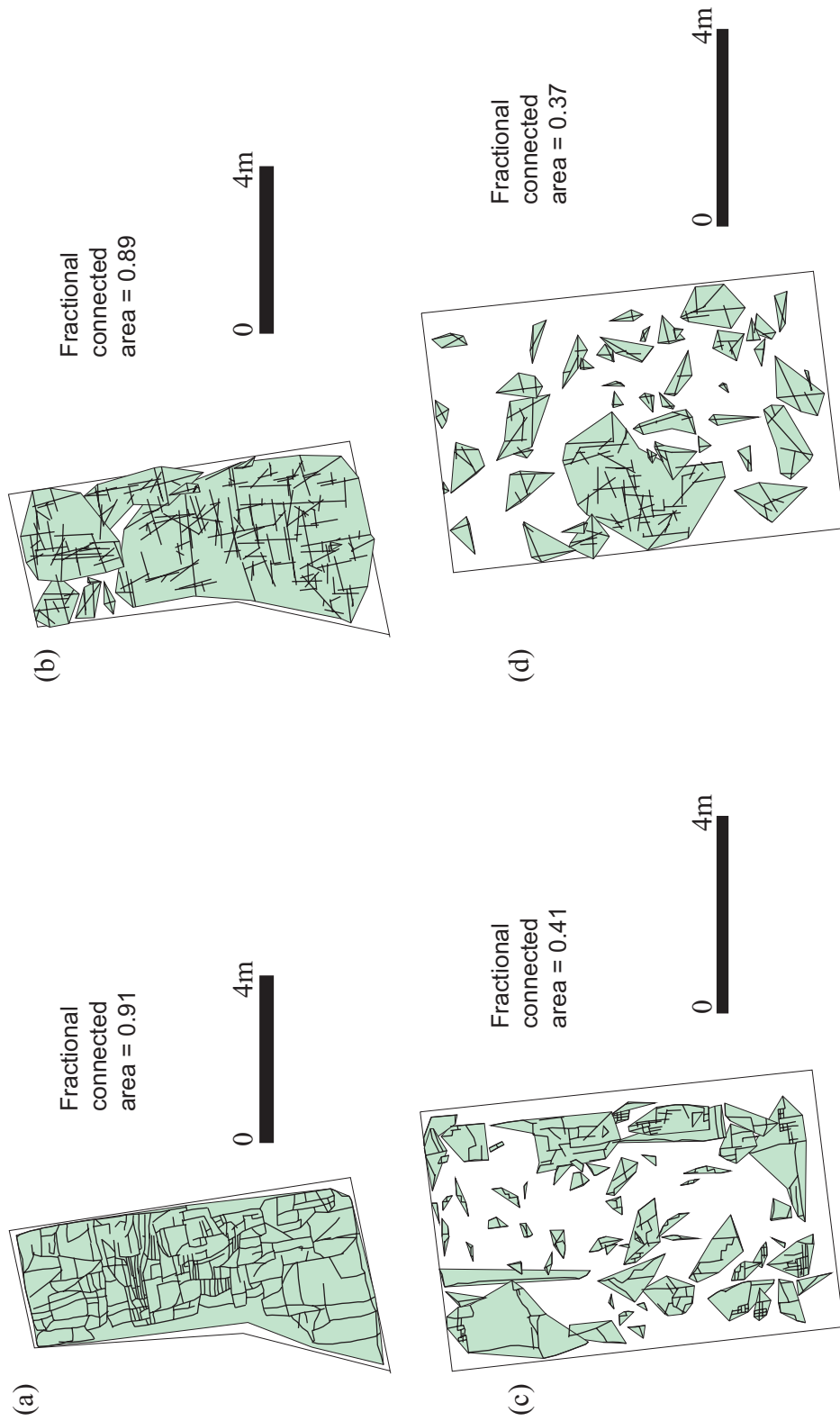


Figure A27: (a) Fracture cluster map for location M11. (b) Cluster map for fractures of location M11, extracted from the simulated map generated for the entire Teton anticline. (c) Fracture cluster map for location M12. (d) Cluster map for fractures of location M12, extracted from the simulated map generated for the entire Teton anticline.

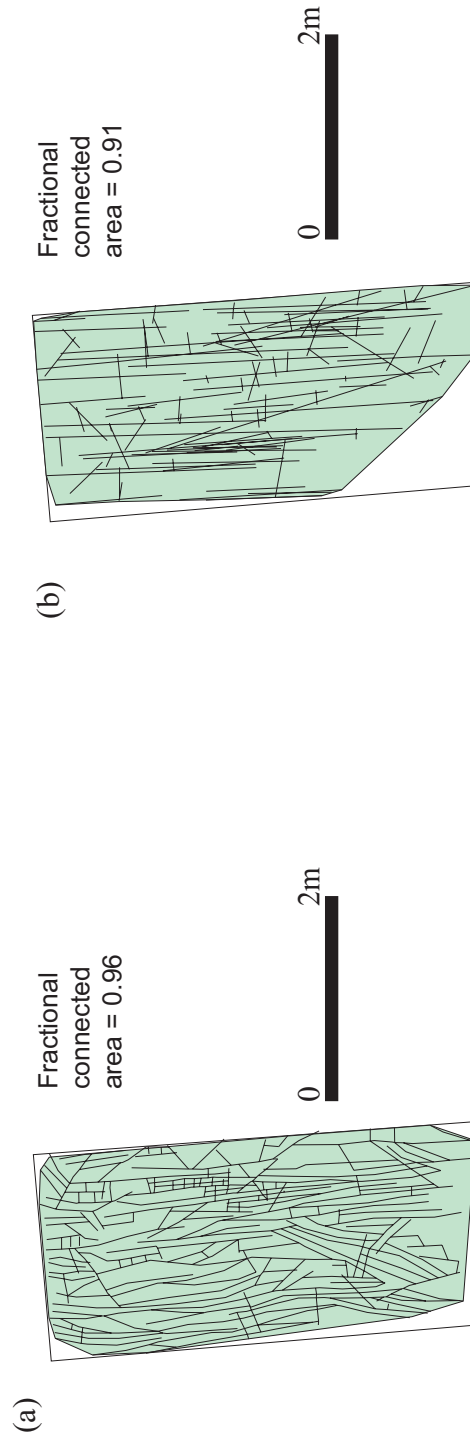


Figure A28: (a) Fracture cluster map for location M13. (b) Cluster map for fractures of location M13, extracted from the simulated map generated for the entire Teton anticline.